

Reduction of broadband trailing edge noise by serrations

Alexandros Vathylakis

Brunel University London

College of Engineering, Design and Physical Sciences



A dissertation submitted for the degree Doctor of
Philosophy

May 2015

Abstract

This thesis aims to investigate and reduce the aerodynamic noise source known as trailing edge noise, or airfoil self-noise, by using passive flow control techniques. Airfoil self-noise is produced when a turbulent boundary layer generated on an airfoil surface is scattered by the airfoil's trailing edge. The investigation is of experimental nature, conducted in the aeroacoustic as well as aerodynamic wind tunnel facilities at Brunel University London and the Institute of Sound and Vibration (ISVR) at the University of Southampton.

The research is relevant for any application in which airfoil blades encounter a smooth non-turbulent inflow and hence where trailing edge noise is a dominant noise source. Potential applications can therefore be fan or rotor blades in aero-engines, wind turbine blades or industrial cooling fans.

The approach taken for the reduction of trailing edge noise utilises passive flow control techniques through the use of trailing edge serrations and the additional support of porous materials. Both of the aforementioned are inspired by the owl's silent flight due to its unique wing structure. The research presented here can be divided in three parts:

The first part comprises an extensive assessment of the performance of non-flat plate trailing edge serrations for airfoil broadband noise and their aerodynamic performance in terms of lift and drag. It is found that serrations can realistically achieve noteworthy broadband airfoil self-noise reductions, however due to the fact that non-flat plate serrations are directly cut into the airfoil body, the blunt sections in the serration root produce an additional noise source of vortex shedding tonal noise.

The second part investigates the two flow mechanisms involved. Regarding the mechanism responsible for broadband noise and the subsequent reductions by the serration geometry, the turbulent boundary layer structures are studied in depth on a serrated trailing edge of a flat plate. Experimental techniques such as hot wire anemometry, liquid crystal flow visualisation, unsteady surface pressure measurements and noise measurements are used. A redistribution of the momentum and turbulent energy near the sawtooth tip and side edges appears to reduce the trailing edge noise scattering-efficiency of the hydrodynamic pressure waves.

For the study of the flow mechanism responsible for the vortex shedding tonal noise increase, noise and velocity measurements along with flow visualisation techniques are

used for the identification and further understanding of this noise source. A highly three-dimensional wake-flow could be identified in the wake past the serration gap, which differs from the longitudinal vortices shed from a straight blunt serration root.

The third part presents the concept of poro-serrated trailing edges as a novel method to substantially improve the overall noise performance of the non-flat plate trailing edge serration type. The use of porous metal foams or thin brush bundles which fill the interstices between adjacent members of the sawtooth can completely suppress the bluntness-induced vortex shedding noise. Most importantly, a turbulent broadband noise reduction of up to 7 dB can be achieved without compromising the aerodynamic performances in lift and drag. The new serrated trailing edges do not cause any noise increase throughout the frequency range investigated here. Through noise and velocity measurements near the trailing edge of an airfoil, the reduction of the broadband noise is found to be primarily caused by the sawtooth geometry. The new serrated trailing edges have the potential to improve the industrial worthiness of the serration technology in achieving low noise radiation.

Acknowledgements

I would like to thank my supervisor Dr. Tze Pei Chong for making this project and great experience possible. I am grateful for the important support, guidance and intellectual advice during this project work, and not to mention his constant availability and good laughs in between the work.

I would like to express my gratitude to Professor Phillip Joseph for providing the test facility at the University of Southampton and his precious advice, and my second supervisor Dr. Jan Wissink for his support whenever it was needed.

I would also like to thank the Engineering and Physical Sciences Research Council for funding this PhD research, and Dr. Averil Horton from the Research and Development Office at Brunel University, for supporting the work towards a possible industrial use.

The technical support provided in the laboratories for preparing and conducting all the experiments was nothing but crucial. Many thanks to the technical staff, Peter Wilson, Kevin Robison, Keith Pamment, Paul Yates, Clive Barret, Chris Allan, Arumugam Ratnasingam, and the mechanical engineering-stores team at Brunel University.

I am grateful to my fellow students and friends Andreas, Bhupinder, Chioma, Eirinaios, Elisa, Emad, Giannis, Laith, Saarim and William who kept me company and supported me during the countless hours of experiments in the laboratories.

I feel blessed to have such friends by my side during all the years at Brunel. Special thanks to Christos, Nikos and Kyriakos, for the truly good company during the undergraduate and postgraduate study period, and Andrea, thank you for this invaluable support in the last years.

Finally, I would like to thank my parents for their tremendous support through all the years, at all times. It is probably beyond words to express your contribution and my gratefulness.

Table of Contents

Chapter 1 Introduction	1
1.1 Aircraft noise	1
1.2 Aircraft noise sources	5
1.3 Wind turbine noise	7
1.4 Aims and objectives.....	10
1.5 Thesis structure	10
1.6 Novelty of research	12
Chapter 2 Literature Review	14
2.1 Aerodynamic sound generation	14
2.1.1 Lighthill’s analogy of aerodynamic sound in free space and the introduction of solid boundaries.....	14
2.1.2 Introduction to airfoil self-noise	16
2.1.3 Airfoil self-noise mechanisms by Brooks et al.	17
2.2 A review of relevant boundary layer theory	19
2.2.1 Wall regions and layers of the turbulent boundary layer	19
2.2.2 Turbulent boundary layer flow structures	21
2.2.3 Predicting turbulent boundary layer broadband noise with the relationship of surface pressure statistics using Amiet’s model	28
2.2.4 The mechanism of laminar boundary layer tonal noise	30
2.2.5 Bluntness noise	33
2.3 Theoretical Background of trailing edge serrations	34
2.3.1 Trailing edge treatments and Biomimicry	34
2.3.2 Howe’s theory.....	37
2.3.3 Serrations and related passive flow control techniques for TE noise reduction	39
2.3.4 Porous materials for airfoil self-noise reduction	46
2.3.5 Trailing edge serrations and laminar boundary layer noise	48
2.4 Discussion	50
Chapter 3 Experimental Setup	51
3.1 Aeroacoustic test facilities	53
3.1.1 Facility at The University of Southampton	53
3.1.1.1 Southampton Institute of Sound and Vibration DARP Rig.....	53
3.1.1.2 DARP Rig microphone array	54

3.1.2 Facility at Brunel University	55
3.1.2.1 Brunel anechoic wind tunnel microphone setup and acoustic camera	57
3.1.2.2 Set up of test models at the Brunel anechoic wind tunnel	58
3.1.3 Measurement metrics and considerations.....	60
3.1.3.1 Acoustic measurement metrics	60
3.1.3.2 Angle of attack correction.....	61
3.2 Aerodynamic testing facilities	62
3.2.1 AF10 Air bench.....	62
3.2.1.1 AF10 Air bench	62
3.2.1.2 Setup of the unsteady surface pressure measurements on the flat plate	66
3.2.1.3 Liquid crystal flow visualisation performed on the flat plate models.....	66
3.2.2 Aerodynamic wind tunnel	68
3.2.2.1 Open circuit aerodynamic wind tunnel.....	68
3.2.2.2 Three component force balance	69
3.3 Airfoil design.....	70
3.4 Water tunnel	73
3.5 Hot wire anemometry with traverse mechanism	74
Chapter 4 An assessment of noise and lift/drag performance of non-flat trailing edge plate serrations	78
4.1 Configurations of the non-flat plate trailing edge	79
4.2 Trailing edge serrations' PWL spectra	82
4.3 Trailing edge serrations' PWL contours	83
4.4 Trailing edge serrations' OAPWL comparison.....	87
4.5 Aerodynamic forces produced by non-flat plate serrations	91
4.6 Discussion	94
Chapter 5 Investigation of the turbulent boundary layer broadband noise and vortex shedding mechanism of non-flat plate trailing edge serrations	96
5.1 Details of test models.....	98
5.2 Noise results	99
5.3 Wall heat transfer on a serrated trailing edge	101
5.4 Unsteady wall pressure on a serrated trailing edge	104
5.4.1 Power spectral density	104
5.4.2 Streamwise and spanwise coherence and phase functions.....	108
5.5 Turbulent boundary layer developed on a serrated sawtooth trailing edge	
5.5.1 Time-averaged turbulence quantities	111

5.5.2 Conditional-averaged velocity perturbations, rms velocity fluctuations and Reynolds shear stresses	115
5.5.3 Coherent-like structure analysis	118
5.5.3.1 General characteristics of the coherent-like structures on a two-dimensional turbulent boundary layer	118
5.5.3.2 Development of the coherent-like structures near the sawtooth side edges	123
5.5.3.3 Development of the coherent-like structures near the sawtooth tip	125
5.6 Identification of vortical structures along the serration edge	130
5.7 Investigation of the vortex shedding mechanism past a non-flat plate serrated trailing edge	136
5.7.1 Water tunnel dye flow visualisation	136
5.7.2 Strouhal number dependency and spanwise coherence in the near wake of non-flat plate serrations	137
5.8 Discussion	140
5.9 Outlook	142
Chapter 6 Poro-Serrated trailing edge devices for airfoil self-noise reduction	144
6.1 Preliminary concepts which returned only partial success	145
6.2 Poro-serration concepts and models	147
6.3 Poro-serration experimental results	150
6.3.1 Noise results	150
6.3.2 Suppression of the bluntness-induced vortex shedding tonal noise	152
6.3.3 Broadband noise reduction	154
6.3.4 Mechanism of broadband noise reduction – by Serration, or by Porosity?	158
6.4 Aerodynamic forces produced by poro-serrated trailing edges	162
6.5 Near wall velocity power spectral density and its implication to the Δ SPL noise contour maps	165
6.6 Discussion	170
Chapter 7 Conclusions and further work	173
7.1 Conclusions overview	173
7.1.1 Non-Flat plate serrations (Chapter 4)	174
7.1.2 Mechanism of broadband noise reduction by serrated trailing edge (Chapter 5) ..	175
7.1.3 “Poro-serrated” trailing edge	176
7.2 Suggestions for future work	178
References	179

Symbols

$2h$	<i>serration length (root-to-tip distance), mm</i>
b	<i>Corcos constant</i>
c	<i>speed of sound, ms^{-1}</i>
C	<i>airfoil chord length, m</i>
f	<i>frequency, Hz</i>
I_y	<i>spanwise correlation length, mm</i>
p	<i>static pressure, Pa</i>
P'	<i>wall pressure fluctuation, Pa</i>
P'_{rms}	<i>root mean square value of the wall pressure, Pa</i>
s	<i>streamwise extent of porous material, mm</i>
S_{pp}	<i>far-field noise, dB/Hz</i>
S_{qq}	<i>wall pressure spectra, dB/Hz</i>
t	<i>time, s</i>
U	<i>mean flow velocity, ms^{-1}</i>
U_c	<i>convection velocity of the turbulent eddies, ms^{-1}</i>
U_m, V_m	<i>mean values for the U and V components of the velocity, ms^{-1}</i>
U_∞	<i>freestream velocity, ms^{-1}</i>
\tilde{u}, \tilde{v}	<i>ensemble-averaged velocity perturbations, ms^{-1}</i>
u', v'	<i>ensemble-averaged rms velocity fluctuations, ms^{-1}</i>
$\langle uv \rangle$	<i>ensemble-averaged Reynolds shear stress, ms^{-1}</i>
x	<i>streamwise direction measuring from the airfoil leading edge, mm</i>
y	<i>wall-normal direction, mm</i>
z	<i>spanwise direction, mm</i>
α	<i>angle of attack for the airfoil, deg</i>
γ^2	<i>spanwise coherence function</i>
δ	<i>boundary layer thickness, mm</i>
δ^*	<i>boundary layer displacement thickness, mm</i>
$\Delta\psi$	<i>difference in fluctuating spectral density measured by the surface-mounted hot-film, dB</i>
ε	<i>bluntness of the saw tooth trailing edge at the root region, mm</i>
λ	<i>serration period, mm</i>

θ	<i>polar angles of the microphone relative to the jet flow centerline, deg</i>
θ_a	<i>angles defining the observers point, deg</i>
ξ	<i>fluctuating spectral density measured by a surface-mounted hot-film sensor,</i>
<i>dB</i>	
ϕ'	<i>fluctuating velocity spectral density, $(\text{ms}^{-1})^2/\text{Hz}$</i>
φ	<i>serration angle, deg</i>
$\langle \rangle$	<i>ensemble-averaged value</i>

Abbreviations

SPL	sound pressure level, dB
PWL	sound power level, dB
OAPWL	overall sound power level, dB
T-S	Tolmien-Schlichting (T-S) instability waves

List of Figures

Figure 1.1 The evolution of the noise emissions of a low by-pass ratio engine (left) and a high by-pass ratio engine.	3
Figure 1.2 The historical development of civil aircraft noise	4
Figure 1.3 Major noise sources of the airframe and engine of a civil aircraft.	5
Figure 1.4 Breakdown of aircraft noise sources during take-off and landing	6
Figure 1.5 Typical noise emissions of a wind turbine over specified distances	7
Figure 1.6 Historical trend of wind turbine size, also compared to the size of a passenger aircraft. .	8
Figure 1.7 Variation of noise levels with a) changing rotor diameter and b) tip speeds.	9
Figure 2.1 Airfoil self- noise mechanisms as defined by Brooks et al. (1989) where a) TBL-TE Noise, b) LBL-TE Noise, c) BTE noise, d) stall noise and e) tip vortex noise.	20
Figure 2.2 Division of various layers in terms of $y^+ = y\delta\nu$ and $y\delta$ at $Re=104$ (from Pope (2011)) ..	21
Figure 2.3 Low speed streaks using hydrogen-bubble wire visualisation. These motions of lower-speed fluid are circled in red. [Sabatino (2014)].....	23
Figure 2.4 $u'-v'$ quadrant division	24
Figure 2.5 a) Anatomy of hairpin eddy attached to the wall; b) streamwise, wall-normal plane view of the hairpin eddy signature [Adrian et al (2000)].	26
Figure 2.6 Conceptual scenario of hairpin vortices on induced low speed fluid, attached to the wall and growing in an environment of overlying larger hairpin packets [Adrian et al. 1991]]	27
Figure 2.7 Comparison of the surface and far field pressure spectra a) for a turbulent boundary layer, b) For laminar boundary layer [Roger and Moreau (2009)]	29
Figure 2.8 Illustrations of the (a) tonal frequencies f_s (main tonal frequency) , f_n (discrete frequencies) and $f_{n_{max}}$ (dominant discrete frequency) and (b) scaling law off s plotted by Chong et al (2012) based in the formulas by Paterson (1973) and Tam (1974).	30
Figure 2.9 Aeroacoustic feedback models proposed in the literature for the generation of airfoil tonal noise. Model A is based on Arbey and Bataille (1983), Model B is based on Descquwntes et al. (2007) and Model C is based on Tam (1974).	31
Figure 2.10 The owl's main characteristics for the achievement of silent flight [Geyer et al (2011)]	34
Figure 2.11 Serrations at the outer vane (left) and fringes at the inner vane (right) from barn owl feathers with magnifications [Bachmann (2010)]	35
Figure 2.12 Figure 2.11.2 Scaled third octave band sound pressure levels from flyover measurements of a barn owl, a harris hawk and a common kestrel.	36
Figure 2.13 Parameters of the trailing edge saw-tooth geometry	37
Figure 2.14 Non-dimensional acoustic spectrum according to Howe's theory [1991a,1991b] comparing a straight trailing edge with various serrations geometries of varying λ/h . [Gruber 2012]	39
Figure 2.15 Investigation by Oerlemans (2009) on the noise reduction tested on a full scale wind turbine using trailing edge treatments	40
Figure 2.16 (a) Brush test set up on flat plate by Herr (2006) and (b) NACA 65 trailing edge brushes by Finez (2010)	41
Figure 2.17 Iso-contours for the visualisation of turbulent structures past a straight edge (left) and the serrated TE (right).[Jones and Sandberg (2010)].	42
Figure 2.18 Flat plate-type insert serrations on airfoil (left); Noise spectra (dB) for $\lambda = 3mm$, $h = 15mm$ at $\alpha = 5^\circ$ (right) by Gruber et al [2006].	42

Figure 2.19 (a) flat plate configuration and flat plate trailing edge serration attachment by Moreau et al (2012) and (b) the corresponding far-field acoustic spectra for $U_\infty=38 \text{ ms}^{-1}$	43
Figure 2.20 (a) Illustrations of a non-flat plate serrated trailing edge and their serration parameters. (b) Colormap of the sound pressure level (ΔSPL) of a serrated trailing edge at $\alpha=4.2^\circ$, where positive values show a noise increase when compared to a straight airfoil trailing edge and vice versa.....	44
Figure 2.21 Coherent structures on non-flat plate serrated trailing edge of a NACA 0012 [Pröbsting (2012)]	45
Figure 2.22 Fully porous airfoils as investigated by Geyer et al (2010a, 2010b)	46
Figure 2.23 Noise performance (sound pressure level scaled with U^5) of airfoils with varying flow resistivity as a function of the chord based Strouhal number, for two s/C values at angle of attack 0° . (Black dots represent non-porous reference airfoil). [Geyer and Sarradj (2014)]...	48
Figure 2.24 Sound pressure level spectra at $\alpha=1.4^\circ$ for four serration types in comparison with the baseline straight trailing edge (dotted line) From Chong et al (2010).....	49
Figure 3.1 DARP Rig elevation view of wind tunnel facility	53
Figure 3.2 a) Darp Rig Nozzle exit with mounted airfoil; (b) Microphone array and test section inside the anechoic chamber.	54
Figure 3.3 Plan, side and front views of the aeroacoustic wind tunnel facility and the anechoic chamber.....	55
Figure 3.4 Distributions of the turbulence intensities at 8 mm downstream of the nozzle exit plane at jet velocity of (a) 10 ms ⁻¹ , (b) 20 ms ⁻¹ , and (c) 30 ms ⁻¹	56
Figure 3.5 Frequency response spectra of the free field microphones used (upper lines) where (a) Brüel & Kjær ½ inch Falcon microphones at the DARP rig and (b) the PCB 377B02 microphones used at Brunel University.	56
Figure 3.6 Airfoil set-up at the anechoic wind tunnel at Brunel University; b) Experimental setup for the measurements of self-noise produced by a flat plate;.....	58
Figure 3.6 Sketch of the AF10 flat plate set up	63
Figure 3.7 Drawing of the serrated Perspex flat plate for the surface pressure measurements through the designed tapings. The same plate was used for hot-wire anemometry measurements. Dimensions displayed in millimetres.	64
Figure 3.8 a) Remote microphone arrangement b) An example of wall pressure power spectra density (PSD) measured by the remote microphone sensor	65
Figure 3. 9 a) copper track at the back side of the liquid crtystal heater plate; (b) front side of heater plate with thermocouple during calibration (no flow); (c) Hue-temperature relationship of the liquid crystal calibration.	67
Figure 3.11 Open circuit aerodynamic wind tunnel at Brunel University	69
Figure 3.12 force balance mechanism mounted on the outer side of the wind tunnel.....	70
Figure 3.13 NACA 0012 airfoil design.....	71
Figure 3.14 Airfoil trailing edge attachments with four different non-flat plate serration designs and one straight baseline trailing edge.	72
Figure 3. 15 Calibration curves for single and cross-wires.....	75
Figure 3. 16 TSI 1299 triple-wire sensor	77
Figure 4.1 Illustration of non-flat plate serrations, showing the serration parameters (left) as well as several trailing edge attachments (right) where (A) serrated geometries, (B)sharp/straight trailing edge and (C) main body of the airfoil.....	79

Figure 4.2 S_{qq} measured at $\alpha = 4.2^\circ$ and $U = 26.7 \text{ ms}^{-1}$ for the a) suction surface and b) pressure surface, both of which are at $x/C = 0.64$. The dotted lines and solid lines represent S_{qq} with and without boundary layer tripping tapes, respectively, near the leading edge of the airfoil.	81
Figure 4.3 PWL spectra for a) 27ms-1 and b) 60 ms-1.	82
Figure 4.4 PWL contours of cases S1, S2 and S3 for varying angles of attack	84
Figure 4.5 SPL contours according to Howe's theory for the cases a) S1, b) S2, c) S2* and d) S3, at $\alpha = 0^\circ$	85
Figure 4.6 Δ PWL contours of varying $2h$, where a) S2 and b) S2* at $\alpha = 0^\circ$.	86
Figure 4.7 OAPWL (left column) and Δ OAPWL(right column) in comparison with the baseline straight trailing edge for 3 different α where a, b for 0° ; c, d for 1.4° and e, f for 4.2° .	88
Figure 4.8 a) Example definition of frequencies f_1 and f_2 for b) the distributions of the NPM versus λ/h and ϕ for different frequency bands I (O), II (x), III(+)	90
Figure 4.9 Comparisons of the aerodynamic forces produced by the S0 trailing edge (baseline), the narrow serrated angle S1 and the wider serration angle S3 at $U = 30 \text{ ms}^{-1}$ where a) C_L ; b) C_D and c) C_L/C_D against the angles of attack, α .	93
Figure 5.1 Distribution of the microphone sensing holes on the sawtooth trailing edge. Same arrangement of the microphone sensing holes also applies to the baseline, straight trailing edge. The coordinate system is indicated.	99
Figure 5.2 Experimental setup for the measurements of self-noise produced by flat plate fitted in turn with a straight trailing edge and a serrated trailing edges. Noise spectra produced by straight trailing edge and serrated sawtooth trailing edge at freestream velocities of 25, 30 and 35 ms^{-1} are measured by the single free field microphone. The microphone array is used to locate the noise source.	100
Figure 5.3 Raw thermochromic liquid crystal images for the (a). Straight trailing edge; and (b). Serrated sawtooth trailing edge, with $2h = 20 \text{ mm}$ and $\phi = 25^\circ$.	102
Figure 5.4 Surface contour map of $\Delta\theta$ ($^\circ\text{C}$) obtained by the liquid crystal technique. The geometrical parameters for the serrated sawtooth trailing edge is $2h = 20 \text{ mm}$ and $\phi = 25^\circ$.	103
Figure 5.5 Raw thermochromic liquid crystal images for the (a). Straight trailing edge; and (b). Serrated sawtooth trailing edge, with $2h = 20 \text{ mm}$ and $\phi = 12.5^\circ$.	104
Figure 5.6 a). Δ SPL (dB); b). Contour maps of $\Delta\eta$ (dB) at different Strouhal numbers, and c). Contour map of $\Delta\varepsilon$ (dB) integrated over $J = (97, 21950) \text{ Hz}$. Note that all the figures in a), b) and c) correspond to the same free jet velocity of 30 ms^{-1} . Same color-scale applies to the contour maps in b) and c).	106
Figure 5.7 Streamwise phase spectra ϕ (rad) for the straight and serrated sawtooth trailing edges of the following microphone pairs: a). B4–C3; b). B2–C1; and c). D2–E1.	108
Figure 5.8 Spanwise coherence γ_2 and the phase spectra ϕ . The solid lines in the coherence γ_2 plots are calculated from the empirical model by Brooks and Hodgson (1981).	109
Figure 5.9 Time-averaged Reynolds shear stresses $-\overline{u'v'}/U_\infty^2$ boundary layer profiles measured at locations (a) C3; (b) C1; and (c) E1 for both of the straight trailing edge and serrated sawtooth trailing edge.	111
Figure 5.10 Comparison of the fluctuating velocity spectral densities of $\Phi_{u'}$ and $\Phi_{v'}$ at $y/\delta^* \approx 1.7$ for locations (a). C3; (b). C1; and (c). E1, between the straight trailing edge and sawtooth trailing edge. Explanation of symbols: $\Phi_{u'}$	112

- Figure 5.11 Comparison of velocity–wall pressure cross spectral densities at location E1 for (a). straight trailing edge ($\Phi_o(u'v').p'$); (b). serrated sawtooth trailing edge ($\Phi^*(u'v').p'$); and (c). $\Delta\Phi = [\Phi_o(u'v').p' - \Phi^*(u'v').p']$113
- Figure 5.12 Distribution of $\Delta\zeta$ across the boundary layer at location E1, which represents cross spectra between the $(u'v')$ and the absolute pressure fluctuations p' (+), or the normalized pressure fluctuations $p'/Prms$ (Δ).114
- Figure 5.13 a). Power spectral densities at location E1 for the straight trailing edge $\Phi_o(p' / Prms)$ and serrated sawtooth trailing edge $\Phi^*(p' / Prms)$; (b). $\Delta\Phi = [\Phi_o(u'v').(p' / Prms) - \Phi^*(u'v').(p' / Prms)]$115
- Figure 5.14 Surface pressure signals and the two threshold lines ($\pm 1.5Prms$) selected to calculate the conditionally-averaged velocity associated with the pressure peaks and troughs. The minor pressure peaks and troughs, which are marked as * in the figure, are not included for the ensemble.116
- Figure 5.15 Contours of U and V for: (a1, a2), $\langle +P \rangle$ surface pressure; (b1, b2), $\langle -P \rangle$ surface pressure. The measurement location is at C3 for the straight trailing edge.118
- Figure 5.16 Distributions of instantaneous u' and v' that correspond to: (a1, a2, a3). Pressure peaks at $y/\delta^* = 1.4, 3.2$ and 5.7 , respectively; (b1, b2, b3). Pressure troughs at $y/\delta^* = 1.4, 3.2$ and 5.7 , respectively. The measurement location is at C3 for the straight trailing edge. The broken lines represent the hyperbola $|u'v'| = 6 \times \overline{-u'v'}$ 120
- Figure 5.17 Fractions of the “intense” $u'v'$ events that correspond to the pressure peaks (black bars) and the pressure troughs (white bars) at different quadrants (Q1, Q2, Q3 and Q4). The subfigures are: (a). $y/\delta^* = 1.4$; (b). $y/\delta^* = 3.2$; and (c). $y/\delta^* = 5.7$. The measurement location is at C3 for the straight trailing edge.121
- Figure 5.18 Contours of $urms/U_\infty$, $vrms/U_\infty$ and $-\langle u'v' \rangle / (U_\infty)^2$ for: (a1, a2, a3), $\langle +P \rangle$ surface pressure; (b1, b2, b3), $\langle -P \rangle$ surface pressure. The measurement location is at C3 for the straight trailing edge.122
- Figure 5.19 Contours of Δ and $\Delta\psi$ for: (a1, a2), $\langle +P \rangle$ surface pressure; (b1, b2), $\langle -P \rangle$ surface pressure. The measurement location is at C1 for both of the straight and serrated sawtooth trailing edge.124
- Figure 5.20 Contours of $-\langle u'v' \rangle / (U_\infty)^2$ for: (a1, a2), $\langle +P \rangle$ surface pressure; (b1, b2), $\langle -P \rangle$ surface pressure. The measurement location is at E1 for both of the straight trailing edge and serrated sawtooth trailing edge.126
- Figure 5.21 Comparison of the surface pressure signal amplitudes measured at location E1 between the straight trailing edge and serrated sawtooth trailing edge. Note that both of the pressure signals were measured by the same microphone and signal ampli127
- Figure 5.22 Schematics to illustrate the propagations of the pressure-driven vortical structures near the sawtooth side edge towards the tip for the $\langle +P \rangle$ and $\langle -P \rangle$ cycles. Top figures: side view; bottom figures: isometric view. Drawings are not to scale.128
- Figure 5.23 Contours of $\langle U \rangle / U_\infty$ for: (a1, a2), $\langle +P \rangle$ surface pressure; (b1, b2), $\langle -P \rangle$ surface pressure. The measurement location is at E1 for both of the straight trailing edge and serrated sawtooth trailing edge.125
- Figure 5.24 Sequence of wake flows produced by a S3-type serrated trailing edge at $\theta = 5^\circ$ tested in a water tunnel.137
- Figure 5.25 Distributions of the Strouhal number of the vortex shedding noise produced by a tripped airfoil versus U, with S1, S2, S3 and 2D-blunt (same ϵ , but with ϕ and $\lambda/h = 0$) trailing edges at $\theta = 4.2^\circ$138
- Figure 5.26 Colour maps of γ^2 for the cases of a) SB, b) S2, and c) S3 trailing edges measured at $\theta = 5^\circ$ and $U = 20 \text{ ms}^{-1}$. 'b', 'r' and 't' denote 'blunt', 'root' and 'tip' respectively.135

Figure 5.27 Contours of streamwise vorticity produced by a NACA0012 airfoil at $x/C = 1.03$, and 3 degree angle of attack, with a (a). Straight trailing edge; and (b). Serrated sawtooth trailing edge of $2h = 20$ mm and $\phi = 25^\circ$	143
Figure 6.1 poro-serrated trailing edges with (a) porous metal foam and (b) brush inserts	147
Figure 6.3 Comparisons of the noise spectral measured at $U = 40$ ms^{-1} for a) S0, S1, S1 ⁺ trailing edges; and b) S0, S3, S3 ⁺ trailing edges.	150
Figure 6.4 Comparisons of the near wake fluctuating velocity spectral density measured at $x/C = 1.03$ and at $U = 40$ ms^{-1} for a) S0; b) S1 and c) S1 ⁺ trailing edges. All the spectral maps correspond to $f = 1$ kHz.	152
Figure 6.5 Comparisons of the near wake Φ , dB measured at $x/C = 1.03$ and at $U = 40$ ms^{-1} for S0, S1, S1 ⁺ trailing edges at: a) $z = 0$ mm (sawtooth tip); b) $z = 1$ mm; c) $z = 2.5$ mm (sawtooth root); d) $z = 4$ mm; and e) $z = 5$ mm (sawtooth tip).....	153
Figure 6.6 Figure 6.6 Colormaps of the ΔSPL , dB, for the vortex shedding tonal noise reduction and turbulent broadband noise reduction by using a) S1 serrated trailing edge; and b) S1 ⁺ poro-serrated trailing edge.	155
Figure 6.7 Colormaps of the ΔSPL , dB, for the vortex shedding tonal noise reduction and turbulent broadband noise reduction by using a) S3 serrated trailing edge; and b) S3 ⁺ poro-serrated trailing edge.	155
Figure 6.8 Comparisons of the acoustic maps at 2.3 kHz at $U = 40$ ms^{-1} for a) baseline S0 trailing edge and b) S1 ⁺ poro-serrated trailing edge.	156
Figure 6.9 Colormaps of the ΔSPL , dB, for the vortex shedding tonal noise reduction and turbulent broadband noise reduction by using a) S3 serrated trailing edge; and b) S3 ⁺ poro-serrated trailing edge. This repeatability test was performed at the ISVR anechoic chamber.	157
Figure 6.10 Colormap of the ΔSPL , dB, for the turbulent broadband noise reduction by using the S3 ⁺ serrated trailing edge.....	158
Figure 6.11 Comparisons of the noise spectral measured at $U = 40$ ms^{-1} between the baseline S0 trailing edge and the S3 ⁺ serrated trailing edge with a) thick; b) medium and c) thin brush bundles that fill the gaps between adjacent members of the sawtooth.....	159
Figure 6.12 Colormap of the ΔSPL , dB, by using the S3 ⁻ serrated trailing edge.	160
Figure 6.13 Colormap of the ΔSPL , dB, by using the SP partially porous trailing edge.	161
Figure 6.14 Comparisons of the aerodynamic forces produced by the S0 trailing edge (baseline), as well as the S1 ⁺ and S3 ⁺ poro-serrated trailing edges at $U = 30$ ms^{-1} for a) CL; b) CD and c) CL/CD against the angles of attack, α	163
Figure 6.15 Schematics illustrating the locations of the hot-film sensors HF1 and HF2 with relative to the (a) S0 trailing edge and (b) S3 ⁺ poro-serrated trailing edge. Drawings are not to scale.	165
Figure 6.16 Comparisons of the near wall fluctuating spectral (ξ , dB) measured by the hot-film sensors at $U = 40$ ms^{-1} for the (a) HF1 _{S0} & HF1 _{S3⁺} and b) HF2 _{S0} & HF2 _{S3⁺}	166
Figure 6.17 Colourmaps of a) $\Delta\xi_1$ and b) $\Delta\xi_2$	167

List of Tables

Table 2.1 Wall regions and layers (from Pope (2011))	20
Table 2.2 Characterisation of coherent structures	22
Table 3.1 Summary of aeroacoustic tests conducted.....	52
Table 4.1 Properties of serration geometries from the models tested	80
Table 5.1: Convection velocities determined by the phase spectral	132
Table 5.2 Schematics to illustrate the propagations of the boundary layer pressure waves of various incidence angles to the different trailing edges. Note that both the wide and narrow serration angles have the same $2h$. Drawings are not to scale.....	134
Table 5.3 Trailing edge geometries for the investigation of vortex shedding mechanism	135
Table 6.1 Development of the preliminary design concepts for the elimination of vortex shedding of non-flat plate serrations. The blue arrows indicate the direction of the airflow.....	146
Table 6.2 Summary of all the trailing edge devices tested in this study. Note the trailing edge drawings are all subjected to the main stream flow from top to bottom. Drawings are not to scale.	149
Table 6.3 Summary of all the noise performances in ΔSPL, dB, for the S3, S3+, S3-, S3Δ, S3o and SP trailing edge devices tested in this study. Positive level of ΔSPL denotes noise reduction, and vice versa. The three zones (I, II and III) in the ΔSPL maps were identified from the $\Delta\xi^2$ contours in Fig. 6.17b.	169

Publications

Either none of this work has been published before submission, or parts of this work have been published as:

Vathylakis A., Chong, T.P, Joseph, P. (2015). Poro-serrated trailing edge devices for airfoil self-noise reduction. *AIAA Journal* 53(11), pp.3379-3394.

Chong, T.P, Vathylakis A., (2015). On the aeroacoustic and flow structures developed on a flat plate with a serrated trailing edge. *Journal of Sound and Vibration*, 354, pp.65-90.

Chong, T.P, Vathylakis, A., Joseph, P. and Gruber, M. (2013). Self-Noise Produced by an Airfoil with Nonflat Plate Trailing-Edge Serrations. *AIAA Journal*, 51(11), pp.2665-2677.

Saravi, S., Cheng, K., Chong, T.P and Vathylakis, A. (2014). Design of Serrate-Semi-Circular Riblets with Application to Skin Friction Reduction on Engineering Surfaces. *International Journal of Flow Control*, 6(3), pp.83-92.

Pending patent application:

Vathylakis, A., and Chong T.P., Noise reduction to the trailing edge of fluid dynamic bodies, United Kingdom GB1410675.1. Application Issued June 16, 2014, patent pending.

Conference papers:

Vathylakis A., Chong T.P, (2013). On the turbulent boundary layers developed on a flat plate with a serrated trailing edge. 19th AIAA/CEAS Aeroacoustics Conference.

Vathylakis A., Chong T.P, Kim JH, (2014). Design of a low-noise aeroacoustic wind tunnel facility at Brunel University. 20th AIAA/CEAS Aeroacoustics Conference.

Chong T.P, Vathylakis A, Joseph, P. and Gruber, M.(2011), On the Noise and Wake flow of an Airfoil with Broken and Serrated Trailing Edges. 17th AIAA/CEAS Aeroacoustics Conference.

Kim JH, Al-Sadawi L,Vathylakis A., Chong T.P, (2014). Trailing Edge Noise Reduction by Passive and Active Flow Controls. 20th AIAA/CEAS Aeroacoustics Conference.

Chapter 1

Introduction

Aerodynamic noise and the science of aeroacoustics have a history of about 60 years [Lighthill (1951, 1954), Crighton (1975)], which arose through the emerging problem of noise pollution by the advancement of technology. It was James Lighthill (1951, 1954) in the early 50s who identified aerodynamic turbulence to be a source of sound, setting a foundation for the investigation of a wide range of aeroacoustic problems which became a matter of serious concern in civil as well as military aeronautical and naval applications. The present research shall contribute on the investigation and reduction of aerodynamic airfoil self-noise, relevant in jet engine fans, rotor blades and high lift devices as well as the arising application of wind turbines.

1.1 Aircraft noise

In the relatively short history of air transport, the development of civil aviation has caused tremendous changes in our daily lives and has become a fundamental pillar of our global society. Aviation today plays a key role in global economy, supporting up to 8% of global economic activity and carrying 35-40% of world trade by value [FAA (2007), ATAG (2014)]. Moreover, the number of air travellers has a trend of doubling every 15-20 years, which is equivalent to an annual growth rate of about 4% to 6%. [Airbus (2013), ACARE (2001)].

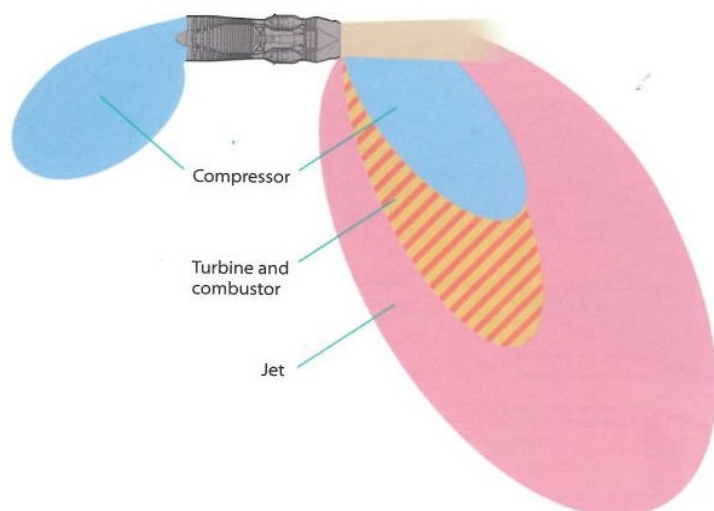
Nonetheless, a major factor obstructing a smooth expansion of the civil aviation sector is the persisting problem of noise in residential areas around airports. Severe health effects have been observed to be the consequence of aircraft noise, such as stress, hypertension, sleep disturbance, ischemic heart disease, hearing impairment and annoyance amongst others [Greiser (2006), Grimwood et al. (2002), CAA (2011)]. A study of Greiser (2006), on behalf of the German federal environmental agency, concluded that aircraft noise clearly and significantly increases the risk of heart disease by 61% for men and 80% for women, when considering a day-time average sound pressure level of 60 dB(A).

Statistically, significant health effects are however found to appear already at average sound pressure levels of 40 dB (A). According to reports from the UK Civil Aviation Authority [CAA (2011)] and the UK National Noise Attitude Survey [Grimwood et al. (2002)], more than 700,000 people alone around London's Heathrow Airport and more than 1 million people in the UK are affected by aircraft noise. Furthermore, noise associated with aircraft does not only affect people on the ground, but also flight crews and passengers within the aircraft. For example, noise levels inside an Airbus A321 during cruise have proved to be also significant in the order of approximately 78 dB (A) [Ozcan et al (2006)]. For this reason, lower noise levels inside new aircraft types are widely promoted by aircraft manufacturers and airlines.

Focusing on the infrastructure and economy of national and international importance, many of Europe's busiest airports, such as London's Heathrow and Gatwick airports, Frankfurt or Munich, are all facing problems regarding their expansion plans because of the noise pollution caused around the airports. Recently, in the cases of London Heathrow and Munich Airport, local referenda ruled out runway expansions, which effectively deny the airport authorities to sustain the required capacities and cope with the increasing passenger traffic and aircraft movements [Hillingdon Council (2013), Süddeutsche Zeitung (2013)]. Another restrictive measure due to noise is the plurality of night flight curfews implemented by many of the busiest airports across Europe and the whole world [ICAO (2013)].

Historically, the issue of aviation noise pollution arose in the late 50s when commercial jet aircraft entered service. Since the 1960s, significant improvements in noise reduction have been achieved, as a typical aircraft launched in the year 2010 comparatively reaches reduced Effective Perceived Noise levels of up to 40dB. As it can be seen in Fig. 1.1, the main reason for this achievement comes from the introduction of turbofan engines with high by-pass ratios. Fan blades at the inlet draw air inside the engine, which are typically larger in diameter when compared to the old, low by-pass ratio engines. A portion of the high speed air enters the compressor, combustion chamber and turbine, whilst a large portion of slower air by passes the core flow through the outer duct. The resultant exhaust jet speed in a high by-pass ratio engine is thus slower than a low by-pass ratio engine, but the propulsion efficiency is higher.

Noise of a typical 1960s engine



Noise of a typical 1990s engine

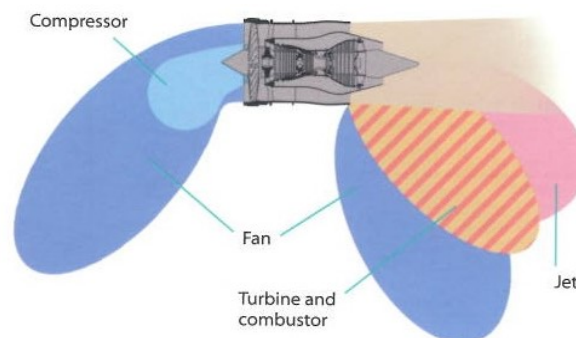


Figure 1.1 The evolution of the noise emissions of a low by-pass ratio engine (left) and a high by-pass ratio engine [Rolls-Royce (2005)].

Along with the improved propulsive efficiency, significant reductions of jet noise are achieved due to the lower jet exhaust speeds. For by-pass ratios exceeding a value approximately of 5 to 1, other noise sources, such as fan noise, become predominant (see Fig. 1.1).

As shown in Fig. 1.2, the change from the low by-pass ratio generation (i.e. B737-200 with bypass ratio of 1-1.7 to 1) to the current engine generation (i.e. A380 with by-pass ratio 8.6 to 1 and the B787 with 9.6 to 1) has brought significant improvements in the noise emissions of an aircraft.

In order to further reduce aircraft noise, two targets set by the authorities are being widely considered by aircraft and engine manufacturers:

Firstly, the International Civil Aviation Authority (ICAO) periodically sets noise standards, which new civil aircraft designs have to meet in order to be certified. These standards were firstly issued in 1969, known as “Stage 2” standards and with the fourth issue, “Stage 4”, to be currently in effect. For each stage, certain levels of Effective Perceived Noise are defined, which should not be exceeded (Fig.1.2) for the successful certification of new aircraft types. This assessment is based on take-off, sideline and landing noise measurements.

Secondly, in 2001, the Advisory Council for Aeronautics Research in Europe (ACARE) set out a target to reduce the perceived aviation noise to a half of the current levels by 2020 (ACARE VISION 2020 as shown in Fig. 1.2)[ACARE (2001)]. This vision aims to reduce the number of people who are significantly affected by aircraft noise in Europe. It was also identified that to achieve these challenging objectives, the promotion of research and development into new low noise engine and airframe technologies is strongly required. Furthermore, the continuation of “Vision 2020” by the European Commission, “Flightpath 2050”[ACARE (2011)], set further ambitious targets of reducing the Effective Perceived Noise levels emitted by 65%, when compared to typical new aircraft of 2000 .

Today, a step towards a future aircraft and engine generation is being observed with interest. The main focus is the development of jet engine technologies such as the geared turbo-fan (GTF) and the "Leading Edge Aviation Propulsion"(LEAP) engine generations. In any case, no relevant aircraft to date has officially reached the target set by Vision 2020 (Fig. 1.2), while the upcoming A320neo (GTF), where neo stands for New Engine Option, is expected to be closest to the aimed threshold¹ [MTU Aero Engines (2012)]. Official noise data have not been published yet, but in this context it has been stated by MTU Aero

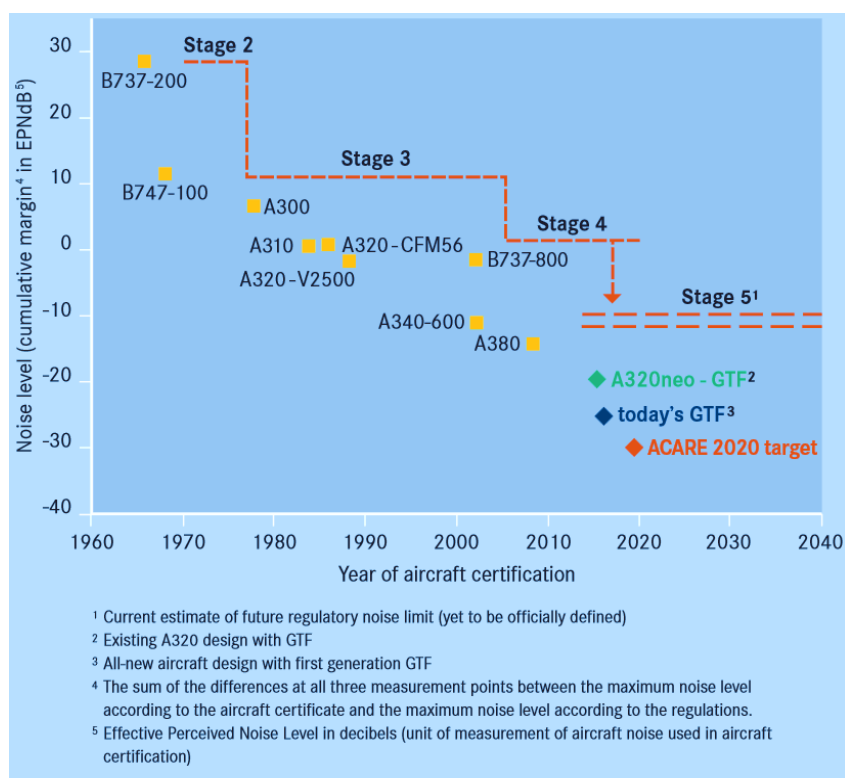


Figure 1.2 The historical development of civil aircraft noise [MTU Aero Engines (2012)]

¹ MTU Aero Engines private communication

Engines “that here’s no doubt that the biggest sources of noise remain the fan and the exhaust jet” [MTU Aero Engines (2012)]. Moreover, promising future engine technologies in terms of efficiency, such as counter rotating or open rotor fans, greatly depend on the improvement of their acoustic performance as they have previously been rejected due to the high noise levels [Flight International (2007), Little et al. (1989)].

In this regard, the advancement of low noise technologies on aircraft currently appears not to be sufficient to achieve the vision 2020 target, with an even greater challenge towards the objectives of “Flightpath 2050”. New concepts are therefore urgently needed in engine technologies, in order to achieve the desired goals, a better living standard and less or no flight restrictions.

1.2 Aircraft noise sources

The noise sources of a civil aircraft are depicted in Fig. 1.3, which can be divided into two categories: Propulsive noise and airframe noise. Propulsive noise is termed as the noise originating from the engine fan and the jet while airframe noise is identified to be generated by all other aircraft structures, namely the fuselage, landing gear, wings and high lift devices as well as existing cavities.

The dominant noise sources vary between take-off and approach/landing. As shown in Fig. 1.4, jet noise and fan noise are the major contributors during take-off and fan noise is the dominant noise source from the engine during approach, accompanied by airframe noise generated from the landing gear and flaps/slats [Traub et al. (2012)].

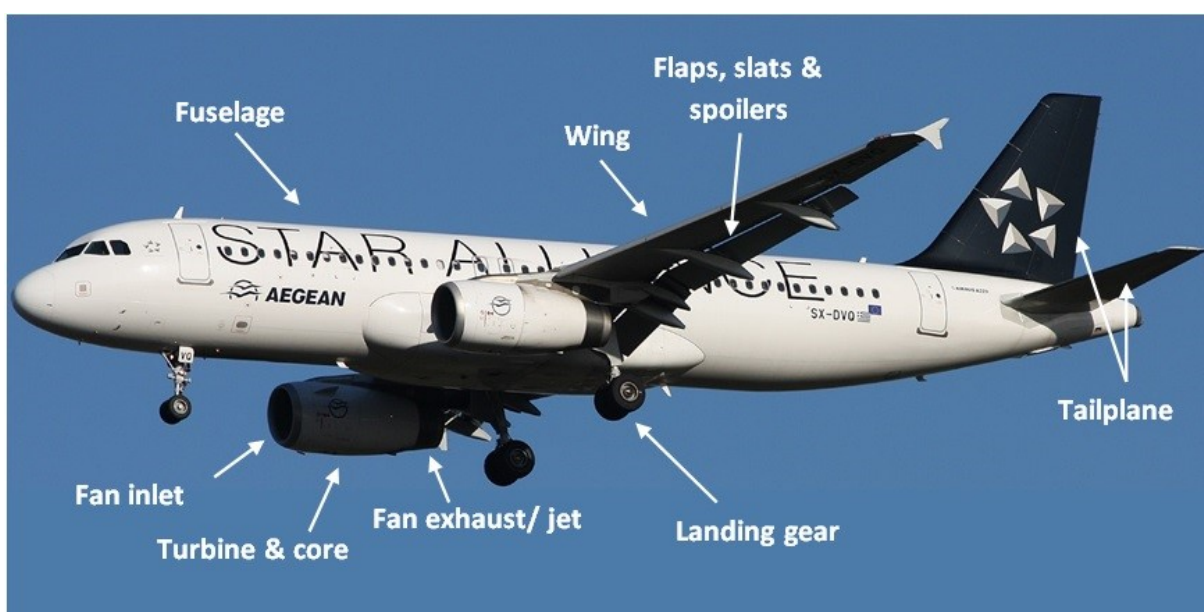


Figure 1.3 Major noise sources of the airframe and engine of a civil aircraft. [data from Traub et al. (2012)]

Fan noise is mainly caused through the incoming airflow interacting with the leading edge of the blades, as well as the interaction of the boundary layer with the airfoil trailing edge. The latter phenomenon creates trailing edge noise, or also known as airfoil self-noise, which will be the main topic of investigation in this thesis. Apart from fan blades, the principle of airfoil self-noise could also be relevant in other sections of an aircraft, such as the engine's outlet guide vanes (OGV), high lift devices (slats and flaps) and the wing itself. To date, there is no breakthrough technology available to drastically reduce these airfoil noise sources. The most promising method thus far is through passive flow control by altering the trailing edge shape from straight to a sawtooth serration pattern. The main objective of this PhD work is to research the serration technology and improve it with the introduction of porous materials. The results presented in this thesis will between others demonstrate that the "poro-serrated" trailing edge device developed here can achieve significant airfoil self-noise reductions, when compared with other current techniques. At the same time aerodynamic performance is maintained as well as a superior structural integrity, when compared to current serration concepts such as flat-plate type serrations. In this way, the industrial worthiness of serrations is improved when considering the aviation and wind turbine industries. The latter is discussed in the next section.

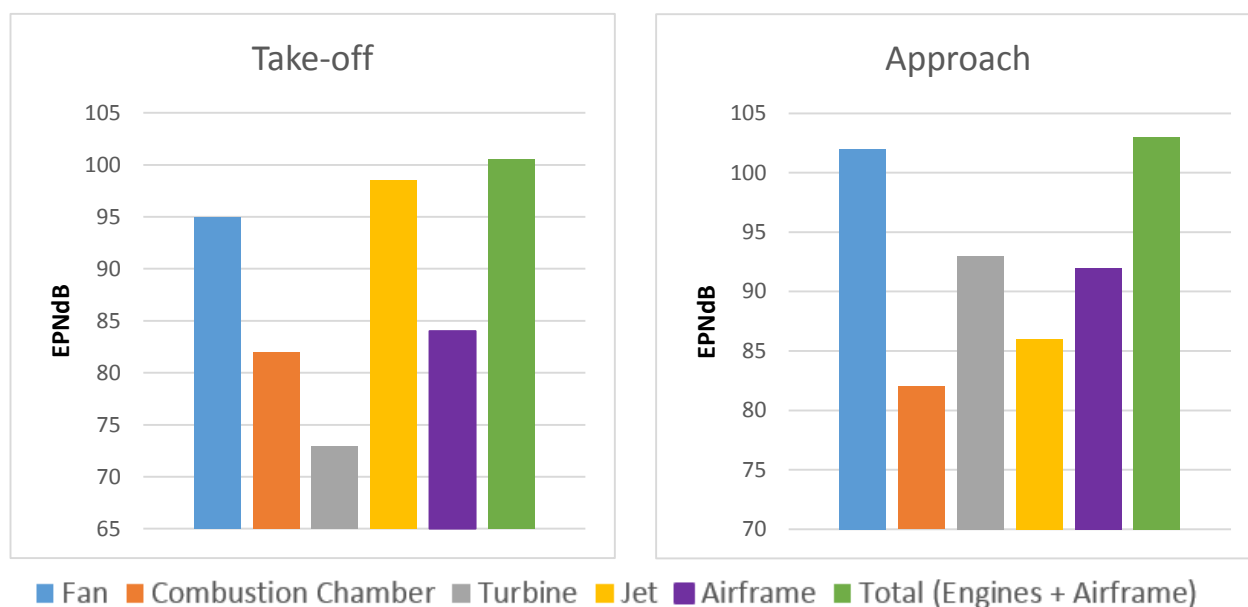


Figure 1.4 Breakdown of aircraft noise sources during take-off and landing, data from Traub et al. (2012)

1.3 Wind turbine noise

The European Wind Energy Association (EWEA) estimates that about 15% of Europe's electricity may come from wind turbines by the year 2020. Therefore, wind turbine installations in the European Union are expected to increase by 64% compared to levels of 2013[EWEA (2014)]. This means a faster deployment of wind turbines, at lower wind speed sites and ideally close to the households and transmission lines. The proliferation of wind turbines as an environmentally more acceptable form of energy has important implications of the fact that noise nuisance, mainly radiated from the turbine blades, is created for communities living in the close proximity.

Fig. 1.5 shows the noise levels generated by a typical wind turbine of 80m to 100m rotor diameter. It can be seen when wind turbine noise propagates past 100 meters, the noise levels drop below 50 dB (A). However, these noise levels may be maintained for a considerable distance of 5 kilometres or more [Morris (2012)]. Wind turbine noise appears to have lower exposure levels when compared to aircraft noise or road and rail noise, but the problem is found in the actual noise characteristics. Wind turbines persistently produce a distinctive swishing noise (i.e. a periodical sound level variation by the blade rotation), perceived as very disturbing due to its amplitude modulation and intermittency. This is particularly the case at lower frequencies, as the noise is not well

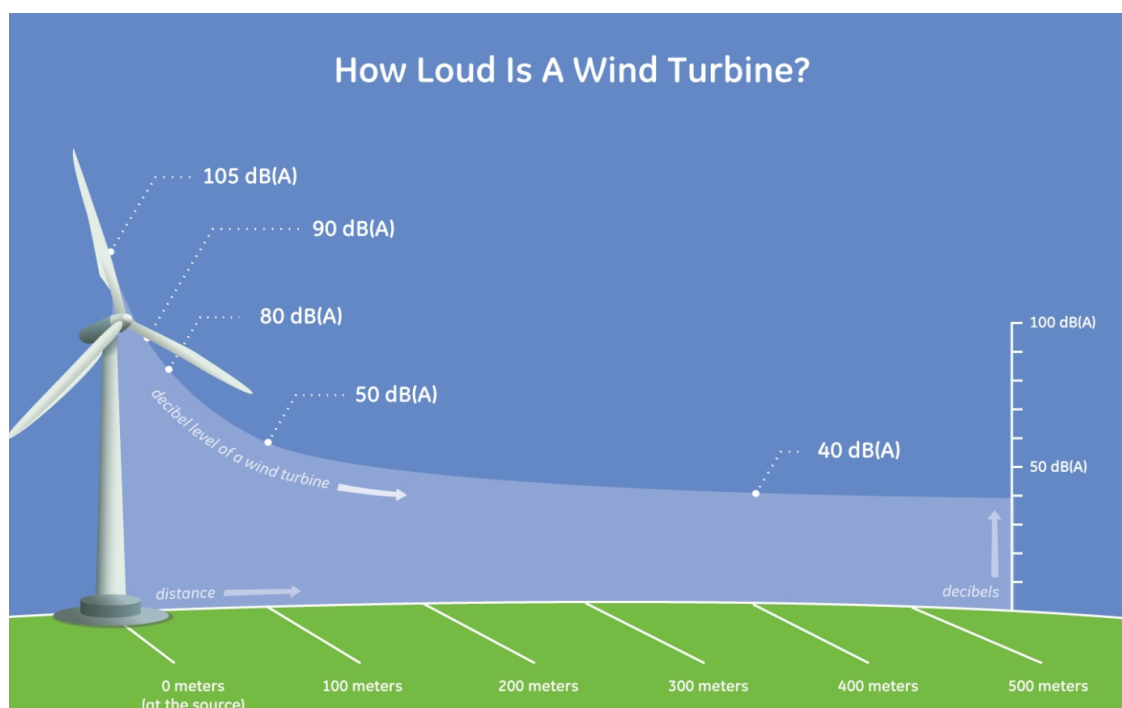


Figure 1.5 Typical noise emissions of a wind turbine over specified distances [General Electric (2014)]

attenuated by the atmosphere, and at night, the downward refraction of sound can promote it as a dominant noise source heard from a considerable distance.

Additionally, there is a trend for drastically larger wind turbines with increased rotor diameter. As seen in Fig. 1.6, the future generation wind turbine generation of onshore wind turbines has an almost doubled rotor diameter of more than 160m when compared to the generation of the years 2005-2010. The influence of rotor diameter on the noise, is shown in Fig. 1.7a, where a direct relationship of increased noise levels can be observed for an increased rotor size. Similarly to aviation noise, wind turbine noise has been reported to have a negative psychological impact and lowered sleep quality. However, because wind turbine noise has appeared to be an issue fairly recently through their growing use, and the lack of related reports, it is difficult to form a neutral view of the issue and its extent. In any case, it has been reported that between 15 and 70 wind farm sites in the UK cause nuisance to the nearby residents [Independent (2009), Telegraph (2013)] and it has been recognised, that the noise impact from wind farms needs to be further studied and improved [Doolan (2013)]. The noise generated by a wind turbine blade is almost entirely “aerodynamic noise” (as mechanical noise is fairly negligible) and

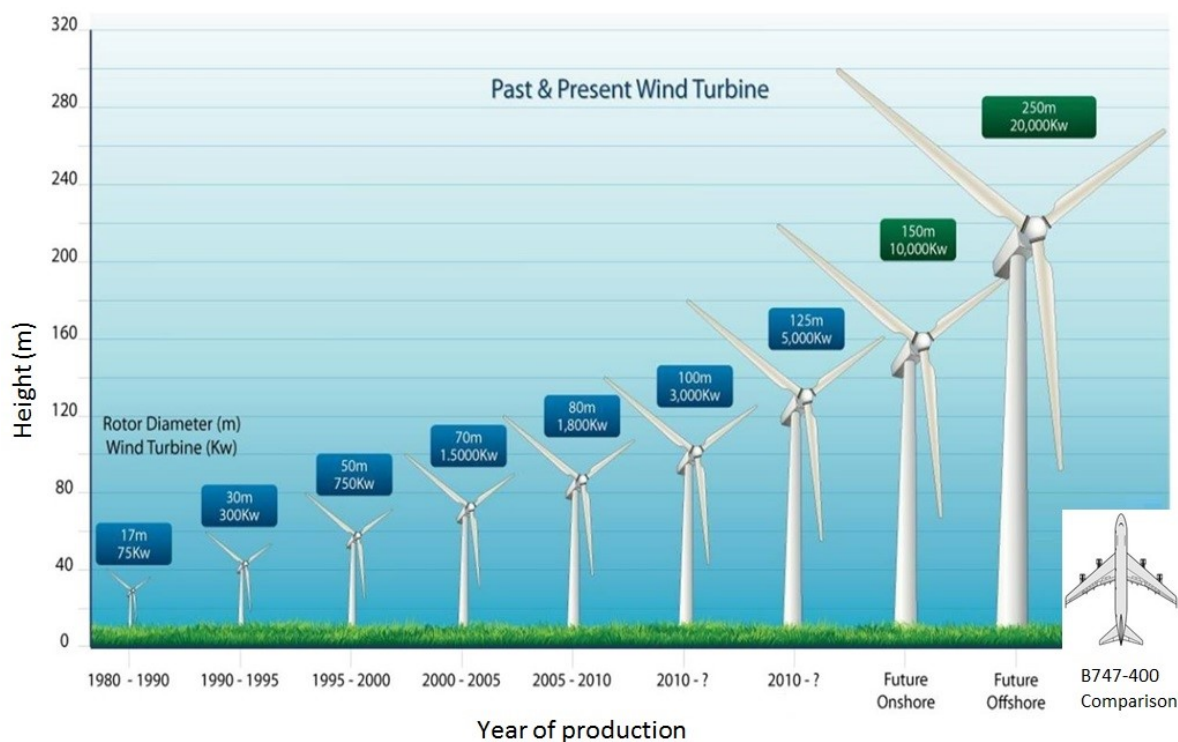


Figure 1.6 Historical trend of wind turbine size, also compared to the size of a passenger aircraft. [SBC (2014)]

predominantly trailing edge noise which is due to the turbulent boundary layer on the blade surface passing over the trailing edge.

[Brooks et al(1989), Oerlemans & Migliore(2004), Oerlemans (2009)]. A common technique to reduce wind turbine noise is the optimisation the blade shape.

However, the shape optimisation is a computationally very demanding process and is not versatile enough to cover different incoming flow regimes. Further measures for restricting wind turbine noise radiation are limitations of the rotor and tip speed. The limitation tip speed (which is the ratio between the speed of the blade tips and the wind speed) is the most direct method to reduce noise levels for onshore wind turbines, which however limits the amount of energy produced. As shown in Fig. 1.7b, small variations of tip speed would make a large difference in the noise emissions, when taking into account that the noise from the blades' trailing edges and tips are reported to vary by the 5th power of blade speed [Castellano (2012)].

So far, the shape optimisation can only achieve limited noise reductions of up to 3dB. Limiting the tip speed is also not the best practise to reduce noise emissions because of the reduced power output. The application of trailing edge serrations on a real size wind turbine blade, which has been attempted by Oerlemans(2009), provides an avenue for further development of the trailing edge serration technology , which will be thoroughly studied in this thesis.

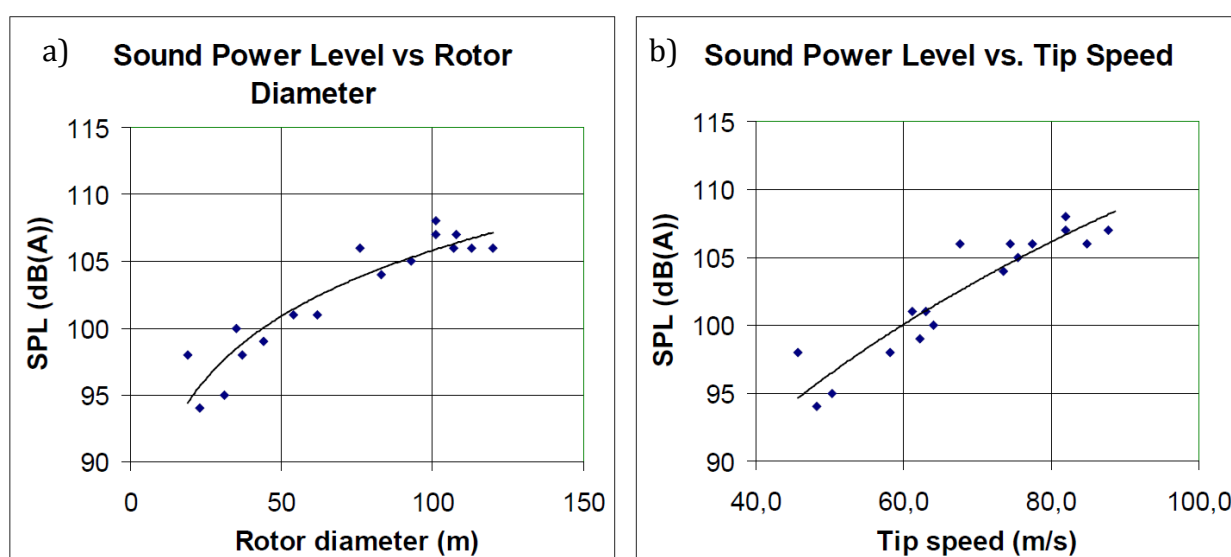


Figure 1.7 Variation of noise levels with (a) changing rotor diameter and (b) tip speeds [Oerlemans (2014)].

1.4 Aims and Objectives

The aim of this research is to experimentally investigate and reduce the noise mechanism known as airfoil self-noise, with the use of non-flat plate trailing edge serrations. The findings can potentially benefit the industries and applications mentioned previously in Sections 1.1 to 1.3. In more detail, the objectives are as follows:

- To assess the airfoil self-noise and lift/drag performance of the already existing concept of non-flat plate serrations. Due to the blunt area found in the serration roots of the airfoil, this concept is known to generate bluntness induced vortex shedding noise, a significant noise generating by-product. Subsequently, the alternative approach of flat plate add-on type inserts resulted into a lacking interest by researchers to thoroughly assess non-flat plate serrations, which is aimed here.
- To provide a better understanding of the flow phenomena over and past a serrated trailing edge. Since certain flow characteristics are directly related to the noise generation and radiation, it is of great interest to be investigated to also provide new solutions. To date, the involved mechanisms have not been fully understood.
- To improve the concept of non-flat plate serrations, reduce vortex shedding noise and simultaneously achieve broadband noise reductions (when compared to a straight/sharp baseline airfoil). It is aimed to reintroduce the interest for further research of this concept through new solutions.

1.5 Thesis Structure

This thesis aims to investigate the mechanism of broadband self-noise reduction using the technique of trailing edge serrations. Furthermore, two concepts will be developed: The concept of non-flat plate trailing edge serrations, and the new concept of adding porous material to these trailing edge devices. The origin of the passive flow control techniques investigated here are inspired by the owl's silent flight achieved through its unique wing structure (see **Chapter 2**: Literature review). The experiments were conducted in both, aeroacoustic and aerodynamic wind tunnel facilities at Brunel University as well as the Institute of Sound and Vibration (ISVR) at Southampton University. Details about the experimental set up can be found in **Chapter 3**. The starting point of this research is the application of non-flat plate type trailing edge serrations which has previously not received much attention. Extensive aeroacoustic results of this serration type will be presented in **Chapter 4**, as it will address the noise performance, as well as the aerodynamic performance (lift and drag) of an airfoil with non-flat plate serrations. **Chapter 5** investigates the turbulent boundary layer structures generated on a serrated trailing edge of a flat plate. The flow structures will be investigated in depth by means of hot wire anemometry, liquid crystal flow visualisation, unsteady surface pressure measurements and noise measurements. The chapter will also address the source of vortex shedding tonal noise which is a by-product of the non-flat plate serrations. Flow visualisation, noise and velocity measurements are used for the identification and further understanding of this noise source. **Chapter 6** presents a new, hybrid trailing edge device, referred to as "poro- serrated" trailing edge. Extensive noise and aerodynamic tests on the poro-serrated trailing edges will be presented and their performance will be discussed in this chapter. **Chapter 7** will summarise and discuss the findings and conclusions of all previous chapters. Some suggestions for future works will also be provided.

1.6 Novelty of Research

The main points of original research contribution are listed below:

- **(Chapter 4)** Extensive study on the broadband noise characteristics of non-flat plate serrations at three different angles of attack (α) 0° , 1.4° and 4.2° , across Reynolds numbers between 2×10^5 and 6×10^5 based on the chord. Furthermore, the lift and drag performance of a NACA 0012 airfoil with non-flat plate serrations was assessed.
- **(Chapter 5)** Noise measurements of the turbulent boundary layer generated on a flat plate with a serrated trailing edge were performed. The results demonstrate that realistic noise reductions by this configuration can be achieved. To investigate the causal effect, the unsteady wall pressure field as well as the spanwise coherence and phase functions of the turbulent eddies were measured. Moreover, simultaneous measurements of unsteady wall pressure and boundary layer fluctuating velocity permitted the investigation of conditionally averaged velocity perturbations, rms velocity fluctuations, Reynolds shear stresses. The characteristics of the coherent structures in a turbulent boundary layer are investigated when passing over a serrated trailing edge. Furthermore, a liquid crystal flow visualisation technique was used for the study of the wall heat transfer and identification of some of the turbulent structures.
- **(Chapter 5)** Assessment of the vortex shedding noise and the related flow mechanism. The flow in the near wake region of non-flat plate serrations was investigated through the analysis of the three-dimensional velocity components and spanwise coherence by using hot wire anemometry. Moreover, an experiment using dye flow visualisation was conducted in a water tunnel, to trace the development of wake flow from the airfoil.
- **(Chapter 6)** A hybrid trailing edge concept is presented, which demonstrates airfoil self-noise reductions throughout the measured frequency range, when compared to a straight baseline trailing edge. The non-flat plate type serrations were combined with a porous material placed in the serration roots, which eliminate vortex shedding noise and maintain the broadband noise benefits of non-flat plate serrations. The noise performance was assessed for different trailing edge models and the wake flow was studied. Furthermore, the lift/drag performance was also investigated. It is worth noting that for the first time noise reductions are achieved throughout the audible frequency range,

without changing the three-dimensional shape of the airfoil and with no compromise in the aerodynamic performance. The poro-serrated trailing edge developed in this work is currently pending a patent application. (patent application no GB1410675.1)

Chapter 2

Literature Review

2.1 Aerodynamic Sound

2.1.1 Lighthill's analogy of aerodynamic sound in free space and the introduction of solid boundaries

In the arising need for the investigation and reduction of jet noise, it was Lighthill (1951, 1954) who successfully identified the origins of a sound wave for the first time, while defining turbulence to be a source of sound. The term "aerodynamic sound" can therefore well sum up the principle of his theory. The sources of sound in a fluid motion are derived by using the exact equations of the fluid motions and their acoustical approximations. Lighthill's analogy is governed by the exact statement of the Navier-Stokes momentum and mass conservation equations (in order to define a flow velocity field at every point of space and time), resulting into the inhomogeneous wave equation (eq. 2.1).

$$\frac{\partial^2 \rho}{\partial t^2} - c^2 \nabla^2 \rho = \frac{\partial^2}{\partial x_i \partial x_j} T_{ij}. \quad (\text{eq. 2.1})$$

Where c is the speed of sound in a uniform acoustic medium at rest ($c^2 = dp/d\rho$), ρ is the fluid density, p the static pressure of the flow field and t the time of the acoustic observation at point x . The terms v_i and v_j are the velocity components and δ_{ij} is the Kronecker delta. T_{ij} is Lighthill's stress tensor (expressed in eq 2.2).

$$T_{ij} = \rho v_i v_j - \tau_{ij} + (p' - c^2 \rho') \delta_{ij} \quad (\text{eq. 2.2})$$

Lighthill's acoustic analogy (eq. 2.1) describes a wave propagating at the speed of sound c in a medium at rest on which fluctuating forces are applied in the form of the expression on the right hand side of the equation - from a quadrupole source field, of strength T_{ij} . Physically, it means that sound is generated through the fluctuating internal stresses of a fluid flow, acting on a stationary and uniform acoustic medium. The exact solution of the equation, where the sound pressure level generated at the point in the flow y , and the

observation point x , reduces to a point quadruple, within a volume V corresponding to the fluid region as

$$p(x, t) = \frac{\partial^2}{\partial x_i \partial x_j} \int_V \frac{T_{ij}(y, t - \frac{|x-y|}{c})}{4\pi c^2 |x-y|} dV \quad (\text{eq. 2.3})$$

Concluding from equation 2.3, turbulence in free space generates sound by a quadrupole source field. The solution of the sound generated can therefore be found if the parameters of the flow are known.

Through the use of dimensional analysis the sound produced in a jet of diameter D by free turbulence can be estimated through equation 2.4 below. This prediction, which was later confirmed by multiple experimental investigations, indicates that the sound is proportional to the eight power of the jet velocity for cold low Mach number (M) jets.

$$\overline{p^2} \sim \rho^2 M^8 \frac{D^2}{|x|^2} \quad \text{for } M < 1 \quad (\text{eq. 2.4})$$

Assuming that jet velocity is doubled, the above dependency would therefore indicate an increase of jet noise in the order of 24dB. The fact that in the past decades jet engine noise has been reduced substantially can be explained through the important effect of lowering the jet velocities for high bypass ratio turbofans.

While all the above principles based on Lighthill's analogy consider flows in free space, taking into account a foreign body in a flow will considerably change the sound production.

As shown by Curle (1955) the sound field is generated by a single dipole when a foreign body is added which is expressed as

$$\overline{p^2} \sim \rho^2 M^6 \frac{D^2}{|x|^2} \quad \text{for } M < 1 \quad (\text{eq. 2.5})$$

The dipole sound field therefore appears proportional to the sixth power of the flow speed which means that the foreign body generates sound in a more effective manner by the factor of M^{-2} than free turbulence.

2.1.2 Introduction to airfoil self-noise

Airfoil self-noise, also known as trailing edge noise, occurs through the interaction between an airfoil and the turbulence generated in its own boundary layer and near wake [Brooks et al. (1989)].

First attempts to identify the source of trailing edge noise were attempted in 1959 by Powell (1959) and in the following researched extensively, with the classical works of Ffowcs Williams and Hall (1970), Chase (1975), Paterson (1976), Howe (1978), and Brooks (1989) amongst others. Trailing edge noise has been characterised as the minimum noise produced by a fan if installation effects are not taken into account, considering that leading edge noise is not prominent as in the case of low pressure loading configurations and low turbulence incoming flow [Roger and Moreau (2002)].

Brooks (1989) identified five different airfoil noise mechanisms, of which four are related to the interaction of hydrodynamic disturbances in the boundary layer with the trailing edge. Those vortical disturbances are subsequently scattered into sound by the geometrical discontinuity of the sharp trailing edge, leading to a radiation with a large increase in the noise generated when compared to fluctuations in free space [Lighthill (1951, 1954)]. For that reason, trailing edge noise is considered as one of the main noise sources, with the development of trailing edge noise theories to have received great attention in research.

A large number of models for the prediction of trailing edge noise arose especially in the seventies, which are based on three different approaches:

- i. Models based on Lighthill's acoustic analogy [Lighthill (1951)] (i.e. the model developed by Ffowcs Williams and Hall (1970)).
- ii. Theories based on the solution of special problems derived by linearized hydroacoustic equations (i.e. models by Amiet [1976] and Chase [1975]).
- iii. Ad hoc approaches.

Some established examples for the prediction of trailing edge noise are made explicit in the classical works of Amiet (1976) and Howe (1978). As used in the present thesis, when a turbulent boundary layer is developed on a flow surface, a model was developed by Amiet to predict the far field noise through the occurring surface pressure fluctuations

near the trailing edge of an airfoil. A detailed discussion and insight into Amiet's model is given in Section 2.2.3 of this chapter.

Past research works related to airfoil self-noise on a straight / sharp trailing edge will be discussed first (Sections 2.1 to 2.2). Subsequently, in Section 2.3, it will be focused on the research related to the reduction of trailing edge noise by the concept of trailing edge serrations and porous materials.

2.1.3 Airfoil self-noise mechanisms by Brooks et al.

Five different self- noise mechanisms have been proposed by Brooks et al. (1989) which were defined through their extensive experimental investigation. The first two from the noise mechanisms listed below are of interest for the present investigation.

- **Turbulent boundary layer – trailing edge noise** (Fig. 2.1a) occurs at high Reynolds numbers as the turbulent boundary layer created over an airfoil convects past the trailing edge and radiates noise. This noise source is known to have mainly a broadband character. Broadband noise is the prominent noise source for non-separated turbulent boundary layer flows. The structures inside a turbulent boundary layer are of great complexity and often seen as “random” structures. Some repeatable identifiable patterns however can further explain phenomena of a certain noise observation. In order to provide a deeper insight into the anatomy of turbulent boundary layers and the corresponding noise mechanisms, they are reviewed in Sections 2.2.1 and 2.2.2.
- **Trailing edge bluntness- vortex shedding noise** (Fig. 2.1c) occurs in the small separated region past an airfoil's blunt trailing edge which can be an important noise source. The radiated noise is of tonal nature superimposed into one distinct broadband peak on the frequency spectrum. Usually when occurring in turbulent boundary layer flows, the audible bluntness noise will dominate as the distinct noise source over turbulent broadband noise. The intensity of bluntness noise is dependent on the boundary layer thickness of the airfoil and the ratio of the actual bluntness at the trailing edge. Bluntness noise is being further analysed in Section 2.2.5 of the literature review.

- **Laminar boundary layer – vortex shedding noise** (Fig. 2.1 b) takes place at low to moderate Reynolds numbers where Tollmien-Schlichting (T-S) instability waves disturb the laminar boundary layer of an airfoil resulting to vortex shedding noise. The noise is of narrowband, tonal nature. It has been observed that T–S waves by themselves may not be the only mechanism responsible for the noise generation. The presence of a separation bubble is assumed which acts as an amplifier for the unstable T–S modes near the trailing edge. Further details about the nature of the tonal noise mechanism are described in Section 2.2.4.
- **Separation – stall noise** (Fig. 2.1d) becomes distinct at high angles of attack at separated flow conditions. As stated by Brooks, an assessment by Paterson et al (1975) suggested that for lightly separated flow, the dominating noise source would originate from the trailing edge, whereas when the airfoil experienced a deep stall, the broadband noise would originate from the chord as a whole.
- **Tip vortex formation noise** (Fig. 2.1e) generates a local separated flow near the tip region of a blade tip. When the flow passes the blade tip a vortex is generated with a thick viscous and highly turbulent core. The investigation by Brooks and Marcolini (1984) was able to isolate the particular noise source quantitatively and research the noise generation of two and three dimensional airfoil models at various conditions.

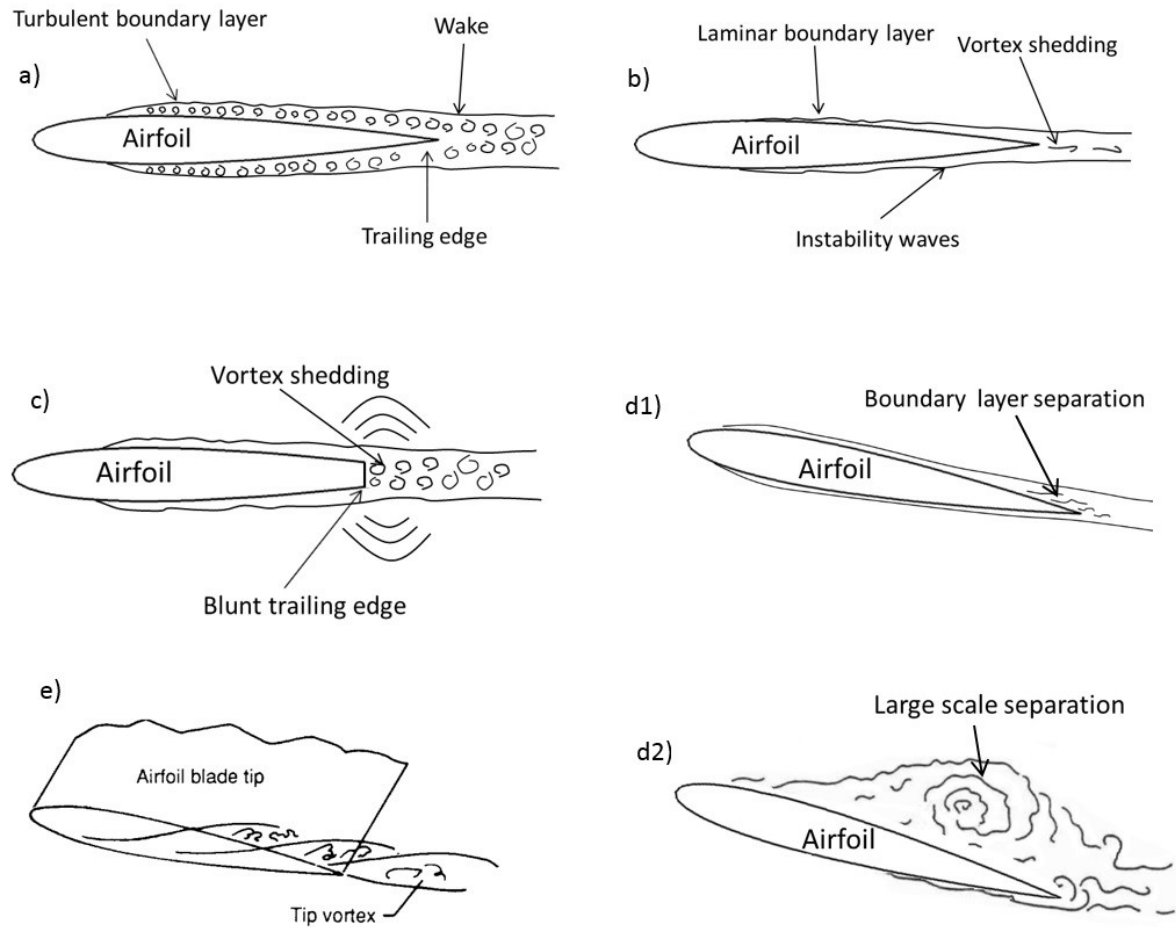


Figure 2.1 Airfoil self-noise mechanisms as defined by Brooks et al. (1989) where (a) Turbulent boundary layer trailing edge noise, (b) laminar boundary layer trailing edge noise, (c) Bluntness vortex shedding noise, d1-2) stall noise and (e) tip vortex noise.

2.2 Boundary Layer Theory

2.2.1 Wall regions and layers of the turbulent boundary layer

The concept of the boundary layer and existence of different layers of a fluid moving relative to the wall was first addressed by Prandtl (1905) in the early 20th century. As it was later specified a boundary layer in turbulent flows consists of a number of flow regions and layers which occur at certain distances from the wall, which are measured in dimensionless wall units denoted by

$$y^+ = \frac{u_\tau y}{\nu} = \frac{y}{l_v} \quad (\text{eq. 2.6})$$

Where y^+ the dimensionless wall unit distance, u_τ the friction velocity, y the normal distance from the wall, ν the kinematic viscosity and l_ν the viscous wall unit. Subsequently, the velocity can also be non-dimensionalised by the wall unit as

$$u^+ = \frac{U}{u_\tau} \quad (\text{eq. 2.7})$$

Pope (2011) summarised a division of the boundary layer into different layers, as certain properties can be defined for each of these regions. While the regions of the inner layer are mainly viscosity-dominated, the direct effects of viscosity are negligible in the regions of the outer layer at $y^+ > 50$. The inner layer is defined by the normal distance from the wall (y) and the boundary layer thickness δ , as $y/\delta < 0.1$. The mean velocity profile in the inner layer is independent from δ and the free stream velocity U_∞ as it is influenced only by viscous effects, hence by the friction velocity u_τ and the dimensionless wall unit y^+ . A detailed overview is provided in Table 2.1 and Fig. 2.2a.

Region:	Location:	Defining property:
Inner layer	$y/\delta < 0.1$	Scaled with u_τ and y^+
Viscous sublayer	$y^+ < 5$	Reynolds shear stress negligible compared to viscous stress
Buffer layer	$5 < y^+ < 30$	Region between viscous sublayer and log-law region
Viscous wall region	$y^+ < 50$	Significant viscous contribution to the shear stress
Outer layer	$y^+ > 50$	Direct effects of viscosity on U negligible
Overlap region	$y^+ > 50, y/\delta < 0.1$	Region of overlap between inner and outer layers
Log-law region	$y^+ > 30, y/\delta < 0.3$	Log law holds

Table 2.1 Wall regions and layers (from Pope (2011))

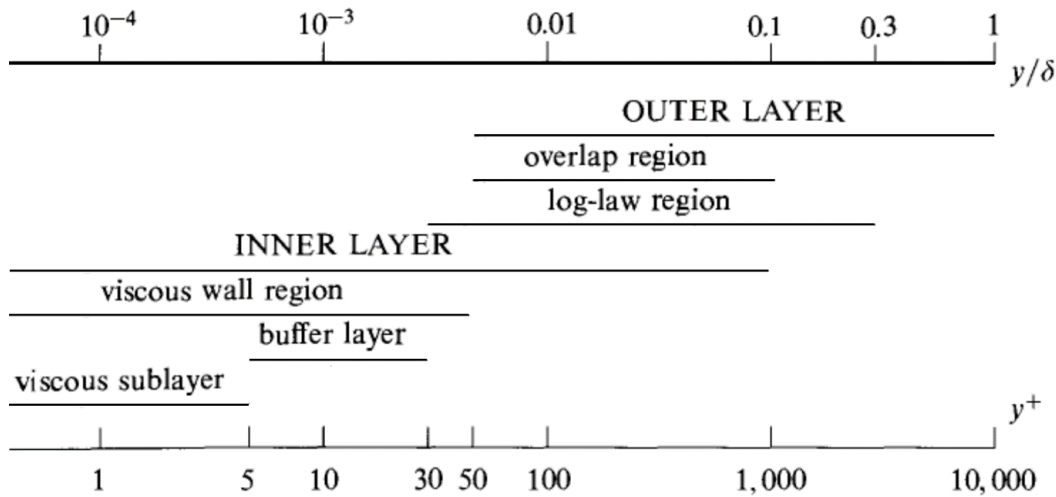


Figure 2.2a Division of various layers in terms of $y^+ = \frac{y}{\delta_\nu}$ and $\frac{y}{\delta}$ at $Re=10^4$ (from Pope (2011))

Regarding the energy spectrum of a turbulent boundary layer, a theoretical representation is shown in Fig 2.2b and an actual collection of experimental measurements is shown in Fig 2.2c where the kinetic energy per mass across the various length scales of turbulence is shown. Moreover, it has been observed that a $-5/3$ power law decay rate of the energy spectrum holds well in the inertial range, which is valid for intermediate eddy diameters that are remote from both largest and shortest scales.

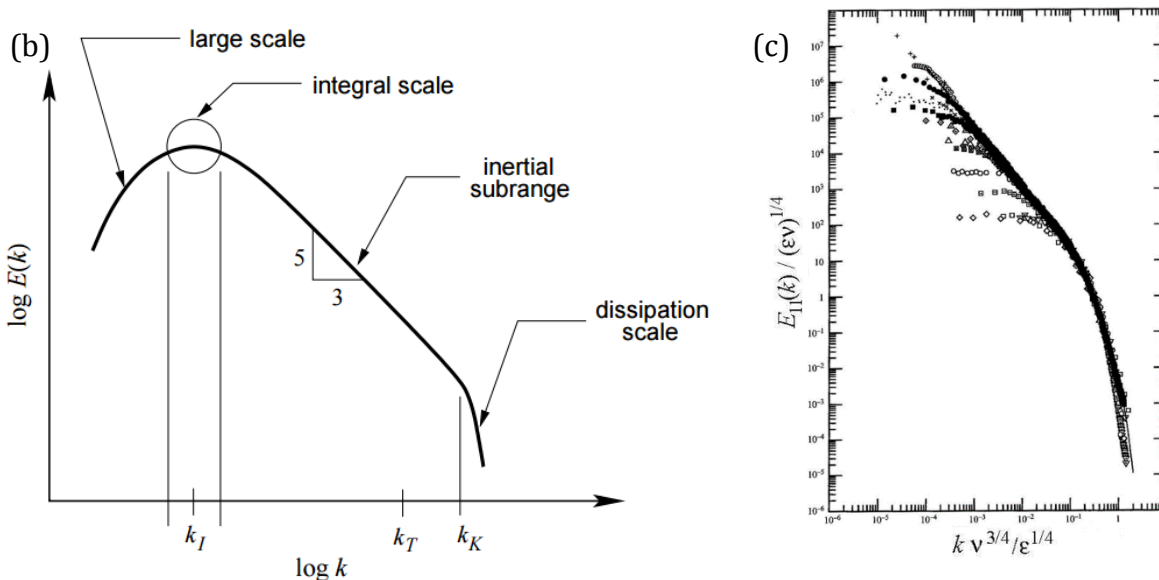


Figure 2.2 Turbulent energy wavenumber spectra (b) theoretical representation [McDonough(2007)] (c) experimental results [Saddoughi and Veeravalli (1994)]

2.2.2 Turbulent boundary layer flow structures

The interaction of the turbulent boundary layer structures with the airfoil trailing edge are the cause for the characteristic broadband noise radiation. Thus the identification certain flow structures in the boundary layer are of great interest for the understanding

of the broadband noise source. This section describes the pure aerodynamic research of turbulent boundary layer structures which can later be related to the noise radiation phenomena described in the later sections.

Since the 1960s a great number of the experimental research on-wall-bounded flows was focused on the structures of a turbulent boundary layer. The structures were found to break down from complex, random, and multiscaled fields of turbulence into more elementary parts, known as coherent structures. The general idea of coherent structures is the existence of a characteristic coherent pattern within the flow structure (spatial coherence) and for a persisting period of time in order to be defined as an organised motion (temporal coherence) [Pope (2011), Adrian (2000)]. They should be able to draw distinguishable attention through the latter coherence criteria when seen on a flow visualisation movie or time averaged statistics of the flow [Adrian (2007)]. Nonetheless, the behaviour of near wall turbulent flows is not yet fully understood due to its immense complexity. The definition of coherent structures therefore provides a simplified approach to categorise a number of identifiable formations amongst other seemingly random structures of the near wall turbulence.

Kline et al. (1990) and Robinson (1991) provided an overview of the quasi-coherent structures in a turbulent boundary layer, which can be summarised in Table 2.2.

Coherent Structures:	Defining Properties:
Low speed streaks	Low-speed fluid in the viscous sublayer.
Ejections	Low-speed fluid outward from the wall dominant in the buffer layer and the log-region
Sweeps	High-speed fluid towards the wall, occur mainly in $y^+ < 12$.
Vortical structures	Hairpin, horseshoe, cane shaped vortical structures.
Large scale motions	In outer layers; Large δ -scale motions consisting of bulges or packages of hairpin vortices.

Table 2.2 Characterisation of coherent structures

Low Speed Streaks correspond to fairly slow moving fluid, approximately half of the mean streamwise velocity and are commonly observed in the near-wall region, mainly in the viscous sublayer and the buffer layer. Their characteristic form exceed a length in x direction of $\Delta x^+ > 1000$ while the spanwise streak spacing near the wall is randomly distributed at lengths of $\bar{\lambda}^+ = \frac{\bar{\lambda} u_\tau}{\nu} = 100 \pm 20$ where $\bar{\lambda}$ the non-dimesionalised mean spanwise spacing between streaks on the viscous length ν/u_τ (where ν the kinematic viscosity) [(Adrian et al. (2000), Smith and Metzler (1983)]. These values have been confirmed by many studies with the acceptance that it is insensitive the Reynolds number. However, it has not been universally confirmed for more developed flows [Gupta et al (1971), Adrian et al. (2000)]. Experiments conducted by Kline et al (1967) and Smith and Metzler (1983) amongst others, contributed greatly to determining the characteristics of the streaks by using hydrogen bubble flow visualisations. As seen in a more recent experiment in Fig. 2.3 [Sabatino (2014)], long streaks in the streamwise direction are made visible through the accumulation of the hydrogen bubbles. As emphasised through the red circles, these coherent structures become visible as they are slower than the mean streamwise velocity, thus forming the (relative to the mean flow) backwards distorted lines.

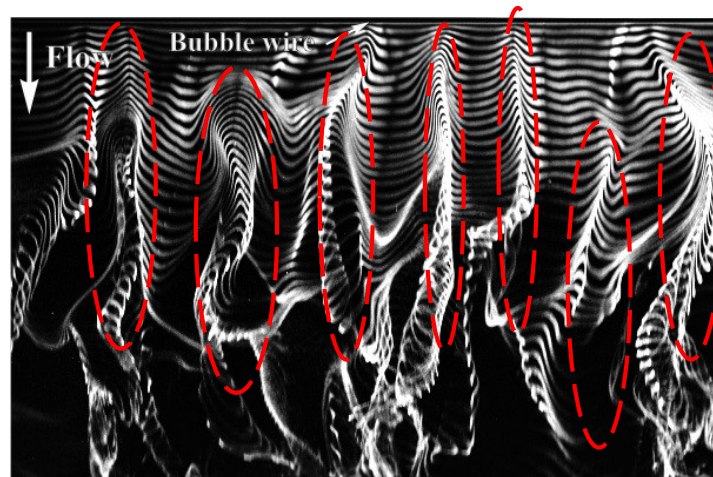


Figure 2.3 Low speed streaks using hydrogen-bubble wire visualisation. These motions of lower-speed fluid are circled in red. [Sabatino (2014)]

The sharp shear layers around the low speed streak mechanism are origin of instabilities which potentially evolve into vortical structures, subsequently inducing *ejections* and *sweep events*. Ejections are relatively rapid streak lifting movements, ejecting low velocity fluid away from the wall. This characteristic behaviour is known as *bursting*. The opposite event where high velocity fluid moves towards the wall is called *sweeping* [Pope (2011),

Johnson et al (1998)]. The method shown in Fig. 2.4 was proposed to define burst and sweeps by dividing the product of the ensemble averaged value of the $\langle U \rangle$ and $\langle V \rangle$ components in four quadrants. A quadrant 2 (Q2) event would therefore occur when the $\langle U \rangle$ velocity is less than the mean flow U_m ($\langle U \rangle - U_m < 0$) and with a vertical velocity $\langle V \rangle$ away from the wall ($\langle V \rangle - V_m > 0$).

Further away from the wall beyond the buffer layer, commonly proposed shapes of vortex structures become dominant in form of a horseshoe or omega shape [Head and Bandyopadhyay (1981)]. With increased Reynolds numbers these structures become elongated and appear more like hairpins, hence they are referred to as *horseshoe and hairpin vortices* as depicted in Fig 2.5a. Both, Fig 2.5a and b provide a good example of the aforementioned quadrant division as it shows the trend of a Q2 event. When focusing on Fig 2.5b, the streamwise, wall-normal plane view illustrates the tendency of the hairpin structure's velocity to be slower than the mean flow in x direction (expressed through “-u”). Additionally the depicted inclination causes a motion away from the wall, resulting into the Q2 event.

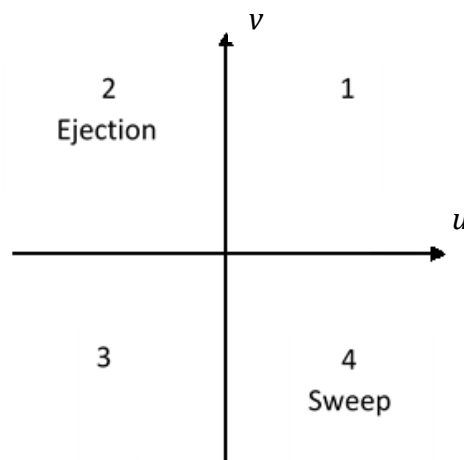


Figure 2.4 u' - v' quadrant division

Regarding the properties of a hairpin, secondary and tertiary hairpin structures might spring from the main structure, which can lead to the formation of a new hairpin which detaches from the primary. Initially, horseshoes can be imagined to arise from a local upward perturbation of a spanwise vortex line in a shear flow. The sections of this vortex type can be distinguished as the head which is being dragged downstream, the legs which rotate faster and move apart and the connection between them termed as neck (Fig. 2.5a).

It is assumed that the velocity induced by the legs rotate and push the head upwards into a higher velocity region [Panton (2001)].

As observed by Kline and Robinson (1989) and Robinson (1993) quasi-streamwise vortex legs are dominant in the buffer layer. Inclined necks and heads are predominant in the outer layer as hairpins of different sizes are distributed, with the most dominant region to be in the logarithmic layer. The induced flow by the head and neck can be associated with an ejection (Q2 event) in the outer layer. The induction of the quasi-streamwise vortices can lead to lifting up low momentum fluid, subsequently causing low-speed streaks in the buffer layer, which will eventually oscillate and break up. This event is commonly recognised as the main mechanism for the generation of turbulent energy. Moreover, due to the ejection event, shear-layers are generated as fluid from the outer layer is required to be transported towards the inner boundary layer regions in form of sweeps, and vice versa, according to the principle of mass continuity. [Kim et al. (1971), Head and Bandyopadhyay (1981), Panton (2001)].

In conditionally averaged analyses, it has become clear that the horseshoe head and the quasi streamwise eddy are basically a single eddy. Generally, the Q2 movement of the eddy is induced by the vortex, while a Q4 event flow is present in the frame in the vicinity of the hairpin as seen in Fig. 2.5a. Subsequently a stagnation point is formed where the Q2 and Q4 event flows cancel out. The opposite movement of the flows has the effect of creating an inclined shear layer and is also possibly the reason for the transition from Q2 to Q4 events seen in variable interval time averaging (VITA) analyses using hot-wire anemometry [Wallace et al. (1977), Adrian et al. (2000)].

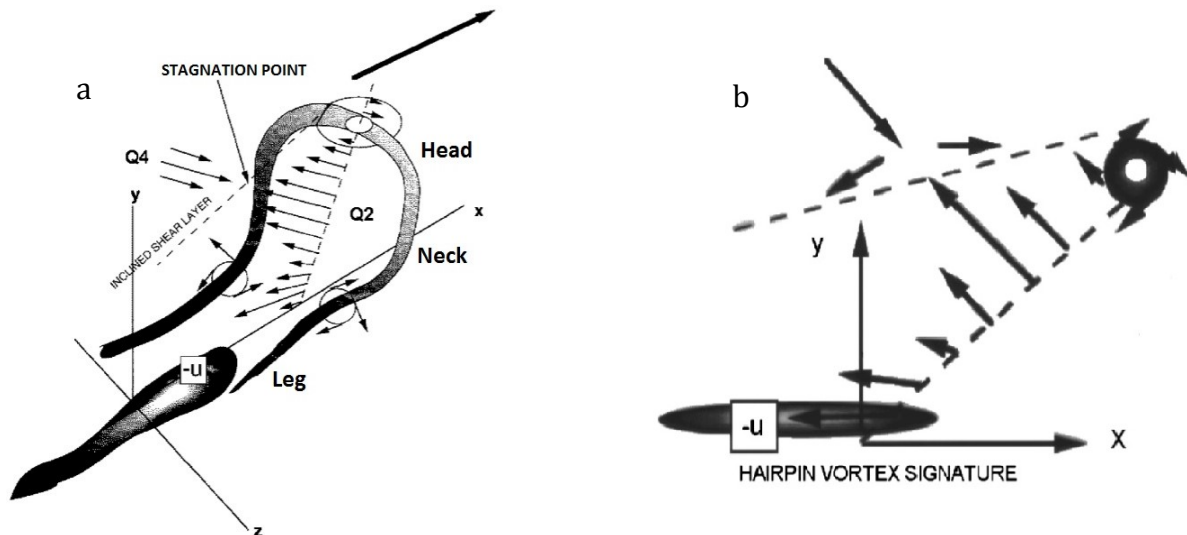


Figure 2.5 (a) Anatomy of hairpin eddy attached to the wall; (b) streamwise, wall-normal plane view of the hairpin eddy signature [Adrian et al (2000)].

In the event of a non-zero spanwise velocity the shape of the Q2-event will certainly not maintain its symmetry, becoming incomplete or one sided i.e. one leg will be stronger than the other which subsequently evolves to a cane-shaped eddy, accordingly known as *canes*. The existence of asymmetries is the most probable and common condition known in real boundary layers. The quasi-streamwise vortex pattern, hairpin, horseshoe and cane shaped vortices originate and are formed from the same basic structure, developed at various stages of their evolution, with different aspect ratios and different degrees of asymmetry [Adrian (2007)].

The inclinations of the developing structures are known to be between approximately 20° and 45° degrees relative to the wall. Head and Bandyopadhyay (1981) suggested that at high Reynolds numbers ensembles of hairpin vortices formed packets while at lower velocities mainly single horseshoe were present. Figure 2.6 shows a conceptual scenario of symmetric hairpin vortices, found on the back of induced low speed fluid (streaks), which is usually the case. Additionally to the principles described previously, it can be also seen that the older the hairpin packet grows, the larger it grows with a higher the velocity of the coherent structure (Fig 2.6 $U_{c1} < U_{c2} < U_{c3}$).

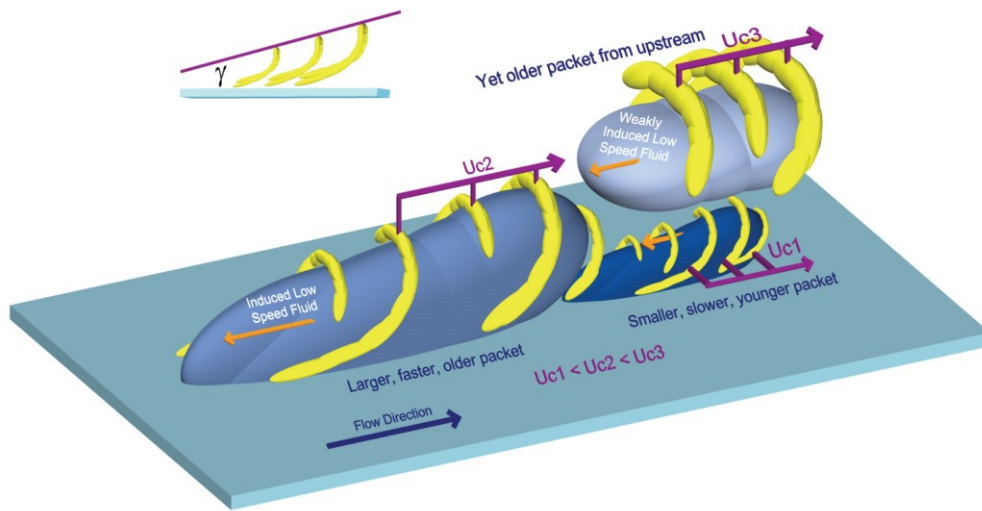


Figure 2.6 Conceptual scenario of hairpin vortices on induced low speed fluid, attached to the wall and growing in an environment of overlying larger hairpin packets [Adrian et al. 1991]

2.2.3 Predicting turbulent boundary layer broadband noise with the relationship of surface pressure statistics using Amiet's model

A direct relationship has been observed to exist by many researchers between the aerodynamic surface pressure spectrum upstream the trailing edge and the actual radiated far-field noise. Amiet (1976) and Howe (1978) developed models in which the surface pressures were used as an equivalent acoustic source, even though the origin of the sound is found to be in the vortical velocity field. In both models, a turbulent boundary layer over a rigid semi-infinite flat plate at 0° incidence in subsonic flow was assumed. Through integrating the far field noise spectra with respect to frequency both reported a scaling with $M^5 (U^5)$. While the main difference of the two models is found in the definition of the aerodynamic near field and its linkage to the far field noise, Howe's model is valid for very low Mach numbers only, while Amiet's approach, which will be utilised in this thesis, is applicable in all subsonic flows.

Amiet's (1976) semi-analytical approach provides a direct relationship of the radiated far field trailing edge noise to the convecting surface pressure spectrum of a turbulent boundary layer upstream of the edge. In a uniform, non-turbulent inflow, noise is regarded to be produced almost solely by the induced surface dipoles near the trailing edge. A basic assumption made by Amiet is to consider the statistical properties of the turbulent boundary layer as stationary i.e. the assumption of frozen turbulence which regards the pressure of the turbulent boundary layer unchanged in the presence of the trailing edge discontinuity.

Fulfilling these hypotheses, the relationship can then be expressed in means of the power spectral density S_{pp} of the far field TE noise as:

$$S_{pp}(x, \omega) \approx \left[\frac{\sin(\theta_a)}{2\pi R} \right]^2 (kC)^2 \frac{L}{2} |I|^2 S_{qq}(\omega) l_y(\omega) \quad (\text{eq. 2.8})$$

Where θ_a and R the angle in the centre line plane and distance to the observer respectively, over an airfoil. k is the wave number, C and L the airfoil chord and span respectively. I represents the radiation integral, S_{qq} the wall pressure fluctuations and l_y the spanwise correlation length.

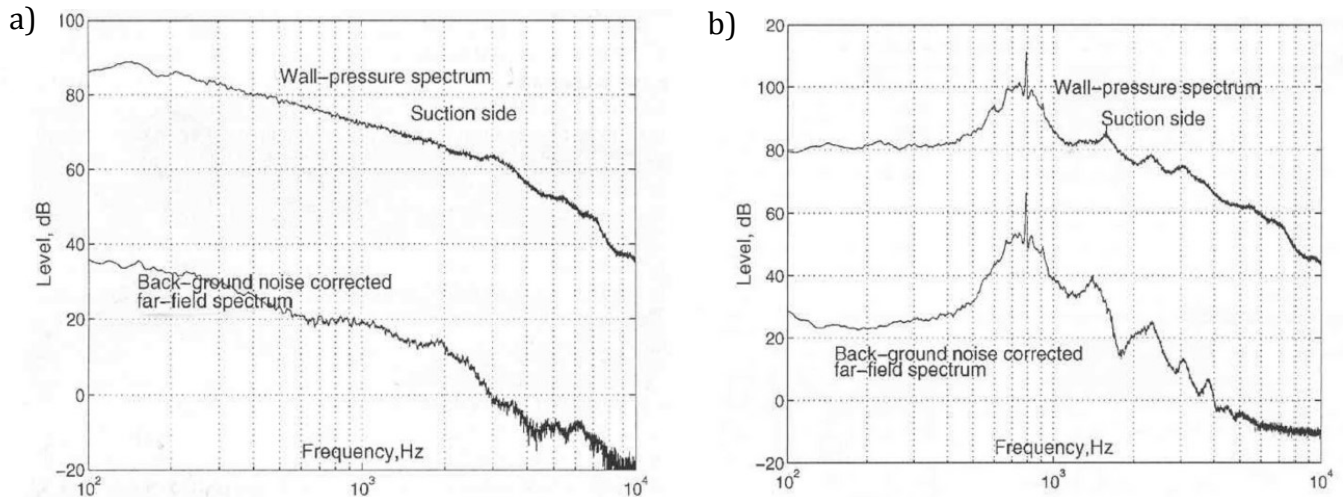


Figure 2.7 Comparison of the surface and far field pressure spectra (a) of a turbulent boundary layer, (b) of a laminar boundary layer [Roger and Moreau (2009)]

Further extensions such as from Roger and Moreau (2009) later provided a leading edge back-scattering correction, of importance in the modification of directivity in lower frequencies, with further extensions of the model taking under consideration the effect of a finite chord.

The very close relationship between the surface and far field pressure can be seen in Fig.2.7, where both of these spectra are plotted in the same graph for (a) a turbulent boundary layer and (b) a laminar boundary layer. In the first case, an example of broadband noise can be observed, whereas in Fig 2.7b, a narrowband hump with discrete tonal frequencies provides a typical example of the instability waves inherent in a laminar boundary layer. It can be seen that the distinct features of the radiated noise very precisely match with the wall pressure in both cases of (a) and (b).

In other words, as expressed in equation 2.9, Amiet's relationship suggests that reductions in the far field radiated noise could be achieved by reducing 3 different factors. Firstly a reduction in the boundary layer pressure spectrum close to the trailing edge S_{qq} , secondly a lower spanwise correlation length l_y , and thirdly the radiation term, $|I|^2$.

$$S_{pp} \propto |I|^2 S_{qq}(\omega) l_y(\omega) \quad (\text{eq. 2.9})$$

2.2.4 The mechanism of laminar boundary layer tonal noise

At low to moderate Reynolds numbers and with low-freestream turbulence intensity, Tollmien–Schlichting (T–S) instability waves are promoted after reaching a critical Reynolds number. On a sharp-edged airfoil, the T–S waves are found to propagate down the trailing edge and scatter into instability tonal noise. As seen in Fig 2.8a, tonal instability noise typically consists of a broad spectral hump centred on frequency, f_s in addition to the presence of a number of discrete tones occurring at frequency f_n . The frequency of the tone of highest Sound Pressure Level defined to be the dominant frequency, $f_{n \max}$. Paterson et al. (1978) has performed a systematic study on isolated airfoil noise in an anechoic environment. Based on calculations of the laminar boundary layer on a flat plate and the experimental observations, it was proposed that the main tonal central frequency scales as $f_s \sim v_j^{1.5}$, where v_j the free stream velocity. The frequency value f_s is found to be independent of the airfoil angle of attack.

Another key observation by Paterson et al. is the existence of the so called “ladder” structure for the dependence of tonal frequency on flow velocity. As seen in Fig 2.8 b the discrete frequency of the tone f_n , follows a power-law of 0.8. With increased freestream velocity, the dominant tonal frequency $f_{n \max}$ is observed to follow a smooth curve followed

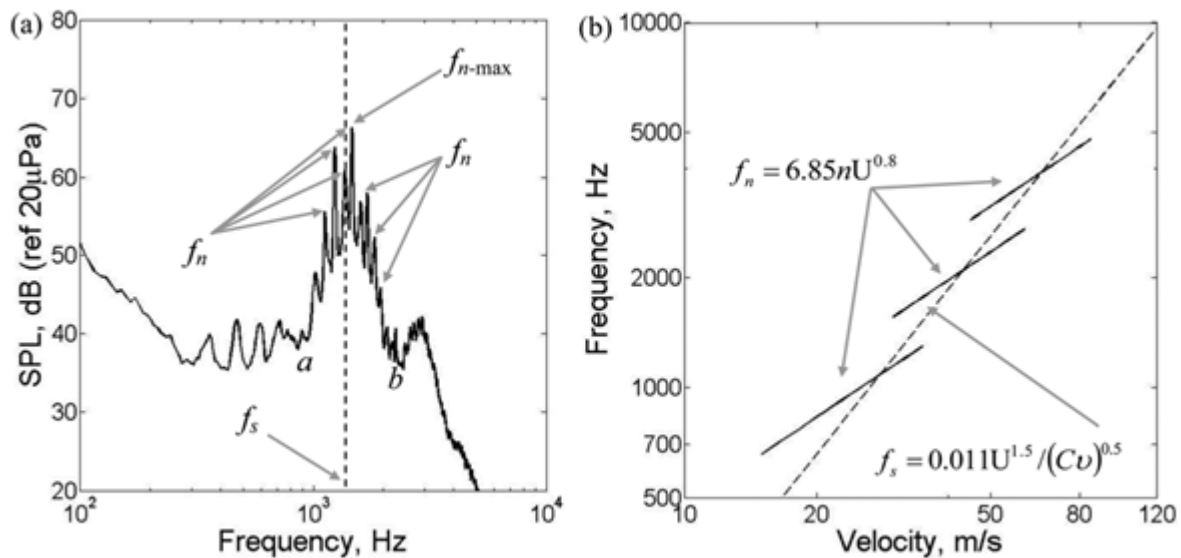


Figure 2.8 Illustrations of the (a) tonal frequencies f_s (main tonal frequency), f_n (discrete frequencies) and $f_{n \max}$ (dominant discrete frequency) and (b) scaling law off's plotted by Chong et al (2012) based in the formulas by Paterson (1973) and Tam (1974).

by a jump to another parallel curve with the same $u_j^{0.8}$ dependence. The $u_j^{1.5}$ dependency therefore represents the average frequency variation of the dominant tone.

Regarding the physical mechanism of the tonal noise, and in particular the ladder structure no overall agreement has been achieved to date. Using the experimental results of Paterson et al. (1973), Tam (1974) deduced the following modified frequency evolution law for the discrete tones, $f_n \propto v_j^{0.8}$. In an attempt to explain the presence of multiple tones in the spectrum Tam (1974) proposed a self-excited feedback-loop concept and conjectured that hydrodynamic instabilities are shed into the downstream wake which then becomes localized at some distances downstream of the trailing edge. Some of these wake instability modes are unstable where they radiate acoustic wave upstream and disturb the boundary layer near the trailing edge.

A closed loop is then formed in which instability modes produce sound which then drives the instability mode, and so on. A schematic of this process is shown in Fig. 2.9 (Model C). The notion of a localized noise source downstream the trailing edge was also proposed by Desquesnes et al. (2007) in a numerical study of low Reynolds number airfoil noise. In their model, the acoustic feedback from the wake propagates upstream beyond the trailing edge up to the points of the boundary layer instabilities on both of the pressure and suction surfaces of the airfoil. The process is illustrated in Fig. 2.9 (Model B).

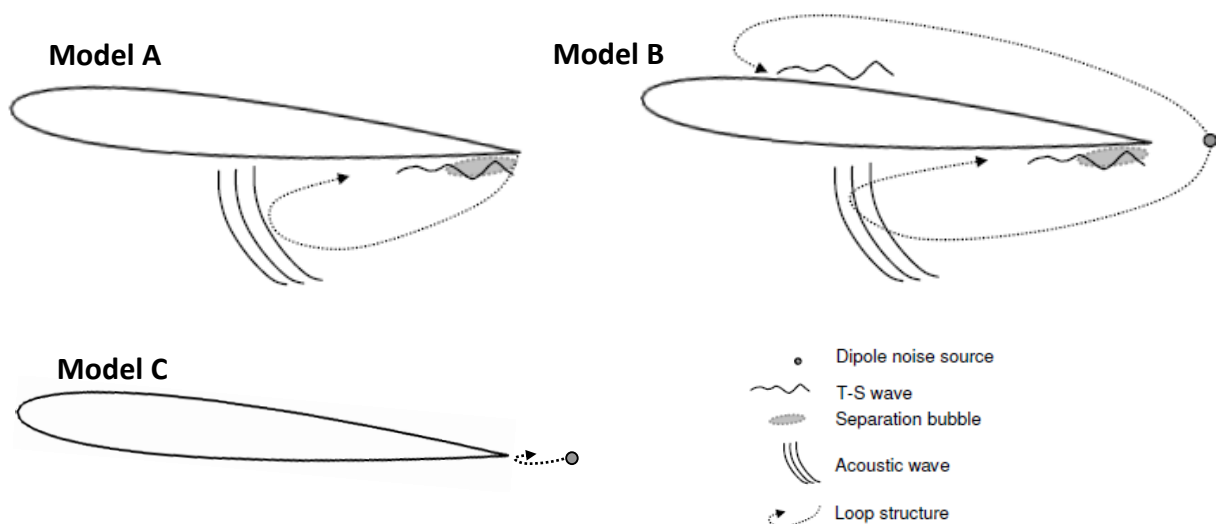


Figure 2.9 Aeroacoustic feedback models proposed in the literature for the generation of airfoil tonal noise. Model A is based on Arbey and Bataille (1983), Model B is based on Descquwntes et al. (2007) and Model C is based on Tam (1974); Chong et al (2010).

In Tam's model, the n^{th} tonal frequency occurs when the total phase change around the loop is equal to $2\pi n$. Tam's feedback hypothesis was later modified by Arbey and Bataille (1983). They argued that the broadband component of the noise spectrum was due to diffraction and scattering of Tollmien-Schlichting (T-S) waves at the trailing edge, whereas the discrete tone contributions are related to the aeroacoustic feedback mechanism discussed above. In their model, noise occurring at frequency f_n is due to a feedback loop between the boundary layer instabilities at the trailing edge and the upstream propagating acoustic wave that reinforces the point upstream of the trailing edge at which the instabilities originated. This mechanism is also illustrated in Fig. 2.9 (Model A). Recently, Kingan and Pearse (2009) also adopted this model to predict the tonal frequencies of laminar airfoils. The most significant difference between the aeroacoustic feedback Model A and Models B/C is that the former ignores the contribution of the unstable wave in the wake flow.

In a more recent study Pröbsting et al (2014) provided further insights towards the understanding of the aeroacoustic source mechanism through high speed PIV in combination with acoustic measurements at low Reynolds number flows. The correlation of the above mentioned methods identified the frequency of the vortical structures passing the trailing edge to correspond with the frequency of the dominant tone $f_{n_{max}}$. This leads to the conclusion that the scattering of vortical structures and the accompanied wall pressure fluctuations cause the tone generating mechanism. Furthermore, the presence of a periodic amplitude modulation in the acoustic pressure was confirmed, which was previously observed in the DNS study by Desquesnes et al (2007). The causes of the periodic modulation however stay unresolved. The frequency scaling with the freestream velocity is of the individual tones matches previous findings as a scaling of $v_j^{0.8}$ is observed over an extensive range.

The presence of an aeroacoustic feedback loop between the hydrodynamic instabilities and the radiated sound has been proven to play an essential role in the mechanism of tonal noise generation. However, the precise details and nature of this loop has not been unequivocally established and considerable uncertainties still exist about its details.

It is postulated that by adding a serrated profile to the TE, the local separation bubble could be suppressed either completely or partially, depending on the serration properties. Also, the effectiveness of the acoustical diffraction process could be reduced near the

serrated edges. The use of serrations is therefore potentially effective in controlling instability tonal noise radiation. The effect of serrations so far investigated for laminar boundary layer noise has been carried out by Chong and Joseph (2013) which will be discussed further in Section 2.3.5.

2.2.5 Bluntness noise

Vortex shedding noise due to bluntness usually is of distinct narrowband nature and appears in the acoustic spectra as a hump centred around a dominant frequency, superimposed to the broadband noise. As bluntness noise is generated in the small separated region past an airfoil's blunt trailing edge, the aforementioned hump could be observed in both, the far field noise spectra as well as the surface pressure fluctuation measured as investigated by Brooks and Hodgson (1981) and specified by Blake (1988). The intensity of bluntness noise depends on the ratio between the boundary layer thickness and the bluntness at the trailing edge of the airfoil. Bluntness noise is found to be generated for cases where the bluntness parameter of the trailing edge ε/δ^* is higher than 0.3, where ε the bluntness in mm and δ^* the displacement thickness. A non-dimensional Strouhal number dependency for the characterisation of the vortex shedding is expressed through the shedding frequency f_d , the bluntness parameter ε and the flow velocity U through

$$St = f_d \varepsilon / U \quad (\text{eq. 2.10})$$

For a straight trailing edge of a given bluntness, a constant Strouhal number is observed throughout the velocity range [Blake (1988) Brooks et al (1989)].

This particular noise mechanism is relevant in the serration case investigated in this PhD project where bluntness noise is superimposed in the broadband noise spectra. More precisely the serrations are directly cut into a straight trailing edge and hence incorporated in the airfoil, resulting into partial bluntness between the two serrations. (as depicted in the later sections, as in Fig. [2.19]). In this thesis, it will be attempted, amongst other contributions, to eliminate the noise generating mechanism involved.

2.3 Theoretical Background of Trailing Edge Serrations

2.3.1 Trailing edge treatments and Biomimicry

The science of biomimicry or biomimetics is the investigation and application of concepts found in nature in order to help solving complex human problems. The concepts of serrations and porous media to be investigated in the present study are also well established in nature and inspired by the observation of the owl's quiet flight.

Graham (1934) was one of the first scientists to identify the three main characteristics which make the flight of the owl so quiet. He is followed by further investigations from Kroeger (1971) and Liley (1998) Bachman and Klan (2010) more recently. The three wing characteristics, also depicted in Fig. 2.10, are the leading edge comb, the periodic trailing edge fringes and a downy, fibrous upper surface of the wing. In this way the owl has evolved about 20 million years ago due to the need to fly silently at least at frequencies between 2 kHz and 20 kHz, which is within the maximum hearing range of its prey, typically mice and voles. Apart from the acoustic aspect, the owl can also achieve a superior aerodynamic efficiency through its wing structure. It is found that it is able to

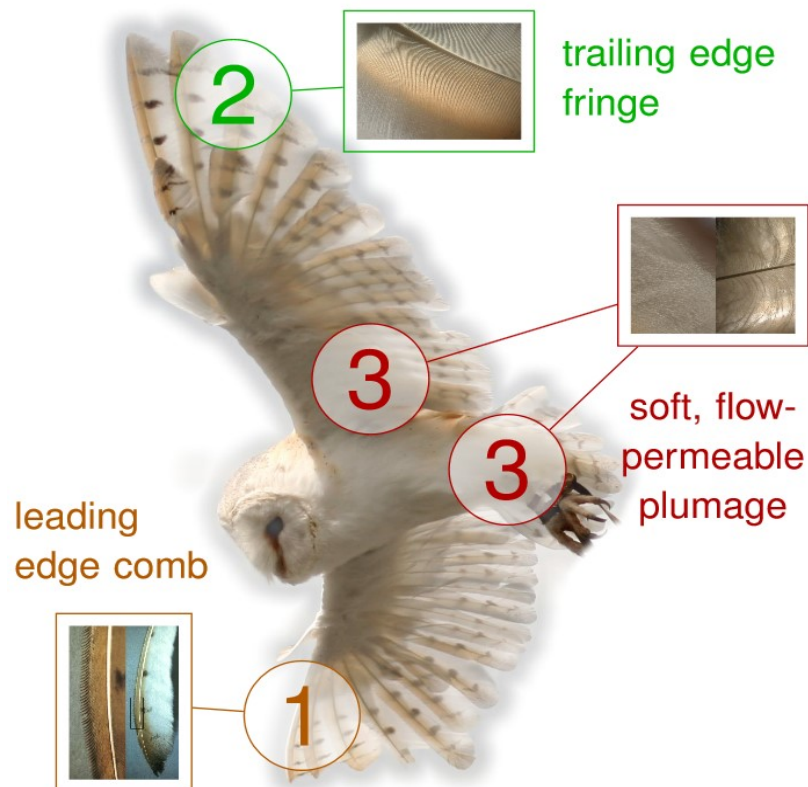


Figure 2.10 The owl's main characteristics for the achievement of silent flight [Geyer et al (2011)]

achieve a very steep flying trajectory of about 24° when approaching the prey. With a fairly low Reynolds numbers ($Re \approx 1.5 \times 10^5$) and the respective lift coefficient ($C_L \approx 1$) considered in this situation, it has been discovered that achieving stable flight with a normal aircraft wing would not be possible as flow separation would occur near the leading edge followed by a stall. This property is obtained through the leading edge structure, as the serrated-like comb inhibits flow separation on the upper surface even if close to a stall [Lilley (1998)]. Kroeger (1971) found that by removing the leading edge comb from the primary feathers, the owl would lose the stability when flying steep paths and it would become as noisy as any other bird. The fringe at the trailing edge might also be considered as a continuous serrated structure. It allows a smoother mixing between the upper and lower surface boundary layers of the wing to convect past its trailing edge. Sound measurements by Kroeger suggested that the noise scattering mechanism is eliminated at the trailing edge by the fringe. This results to a change in the power law from U^5 to U^6 which comprises a significant noise reduction when considering the low flight speed of the owl. The result of the total sound power level indicates a rather favourable noise energy distribution over the frequency spectrum due to the fact that peaks were observed, which however were well below the human's audible range. According to Lilley (1998) an owl, when considering only the fringe, is 6-7dB quieter when compared to a bird without this feature of comparable mass and flight characteristics.

As seen in Fig 2.11, the fibres of the down feathers have a very fine structure which have a length scale just larger than the scale of Kolmogorov eddies. It is believed that in this way the compliant wing surface is able to absorb the turbulent energy on the boundary layer, causing a bypass dissipation mechanism in order to make it a further important factor for the noise reduction beyond 2 kHz. A recent test conducted by Geyer et al. (2014) presents the superior noise characteristics of the owl where flyover measurements of a

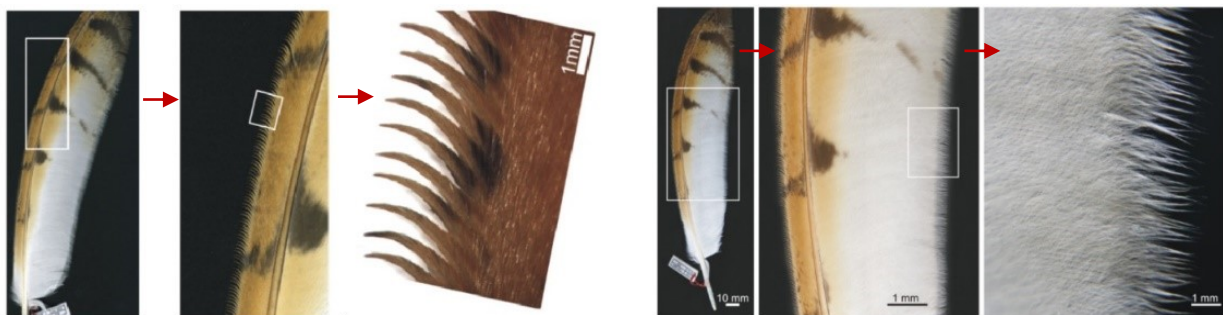


Figure 2.11 Serrations at the outer vane (left) and fringes at the inner vane (right) from barn owl feathers with magnifications [Bachmann (2010)].

barn owl were compared to flyovers of a harris hawk and a common kestrel. In agreement with previous studies, the advantages of the owl's silent flight can be observed mainly in the mid-to high frequency range as it is shown in Fig. 2.12. The particular results are normalized to a distance of 1 m and scaled by using the fifth power of the Mach number, commonly used for the scaling of trailing edge noise.

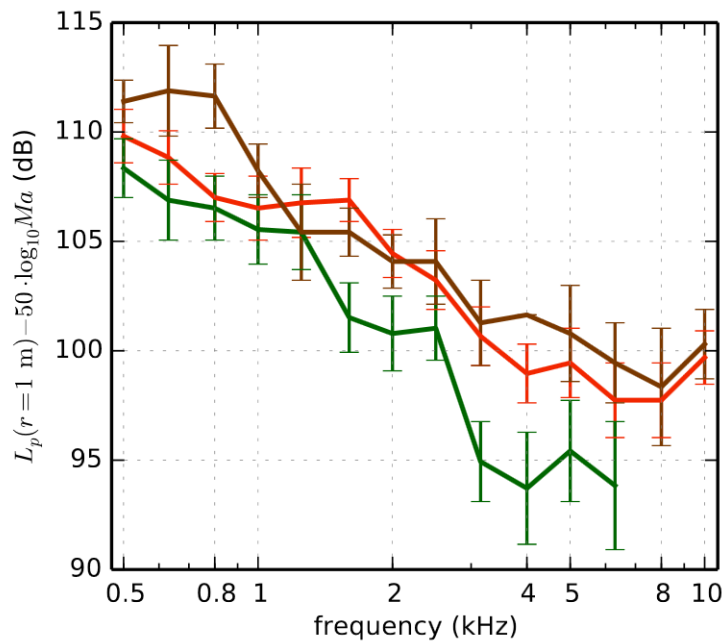


Figure 2.12 Scaled third octave band sound pressure levels from flyover measurements of a barn owl (---), a harris hawk (---) and a common kestrel (---).

2.3.2 Howe's theory

While serrations on the leading edge appeared to be of certain interest since the 1970s, no publications indicated their application on the trailing edge until Ver (1987) investigated their use in the late 1980s. When applied on the exhaust of a jet engine jet noise reductions of up to 5dB were reported. Howe [1991a, 1991b] made an analytical approach to the potential self-noise reductions by trailing edge serrations where he derived an analytical model for the prediction of trailing edge noise over a flat plate with a serrated trailing edge.

As shown in Fig.2.13 the geometrical characteristics of the serrations can be defined as the root-to-tip distance $2h$ and their spanwise wavelength λ , resulting in a serration angle ϕ . Howe suggests that at high frequencies a turbulent boundary layer eddy convecting past a trailing edge, of wave-number = $(K_1, 0, K_3)$, where K_1 the streamwise component and K_3 the spanwise component on an airfoil, generate significant noise only when the arriving wave-number component is normal to the edge. At these frequencies the large eddies are found to satisfy $\left|\frac{K_3}{K_1}\right| \leq 1$, indicating that the major noise sources occur when eddies approach the edge at angles greater than 45° to the mean flow. This in turn implies that an optimal attenuation for trailing edge noise occurs when the edge is inclined at an angle smaller than 45° to the mean flow direction which concludes to the effectiveness of serrations being at $\phi \leq 45^\circ$.

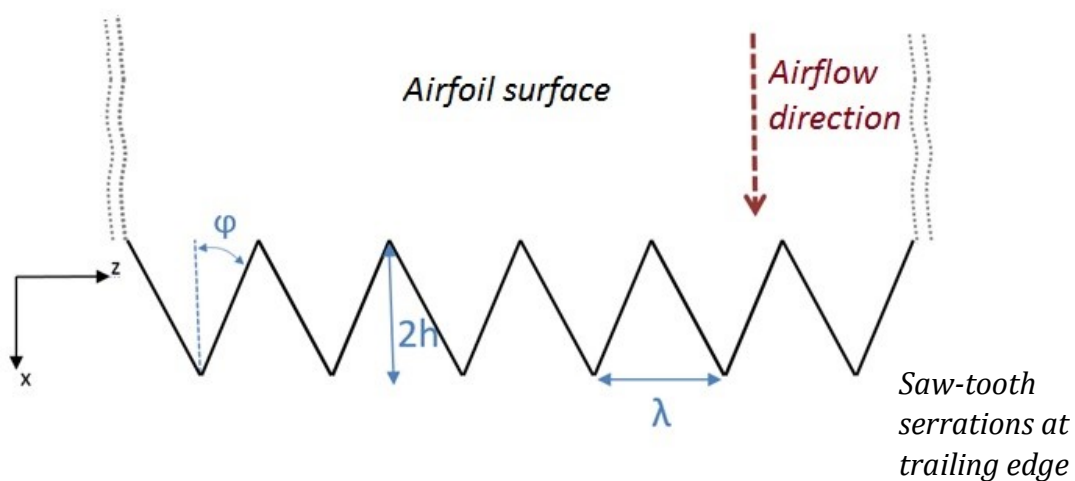


Figure 2.13 Parameters of the trailing edge saw-tooth geometry.

More precisely, the model considered a thin rigid flat plate of infinite span, zero angle of attack at a low Mach number. Considering this model, the acoustic pressure frequency spectrum $\Phi(\omega, x)$ where ω is the frequency at an observer location $|x|$ from the trailing edge, is defined by:

$$\frac{\Phi(\omega, x)}{(\rho v_*^2)^2 \left(\frac{l}{c}\right) \left(\frac{\delta}{|x|}\right)^2} = \left(\frac{C_m}{\pi}\right) \sin^2\left(\frac{\theta_a}{2}\right) \sin(\beta) \Psi(\omega), \quad |x| \rightarrow \infty \quad (\text{eq. 2.9})$$

Where ρ the fluid density, v_τ the friction velocity ($\approx 0.03U$), l the flat plate span, c the speed of sound, δ the boundary layer thickness, $C_m \approx 0.1553$, θ_a and β are the angles defining the observers point x . The non-dimensional far field pressure spectrum $\Psi(\omega)$ for a serrated trailing edge is then expressed as

$$\Psi(\omega) = \left(1 + \frac{1}{2} \epsilon \frac{\vartheta}{\delta \epsilon}\right) f\left(\frac{\omega \delta}{U_c}, \frac{h}{\lambda}, \frac{h}{\delta}; \epsilon\right), \quad (\text{eq. 2.10})$$

where

$$f\left(\frac{\omega \delta}{U_c}, \frac{h}{\lambda}, \frac{h}{\delta}; \epsilon\right) = \frac{1}{AB + \epsilon^2} \left(1 + \frac{64 \left(\frac{h}{\lambda}\right)^3 \left(\frac{\delta}{h}\right) (\cosh\{C\sqrt{A+\epsilon^2}\} - \cos(\frac{2\omega h}{U_c}))}{(\sqrt{A+\epsilon^2})(AB + \epsilon^2) \sinh(C\sqrt{A+\epsilon^2})}\right) \quad (\text{eq. 2.11})$$

where $A = \left(\frac{\omega \delta}{U_c}\right)^2$, $B = 1 + (4h/\lambda)^2$, $C = \lambda/2\delta$, $\epsilon = 1.33$

For the case of a non-serrated, straight trailing edge where $h \rightarrow 0$, Ψ is reduced to

$$\Psi_0(\omega) = \frac{A}{(A + \epsilon^2)^2} \quad (\text{eq. 2.12})$$

Howe's theory concludes potential reductions of up to $10 \times \log_{10} \left(1 + \left(\frac{4h}{\lambda}\right)^2\right)$ dB for a sawtooth serration at high acoustic frequencies of $\frac{\omega h}{U} \gg 1$ with the aforementioned condition of $\varphi < 45^\circ$ and $\frac{\lambda}{h} < 4$. Subsequently the smaller the angle φ , where $\frac{\lambda}{h} \rightarrow 0$, the greater the attenuations achieved.

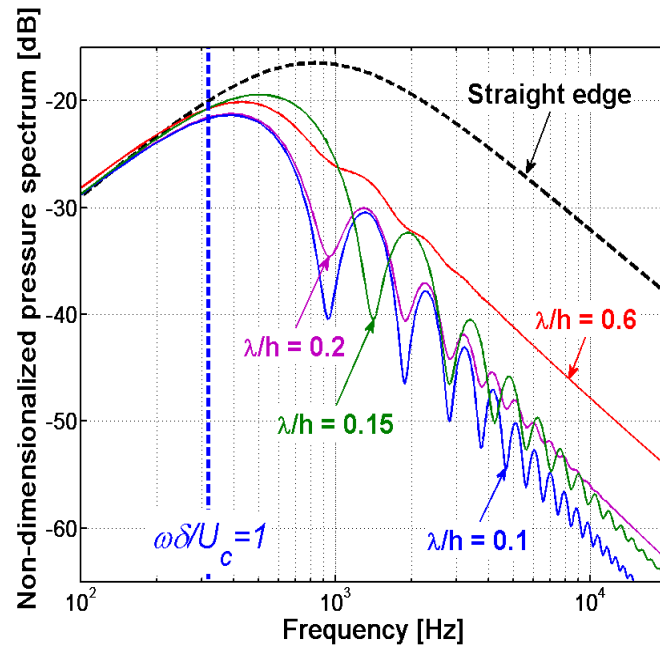


Figure 2.14 Non-dimensional acoustic spectrum according to Howe's theory [1991a,1991b] comparing a straight trailing edge with various serrations geometries of varying λ/h . [Gruber 2012]

Figure 2.14 depicts the non-dimensionalised acoustic spectrum which demonstrates the potential noise reductions by various serration geometries compared with a straight trailing edge. It can be seen that noise reductions indeed occur when $\frac{\omega h}{U} \gg 1$ and increase when $\frac{\lambda}{h} \rightarrow 0$.

2.3.3 Serrations and related passive flow control techniques for TE noise reduction

After Howe's initiative with an analytical approach, many other researchers continued to investigate trailing edge serrations. For example a project for the *Investigation of Serrated Trailing Edge Noise* (STENO), Oerlemans(2009) , Gruber *et al* (2010) and Chong *et al* (2012) between others. They can confirm parts of Howe's theory, but none of them can replicate the distinctively large noise reductions levels predicted by Howe.

From the aforementioned, the STENO project [Dassen *et al.* (1996), Braun *et al.* (1998, 1999),] and Oerlemans (2009) combined wind tunnel testing with and real scale wind turbine blades. As part of STENO, [Dassen *et al* (1996)] five serrated trailing edge flat plate models and eight different airfoils were tested and compared to their equivalent straight

trailing edge. Reductions up to 8-10dB were obtained in certain frequency ranges. However, the presented data was limited to certain frequencies of 1, 2 and 4 kHz. After further preparations the serrations were applied on wind turbines, which yielded only partially successful results [Braun et al (1998, 1999)]. More precisely, the maximum achieved reduction of the overall sound pressure level was up to 3.5 dB at certain incidence angles, nevertheless it was reported that a high frequency noise increase diminished any overall reductions beyond the 3.5dB threshold.

Oerlemans(2009) used a 94-m diameter three-bladed wind turbine for a direct comparison of the noise emission. With the shape of a NACA 64418 airfoil due to its common use for wind turbines, a straight trailing edge was compared to an (1) optimised airfoil shaped blade (SIROCCO) and (2) a serrated trailing edge add-on. As seen in Fig.2.15 noise reductions were discovered over certain frequency ranges for both shapes. A noise reduction of up to 5dB for frequencies up to 1 kHz was obtained for the serrated trailing edge. However, beyond this frequency a noise level increase is also observed. This noise increase thus undermines the overall noise performance of the trailing edge serration.

Herr (2006) tested a serration related trailing edge treatment (Fig 2.16a), where a brush type attachment was used on a flat plate. The brushes, consisting of one single row of propylene fibres, were described as an extreme form of serrations of which wavelength is close to zero. Reductions of 2 to 10 dB were reported within approximately 1 to 16 kHz,

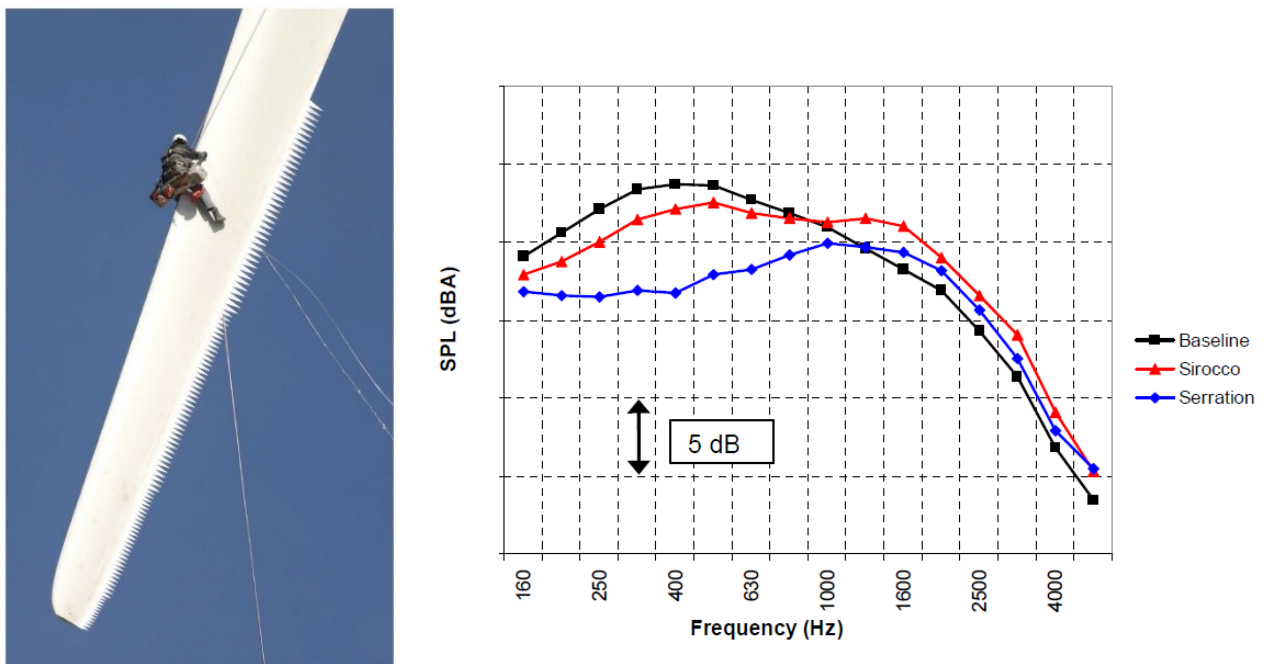


Figure 2.15 Investigation by Oerlemans (2009) on the noise reduction tested on a full scale wind turbine using trailing edge treatments

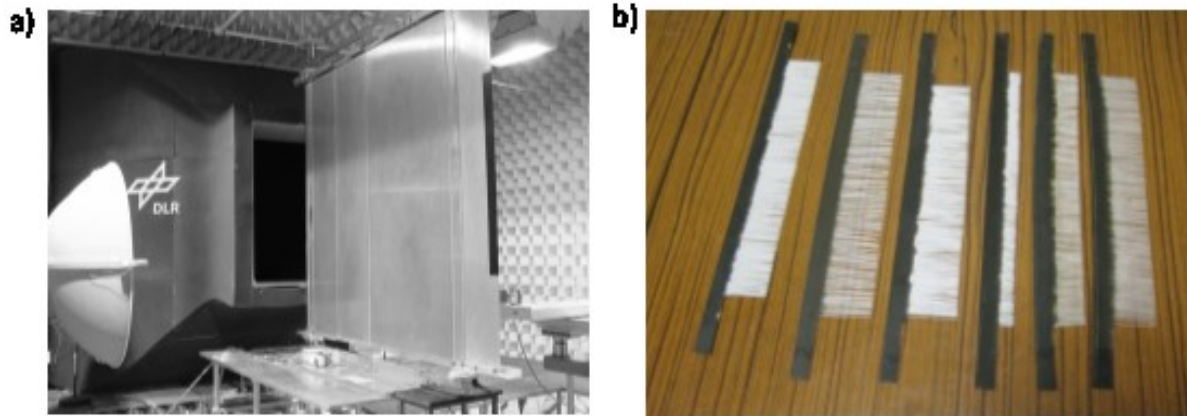


Figure 2.16 (a) Brush test set up on flat plate by Herr (2006) and (b) NACA 65 trailing edge brushes by Finez (2010)

taking under consideration that vortex shedding noise was suppressed by the baseline trailing edge additionally to the actual TBL-broadband noise. Various brush types and sizes were tested and it was found that the thickest brush type achieved the greatest reductions. The broadband noise reduction was obtained in the range of Strouhal numbers ($St = f\varepsilon/U_\infty$, where ε the TE thickness) between $0.02 \leq St \leq 0.2$. A noise increase was observed when $St > 0.2$ which however is close to the non-audible frequency range. Herr attributed the noise reduction to the viscous damping of the unsteady turbulent flow pressure in the region of the brushes. A similar test conducted by Finez *et al.* (2010) who investigated trailing edge brushes on a cambered NACA 65(12)-10 airfoil (Fig 2.16b). The reductions achieved were in the order of 3 dB in a frequency range of 200Hz to 2000Hz. Through a space-time correlation analysis, it was also found that the spanwise pressure based correlation length was reduced by almost 25%. This might explaining the 1.3dB noise reduction measured in the far field.

Jones and Sandberg (2010) investigated serrations numerically using Direct Numerical Simulations (DNS) at low Reynolds numbers. The investigation was performed on a symmetric NACA 0012 airfoil with an additional flat plate trailing edge extension to incorporate the serrations. Two serrations lengths were tested corresponding to an approximate size of δ and 2δ respectively at an angle of attack of 5° . It was found that the longer serrations predicted a greater reduction in the range of 6-10 dB mostly at Strouhal numbers based on the airfoil chord of $St > 5$, analogically with Howe's analytical work. The shorter serrations provided reductions of a smaller extent for $5 \leq St \leq 20$, while at $St > 20$ a noise increase was observed.

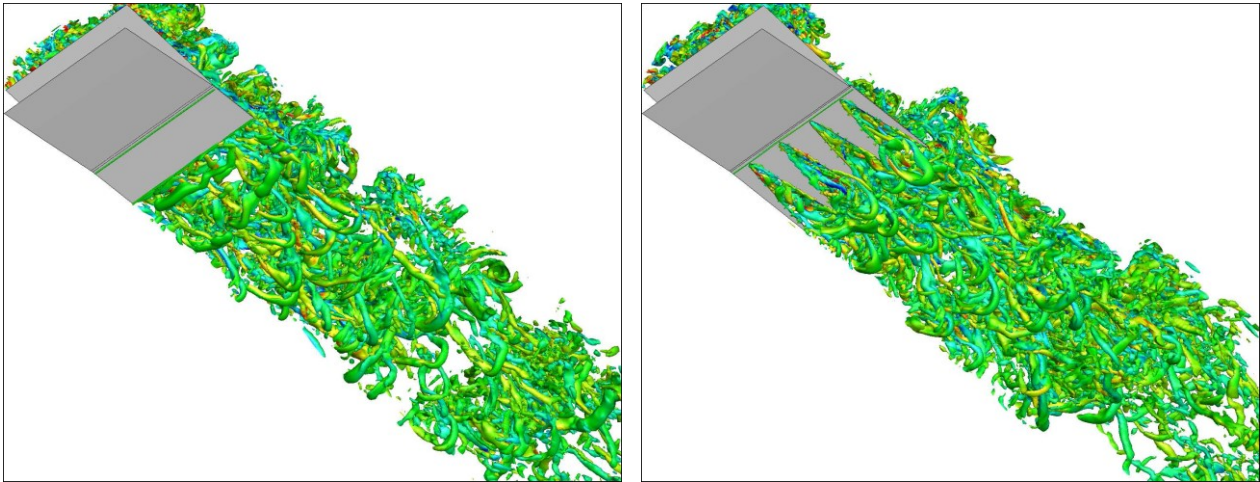


Figure 2.17 Iso-contours for the visualisation of turbulent structures past a straight edge (left) and the serrated TE (right). [Jones and Sandberg (2010)].

Another interesting observation by Jones and Sandberg (2010) was that the sound radiation appeared to be caused solely through the changes in the scattering process itself, and not so much by the changes of hydrodynamic behaviour over the serrated edge. This assumption was reinforced from the finding that the boundary layer properties and spanwise correlation levels remained largely unchanged, or were insignificant, if compared with the straight trailing edge. As it can be seen in Fig 2.17 a tendency for horseshoe-type vortices was found in the serrated case, which were formed in the gaps between the serrations convecting to the wake.

A similar, add on type, serration was investigated experimentally by Gruber et al. (2010) and Gruber (2012). Flat plate inserts of numerous serration geometries were attached to a NACA65 (12)-10 airfoil (Fig 2.18a) for Mach numbers between $M=0.06$ and $M=0.24$.

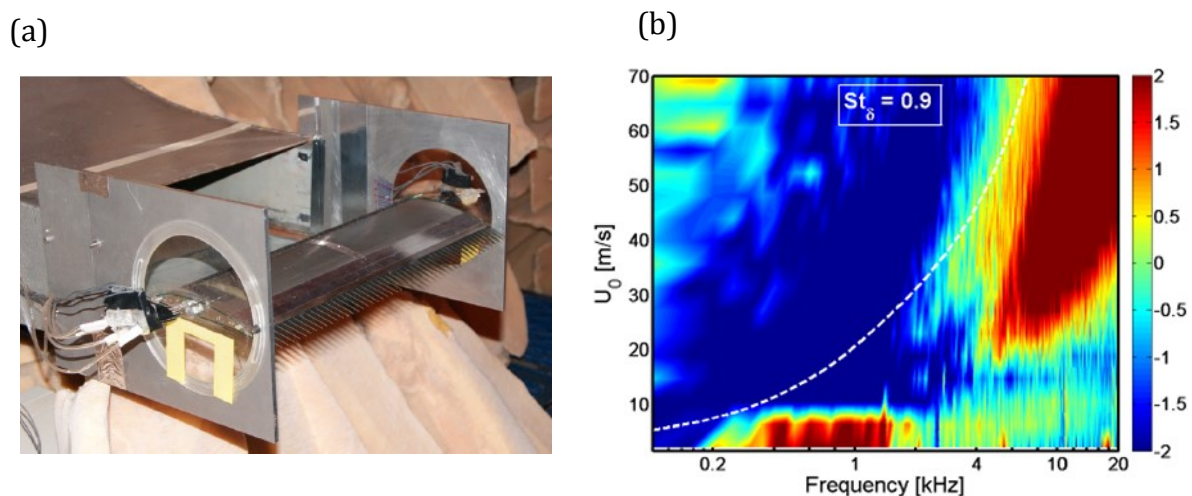


Figure 2.18 (a) Flat plate-type insert serrations on airfoil ; (b) Noise spectra (dB) for $\lambda = 3\text{mm}$, $h = 15\text{mm}$ at $\alpha = 5^\circ$ by Gruber et al [2006].

Gruber's findings did not agree with Jones and Sandberg (2010) and Howe (1991a, 1991b) regarding the boundary layer thickness which appeared to increase significantly, up to 12%, towards the serrated tip. Noise reductions of up to 5dB were obtained in the low frequency range where $f\delta/U_m < 1$, while for $f\delta/U_m > 1$ a noise increase was observed. It should be noted that the turbulent boundary layer thickness δ for $f\delta/U_m$ was not measured directly but was estimated using XFOil. It was found that reductions were obtained when $h/\delta > 0.5$. This implies that noise reduction would require the serration length to be greater than the local turbulent boundary layer thickness. For the noise increase at $f\delta/U_m > 1$ it was presumably caused by a leaking cross-flow through the valleys of the serrations. As it can be seen in Fig. 2.18b critical parameters of the serrations were found to be h/δ and h/λ at lower frequencies. If compared to Howe's theory, the noise reductions achieved were below the analytical predictions. In order to overcome the increase at high frequencies, Gruber used added slits to the serrations. In this way reductions of up to 5dB were achieved, while the high frequency increase was significantly limited to a maximum of 1dB.

Moreau *et al.* (2012) conducted a test with serrations of 0.5mm thickness, attached on a tapered flat plate trailing edge at low-to-moderate Reynolds numbers (Fig 2.19a). As seen in Fig 2.19b, broadband reductions of 3dB were found, where larger serration angles appeared to be more effective, contrary to Howe's predictions. Additionally, the vortex shedding noise from the straight reference configuration was diminished, obtaining reductions of up to 13dB at high frequencies.

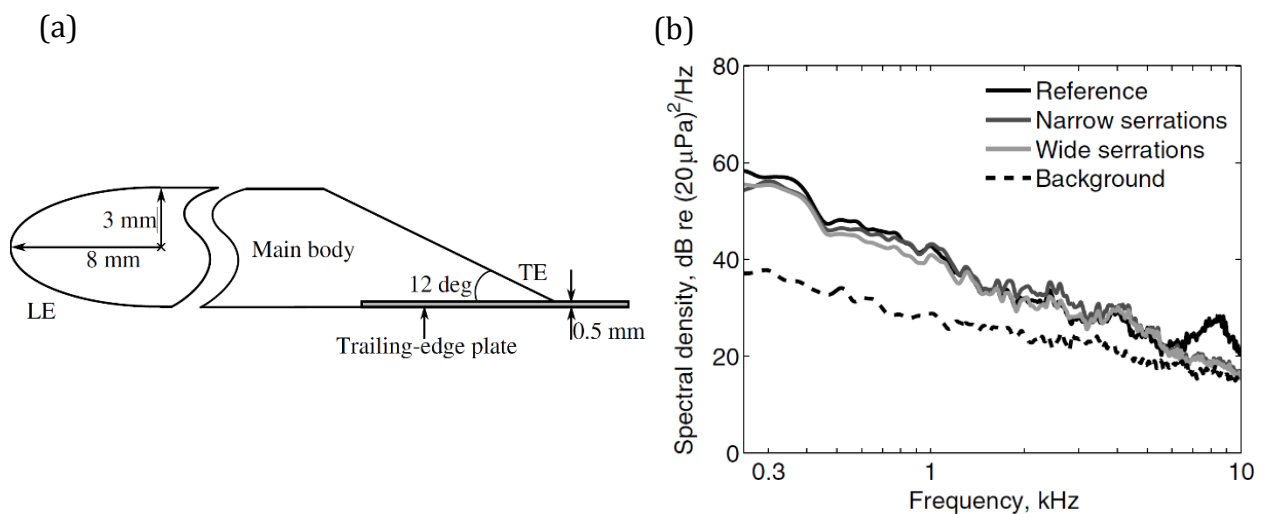


Figure 2.19 (a) flat plate configuration and flat plate trailing edge serration attachment by Moreau *et al* (2012) and (b) the corresponding far-field acoustic spectra for $U_\infty=38 \text{ ms}^{-1}$

While all the above serration types are flat plate attachments extending the trailing edge, Chong *et al.* (2013) presented serrations which were directly cut into the trailing edge section of a NACA0012 airfoil, thus keeping its original shape. This configuration, as shown in Fig 2.20a, provides a greater strength and structural integrity than the flat plate serration. This could be an important advantage if considered to be used in commercial applications, which would furthermore comprise easier manufacturing process. Fig. 2.19b shows the noise performance of a non-flat plate serrated trailing edge through the difference of its sound pressure level when compared to a baseline straight trailing edge (Δ SPL) where negative values point out noise increase and vice versa. As seen in Fig 2.19b, noise reductions up to 7-8 dB were achieved, however another noise became discernible: Vortex shedding noise generated due to the bluntness near the serration root (depicted between the lines of f_1 and f_2 in Fig 2.20b). The observation was made that serrations of larger angles produced less vortex shedding noise, which can be explained as the blunt area is reduced when compared to a larger number of narrower serrations. In the attempt to eliminate this noise source, a woven wire mesh was used to cover the gaps of the serrated trailing edge, which inhibited parts of the vortex shedding noise. On the other hand, a high frequency noise increase was again noticed which is believed to be due to the surface roughness induced by the mesh.

With the similar concept as above by Chong *et al.* (2013), Pröbsting (2011) provides some aerodynamic results of the non-flat plate type serrated trailing edge on a NACA0012 airfoil of 0.4m chord length for speeds up to 35 m/s. By utilizing a tomographic PIV

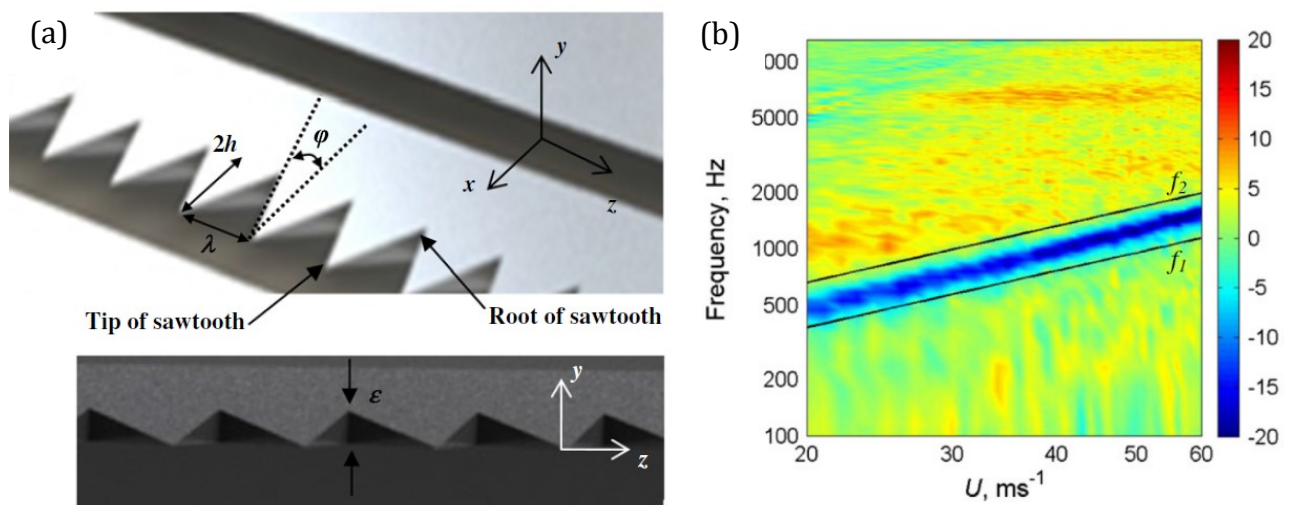


Figure 2. 20 (a) Illustrations of a non-flat plate serrated trailing edge and their serration parameters. (b) Colormap of the sound pressure level (Δ SPL) of a serrated trailing edge at $\alpha=4.2^\circ$, where positive values show a noise increase when compared to a straight airfoil trailing edge and vice versa.

technique, a subset of coherent structures near the trailing edge was identified. Due to the blunt root for the serration, vortex shedding events have also been identified on the sawtooth surface, which apparently can produce tonal noise of the similar shedding frequency. Pröbsting postulated that the reduction in broadband noise by trailing edge serrations might be related to a redistribution of energy within the turbulence spectrum through this shedding event.

It is worth mentioning that in all above cases the resulting reductions were clearly less compared to the predictions of Howe's model. Additionally, in all experimental investigations where trailing edge serrations were attached on an airfoil, a noise increase was observed (high frequency increase for the flat plate type serrations and vortex shedding noise due to bluntness for the integrated serration type), which often negated the noise performance. An important step towards the development of a trailing edge concept shall be presented in this thesis, where reductions are achieved throughout the audible frequency range and the aerodynamic performance is not compromised by the trailing edge treatment.

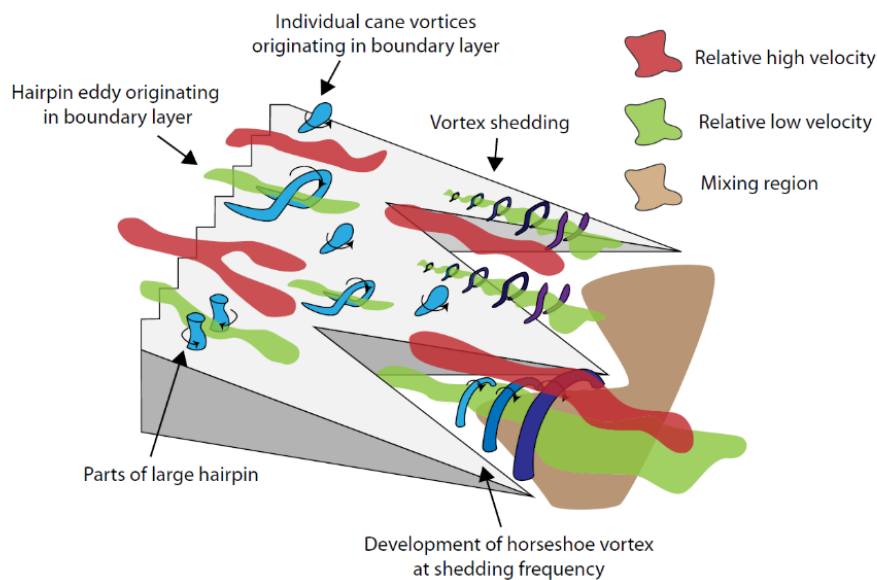


Figure 2.21 Coherent structures on non-flat plate serrated trailing edge of a NACA 0012 [Pröbsting (2012)]

2.3.4 Porous materials for airfoil self-noise reduction

The use of porous materials to reduce flow-generated noise has been firstly adopted in the investigation of perforated duct liners [Tsui and Flandro (1977)], porous baffles [Ver (1982)] and circular perforated cylinders for train pantographs [Ikeda et al. (2004)]. However, the application of porous materials on airfoils initially appeared to be fairly limited with Fink et al. (1980), Revel et al. (1997) and later with more persistent research by Sarradj and Geyer (2007) and Geyer et al [2010a, 2010b, 2011,2014]. The experiment undertaken by Herr (2006) as described in section 2.3.3 might also be related due to the porous nature of the tested brushes.

Howe (1979) investigated the noise mechanism of a turbulent boundary layer passing a perforated trailing edge of an airfoil. Noise reductions beyond 7dB were reported in this theoretical approach. Howe suggested to limit the length of the perforated section of the trailing edge to an extent comparable with the size of the largest turbulent eddies. Moreover, the porosity should ideally have a gradual increase, i.e. the level of porosity should decrease towards the tip of the trailing edge, as this would resulting to a smoother rate of change regarding the acoustic surface impedance.

Geyer et al (2010a, 2010b) investigated the reduction of trailing edge noise using fully porous SD7003 airfoils of 0.4m span and chord 0.235m (Fig.2.22). Using up to 16 materials in the aforementioned studies, it was concluded that the noise levels strongly, but not solely, depend on the flow resistivity of each entirely porous airfoil.

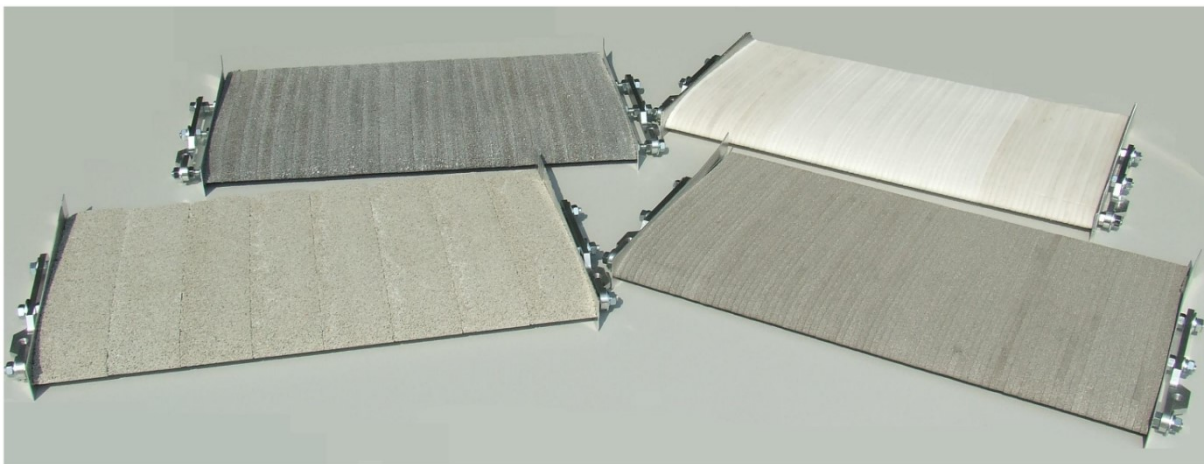


Figure 2.22 Fully porous airfoils as investigated by Geyer et al (2010a, 2010b)

Flow resistivity (r) is defined as

$$r = \frac{\Delta p}{U_{fl} * d} \quad (\text{eq. 2.13})$$

where Δp is the pressure difference across a sample of a porous material, U_{fl} the flow velocity and d the thickness of the porous material sample. Thus, the parameter of flow resistivity is a measure to define the resistance of a porous material against the permeation of a fluid flow. A value of 0 would mean that the material is permeable without resistance and an infinite value (∞) indicates that the material is impermeable [Scheidegger (1974)].

Apart from flow resistivity, other factors which presumably influence the noise performance might be the microstructure, the size of the pores and the surface roughness of the material. The latter is believed to be a significant contributor to high frequency noise increase. When compared to a baseline, non-porous airfoil, the noise reductions achieved by Geyer et al (2010a, 2010b) were in the range of 10dB in low to mid frequencies, and in some cases ~ 15 dB or more within the mid-frequency range. A further observation was that the turbulent boundary layer thickness and boundary layer displacement thickness were larger than of the non-porous airfoil. Moreover, contrary to the theory of non-porous airfoils, an increased turbulent boundary layer thickness and boundary layer displacement thickness by the porous materials, yielded larger noise reductions at the trailing edge of the porous airfoil. The drawback of a fully porous airfoil however is the substantial decrease of lift and increase of drag.

Geyer and Sarradj (2014) further investigated the varying streamwise extent of the porous material (herein denoted as “s”) between 5% and 50% of the chord length (s/C from 0.05 to 0.5) from the trailing edge, including a non-porous and a fully porous case. It was observed that noise reductions improved as the extent of the porous material increased. The extent of porous material however is inversely proportional regarding the aerodynamic performance (i.e. reduced lift and increased drag). For medium to high flow resistivity materials, the results appeared to be more suitable for achieving noise reductions for these partially blunt trailing edges. The reductions were mainly observed in in the mid-frequency range while a noise increase was commonly observed in the low and high frequencies of most of the materials. Figure 2.23 shows the aforementioned findings for two cases where $s/C = 0.05$ (Fig 2.23a) and $s/C = 1$ (Fig.2.23b).

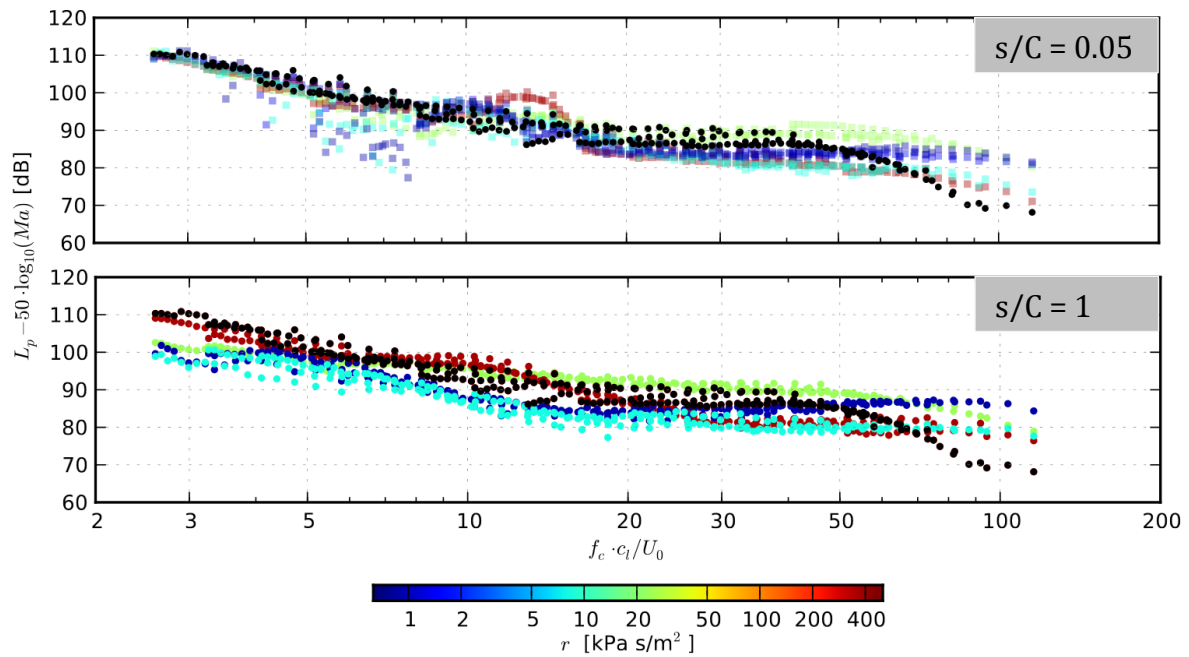


Figure 2.23 Noise performance (sound pressure level scaled with U^5) of airfoils with varying flow resistivity as a function of the chord based Strouhal number, for two s/C values at angle of attack 0° . (Black dots represent non-porous reference airfoil). [Geyer and Sarradj (2014)]

2.3.5 Trailing edge serrations and laminar boundary layer noise

While all previously mentioned passive flow control techniques focus on the reduction of turbulent boundary layer broadband noise, the application and research of trailing edge serrations for laminar boundary tonal noise is fairly limited. Chong et al (2010) investigated non-flat plate trailing edge serrations in these flow conditions. As it can be seen in Fig. 2.24, sound pressure level reductions of about 30 dB of boundary-layer instability tonal noise could be achieved. In addition, no significant noise penalty from the radiation of the vortex shedding near the blunt root of the sawtooth trailing edge was present, which implies that the wake flow for an untripped airfoil is characterized by a weak vortex shedding.

Regarding the noise reducing mechanism, it is believed that the introduction of a serrated trailing edge can force an otherwise laminar or separated boundary layer near a sharp trailing edge to bypass transition to turbulence. Thus a dissolving of the noise amplifying separation bubble leads to the suppression of the boundary-layer instability tonal noise. Due to the fact that the separation bubble shifted towards the trailing edge region when at higher angles of attack (i.e. at $\alpha=1.4^\circ$ and 4.2°) the noise reductions were greater in these cases when compared to $\alpha=0^\circ$.

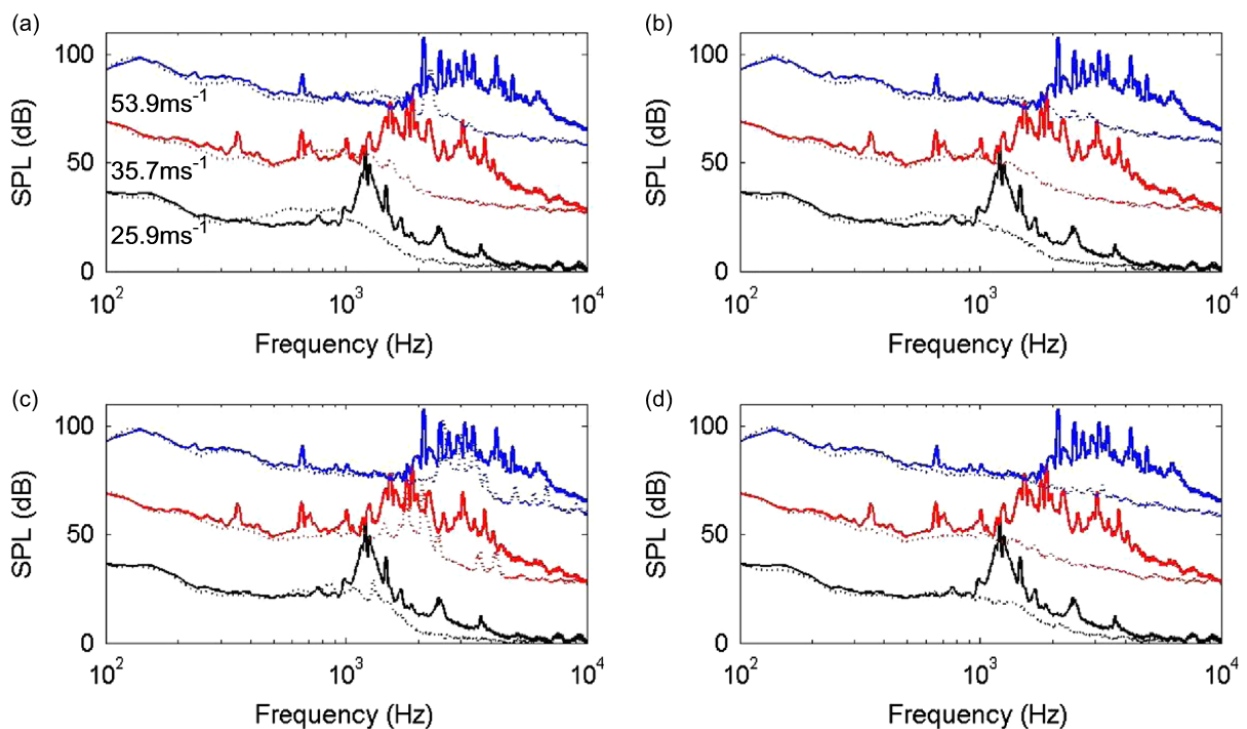


Figure 2.24 Sound pressure level spectra at $\alpha=1.4^\circ$ for four serration types in comparison with the baseline straight trailing edge (dotted line) where serrations have a geometry of a) $\phi=7^\circ$, $2h=20\text{mm}$ b) $\phi=12^\circ$, $2h=20\text{mm}$ c) $\phi=12^\circ$, $2h=10\text{mm}$ and d) $\phi=24^\circ$, $2h=20\text{mm}$. From Chong et al (2010).

2.4 Discussion

This chapter provided a review of the related research conducted to date. The aerodynamic noise sources known as trailing edge noise, as well as bluntness induced vortex shedding noise are the mechanisms of focus in this thesis.

The interaction of the turbulent boundary layer structures with the airfoil trailing edge are the cause for the characteristic broadband character of trailing edge noise. Thus the identification “coherent” structures in the boundary layer are of great interest for the understanding of the broadband noise source. The wall pressure field measured in such conditions can be regarded to be induced by these structures and therefore provide an established method to relate the boundary layer fluctuations with the far field noise. Regarding passive flow control techniques for the reduction of turbulent boundary layer broadband noise, there are two popular techniques both inspired by the owl’s silent flight: Trailing edge serrations (which are in turn divided into flat plate and non-flat plate serrations) and porous materials. In the case of serrations, in all experimental investigations of flat plate inserts a high frequency noise increase was observed, while for the flat plate type serrations, vortex shedding noise occurred due to bluntness and often negated the noise performance.

In the case of porous materials, fully porous airfoils have shown significant noise reductions in certain cases of flow resistivity. On the other hand, a large loss in lift performance was found at the same time. For partially porous airfoils, this disadvantage was still present but could be limited to a smaller extent. The noise reductions of the particular case were mainly observed in in the mid-frequency range while a noise increase was commonly observed in the low and high frequencies of most of the materials.

In overall, it can be concluded that there is a lack of technologies and techniques capable of significantly reducing the self-noise of a sharp straight airfoil in a consequent manner.

Chapter 3

Experimental Setup

The following chapter describes the experimental facilities and set-ups used during the investigations of the present thesis. The majority of experiments was performed at Brunel University and some tests were conducted at the University of Southampton. The experiments can be categorised in aerodynamic testing and aeroacoustic testing as listed below:

- 1) Aeroacoustic tests were conducted in two open-jet wind tunnels:
 - a) The anechoic open jet wind tunnel in the Institute of Sound and vibration (ISVR) in Southampton, namely the DARP Rig (as presented in section 3.1.1),
 - b) The newly built aeroacoustic wind tunnel at Brunel University which became available at a later stage of this PhD project. It is described in section 3.1.2.
- 2) Experiments of solely aerodynamic / fluid dynamic nature were conducted in three facilities at Brunel University:
 - a) A vertical small scale wind-tunnel as described in section 3.2.1
 - b) An open circuit suction type wind tunnel, described in section 3.2.2
 - c) A water tunnel as described in section 3.4.
- 3) Several experimental techniques were used in this PhD study, which comprise hot wire anemometry (single, cross, and triple hot-wires), surface mounted hot-film measurements, liquid crystal flow visualisation, as well as acoustic far field and unsteady surface pressure measurements using microphone arrays. These experimental setups will also be presented in this chapter. The main analysis techniques and measurement metrics will be provided here, while more specific analysis methods are presented directly in the relevant chapter for practical reasons.

3.1 Aeroacoustic facilities

As shown in Table 3.1, the experiment carried out at the Southampton DARP Rig focused on the trailing edge noise measurements of a NACA0012 airfoil followed by hot-film measurements near the airfoil trailing edge. At the anechoic facility at Brunel, the trailing edge noise was measured amongst hot-wire anemometry on a NACA0012 airfoil as well as on a flat plate. Before proceeding to the details of the facilities, a summary is provided in Table 3.1 below.

	Tested speed range	Turbulence intensity	Test conducted	Test section cross sectional area
DARP Rig Southampton	20-60 m/s	<0.4%	<u>Airfoil</u> TE-noise, hot film	150mm x 450mm
Brunel Aeroacoustic Wind Tunnel	20-60 m/s	<0.3%	<u>Flat plate & airfoil</u> TE-noise, hot wire anemometry, acoustic camera	100mm x 300mm

Table 3.1 Summary of aeroacoustic tests conducted

3.1.1.1 Southampton Institute of Sound and Vibration DARP Rig

The open jet wind tunnel at Southampton has been designed and assessed for its performance by Chong et al (2009), with a more recent upgrade that a centrifugal fan has replaced the former pressurised air reservoir for an improved air supply system.

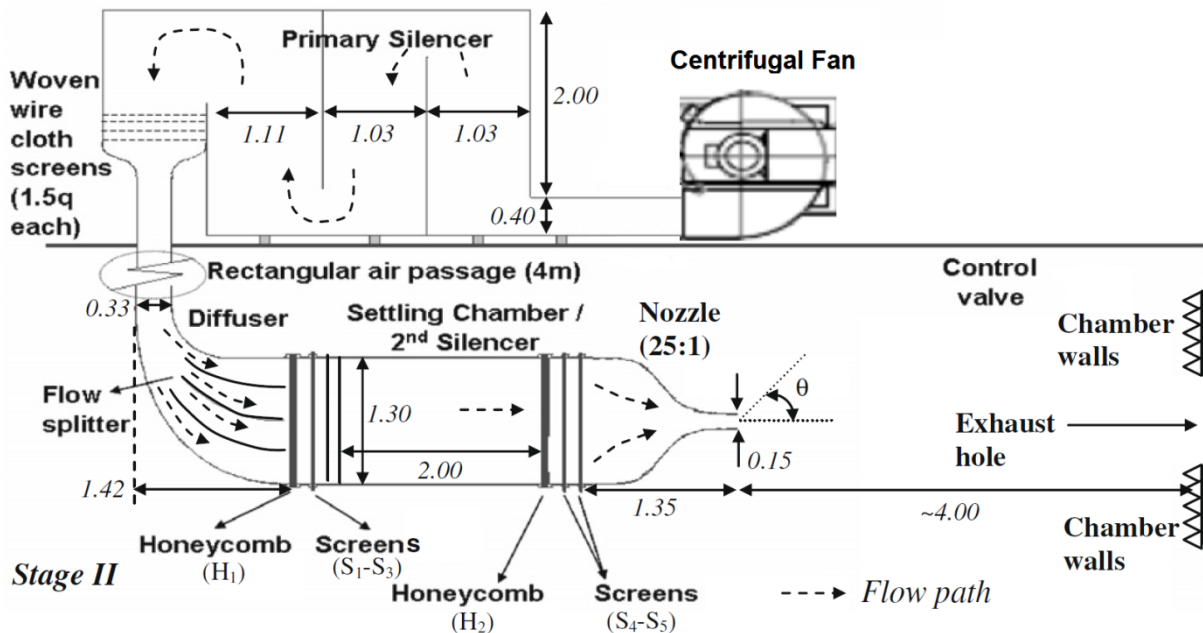


Figure 3.1 DARP Rig side view of wind tunnel facility (dimensions in meters)

The DARP rig is an open jet, blow down wind tunnel with the nozzle placed inside an anechoic chamber of the dimensions of 8m x 8m x 8m. A 110 kW AC-powered centrifugal fan is capable to produce a maximum mass flow rate of about 8.0 kg s^{-1} for velocities from 10 ms $^{-1}$ of up to about 100ms $^{-1}$ (i.e. up to $M \approx 0.3$). The nozzle has a contraction area ratio with a ratio of 25:1 which further accelerates the flow while minimising any lateral velocity fluctuations. The nozzle exit area has the dimensions 0.15m x 0.45m. The side view of the facility is shown in Fig.3.1. The air supplied by the centrifugal fan is guided through a “3 pass” plenum chamber type silencer with the interior surfaces incorporating a basalt wool liner of 150mm thickness with a facing woven glass fabric cloth in order to inhibit flow delamination. The air then passes through the vertical duct into a 90° bend diffuser in order to align the flow along the exit nozzle axis. After that a second, straight silencer with incorporated woven wire mesh grids and honeycomb screens ensures low-turbulence flow to propagate towards the nozzle and exit to the test section and the exhaust hole. The measured turbulence intensity of this facility is found to be in the order of about 0.4%.

As seen in Fig 3.2a, two side walls smoothly extend from nozzle sides allowing to mount the airfoil model. As soon as the airfoil is attached and the angle of attack is selected the airfoil can subsequently be fixed in position with two screws on each side.

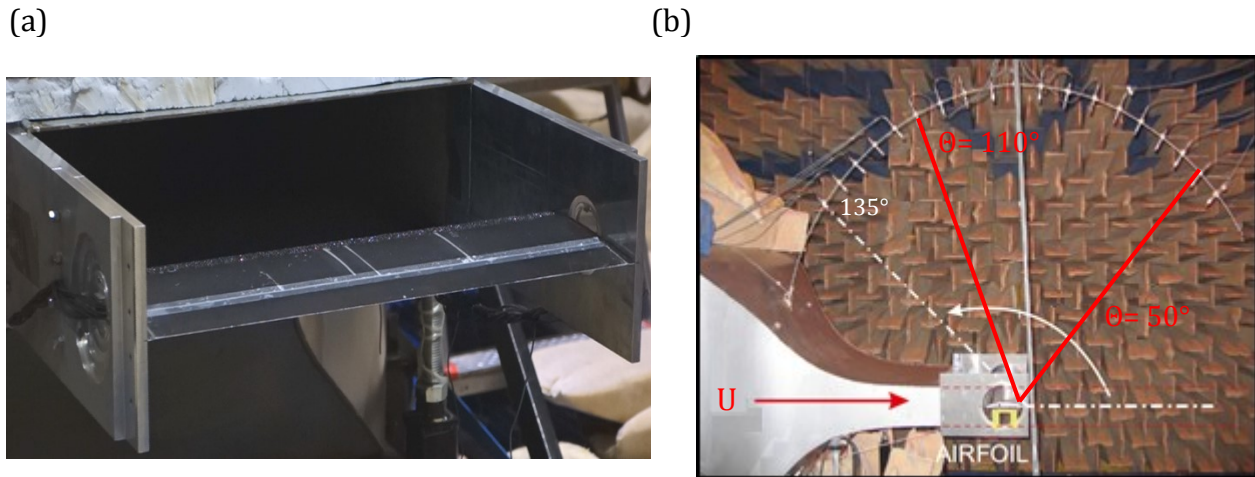


Figure 3.2 (a) Darp Rig Nozzle exit with mounted airfoil; (b) Microphone array and test section inside the anechoic chamber.

3.1.1.2 DARP Rig microphone array

In order to measure the far field noise radiation, an array of 19 Brüel & Kjær $\frac{1}{2}$ inch microphones was located 1.2m from the airfoil trailing edge along a circular arc as shown in Fig 3.2b. The frequency response of the microphones is 20Hz- 40 kHz as shown in Fig 3.4.2 b. The formed arc reaches from an angles from 45° up to 135° with an increment of 5° per microphone. The microphone defined with the angle of 0° is set to be parallel to the direction of propagation of the jet and 90° directly above the trailing edge. However, as also mentioned in Section 3.1.1, the far-field noise measurements were taken for the polar angles from $\theta_1 = 50^\circ$ to $\theta_2 = 110^\circ$ from the airfoil trailing edge at midspan. The angle at $\theta < 50^\circ$ and $\theta > 110^\circ$ were not attempted due to the potential acoustic interference from the jet noise and the acoustic reflection of the solid wind-tunnel wall, respectively.

The microphones were connected to an in-house built amplifier and the acquired data was logged by a computer using LABVIEW. A total of five NI PXI-4472 data acquisition cards (of which each has 8 input channels) were connected to microphone channels with an available sampling rate of 102.4 kS/s per channel. The microphones were calibrated through a Brüel & Kjær pistonphone.

3.1.2.1 Brunel aeroacoustic wind tunnel

An aeroacoustic research facility has been constructed at Brunel University, which became available at a later stage of this PhD work. The facility aims to achieve low noise radiation and low residual turbulence in the free jet and is intended for airfoil noise studies mainly in low-to-moderate pressure loading configurations. As a blower type wind tunnel it is capable to produce a maximum mass flow rate of about 3.0 kgs^{-1} . A nozzle

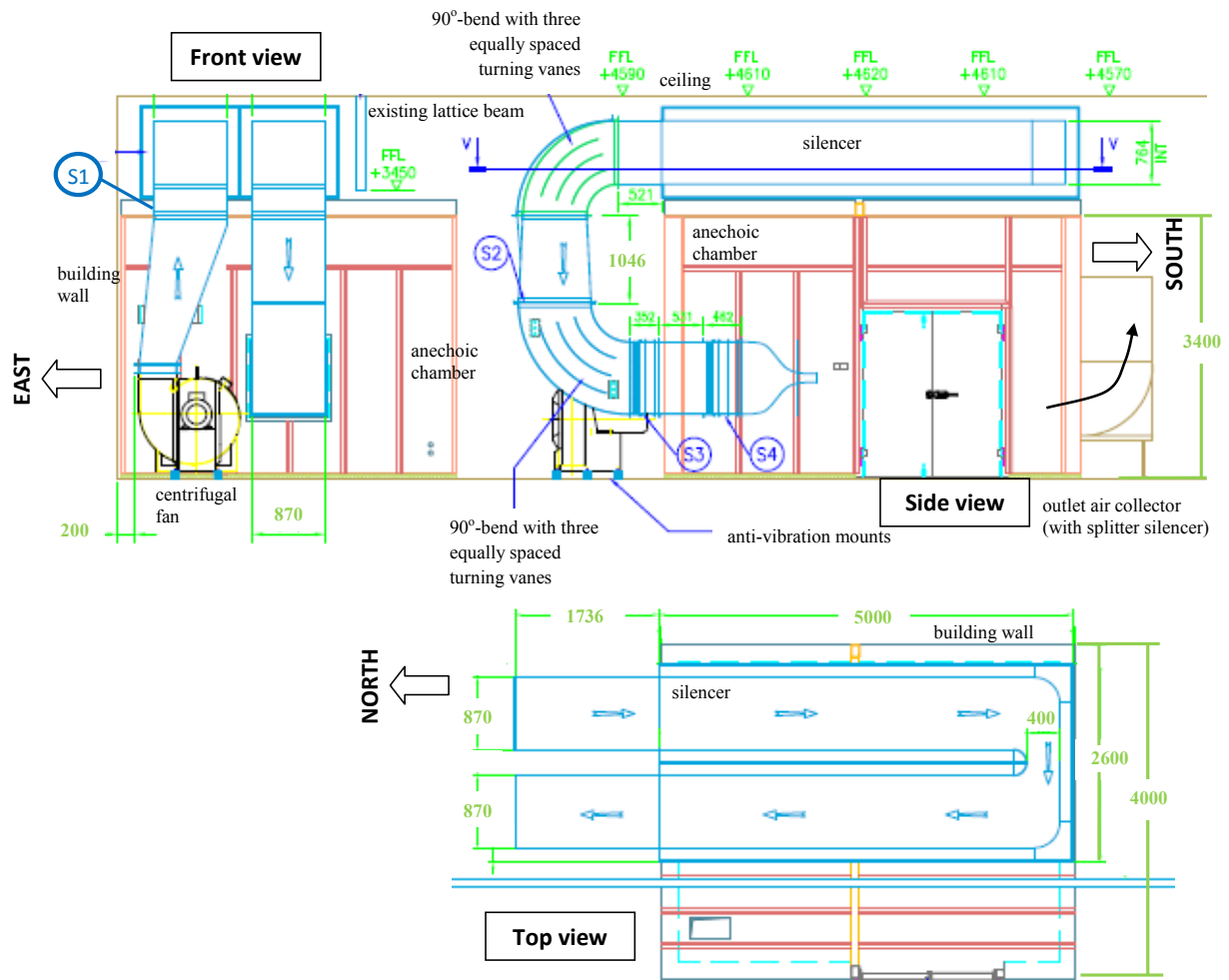


Figure 3.3 Plan, side and front views of the aeroacoustic wind tunnel facility and the anechoic chamber.

similar to the DARP rig in Southampton (*Area Ratio* $AR= 25:1$) has been manufactured and installed. The scaling factor between the DARP nozzle and the Brunel nozzle is $2/3$, which results in the following dimensions for the Brunel nozzle: inlet = $867 \text{ mm} \times 867 \text{ mm}$; outlet = $100 \text{ mm} \times 300 \text{ mm}$. With the given configuration, a maximum free jet velocity of approximately 80 ms^{-1} can be reached. The nozzle and its test section are placed within an anechoic chamber with the dimensions of 4 m (width) \times 5 m (length) \times 3.4 m (height).

The plan, side and front views of the aeroacoustic wind tunnel are shown in Fig. 3.3. A 30 kW AC-powered centrifugal fan is placed at the north side to propel air vertically upward through an offset diffuser. In order to obtain the maximum mass flow rate of 3.0 kgs^{-1} the pressure rise which the fan generates is in the order of 8kPa, after taking into account of the cumulative static pressure loss of the wind tunnel components. From there, the expanded air is turned towards a 90° -bend duct ($AR = 1$) before enters the silencer, which is placed on top of the anechoic chamber. The air inside the silencer is flowing towards the south side, before turning 180° at the far end and continuing its journey in the opposite direction towards the north side. After reaching the north end, the air exits the silencer and is turned by a 90° -bend duct towards the floor. From there, the air is slightly expanded before it is turned again towards 90° anti-clockwise with a constant area duct and enters the anechoic chamber from the north side. After passing a series of flow conditioning devices (woven wire mesh screens and honeycombs), the air accelerates

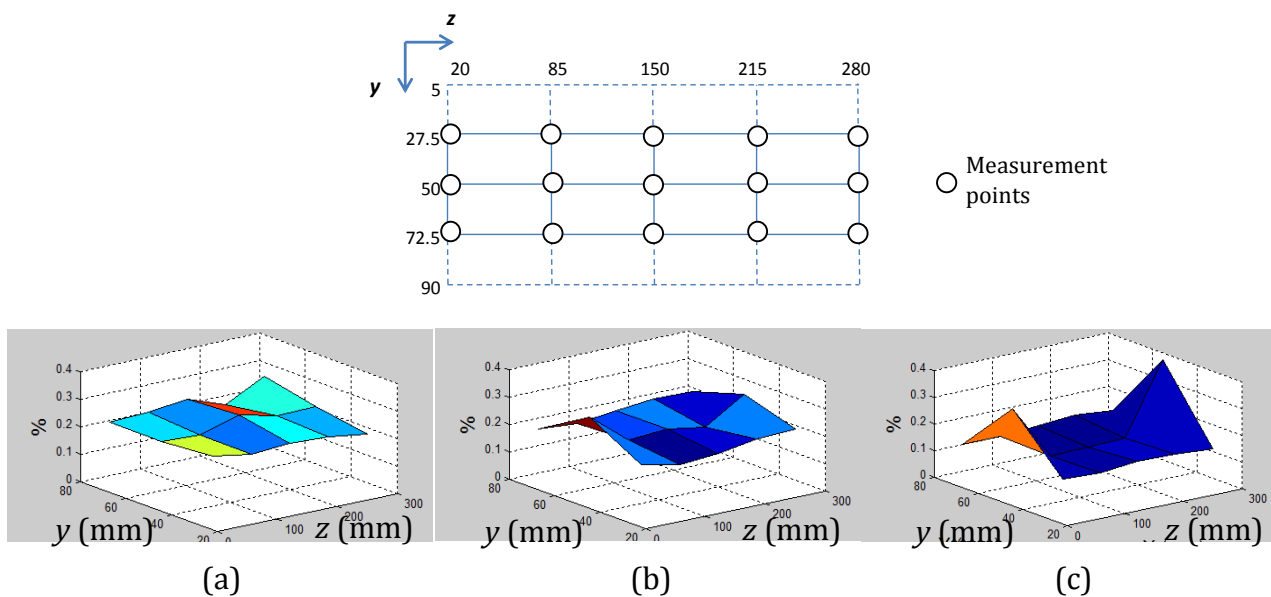


Figure 3.4 Distributions of the turbulence intensities at 8 mm downstream of the nozzle exit plane at jet velocity of (a) 10 ms^{-1} , (b) 20 ms^{-1} , and (c) 30 ms^{-1} .

inside the nozzle and discharging inside the anechoic chamber. As seen in Fig.3.4, the potential core of the free jet has a typical range of turbulence intensity between 0.1–0.3 percent. The expanded jet will then reach the acoustically lined outlet attenuator turning upwards through a splitter-type silencer, exiting the anechoic chamber.

An electric inverter is used to digitally adjust the current input to the centrifugal fan, thus controlling the mass flow rate (the exit jet velocity) of the nozzle in an accurate manner. In order to isolate the centrifugal fan from any possible transmission of vibration towards

the anechoic chamber, four anti-vibration mounts were used to isolate the centrifugal fan from the floor and a flexible vinyl tube is used to connect the centrifugal fan to the wind tunnel duct. Both measures have proven to be effective in dampening the vibration.

The silencer is selected in form of a “2-pass” plenum chamber. All its interior surfaces are lined with a basalt wool dissipative liner of 150 mm thickness with a 4 mm thick facing cloth (Thermal 650 E-glass Needle mat) to inhibit the flow delamination. The basalt wool liners are held together by perforated metal frames. The outer wall of the silencer is made from the 18 mm thick plywood. The choice of the acoustic material is based on the objective of achieving low flow resistivity and high density. Furthermore, woven wire screens and/or honeycombs are placed in positions S1 to S4 as shown in Fig 3.3 to provide adequate flow straightening.

3.1.2.2 Brunel anechoic wind tunnel microphone setup and acoustic camera

The microphone for the airfoil noise measurements was placed at a polar angle of $\Theta = 90^\circ$ at a distance of 1 meter from the trailing edge midspan. The microphone used was a $\frac{1}{2}$ inch PCB Piezotronics prepolarised 377B02 free-field condenser microphone with a sensitivity sensitivity of 50 mV/Pa (± 1.5 dB) and a dynamic range between 15 and 146dB. The microphone was used with a preamplifier (model 426E01) and a model 480C02 signal conditioner. The same microphone type was used for the wall pressure measurements to be described in the later sections.

A „Ring 32-35 AC Pro“ acoustic camera with a 0.35 m diameter carbon-body ring array consisting of 32 microphones was used to beamform the noise source radiated from the airfoil. The array incorporates 32 advanced disturbance tolerant $\frac{1}{4}$ ” symmetrically buffered electret pressure receivers which are based on a Sennheiser microphone capsule

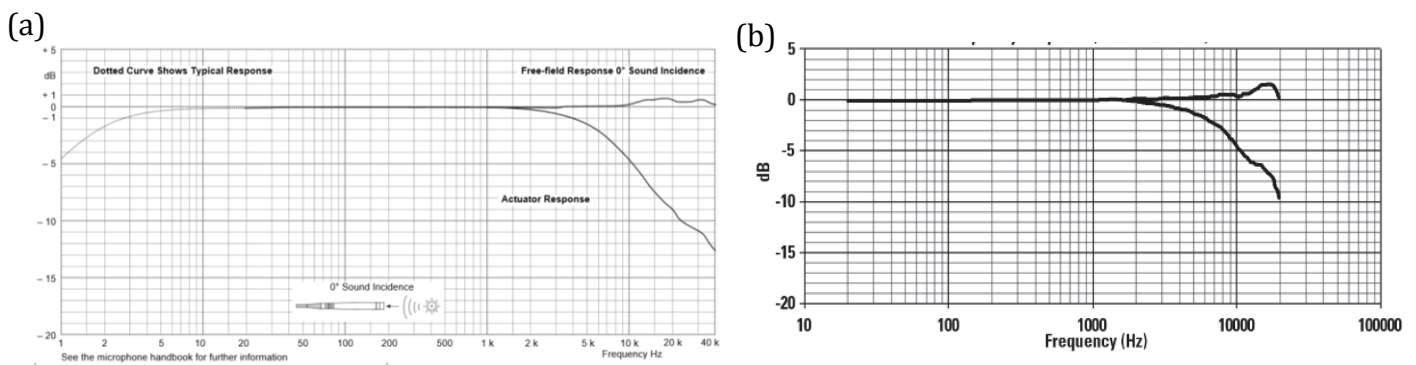


Figure 3.5 Frequency response spectra of the free field microphones used (upper lines) where (a) Brüel & Kjær $\frac{1}{2}$ inch Falcon microphones at the DARP rig and (b) the PCB 377B02 microphones used at Brunel University.

model 4211. The frequency response of the microphones is 20Hz-20kHz (± 3 dB, with a dynamic range of 28-130dB (A-weighted)).

An integrated fixed focus camera is placed in the middle of the round array. The acoustic mapping data is acquired through a 24bit mcdRec (2x ADC 112_MLN) data recorder with a sampling rate of up to 192 KS/s per analog channel by using two 20 meter differential SymBus microphone connector cables. The NoiseImage v4.4.2 software was used for the acquisition. The array was placed on a tripod where its centre pointed upwards, focusing on the trailing edge of the tested airfoil at a polar angle $\theta=90^\circ$.

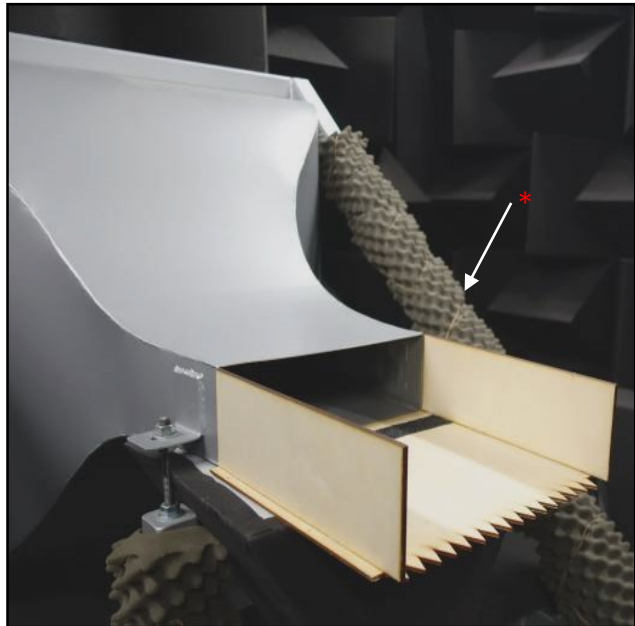
3.1.2.3 Set up of test models at the Brunel anechoic wind tunnel

For all the noise tests, the same airfoil model was taken. Hence the same NACA 0012 airfoil used in Southampton was also used at the aeroacoustic wind tunnel in Brunel. (The airfoil details are provided in the following in Section 3.3.1). The airfoil was held by two side plates which allow adjustment of the angles of attack, as illustrated in Fig. 3.6a.

(a)



(b)



* - these struts have since been removed from the wind tunnel i.e. for the airfoil tests

Figure 3.6 a) Airfoil set-up at the anechoic wind tunnel at Brunel University with a single microphone above the trailing edge; b) Experimental setup for the measurements of self-noise produced by a flat plate

In another experiment, a flat plate was used. As seen in Fig. 3.6b, the flat plate model with dimensions 300 mm (width) x 295 mm (length) was attached flush and smoothly extended one side of the nozzle exit. Rough sandpaper was applied near the nozzle outlet to establish early transition of the boundary layer. The trailing edge of the flat plate can be interchanged between a straight type and a serrated sawtooth type. In the particular flat plate configuration flow is only present on one side of the surface as there is no flow at the underside. Some theories [Amiet (1976)], Howe (1999)] assume a full Kutta condition at the trailing edge when formulating expression for the far field noise. The radiated trailing edge self-noise level is therefore expected to be considerably lower than when there is flow on both sides of the surface, such as in the case of an airfoil. However even in these low-noise conditions, it can be seen in Fig 3.6d that the background noise is still low enough to reliably measure the broadband noise on a flat plate.

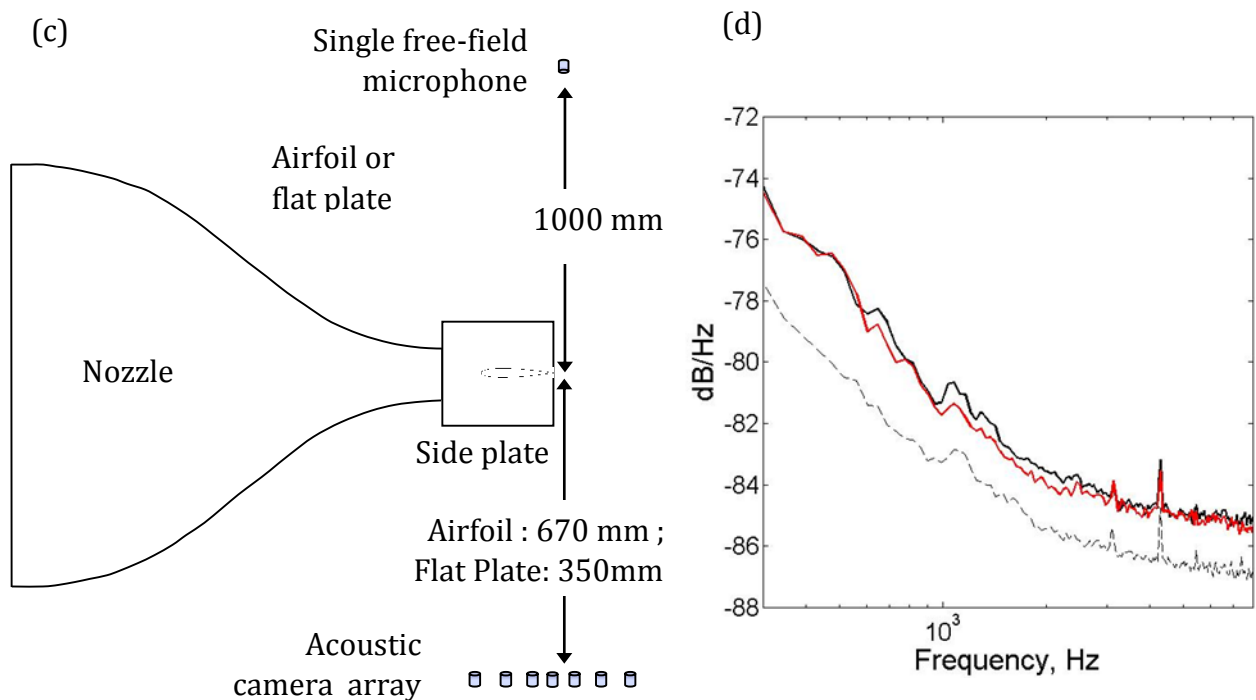


Figure 3.6 (c) Experimental set up for the aeroacoustic tests at the Brunel anechoic wind tunnel. A far field microphone was set up at a polar angle, $\theta = 90^\circ$ above the trailing edge and an acoustic camera & microphone array was set up direct beneath the trailing edge. (d) Trailing edge self-noise measurements of an attached flat plate at a freestream velocity of 30 ms^{-1} : straight trailing edge (—); serrated sawtooth trailing edge (—) and the wind tunnel background noise produced by the bare jet (- -).

As seen in Fig. 3.6c, for both set ups the single free-field microphone was placed at a polar angle $\theta=90^\circ$ and a distance of 1m from the trailing edge. The position of the acoustic camera varied between the two cases (670 mm for the airfoil and 350mm for the flat plate). The acoustic camera array test was conducted separately from all other tests and hence it was removed whenever not in use.

3.1.3.1 Acoustic measurement metrics

The far field noise radiation acquired through the free-field microphones is converted to the sound pressure level (SPL), sound power level (PWL) as well as the overall sound power level (OAPWL).

The sound pressure level is defined as

$$SPL(f) = 10 \log \left(\frac{S_{pp}(f)}{p_0^2} \right) \quad (3.1)$$

Where S_{pp} is the acquired mean square pressure and p_0 is the reference sound pressure (typical value for air) at 2×10^{-5} Pa.

Assuming the cylindrical spreading of waves from the airfoil trailing edge, the sound power level radiated per unit span in the range of angles between $\theta_1 < \theta < \theta_2$ can be approximated by

$$W(f) = \frac{2\pi \int S_{pp}(f, \theta) \Delta\theta}{\rho c_0}, \theta_1 < \theta < \theta_2, \quad (eq. 3.2)$$

$$PWL(f) = 10 \log_{10} \left[\frac{W(f)}{W_{ref}} \right] \quad (eq. 3.3)$$

Where $S_{pp}(f, \theta)$ is the measured acoustic pressure PSD at a polar angle θ , $\Delta\theta$ the (rad) angle between adjacent microphones and $W(f)$ the sound power integrated for the radiation angles from θ_1 to θ_2 . In the current work θ_1 was at an angle of 50° and θ_2 at 110° . $W_{ref} = 10^{-12}$ W is the reference sound power level for air.

The overall sound power level (OAPWL) of the airfoil noise at a particular flow velocity can also be defined by

$$OAPWL = 10 \log_{10} \left[\frac{\int_f W(f) df}{W_{ref}} \right] \quad (eq. 3.4)$$

A calibration is performed with a conventional Brüel & Kjaer 4231 calibrator providing a constant signal of 94 dB at 1 kHz for 20 seconds in order to determine the exact S_{pp} .

3.1.3.2 Angle of attack correction

Brooks (1989) proposed corrections to the angle of attack setting when a 2D airfoil is tested in an open jet wind tunnel setup. This is because the air exiting the open nozzle exit will experience a flow curvature and downwash deflection of the incident flow by the presence of the airfoil which would not occur in the free air. This has the result of reducing the effective angle of attack. The proposed corrections for an open jet wind tunnel are expressed through the relationship shown in equations 3.5 and 3.6 of the corrected angle of attack $\alpha_{corrected}$ in the free air, which will be referred to as α throughout this thesis. In order to correspond the lift of the geometrical angle α_t in the open jet wind tunnel, the factor ζ is introduced, forming the relationship seen below.

$$\alpha_{corrected} = \alpha = \alpha_t / \zeta \quad (\text{eq. 3.5})$$

With the consideration of ζ as follows,

$$\zeta = (1 + 2\sigma)^2 + \sqrt{12\sigma} ; \sigma = \frac{\pi^2}{48} \left(\frac{c}{H}\right)^2 \quad (\text{eq.3.6})$$

where c the airfoil chord and H the vertical open jet dimension of the wind tunnel for a horizontally aligned airfoil. In the present investigation the airfoil test models were set at geometrical angles α_t of 0° , 5° , 10° and 15° which correspond to the effective angles of attack α as shown in Table 3.2.

	ζ	$\alpha_t(^{\circ})$	0	5	10	15
<i>DARP</i>	3.56	$\alpha(^{\circ})$	0	1.40	2.81	4.21
<i>BRUNEL</i>	6.06	$\alpha(^{\circ})$	0	0.82	1.65	2.47

Table 3.2 Angle of attack corrections for the two open jet wind tunnel facilities used where α_t the geometrical angle and α the corrected, effective angle of attack.

3.2 Aerodynamic testing facilities

Table 3.3 summarises the facilities used only for flow measurements (since these facilities are not acoustically efficient). A wind tunnel used for boundary layer measurements on a flat plate is described in section 3.2.1. Section 3.2.2 presents the open circuit wind tunnel used for near wake measurements of an airfoil with trailing edge serrations.

	Tested speed range	Turbulence intensity	Test conducted	Test section cross sectional area
AF10 Air bench, small scale wind tunnel	15-30m/s	0.3%	Flat plate Hot Wire, Surface pressure Liquid crystal	150mm × 50mm
Brunel Aerodynamic Research Wind Tunnel	15-35 m/s	0.1-0.2%	Airfoil Hot wire anemometry, Lift/Drag	500mm × 500mm

Table 3.3 Overview of the aerodynamic facilities used (no flow measurements conducted in these facilities).

3.2.1.1 AF10 Air bench

A small scale wind tunnel was used for boundary layer measurements to investigate the turbulent structures near the trailing edge region of the flat plate. The wind tunnel is a TecQuipment AF10 vertical air bench, with an adjustable speed of up to 35 ms⁻¹.

The flat plates were attached directly to the nozzle exit with a cross sectional (test-section) area of 150 mm x 50 mm so that they essentially comprise one of the flow surfaces extended from the nozzle lips as presented in Fig 3.6. The dimensions of the flat plate test models are 295 mm (streamwise) x 150 mm (spanwise). A total of three flat plate models was used for the measurements using this facility: two Perspex flat plates

for boundary layer and wall pressure measurements and one heatable flat plate used for liquid crystal flow visualisation.

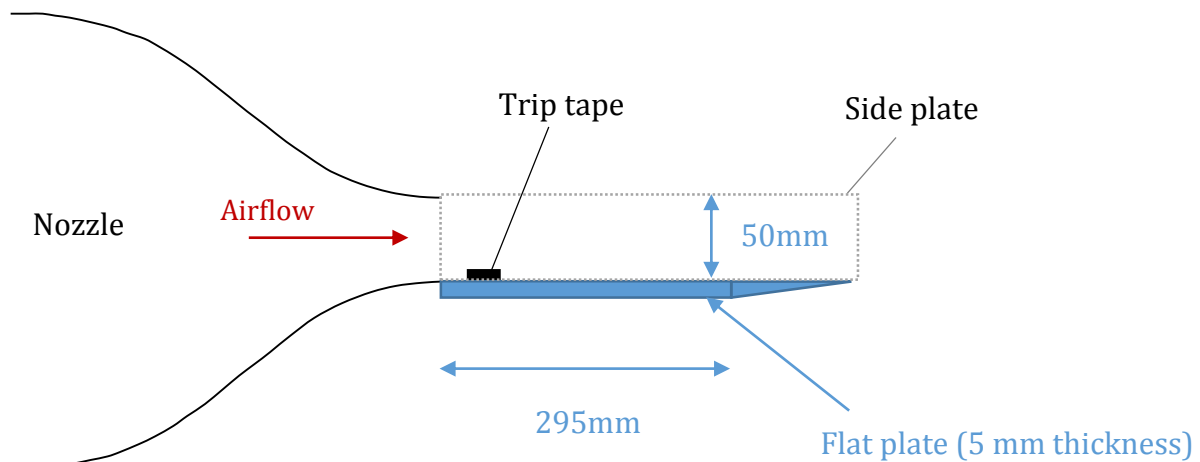


Figure 3.7 Sketch of the AF10 flat plate set up

3.2.1.2 Setup of the unsteady surface pressure measurements on the flat plate

This section describes the experimental setup for the unsteady surface pressure measurements on the flat plates. Two Perspex flat plates were used, the model has an unserrated, straight trailing edge. The flow surface is flat up to the trailing edge and a small bevel angle is present at the back side near the trailing edge to allow a gradual tapering across the plate thickness of 5 mm (see Fig 3.7). Note that there is no flow at the back side of the test model. This configuration ensures a sharp trailing edge on the flow side to be present. Another plate model has a serrated trailing edge with the following specifications: Root-to-tip distance ($2h$) = 20 mm, and a serration angle (ϕ) = 22.5° as seen in Fig. 3.7. Similarly, a small bevel angle is present near the trailing edge at the back side where no flow is present.

There are 34 microphone sensing holes near the trailing edges of each flat plate model. Each sensing hole is 0.5 mm in diameter and 0.1 mm deep, and is followed by a recess hole inside the flat plate of 1 mm diameter. The depth of the recess hole is different, depending upon the location with respect to the trailing edge due to the above mentioned tapering. The recess holes are designed to hold a small metal tube of 0.5 mm internal diameter, and the metal tube will be connected to a plastic tube as part of the remote microphone system. The sensing holes are distributed in identical rectilinear grids for both of the

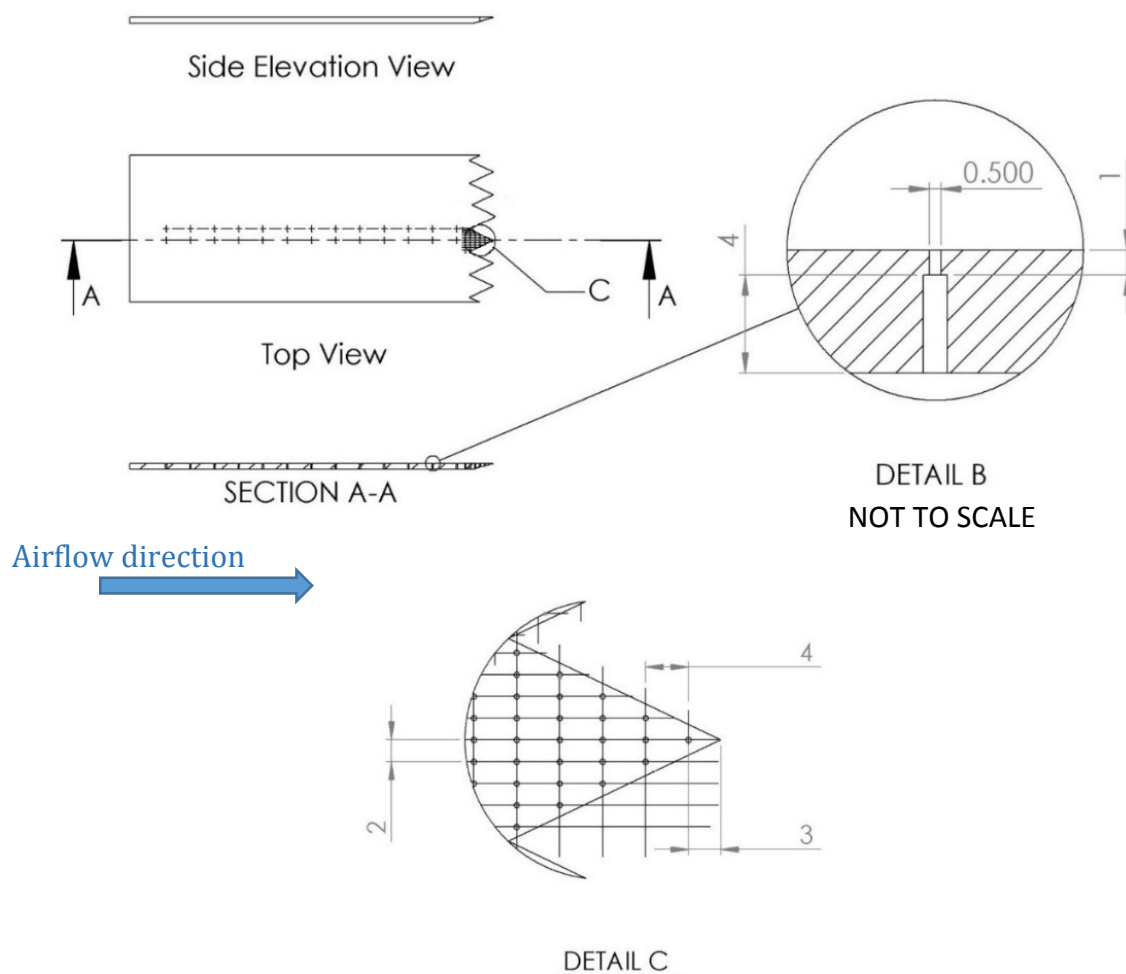


Figure 3.8 Drawing of the serrated Perspex flat plate for the surface pressure measurements through the designed tapings. The same plate was used for hot-wire anemometry measurements. Dimensions displayed in millimetres.

baseline and serrated trailing edges. This configuration allows the wall pressure power spectral density (*PSD*) and streamwise, spanwise and oblique coherence functions to be compared directly between the straight and serrated trailing edges.

Two preamplified, prepolarised $\frac{1}{2}$ inch PCB Piezotronics 377B02 condenser microphones were used to measure the power spectral density of the wall pressure from several distributed sensing holes (0.5 mm diameter) within the trailing edge region as shown in Fig. 3.8. A small sensing hole is necessary to maintain the spatial resolution of the measured pressure and to minimise the attenuation of eddies with small wavelength. The microphones are connected to the sensing holes via a remote microphone array. The initial attempt to measure the surface pressure by a probe-tube arrangement with a side-branch and an infinite tube ending [Franzoni (1998)] was not successful due to the poor

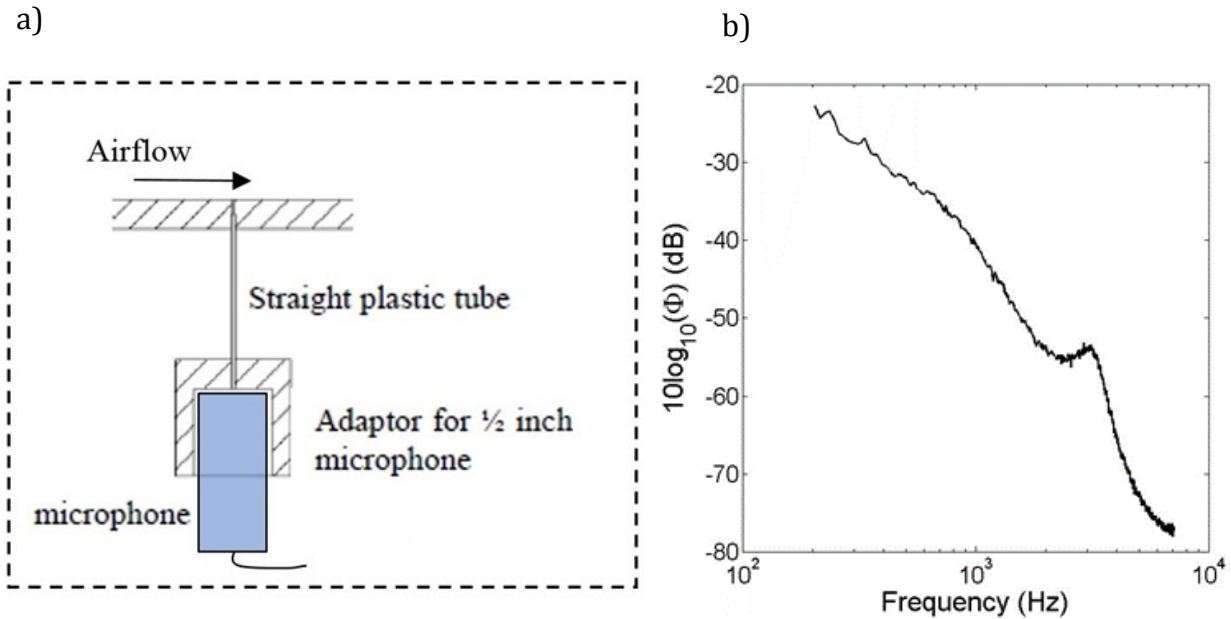


Figure 3.9 (a) Remote microphone arrangement (b) An example of wall pressure power spectra density (PSD) measured by the remote microphone sensor.

signal to noise ratio. Instead a more traditional way was adopted with a simpler design of the probe-tube arrangement. As shown in Fig. 3.9a, the microphone is always positioned directly underneath the sensing hole so that a straight line of sight can be drawn from the centre of the sensing hole, via a straight plastic tube of 0.5 mm internal diameter and 20 mm long, and into the centre of the microphone. Owing to the minimal sudden area variation along the tube duct, and the relatively short plastic tube, strong acoustic resonance in the form of standing wave is not expected to be significant in this particular remote arrangement. This can be confirmed in Fig. 3.9b which shows an example of the measured wall pressure PSD. The frequency as shown previously in fig 3.4.2 is 20Hz-20 kHz, ensuring accurate measurements up to the desired frequencies. Because the backside of the test plate is outside of the flow, there is a large degree of freedom in positioning the remote microphone system outside of the wind tunnel in order to ensure that a straight line of sign between the sensing hole and the microphone is always maintained. Most importantly, the remote microphone arrangement also allows the wall pressure measurements to take place relatively close to the trailing edge.

In this study no magnitude calibration of the two microphones was performed either in the free field condition or in the remote configuration. Considering that one of the main objectives using this set up is to investigate the difference of wall pressure PSD levels between the baseline and serrated trailing edges, an absolute magnitude level may not be

necessary. However, phase calibration between the two microphones had been performed in an anechoic chamber. During the phase calibration both of the microphones were exposed to a loudspeaker driven by a white noise signal input. Good coherence between the microphone signals is obtained and the phase angles are generally small within a wide frequency range. During acquisition of the unsteady wall pressure by the microphones, the sampling frequency and sampling time were set at 40 kHz and 10 seconds, respectively. The digitization of the analogue signals was performed by a 24-bit National Instrument A/D card. The wall pressure data was windowed-FFT (4096 point) and averaged to obtain the PSD with a resolution of 1 Hz bandwidth.

3.2.1.3 Liquid Crystal Flow Visualisation performed on the flat plate models

Optically active (chiral nematic) liquid crystals have a naturally twisted structure which is formed by different molecule layers. The twisting structure provides an unusual optical property which is called a selective reflection. In this case only incident light with a specific wavelength equal to the crystal pitch will be reflected. When a liquid crystal is applied to a test surface as a thin coating, the pitch of the helical structure in the crystals can be made to respond solely to the variation in surface temperature.

The liquid crystal slurry and binder was supplied by Hallcrest. According to the specification, the liquid crystal has an active colour bandwidth of about 10°C, with the visible colour starting at approximately 25°C. This means that the heated surface will change the liquid crystal's colour from red at 25°C through the visible spectrum to blue at 35°C. During preparation the mixture of the crystal slurry and binder was sprayed on the heater plate matt-black surface in 4-5 coatings. As stated by Baughn (1995), poor colour display will result if the coating is either too thin or too thick. The amount of the mixture was estimated beforehand. Based on mass conversion and losses estimation through spraying, the thickness of the nominal coating is estimated to be 30 µm.

In order to quantify the surface temperature of a turbulent boundary layer in a non-isothermal flow, a heater flat plate is designed from a 295 mm x 150 mm printed circuit board (PCB). The PCB contains an etched copper track in a non-metallic substrate on the one side of the surface. As shown in Fig. 3.10a, the continuous, single-filed copper track is designed to heat up the plate surface uniformly, which includes the sawtooth region of the serrated trailing edge, when connected to a direct current (DC) power supply. A 0.2 mm

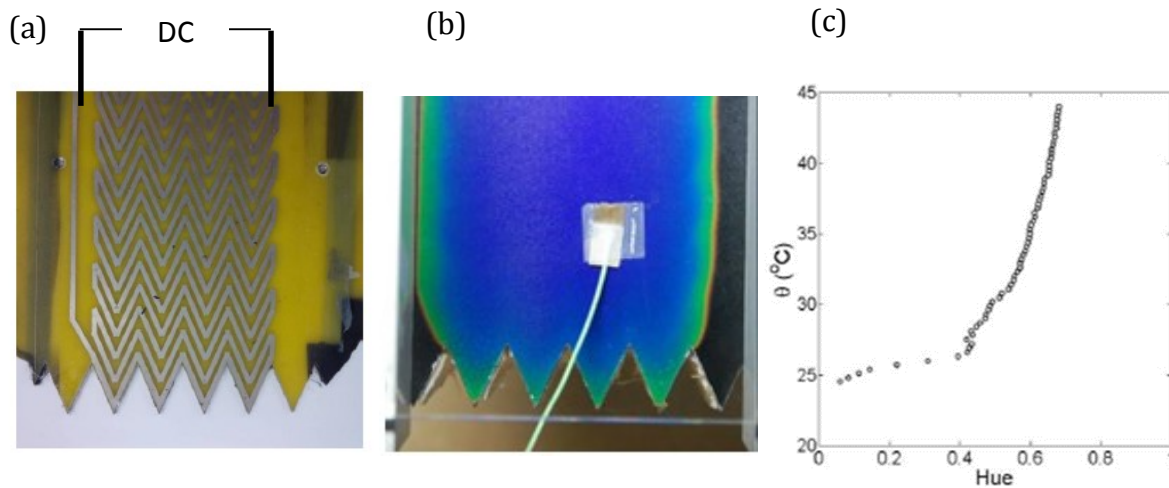


Figure 3.10 a) copper track at the back side of the liquid crystal heater plate; b) front side of heater plate with thermocouple during calibration (no flow); c) Hue-temperature relationship of the liquid crystal calibration.

thick plastic film, which has the same overall size as the PCB board, was attached to the metallic (copper track) side. Matt black paint was sprayed to the thin film and after a long settling time the liquid crystal coating was applied uniformly to the surface using an artist airbrush with compressed air. However, it was found that the heat is not dissipated well in the thin plastic film and the pattern of the copper track is visible from the liquid crystal colour display. An alternative approach is therefore adopted through reversing the PCB in order to use the substrate side as the flow surface, which is then covered by a similar order of thin plastic film, matt black paint and liquid crystal. In this arrangement the heat is better distributed and the colour changes can be observed. In order to minimise heat loss by conduction, a 75 mm thick Styrofoam sheet was attached to the non-flow surface which is the metallic side of the PCB. Note that only one PCB heater plate is manufactured. The trailing edge serrated with exactly the same serration parameters as in the surface pressure and hot-wire test, where $2h = 20$ mm, $\phi = 22.5^\circ$. In order to change the trailing edge from a serrated type to a straight type, several add-on triangular plates were inserted to the trailing edge to form a continuous surface across the span.

A 60W fluorescent strip light that has approximately the same length as the test plate was used to illuminate the liquid crystal surface. It was found that the optimum viewing angle is approximately perpendicular to the coating surface. The images were captured by a digital camera. The illumination and recording arrangement was kept exactly the same for both the calibration process and during the measurements.

The variation of the liquid crystal colour was calibrated against the surface temperature, which was measured by a K-type glue-on type thermocouple. For the calibration, a room

temperature below 25°C needs to be first ensured. The electrical power for heating the test surface was controlled by a DC power supply. The current was adjusted to raise the surface temperature in a number of steps. During each particular input electrical power, the picture will only be taken after a steady state temperature is indicated. The electrical power will then be increased again until the next steady state temperature is increased approximately by 0.3°C – 0.5°C above the previous one. This process is repeated until the maximum liquid crystal activation temperature had passed. In this way, the visible colour spectrum of the liquid crystal is fully utilised.

After the calibration is done, the recorded pictures are converted from Red, Green and Blue (RGB) colour indices to Hue, Saturation and colour Intensity (HSI) indices. It was found that the Hue exhibits the best sensitivity to the temperature. The interrogation area in the digital images is selected to be the area encompassing the location near the thermocouple. The calculated averaged Hue value is then correlated with the corresponding temperature reading from the thermocouple. The Hue-temperature relationship pertaining to the current test is shown in Fig. 3.10c. From the figure, steeper gradients occurred at temperatures between 25°C – 27°C. Above this range the change of Hue with respect to the temperature becomes more gradual. It was found that the Hue value displayed by the liquid crystal actually continues to increase beyond the saturated temperature specified by the company. During the conversion of the surface temperature a lookup table method was employed to correlate the Hue-temperature relationship of the liquid crystal.

During the measurements the surface is only heated slightly as the characteristics of the turbulent boundary layer should not be altered by a considerable amount.

3.2.2.1 Open Circuit Aerodynamic Wind Tunnel

The wind tunnel presented in this section, is a suction-type, open-circuit wind tunnel in the Aerodynamics Laboratories at Brunel University (Figure 3.11). When the air is drawn from the laboratory into the wind tunnel, it enters the nozzle (area ratio ~3:1) through several honeycombs and mesh screens to straighten the flow and reduce the freestream turbulence intensity. The test section is closed, with square dimensions 500mm (height) × 500mm (width). An axial fan is placed at the exit of the diffuser, which is driven by a 7.5 kW motor. The maximum velocity that can be achieved in the test section is 35ms⁻¹.

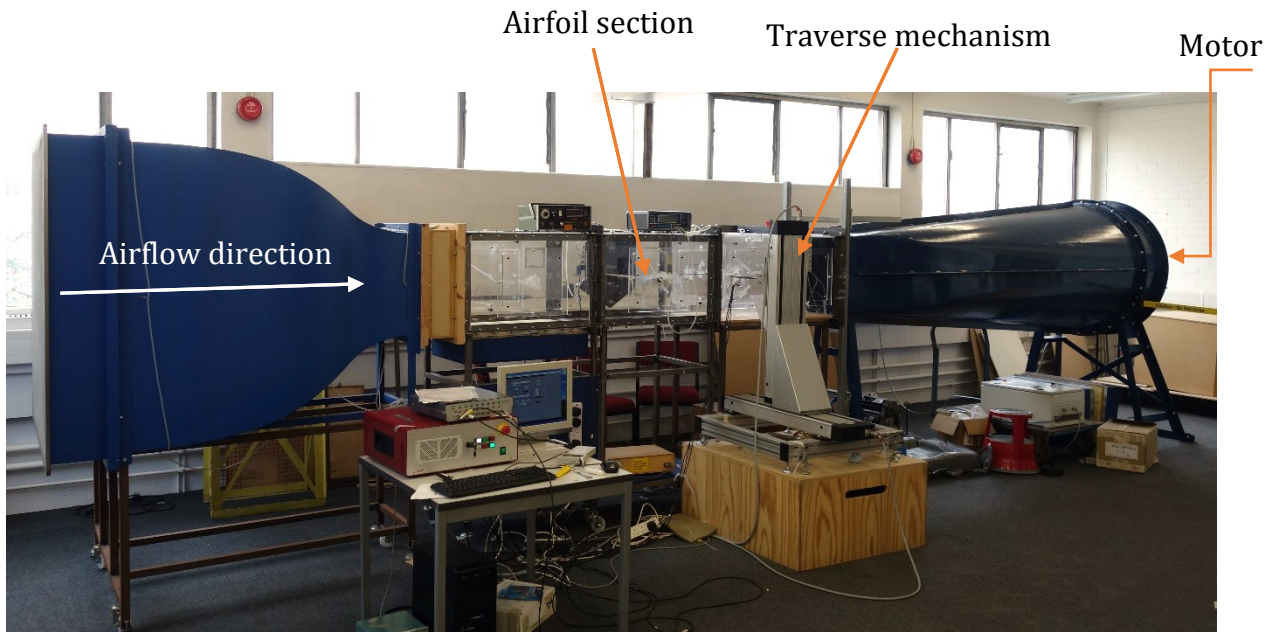


Figure 3.11 Open circuit aerodynamic wind tunnel at Brunel University

There are several interchangeable side windows which allow a flexible adjustment of the configurations when a different positioning of the traverse or the test equipment was required.

3.2.2.2 Three component force balance

A three component force balance by Plint & Partners is used to measure the aerodynamic forces produced by the airfoil inside the wind tunnel (Fig 3.12). Apart from force-balance measurements it was used in all tests to hold the airfoil in the wind tunnel and adjust the angle of attack through the rotating dial mechanism. The force balance mechanism consists of a mounting plate, which was used to secure the device to the wind tunnel, and a triangular force plate. The force plate and the mounting plate were connected via three spherical universal joints. The forces incurred by the airfoil were transmitted to three strain gauges via the cables, allowing lift and drag components of the mounted airfoil to be measured. The forces can be measured by the reaction of the force plate connected to three strain gauge load cells which indicate front lift (fore), rear lift (aft) and drag. In order to calibrate the load cells, the force balance is dismounted from the wind tunnel and weights between 0.5kg to 5kg are applied vertically for the lift components and horizontally, by using a pulley, for the drag force. The accuracy of the readings is found to be $\pm 0.05\text{N}$.

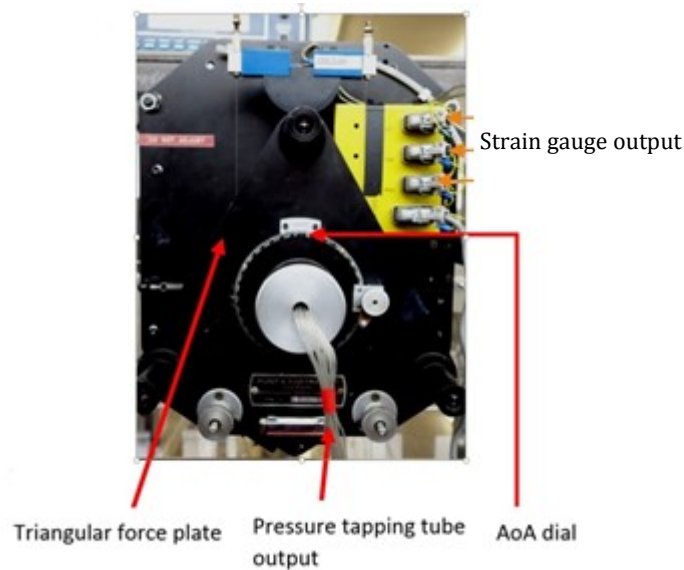


Figure 3.12 force balance mechanism mounted on the outer side of the wind tunnel.

The lift coefficient C_L is defined as

$$C_L = \frac{L}{\frac{1}{2} \rho v^2 S} \quad (\text{eq 3.7})$$

Where ρ the density of air, v the freestream velocity and S the planform area of the airfoil. L is the lift force determined from the force balance.

Similarly, the drag coefficient C_D is defined as

$$C_D = \frac{D}{\frac{1}{2} \rho v^2 S} \quad (\text{eq 3.8})$$

Where D is the drag force measured by the force balance.

3.3 Airfoil Design

Two identical NACA0012 airfoil models were used for the experiments. The chord length, C , is 150mm for both cases. The only difference is found in the span as the one model has a span of 450mm and the other one 500mm, as they were used in different wind tunnel facilities. A schematic showing the airfoil design is shown in Fig.3.13.

The airfoil models have 16 pressure taps of 0.4 mm diameter, placed midspan in the streamwise direction on pressure and suction side respectively. This allowed measurements of static pressure to be taken and thus, the calculation of the static pressure coefficient distribution. However, the pressure coefficients on the suction and pressure sides are not converted to the lift coefficient because these are not measured at

the trailing edge region. The lift coefficient was instead measured directly via the force balance described with the three component force balance (Section 3.2.2.2).

Fifteen miniature microphones (Knowles WP-3502) were also embedded inside the airfoil's main body on both, the suction and pressure surface. Each of these microphones is used to measure the wall pressure fluctuations via sensing holes of 0.5 mm in diameter on both of the lower and upper surfaces of the midspan plane along the airfoil chord that cover $0.09 < x/C < 0.64$, where x is the streamwise direction. It should be noted that the airfoil was painted black after manufacturing in order to provide an even smoother surface finish.

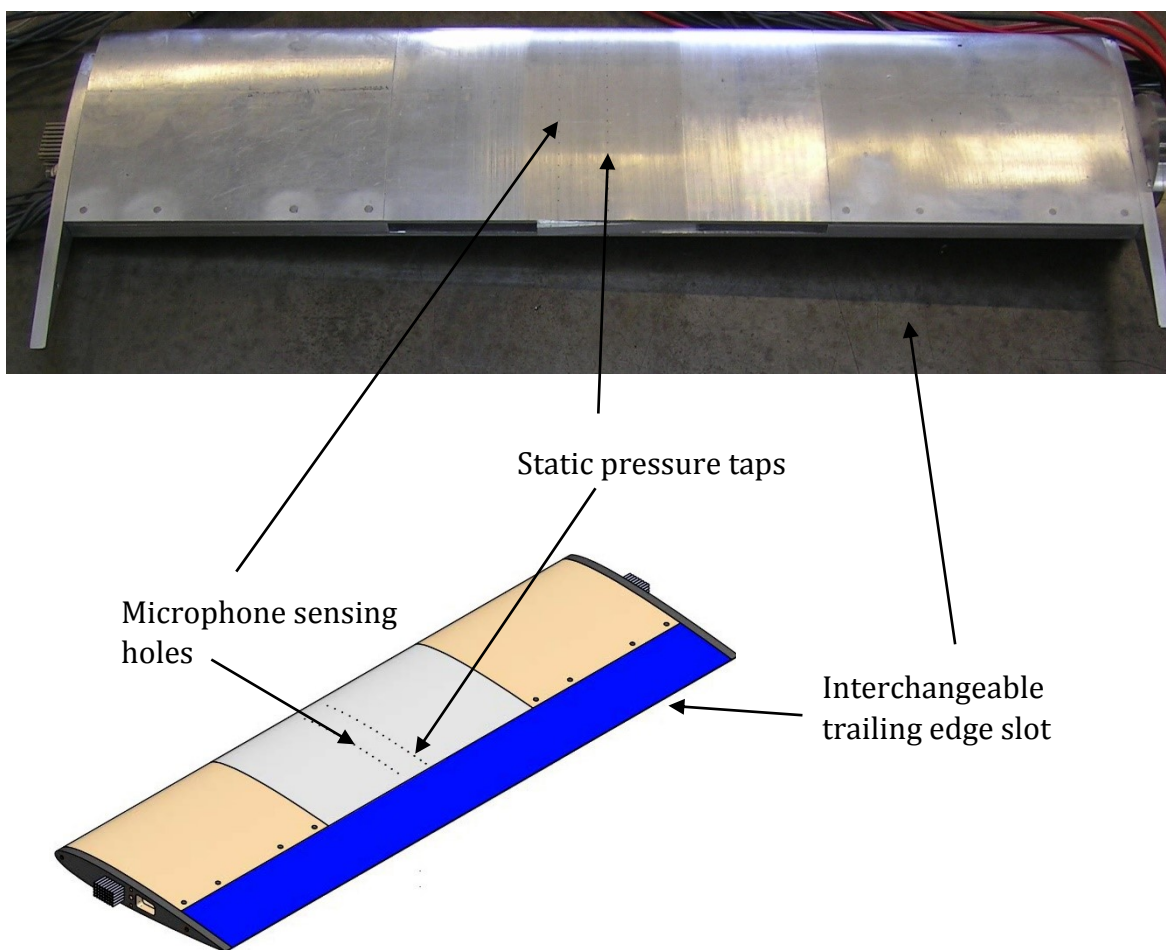


Figure 3.13a) NACA 0012 airfoil design

The airfoil models have been designed to accommodate the straight and serrated trailing edge designs without changing the cross sectional shape of the airfoil. From $x/C = 0$ (leading edge) the main airfoil body is designed up to $x/C = 0.79$. Further downstream, at $0.79 < x/C < 1.0$, is the section which is interchangeable for the different trailing edge models. Once attached, the serration designs form a continuous profile, giving the appearance that the serrations are cut into the main body of the NACA0012. Four different serrated trailing edge designs (referred to as S1, S2, S3 and S2* as labelled in Fig. 3.13b) and one baseline straight trailing edge ("S0") have been manufactured. It can be seen in Fig 3.13 that each of the four serrated trailing edges varies in terms of the serration geometry. More precisely, the serration angle (ϕ) and the serration length ($2h$) are changed where S1, S2 and S3 share the same $2h$ ($=20\text{mm}$) but differ in ϕ ($=7^\circ, 12^\circ$ and 25° respectively). S2* in turn has a $\phi=12^\circ$ but a shorter serration length $2h$ ($=10\text{mm}$). In order to provide a better overview, a detailed summary of the serration properties will be present in the relevant chapters.

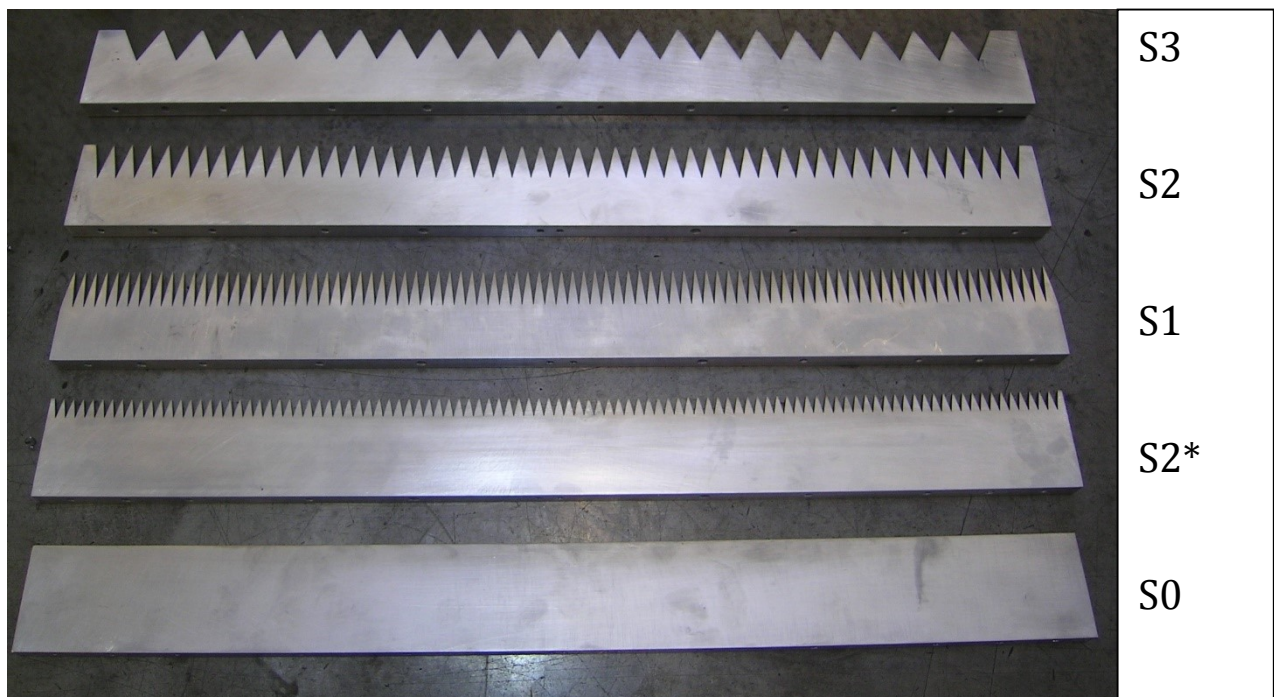


Figure 3.13.b) Airfoil trailing edge attachments with four different non-flat plate serration designs and one straight baseline trailing edge.

3.4 Water tunnel

In order to investigate the mechanism behind the narrowband vortex shedding noise generation, a water tunnel as shown in Fig. 3.14 was used for a flow visualisation test. The water tunnel consists of a 300×450 mm cross-sectional area. The airfoil was mounted on a flat plate on the top of the water tunnel, positioned at $\theta = 5^\circ$ relative to the mean flow direction. Blue colour dye was injected at a constant flow rate into the water near the trailing edge, which was recorded by a digital camera. A flow speed of 0.04 ms^{-1} was selected, corresponding to a Reynolds number of approximately 0.9×10^4 based on the airfoil's chord length. This particular flow rate was selected, as it appeared to provide the

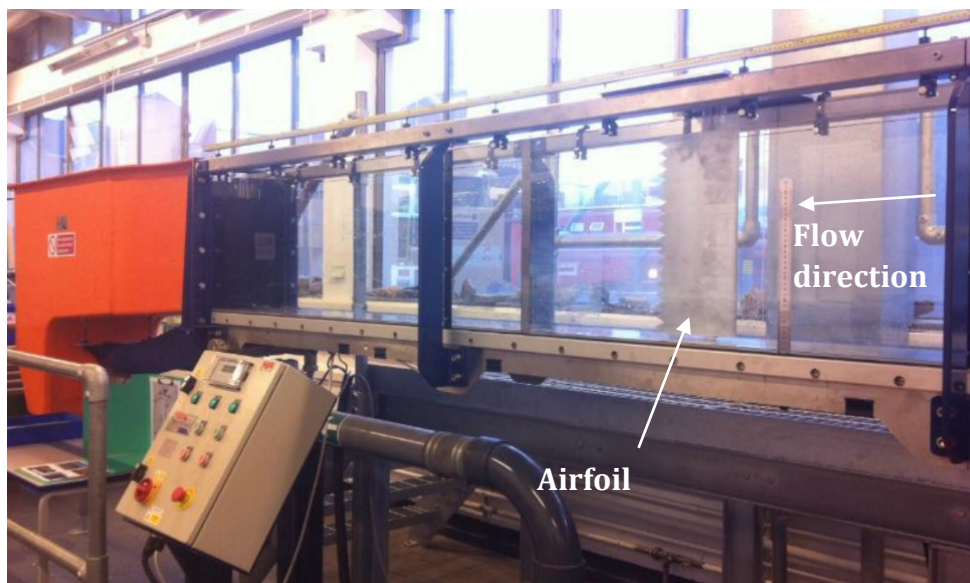


Figure 3.14 Water tunnel with airfoil/hydrofoil

clearest pattern for visualising the vortex shedding mechanism. Although the Reynolds number for this hydrodynamic test is fairly low, the airfoil was tripped near the leading edge in order to produce a turbulent-like boundary layer at the trailing edge, roughly equivalent to the turbulent noise source generated in the acoustic tests conducted for this thesis. A separate NACA 0012 airfoil of 200 mm chord was manufactured for the water tunnel test with the identical trailing edge serration angle ($\varphi=25^\circ$) to the “S3” case from the aeroacoustic tests. Regarding the serration geometry, as the overall chord length is larger than the airfoil used for the aeroacoustic tests, it should be noted that both airfoil models have the same $2h/C$ value ($=0.13$).

3.5 Hot wire anemometry with traverse mechanism

A 2-axis traverse system, model TSI-Isel T2D, was used for all hot wire anemometry measurements. The accuracy of movement was within 0.01mm. The traverse mechanism was connected through its central unit box to the central computer, which controlled the traverse movements and the data acquisition software, Thermal Pro by TSI.

The hot wire anemometry conducted in this thesis include measurements using hot-film, single-wire, cross-wire and triple-wire probes. If not otherwise specified, an overheat ratio of 1.8 was used for the hot wires. However, in some cases it was required to minimise thermal destabilisation in the boundary layer (i.e. in the case of surface mount hot film sensors) or to avoid thermal interference between two probes (i.e. in coherence measurements). In these cases, the overheat ratio will be stated again in the according experiment of the chapter. The signals from the anemometers were digitised by a 12-bit A/D card (TSI ADCPCI).

In order to ensure that movement of the traverse and the attached hotwire probe are exactly aligned to the airfoil axes, a PRO360 Angle Gauge and Inclinator (accuracy within 0.1°) was used. Moreover, the angle gauge was used during the calibrations of any hot-wire probe when an angle adjustment was required, by placing the gauge on top of the probe support or a directly parallel moving surface of the straight probe holder.

A Furness Controls FC0510 manometer was used for the velocity adjustments needed for the calibrations or test run set ups. It was connected to a FC065 pitot tube featuring a conventional 90° bent shaft. The flow and differential pressures can be measured as accurate as 0.001Pa.

All single and cross wire measurements were conducted using two DISA 55M10 constant temperature anemometers, while a multi-channel Dantec 55N80 constant temperature anemometer was used for the triple-wire and surface mounted hot film measurements.

The single hot-wire probes used were 5µm diameter and 1.25mm long Dantec 55P11 tungsten wire probes. The calibration was carried out inside the empty wind tunnel facility. During calibration the ambient temperature (T_c) is noted. Similarly, the ambient temperature (T_a) was recorded during each conducted data acquisition. For the data analysis, a temperature correction is applied to obtain the corrected voltage E_{corr} :

$$E_{corr} = E_{acq} \left(\frac{T_w - T_c}{T_w - T_a} \right)^{0.5} \quad (\text{eq 3.9})$$

Where E_{acq} is the voltage recorded during data acquisition and T_w is the hot wire operating temperature, which is based on the overheat ratio and property of the wire material. The conversion from E_{corr} to velocity is then obtained through interpolating a 4th polynomial voltage-velocity calibration curve:

$$U = C_0 + C_1 E_{corr} + C_2 E_{corr}^2 + C_3 E_{corr}^3 + C_4 E_{corr}^4 \quad (\text{eq 3.10})$$

Where C_0 to C_4 are the coefficients obtained from the calibration curve using a standard least square best fit.

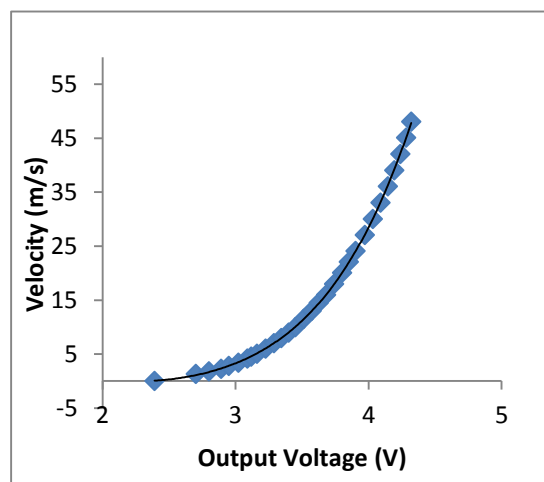


Figure 3.15 Calibration curve for a single hot wire probe.

The 55P61 probe type cross-wire is used to measure the two-component velocities u and v , where u is the velocity component in the streamwise direction, and v is the velocity component in the vertical direction. The diameter and length for each wire are $5 \mu\text{m}$ and 1.25 mm respectively. The probe axis is mounted parallel to the direction of main flow, so that the predominant flow vector attacks the two wires under 45° .

A full velocity versus yaw-angle calibration technique (lookup table method) was employed to convert the acquired voltages into the velocities. This calibration method eliminates the potential error incurred by the function of velocities to the yaw coefficients. More precisely, thirteen yaw angles ($\pm 45^\circ$, $\pm 40^\circ$, $\pm 32^\circ$, $\pm 24^\circ$, $\pm 16^\circ$, $\pm 8^\circ$ and 0°) were selected to conduct a full velocity calibration for each of them. As the freestream velocity during the cross wire experiments was conducted at 30 ms^{-1} , the calibration velocities were selected to be between 0 ms^{-1} and 35 ms^{-1} (21 points), measured in the freestream of the open circuit wind tunnel (described in Section 3.2.2.1). Thus, based on a total of 273 calibration points it is possible to relate each point from the data acquisition in the E1, E2

plane (where E_1 and E_2 are the output voltages of the two wires) to a point in the u, v plane (where u and v the x and y components respectively). In case the acquired data do not directly coincide with the calibration values, an interpolation method involving the derivatives of the voltages with the respect to velocity components is applied [Lekakis (1996)].

Due to the physical size of the cross wire the nearest point in the boundary layer is approximately 1 mm from the wall. As the cross-wire is used in the flat plate experiment, where the surface is made from a non-metallic, near wall corrections for the cross wire probe at this height are not necessary.

Regarding the triple hot-film probe used, the type 1299 probe from TSI contains three platinum films allowing three component velocity measurements (Fig 3.16), having a greater structural strength compared to wire probes, and greater resistance which will not shift in a high velocity environment or due to particle impact. The yaw, pitch and roll calibration of the probe was conducted directly by the manufacturer. Since the main factor causing a deviation of the wires' directional sensitivity is the change of geometry over time, the error in velocity is expected to be insignificant, as the triple wire measurement was conducted immediately after the arrival from the supplier. A single velocity calibration was then carried out on each day of testing (directly facing the airflow at 0° roll pitch and yaw). The interpretation of triple-sensor signals is conducted by using Jørgensen's effective cooling relation which is based on the solution of the three response equations. The equations for the particular probe type are linear functions of u^2 , v^2 and w^2 and are solved using matrix inversion techniques. The entire process of converting the acquired voltage signals to the u, v and w velocities as used here is summarised by Lekakis et al (1989).

The uncertainty of the velocity samples of the described hot wire probes are in the typical range of 3%. As reported by Jørgensen (2005), the major factors of the error may come from the temperature variations in the flow and the linearisation (curve fitting). Another contribution might be the fact that the calibration was conducted in a wind tunnel with a pitot static tube/micro manometer arrangement instead of a dedicated calibrator device.

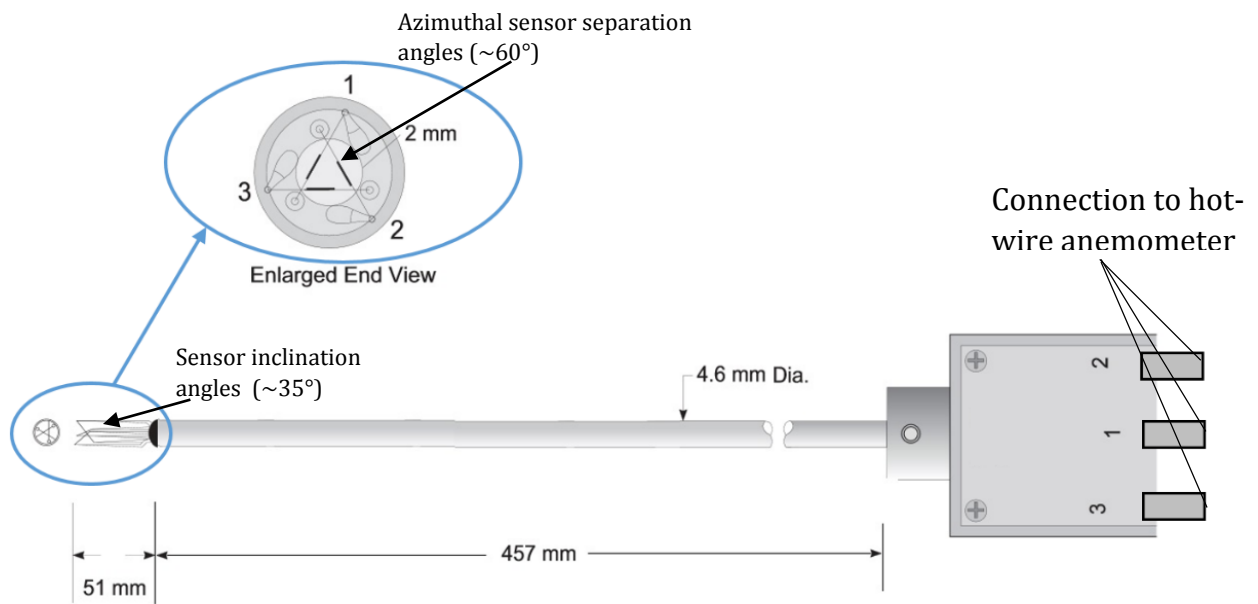


Figure 3.16 TSI 1299 triple-wire sensor

Chapter 4

An assessment of noise and lift/drag performance of non-flat trailing edge plate serrations

The following chapter focuses on the performance characteristics of non-flat plate type serrated trailing edges. Several non-flat plate serration geometries will be under investigation in terms of noise and the aerodynamic performance in order to identify the advantages and disadvantages of the concept. The non-flat plate serrations will be assessed at three effective angles of attack (α) 0° , 1.4° and 4.2° for different serration geometries. The reason for this angle of attack selection is the fact that they represent the geometrical angles of (0°), 10° and 15° respectively. A higher angle of attack than the 15° was not considered due to the limitation of the nozzle exit height. The radiated sound power level (PWL) spectra will be presented for the serrated trailing edges and the baseline case in section 4.2. In Section 4.3 a detailed noise performance characterisation through Δ PWL contours will be presented. The Δ PWL is defined as the difference of sound power level between a straight baseline trailing edge and a serrated trailing edge. The overall sound power level (OAPWL), which is obtained by integrating the PWL across a range of frequencies will be presented in Section 4.4. Another parameter defined as the overall noise performance metric (NPM) allows a selective evaluation of the noise performance in the frequency range of interest. Section 4.5 evaluates the results of the variation of the lift coefficient, drag coefficient and lift-to-drag ratio of an airfoil with trailing edge serrations.

4.1 Configurations of the non-flat plate trailing edge

As previously introduced in Chapter 2 and illustrated in Fig. 4.1, the serration characteristics are described in terms of the serration length ($2h$), period (λ), and serration angle (φ). For the particular trailing edge concept an arising bluntness factor, ε , is introduced in order to define the bluntness exposed by cutting the serrations directly into the airfoil main body.

A total of five trailing edge models, including one straight trailing edge to serve as a baseline case, was tested. Three serrated trailing edges named as S1, S2 and S3 consist of the same serration length $2h=20\text{mm}$, with a varying serration angle φ to be 7° , 12° and 25° respectively. Between trailing edge design S2 and S2* the serration angle remains the same, however in the case of S2* a shorter length $2h = 10\text{mm}$ is used. A summary of these trailing edges is provided in Table 4.1.

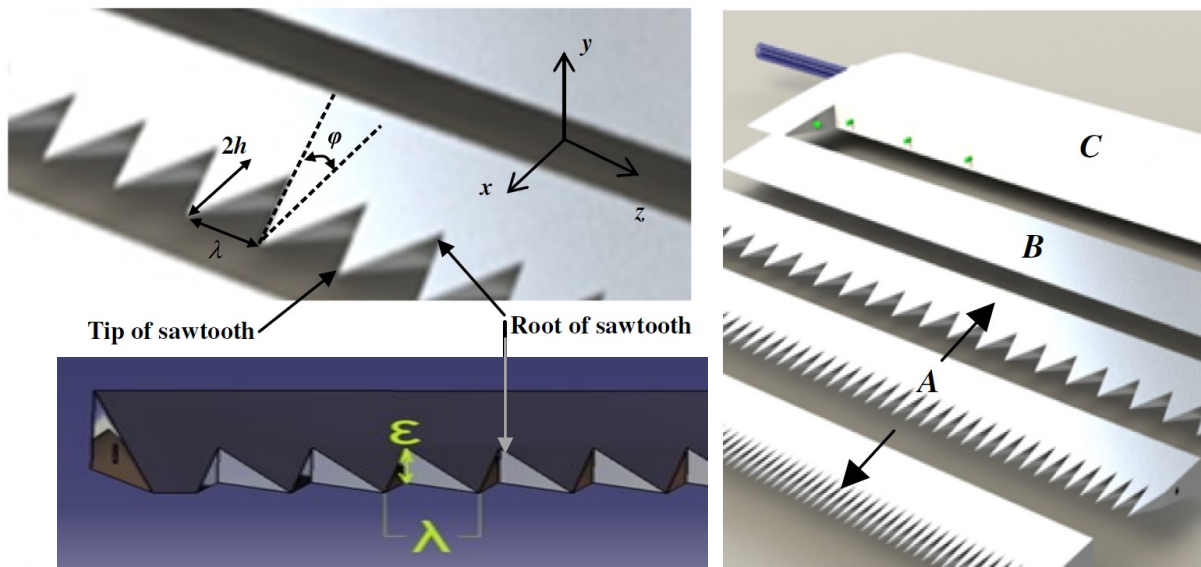


Figure 4.1 Illustration of non-flat plate serrations, showing the serration parameters (left) as well as several trailing edge attachments (right) where (A) serrated geometries, (B) sharp/straight trailing edge and (C) main body of the airfoil.

All the noise results presented in this chapter were taken at the DARP Rig of Southampton University at jet speeds between 20 ms^{-1} and 60 ms^{-1} with a step size of 0.2 ms^{-1} . The corresponding Reynolds numbers based on the airfoil chord are between 2×10^5 and 6×10^5 . The farfield noise was measured through the microphone array described in Section 3.1.1.2 at a sampling frequency of 30 kHz for 13.33 seconds.

Description	Notation	Serr. Length $2h$, mm	λ/h [φ ,deg]	Bluntness (ϵ), mm
Straight/baseline	S0	n/a	n/a	n/a
Serrated	S1	20	0.49[7°]	5.7
Serrated	S2	20	0.85[12°]	5.7
Serrated	S2*	10	0.85 [12°]	3.1
Serrated	S3	20	1.87[25°]	5.7

Table 4.1 Properties of serration geometries from the models tested

In order to generate a turbulent boundary layer over the airfoil, thereby allowing the investigation of turbulent boundary layer broadband noise, a tripping tape in form of a rough sand paper strip of about 0.9mm roughness height was placed at about 15% of the airfoil chord on its suction and pressure sides. The roughness height was chosen to be larger than the height of the inner layer (which thickness was measured by a single hot-wire) in order to ensure turbulent flow.

In order to show the effect of the tripping tape, Fig. 4.2 shows the wall pressure spectra measured by the integrated surface pressure microphone of the airfoil at $x/C = 0.64$. The dotted lines and solid lines represent the S_{qq} with and without boundary layer tripping tapes respectively. In Fig. 4.2a the suction surface spectra are presented. It can be seen that in the untripped case, various peaks arise at around 1 kHz, occurring due to boundary-layer instability noise radiating to the far field. In Fig. 4.2b, the wall pressure spectra S_{qq} at the pressure surface differ considerably. Without the use of the boundary-layer trip, the S_{qq} is comparatively low in level and less smooth than when tripping is applied. However, the boundary layer becomes turbulent when the trip is introduced as manifested by the considerably higher wall pressure spectrum level. In conclusion, boundary layers at both the suction and pressure surfaces boundary layers at both the suction and pressure surfaces are turbulent near the trailing edge when tripping elements are applied on their respective surfaces. Without tripping, the boundary layer at the

pressure surface is laminar (or separated) near the trailing edge. On the suction surface, the boundary layer may become turbulent near the trailing edge without the use of tripping tape.

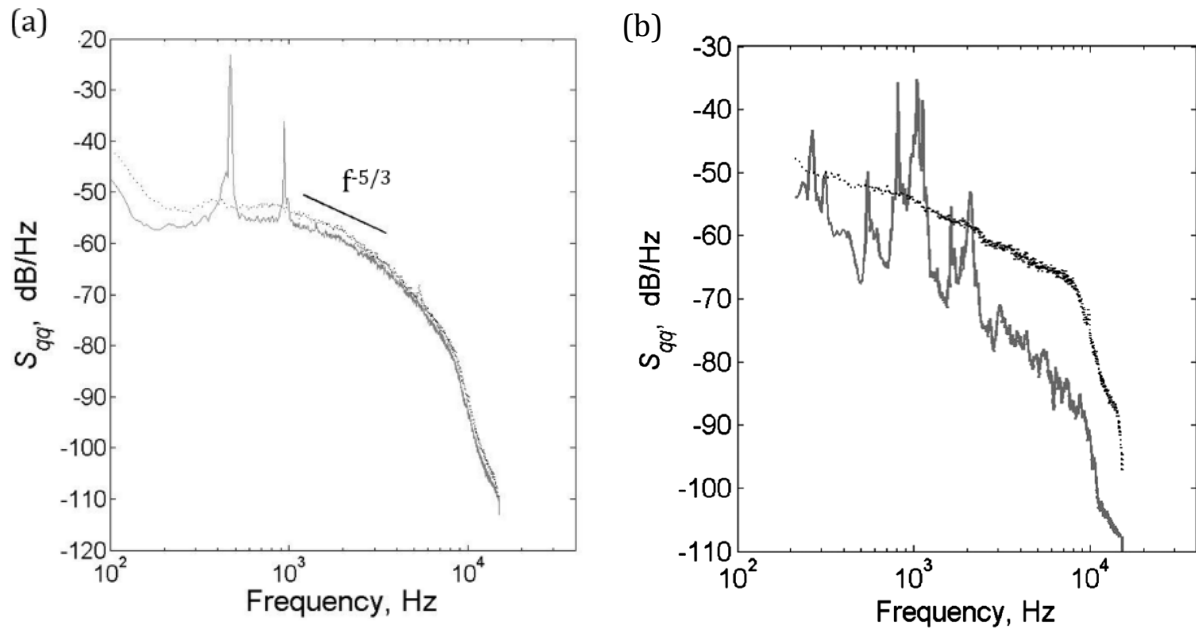


Figure 4.2 $S_{qq'}$ measured at $\alpha = 4.2^\circ$ and $U = 26.7 \text{ ms}^{-1}$ for the a) suction surface and b) pressure surface, both of which are at $x/C = 0.64$. The dotted lines (•••••) and solid lines (—) represent $S_{qq'}$ with and without boundary layer tripping tapes, respectively, near the leading edge of the airfoil.

4.2 Trailing edge serrations' PWL spectra

Figures 4.3 a and b show the sound power level (PWL) spectra (defined in equation 3.3) for the four serration cases (S1, S2, S2*, S3) and the baseline (S0), for jet speeds of 27 ms^{-1} and 60 ms^{-1} respectively. The results in Fig. 4.3 correspond to the measurements taken at an effective angle α of 1.4° .

These results provide an example of the non-flat plate serrations performance and their potential to achieve broadband noise reductions, usually in the mid to high frequency range. The obvious disadvantage, however, is the noise increase encountered in form of a narrowband tone due to the vortex shedding induced by the blunt serration interstices. It can be observed that the tone produced by the non-flat plate serrated trailing edges has a trend of decreasing magnitude when the serration angle φ is increased. The fact that vortex shedding tonal noise decreases with a larger serration angle φ (or λ/h) is due to a reduced amount of saw-teeth and therefore a smaller overall area of the blunt serration interstices. In terms of broadband noise reduction (i.e. mainly at frequencies higher than the vortex shedding tone), a better performance is generally observed as the serration angle φ is decreased, which is consistent with Howe's theoretical findings. This fact will be further proven in Section 4.3.

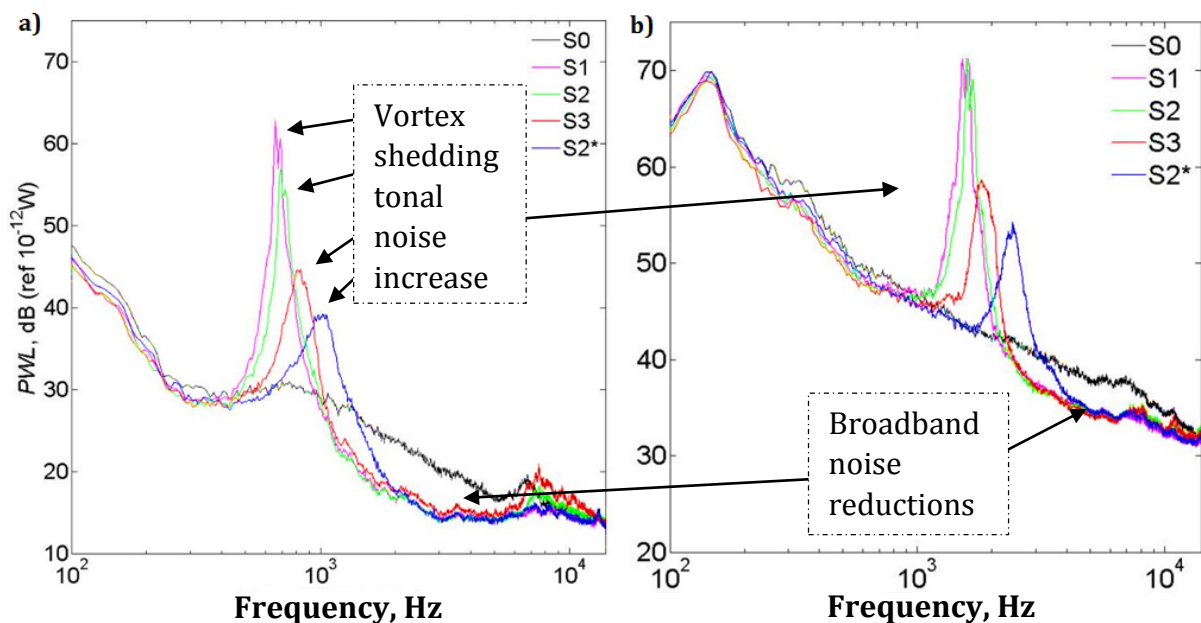


Figure 4.3 PWL spectra for a) 27 ms^{-1} and b) 60 ms^{-1} .

In the case of a shorter serration length, $2h$, it is shown in Fig 4.3 that the vortex shedding noise is reduced when comparing the cases S2* ($2h=10\text{mm}$) and S2 ($2h=20\text{mm}$). On the other hand, it can be seen that the broadband noise reductions are compromised for the shorter serration length, where the frequency range of reductions is limited.

In the following section, the general trend of the PWL produced by the non-flat plate serrated trailing edges will be presented at further velocities and angles of attack.

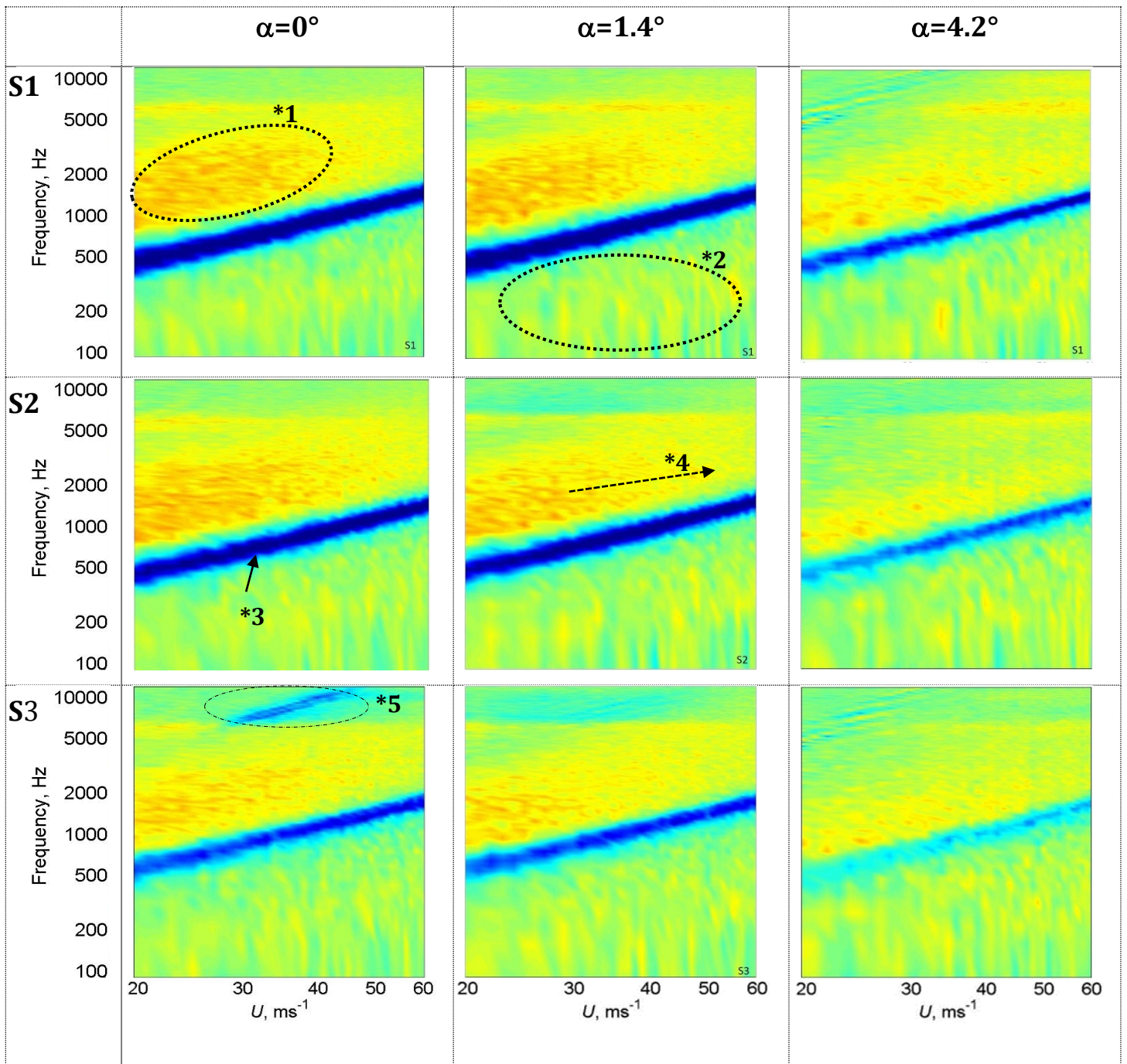
4.3 Trailing edge serrations' PWL contours

In order to demonstrate a more complete picture on the noise characteristics of the serrated trailing edge models, contour maps of the ΔPWL are presented, which essentially compare the difference between the baseline and serrated trailing edge cases ($\text{PWL}_{\text{baseline}} - \text{PWL}_{\text{serration}}$) within a wide velocity range. Therefore a positive ΔPWL denotes that noise reductions have been achieved by the serrated trailing edge, and the opposite is true for negative ΔPWL values.

The colour maps of all test cases of same $2h$ are presented in Fig 4.4 (at $\alpha=0^\circ; 1.4^\circ; 4.2^\circ$), and a comparison of the theoretical reductions by Howe (at $\alpha=0^\circ$) for the equivalent trailing edge serration geometries tested here, is modelled in Fig. 4.5. In all ΔPWL contour maps shown, the velocity range is from 20 to 60 ms^{-1} .

The results in Fig 4.4 confirm that the largest broadband noise reductions (as in Fig 4.4 *1) are achieved through the narrowest serration angle, case S1. When focusing on the trend of broadband noise reductions, it can be clearly seen that the reduction level increases when the serration angle φ decreases.

For the angles of attack of 0° and 1.4° , there is little difference towards the levels of broadband noise reduction and the tonal noise increase between them. However, the ΔPWL levels at 4.2° are quite different: The benefit from the serrations on broadband noise reduction becomes less effective, but the extraneous vortex shedding tonal noise (as in Fig. 4.4 *3) becomes less severe.



*1 Broadband noise reductions; *2 Low frequency noise reduction;

*3 Vortex shedding noise, reduces when φ and α increase.

*4 Broadband noise reductions become less with increased U .

*5 Note that the tonal rung is not a feature in a number of repeated tests, such as in Chapter 6 (Fig 6.7). Therefore it is likely that the particular high frequency tonal rung is not related to the trailing edge serration.

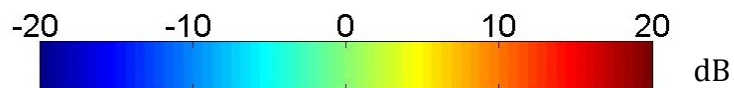


Figure 4.4 PWL contours of cases S1, S2 and S3 for varying angles of attack

Regarding the relationship between broadband noise reductions and serration angle, the current findings may agree with Howe's conjecture. However, when the actual level of broadband noise reduction observed in the measurement (Fig. 4.4) is compared with his theoretical model (Fig. 4.5), it becomes clear that the predicted noise reduction levels are much larger in comparison to the experimental results presented here. The discrepancy is in the order of 15-25dB. However, in the case of larger serration angles, such as the S3 case, the difference becomes smaller. Deviations with a similar behaviour have been

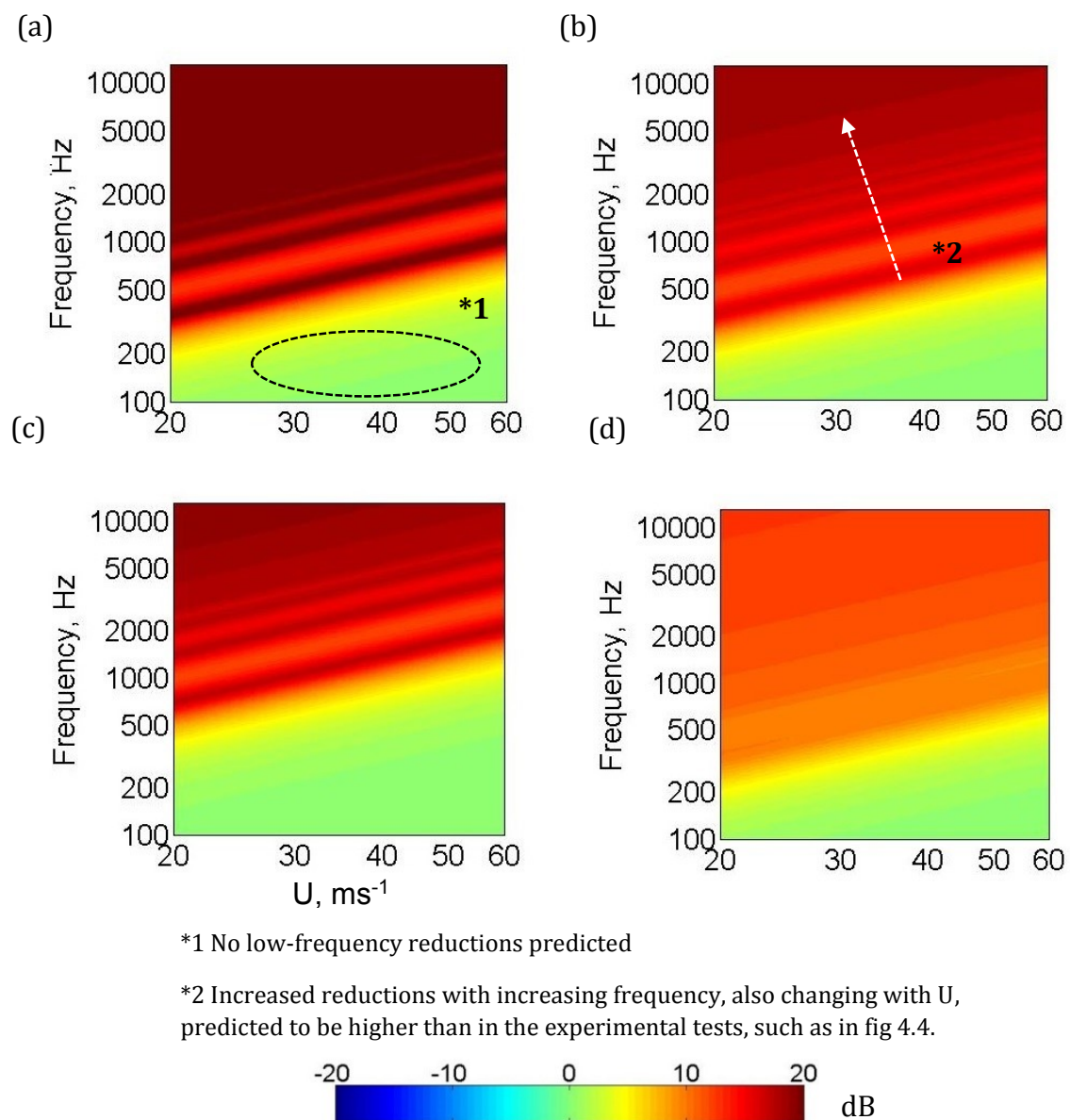


Figure 4.5 Figure 4.5 SPL contours according to Howe's theory for the cases a) S1, b) S2, c) S2* and d) S3, at $\alpha=0^\circ$

observed by other researchers such as Gruber (2011) and Moreau et al. (2012), thus questioning the accuracy of Howe's theoretical model.

It is interesting to point out that noise reductions for the non-flat plate serrations occur at lower frequencies (Fig 4.4 *2), whereas this is neither the case in Howe's predicted noise contours (Fig 4.5 *1) nor in the flat plate inserts tested by Gruber (2011).

When the current concept of non-flat plate serrations is compared with Gruber (2011), who investigated the dependence of trailing edge noise reductions with the flat plate type serration, both agree that a larger broadband noise reduction entails a smaller serration angle. Nonetheless, the flat plate trailing edge serrations by Gruber were found to generate a persisting high frequency increase of up to 3 dB, which is minimal or absent in the current non-flat plate trailing edge serrations (>8kHz) . The high frequency noise increase can be attributed to the presence of small jets through the troughs of the serration.

Comparing the pair of serrations S2 and S2* (Fig 4.6) which have the same φ and λ/h but different $2h$, a larger level of sound power reduction is achieved by the longer serration length $2h$. On the other hand, the vortex shedding noise decreases for a shorter serration length due to the smaller bluntness ε exposed. The larger broadband noise reduction in the case of the S2 is because the serration can exert its impact to the turbulent boundary layer further upstream of the trailing edge while the shorter serration length, S2*, is less effective on a thick turbulent boundary layer.

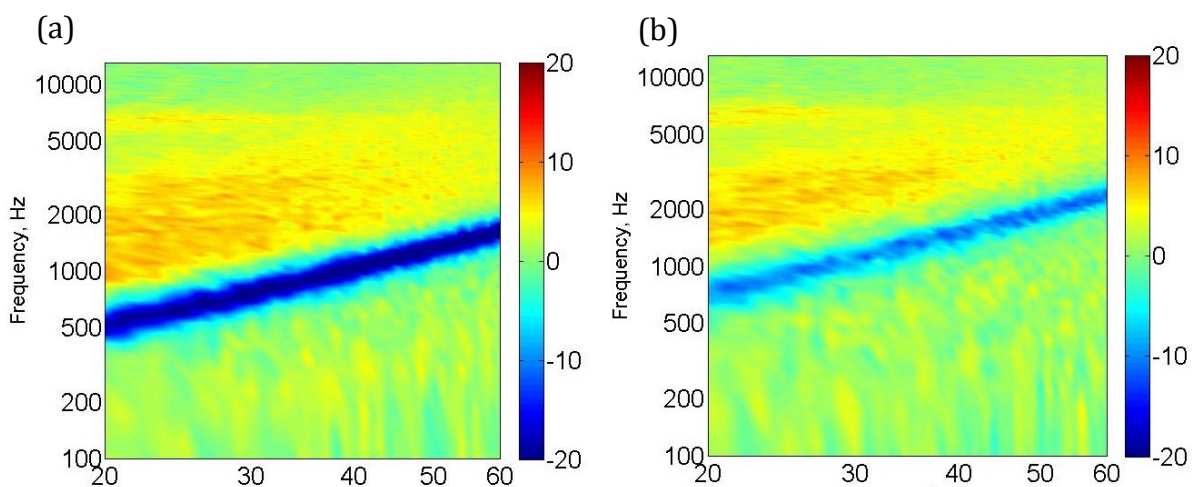


Figure 4.6 $\Delta P W L$ contours of varying $2h$, where a) S2 and b) S2* at $\alpha=0^\circ$.

4.4 Trailing edge serrations' OAPWL comparison

Due to the varying parameters of noise increase and reductions when compared to the baseline case, an evaluation of the overall sound power level (OAPWL) is made in this section. When the OAPWL radiated by the straight trailing edge is subtracted by the OAPWL radiated by a particular type of serrated trailing edge ($OAPWL_{\text{straight}} - OAPWL_{\text{serrated}}$) the parameter is represented by $\Delta OAPWL$. A positive $\Delta OAPWL$ therefore represents an overall sound power reduction, and the opposite is true for a negative Δ . The OAPWL and $\Delta OAPWL$ performance of these models are presented against the mean flow velocity for the S0–S3 and S2* trailing-edge serrations as shown in Fig. 4.7 where a, b represent $\alpha = 0^\circ$; c, d $\alpha = 1.4^\circ$; and d, e = 4.2° .

In nearly all cases the serrated trailing edge shown in Fig 4.7 (a, c, e) the sound power scale with U^{6-7} , which does not appear to vary significantly with angle of attack. This velocity dependence is usually associated with vortex shedding noise from bluff bodies [Hutcheson and Brooks (2006)] or an airfoil with a blunt trailing edge [Brooks et al. (1989)]. For the S0 baseline case, a velocity scaling of $W_{S0} \propto U^{5.5-6}$ has also been observed. This indicates that although a dipole radiation from the trailing edge is still the dominant mechanism, other noise sources (e.g., the leading-edge noise) might slightly contribute to the OAPWL, especially in the higher velocity region.

Generally, the S1 serrated case produces higher overall noise levels than the S0 baseline case across the whole velocity range and all the angles of attack, owing to the strongest dominance of the vortex shedding noise.

At $\alpha = 0^\circ$ and 1.4° there is a very high noise increase visible for S1 and S2. In case of the S2* and S3 trailing edges, the level of the vortex shedding noise decreases resulting to improved $\Delta OAPWL$, with the S2* having a clearly better performance at these angles of attack and partial $\Delta OAPWL$ improvements.

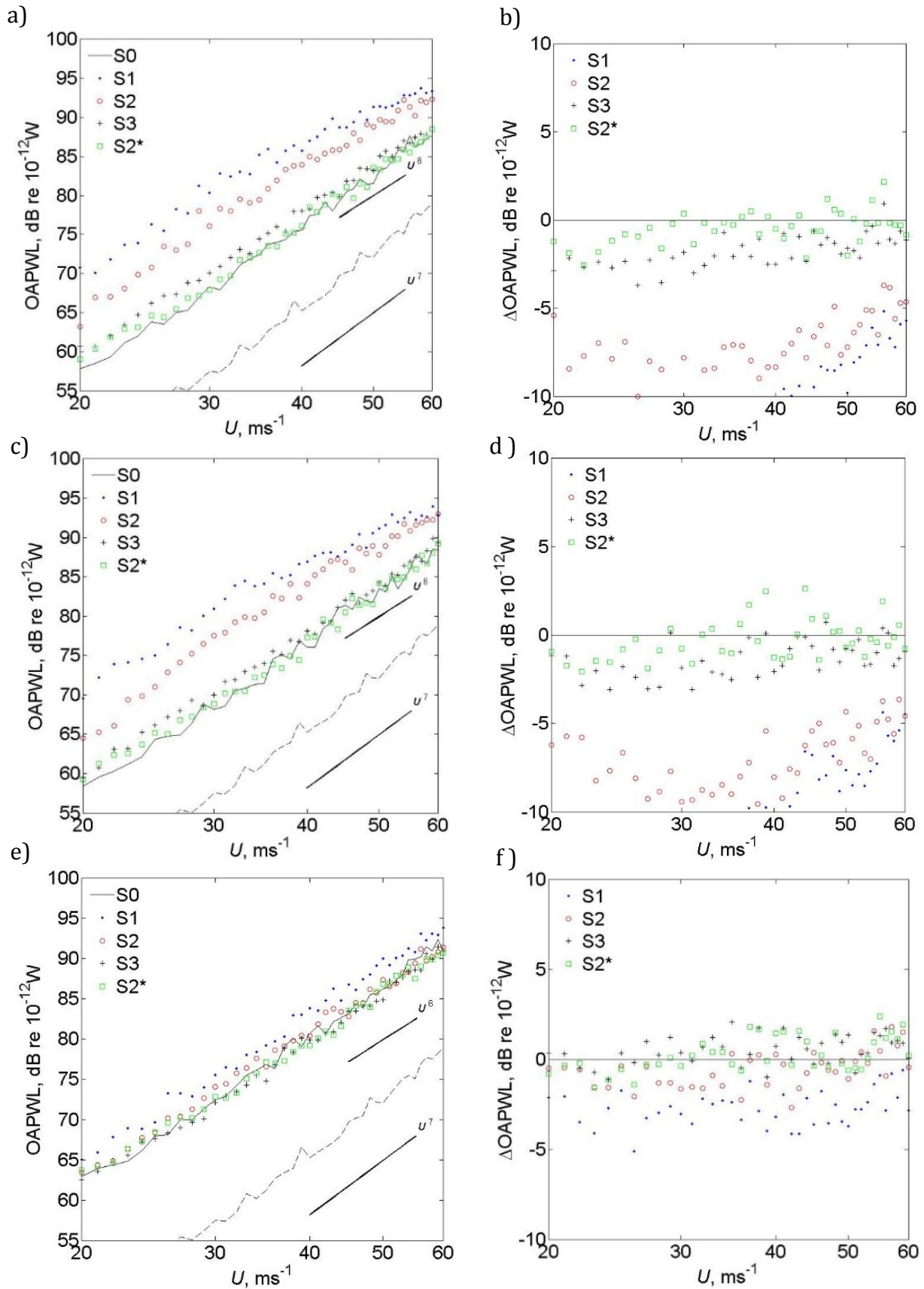


Figure 4. 7 OAPWL (left column) and $\Delta OAPWL$ (right column) in comparison with the baseline straight trailing edge for 3 different α where a, b for 0° ; c, d for 1.4° and e, f for 4.2° .

At $\alpha = 4.2^\circ$ the S2 case varies between an increase and a reduction across the velocity range, whereas the S2* and S3 edges consistently reduce the OAPWL up to ~ 2 dB relative to the S0 baseline case, especially at higher velocities.

For all three angles of attack, the S2* case, which is worth noting that consists of the smallest bluntness ϵ , the Δ OAPWL fluctuate between positive and negative values across the velocity range. This suggests that the overall noise performance of this particular serration geometry is not compromised too severely by the bluntness-induced vortex shedding noise. However, the level of broadband noise reduction is also smaller when compared to the other serration geometries, hence a large positive Δ OAPWL cannot be produced throughout the velocity range and angles of attack.

In order to individually study the impact of vortex shedding noise and the amount of broadband noise reductions of each serrated trailing edge, the noise performance is divided in the following into three frequency bands:

1) Frequency band I: the entire frequency band is to deduce the “overall” performance:
 $0 < f < \infty$ or $J = (0, \infty)$. (eq. 4.1)

2) Frequency band II: the frequency bandwidth corresponding to that in which the sound power is reduced compared to the baseline case (S0):

$$f < f_1 \text{ and } f > f_2 \text{ or } J = (0, f_1) \cup (f_2, \infty). \quad (\text{eq. 4.2})$$

3) Frequency band III: the frequency bandwidth corresponding to that in which the sound power is increased compared to the baseline case (S0):

$$f_1 < f < f_2 \text{ or } J = (f_1, f_2). \quad (\text{eq.4.3})$$

Here, f_1 and f_2 denote the lower and upper frequency limits within which vortex shedding noise due to bluntness at the trailing edge is significant as shown in Fig 4.8. Both f_1 and f_2 increase with the mean flow speed. In each frequency band (I, II, and III), an overall noise performance metric (NPM) is given by

$$\text{NPM} = 10 \log_{10} \left(\int_{f \in J} W_{\text{baseline}} df / \int_{f \in J} W_{\text{serration}} df \right) \quad (\text{eq.4.4})$$

Figure 4.8b shows the variation of NPM versus λ/h and ϕ across $U = 20 - 60 \text{ ms}^{-1}$ for the angle of attack of 4.2° , where positive NPM represent sound power reductions and vice

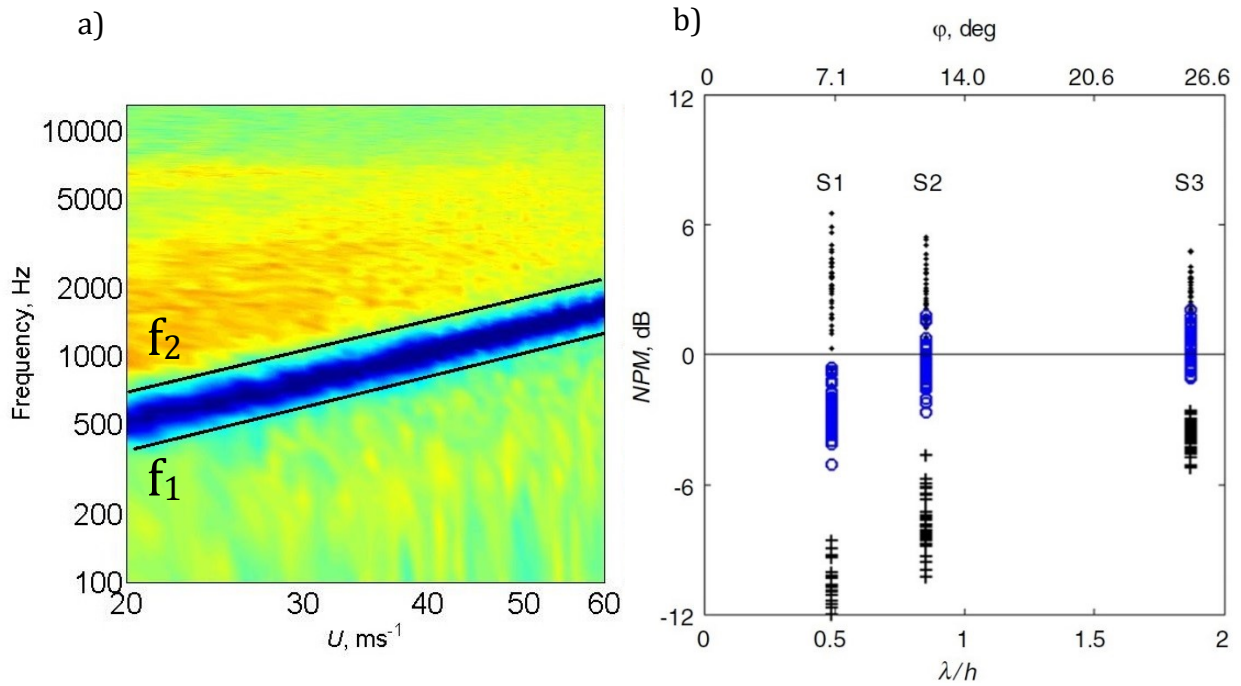


Figure 4.8 a) Example definition of frequencies f_1 and f_2 for b) the distributions of the NPM versus λ/h and ϕ for different frequency bands I (O), II (x), III (+) at the effective angle of attack of 4.2° .

versa. The serrated trailing edges shown here all have the same $2h$ and ε . By examining the variations of sound power reductions (frequency band II), a maximum sound power reduction of up to 6.5-7 dB is achievable within the range of serration angle ϕ investigated here. Sound power increase (frequency band III) caused by the serration bluntness is most significant at small values of ϕ but reduces as ϕ increases.

Finally, by examining the overall sound power reduction across the entire bandwidth (frequency band I), it can be seen that an overall reduction across all frequencies is only achieved for the serration with the largest ϕ . Because the amount of sound power reduction (frequency band II) is relatively insensitive to ϕ in comparison to the sound power increase (frequency band III), the optimum serration geometry, as far as the non-flat plate type is concerned, is thus limited by the narrowband noise radiation due to the vortex shedding (frequency band III). Serration S3 with the largest ϕ therefore gives the best noise performance overall.

In summary, for the S1, S2 and S3 cases, an anti-correlation with regard to the broadband noise reduction and tonal noise increase exists. It is apparent that the negative impact of tonal noise is the greatest when both, the angle of attack and serration angle ϕ are small. Conversely the positive outcome of the broadband noise reduction is the greatest when the angle of attack and ϕ are small. In comparison, the level of broadband noise reduction is relatively small compared to the level of tonal noise increase. Therefore, the overall

noise performance for a non-flat plate serrated trailing edge is largely dictated by the level of vortex shedding tonal noise produced by the exposed bluntness, and it is of paramount importance to seek alternative solutions to suppress this unwanted noise source.

4.5 Aerodynamic forces produced by non-flat plate serrations

Aerodynamic measurements were taken in the conventional closed test section wind tunnel at Brunel University which is described in Section 3.2.2.1. The NACA0012 airfoil model (see Section 3.3.1) accommodates the same non-flat plate inserts used in the aeroacoustic measurements in order to quantify their aerodynamic performance for angles of attack from 0° to 20° by using the 3-component force balance strain gauge described in Section 3.2.2.2. Fig. 4.9a shows the lift coefficient C_L , Fig. 4.9b the drag coefficient C_D and Fig. 4.9c the lift-to-drag ratio C_L/C_D versus angle of attack (α) for the serrated cases of S1 and S3 against the baseline sharp trailing edge measured at a velocity of 24ms^{-1} .

It can be seen that for the S0 baseline trailing edge, C_L increases with an average rate of approximately 0.1 per degree up to an angle of attack of $\alpha \approx 5^\circ$. Beyond that angle the C_L increases at a smaller rate and deviating from the thin airfoil theory. This may be attributed to the thickening of the boundary layer at the suction side of the airfoil and the dominance of viscous effects. The stall angle is seen to occur after $\alpha \approx 12^\circ$, beyond which the C_L drops significantly and remains fairly constant at $14^\circ < \alpha < 20^\circ$. When the baseline trailing edge is compared to the S1 and S3 trailing edges, the C_L variations remain in similar levels until about $\alpha = 5^\circ$. For the angles $5^\circ < \alpha < 12^\circ$ the serrated trailing edges generate slightly less lift, varying up to 5%. Beyond the point of the stall angle at $12^\circ < \alpha < 20^\circ$ the levels of lift in the post-stall regime continue to perform worse, with reductions up to 10% when compared to S0.

The drag coefficient in Fig. 4.9b shows to increase linearly up to about $\alpha = 5^\circ$ and continues to increase at a slightly higher rate until it reaches $\alpha = 11^\circ$. A large increase in C_D is then observed at the stall angle ($\alpha = 12^\circ$). For $12^\circ < \alpha < 20^\circ$ the drag coefficient continues to increase at a higher rate when compared prior to the stall. When the baseline is compared with the serrated trailing edges, the same behaviour is observed until deviations start to

occur after $\alpha \approx 5^\circ$. The drag coefficient of the serrations is then reduced until prior to the stall ($5^\circ < \alpha < 12^\circ$), with reductions of up to $\sim 9\%$. In the post-stall regime ($12^\circ < \alpha < 20^\circ$), the levels of drag are persistently lower, achieving reductions for the S1 and S3 cases of up to 7% when compared to S0.

Figure 4.9c shows the C_L/C_D versus α for the S0, S1 and S3 trailing edges. For the S0 baseline case, it can be seen that the ratio of C_L/C_D steadily increases with α for the baseline case, reaching a maximum value at $\alpha \approx 6^\circ$. Between $6^\circ < \alpha < 9^\circ$, the C_L/C_D value slightly decreases. After that, the C_L/C_D drop at a larger rate which further increases past the stall angle of 12° . At the post-stall regime $\alpha > 12^\circ$, the C_L/C_D steadily declines with α . Comparing the S1 and S3 cases with the baseline, the C_L/C_D matches for up to $\alpha = 4^\circ$. For $4^\circ < \alpha < 6^\circ$, minor fluctuations are observed for the S3 case, however, in both cases, the C_L/C_D continues after 6° to the same levels (with slightly higher values in parts) until the stall angle. In the post-stall regime $\alpha > 12^\circ$ the values of the serrated cases are slightly lower than for the baseline, varying between 0-5%.

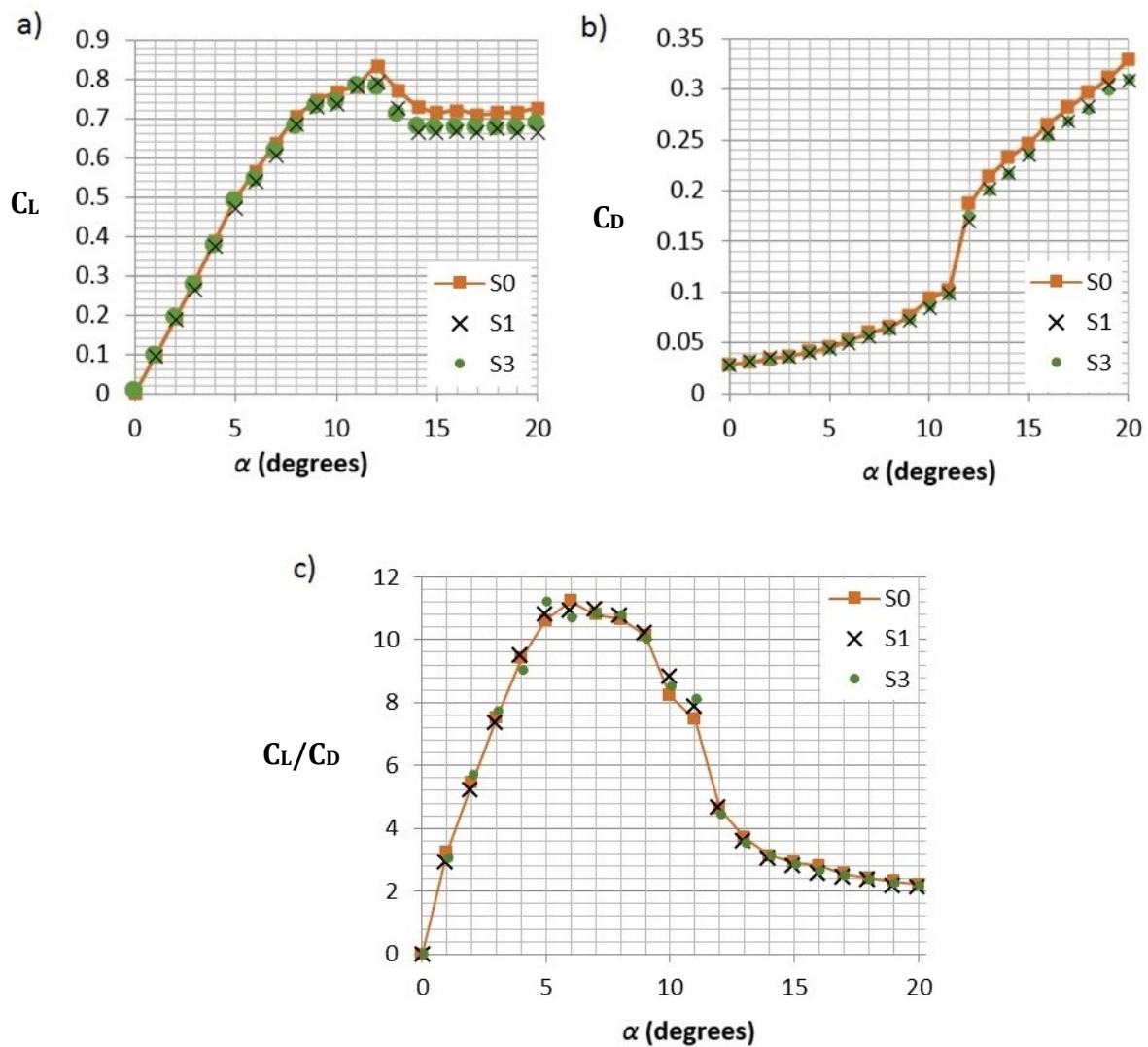


Figure 4.9 Comparisons of the aerodynamic forces produced by the S0 trailing edge (baseline), the narrow serrated angle S1 and the wider serration angle S3 at $U = 30 \text{ ms}^{-1}$ where a) C_L ; b) C_D and c) C_L/C_D against the angles of attack, α .

In all cases, the variations of the serrated trailing edge with the baseline can be divided in three parts. First the range of about $0^\circ < \alpha < 4^\circ$, where C_L , C_D and C_L/C_D do not show any noteworthy difference between serration and straight trailing edge. Secondly, from $\alpha \approx 5^\circ$ up to the stall angle at $\alpha = 12^\circ$, the serrations produce slightly less lift but also slightly less drag. Therefore, the C_L/C_D of both serrations maintains very close levels to the baseline case. Thirdly, in the post-stall regime at $\alpha > 12^\circ$ the lift by the serrated trailing edge decreases by up to 10% but at the same time $\sim 7\%$ reduced drag is achieved. Thus, in overall the values of C_L/C_D are just slightly reduced.

4.6 Discussion

This chapter focused on the performance of non-flat plate serrations for turbulent boundary layer broadband noise and their aerodynamic performance in terms of lift and drag.

In terms of noise performance, the non-flat plate serrated trailing edge was investigated for different trailing edge geometries and angles of attack. Broadband noise reductions of up to 6.5-7 dB were achieved. However, high levels of vortex shedding noise were caused by the partial bluntness of the non-flat plate serrated trailing edge. Further analysis and discussion of this noise mechanism will be presented in Chapter 5. In general, the level of overall noise reduction by the non-flat plate serrated trailing edges is not very significant due to the presence of the vortex shedding tonal noise. A new concept to reduce the turbulent broadband noise and simultaneously suppress the vortex shedding tonal noise has been developed. This will be further discussed in Chapter 6.

The presented results agree with the trends of Howe's theory and the experimental investigation of Gruber (2011) in terms of broadband noise reduction, where smaller serration angles (φ) achieve the greater reductions in broadband noise. However, as in all other related research works, the levels of reduction are smaller when compared to Howe's theoretical model. When compared to flat plate serrations by Gruber, non-flat plate-type serrations have a better noise performance at a high frequency.

Contrary to the broadband noise trend with the serration geometry, the level of the narrowband vortex shedding noise will reduce when a large serration angle (φ) is used. Small to moderate self-noise reductions can still be achieved by the non-flat plate type serrated trailing edge if:

- 1) The serration angle (φ) is sufficiently large. As mentioned, the results also agree with Gruber et al. (2011) and Howe (1989) in that maximum broadband noise reduction would require a smaller φ . However, the recommendation of a large φ in this case for the broadband noise reduction is based on the consideration of minimising the narrowband vortex shedding noise.

- 2) The serration length ($2h$) of the saw-tooth should be equal to or greater than the turbulent boundary-layer thickness. For a non-flat plate type serration, a slightly smaller

2h is also desirable, because it will generate a lower level of the narrowband vortex shedding noise due to the smaller bluntness (ϵ).

3) At $\alpha = 4.2^\circ$ the noise increase by vortex shedding as well as the broadband noise reductions are moderated, compared to $\alpha = 0^\circ$ or 1.4° . Thus, as vortex shedding noise proved to be a dominant factor, the greatest overall reductions were achieved at an angle of attack of 4.2° , reaching 2.5-3dB at certain higher velocities.

In terms of aerodynamic performance, a narrow (S1) and a wide (S3) serration model was tested. The variations of the serrated trailing edges with the baseline start to appear at $\alpha < 4^\circ$, where the levels of C_L and C_D become simultaneously less, which results to the C_L/C_D being very similar to the baseline case. Hence, the C_L/C_D for both tested serration cases (S1, S3) stays very close to the levels to the baseline case up to the stall angle. Small deviations are only observed in the C_L/C_D only past the stall angle, where the difference of reduced lift reaches up to 10% compared to $\sim 7\%$ reduced drag, leading to lower values of C_L/C_D .

Chapter 5

Investigation of the turbulent boundary layer broadband noise and vortex shedding mechanism of non-flat plate trailing edge serrations

As previously presented in Chapters 3 and 4, the noise performance of non-flat plate trailing edge serrations, along with flat plate serrations, has been assessed thoroughly by researchers. However, it appears that a more fundamental study on the mechanism of self-noise reduction by serrated trailing edges remains quite scarce. In this Chapter, an experimental study on the turbulent flow over a serrated trailing edge is presented. A variety of experiments was conducted for 1) the investigation of the flow mechanism over a sawtooth serrated trailing edge and 2) the bluntness-induced vortex shedding tonal noise mechanism of a non-flat plate serration. A detailed overview is summarised below:

1. For the investigation on the flow mechanism over a sawtooth serrated trailing edge, it is of great interest to study properties in the flow which might be directly related to the far field noise. The model proposed by Amiet (1976) (see Section 2.2.3) expresses the far field noise S_{pp} in terms of the spanwise correlation length l_y and the surface pressure spectrum S_{qq} near the trailing edge, and a radiation term $L(\omega)$, of the form: $S_{pp}(\omega) \propto L(\omega)l_y(\omega)S_{qq}(\omega)$. Possible redistributions of energy within the turbulence spectrum, could additionally influence the far field noise radiation. These quantities are of importance only at distances very close to the serrated trailing edge. In order to achieve that, tests were carried out on a flat plate. In the particular case, the flow is present only on one side of the plate surface, allowing more flexibility to arrange and take measurements directly at the trailing edge. To this effect, additional noise measurements were conducted, showing that broadband noise reductions can be realistically achieved in the flat plate configuration by the serrated sawtooth trailing edge (see section 5.2). The turbulence-induced broadband noise sources at the sawtooth serrated trailing

edge are studied by several experimental techniques such as hot wire anemometry, wall pressure measurements and liquid crystal flow visualisation. The variation of the turbulent heat transfer will be investigated through the liquid crystal flow visualisation in Section 5.3. In Section 5.4 the variations of wall pressure power spectral density and the spanwise coherence (which relates to the spanwise correlation length) are studied. In Section 5.5 a conditional-averaging technique was applied to study the boundary layer properties by relating the hot wire data with the surface pressure readings. Section 5.6 combines the liquid crystal results and the unsteady surface pressure readings for the analysis of the vortical structures observed along the sawtooth tip.

2. The second part investigates the flow in the near wake, behind the partially blunt trailing edge of the non-flat plate type serrations in order to provide a better understanding of the vortex shedding tonal noise mechanism. An experiment using dye flow visualisation was conducted in a water tunnel, to trace the development of wake flow from the airfoil. Using a pair of single hot-wire probes, where one remains stationary and the other one is traversed in spanwise direction, the spanwise coherence is studied in the near wake. The vortex shedding generated by a fully blunt trailing edge is compared with the serrated trailing edge in terms of the Strouhal number dependency.

5.1 Details of test models

All aerodynamic flow measurements (Sections 5.3 to 5.6) were conducted in the open jet wind tunnel facility which has been described in detail in Section 3.4.1.1. Throughout the experiments, the freestream velocity was maintained at 30 ms^{-1} . The cross sectional area of the nozzle outlet is $50 \text{ mm} \times 150 \text{ mm}$. All interchangeable flat plate extensions attached to the one side of the nozzle exit have the same dimensions of $50 \text{ mm} \times 295 \text{ mm}$. Note that the background noise level produced by this open jet wind tunnel is excessive and cannot be used for any meaningful noise measurement. The aeroacoustic noise measurements were instead conducted in an aeroacoustic facility which was built in a later stage of this PhD project. Note that this facility only became available after all the flow measurements have been completed. The cross sectional area of the aeroacoustic facility's nozzle exit is $100 \text{ mm} \times 300 \text{ mm}$. A flat plate extension of $300 \text{ mm} \times 295 \text{ mm}$ was flush mounted to one side of the exit nozzle. The length and tripping location of the flat plates used in both facilities was kept the same to ensure that the turbulent boundary layer characteristics at the trailing edge does not change. In all cases, a rough sandpaper strip was used to trip the flat plate boundary layer to turbulent near the nozzle outlet.

The baseline model has a sharp, straight trailing edge. The upper side of the flow surface is flat up to the trailing edge, and a small bevel angle is present at the back side to allow a gradual tapering across the total plate thickness of 5 mm (see Section 3.2.1.1). Note that there is no flow at the underside of the test model. Another flat plate model has a serrated sawtooth trailing edge with the following specifications: root-to-tip distance ($2h$) = 20 mm , and a serration angle (ϕ) = 25° , where the symbols are explained in Fig. 5.1. Similarly, a small bevel angle is present near the trailing edge at the back side where no flow is present.

There are 34 microphone ports near the trailing edges of each flat plate model. Each port is 0.5 mm in diameter and 1 mm deep, which is followed by a recess hole inside the flat plate of 1 mm diameter. The depth of the recess hole is different, depending upon the location with respect to the trailing edge. The recess holes are used to hold a small metal tube of 0.5 mm and 1 mm internal and external diameter respectively, which will be connected to a plastic tube as part of a remote microphone system. As shown in Fig. 5.1,

these sensing holes are named individually and distributed in identical rectilinear grids for both of the straight and serrated sawtooth trailing edges. This configuration allows the wall pressure power spectral density (PSD) and streamwise, spanwise and oblique coherence functions to be compared directly between the straight and serrated sawtooth trailing edges.

A third test model, herein referred as the heater plate, is manufactured for a thermochromic liquid crystal flow visualization experiment. The experiment was carried out in non-isothermal conditions, where the flat plate test model was slightly heated up. A detailed description of the preparation of the heater plate is found in Section 3.2.1.2

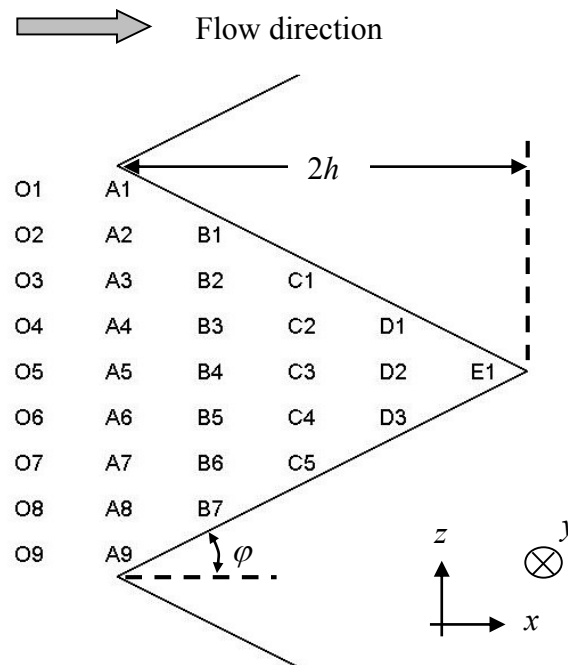


Figure 5.1 Distribution of the microphone sensing holes on the sawtooth trailing edge. Same arrangement of the microphone sensing holes also applies to the baseline, straight trailing edge. The coordinate system is indicated.

5.2 Noise Results

Figure 5.2 shows the far field noise measured over the flat plate fitted with a straight trailing edge as well as a serrated sawtooth trailing edge ($2h = 20$ mm, $\phi = 25^\circ$). A $\frac{1}{2}$ inch free field type, pre-polarized condenser microphone was placed 1 m above the trailing edge at mid span and at a polar angle of 90° . Across a fairly broad frequency range, the acoustic PSD measured at 25, 30 and 35 ms^{-1} demonstrate that the serrated sawtooth trailing edge consistently produces 0.5–1.0 dB lower noise levels when compared to the

noise spectra produced by the straight trailing edge. For clarity, the background noise (without the flat plate) for each velocity case is not shown in the figure, although it can be confirmed that they are all at least 3 dB lower than the noise level produced by the flat plate.

The Acoustic Camera ring-array is also used and positioned as illustrated in Fig. 5.2 in order to locate the noise source. Acoustic beamforming was carried out at a free jet velocity of 30 ms^{-1} . Noise reductions are dominant at the frequency range of $1 < f < 2.5 \text{ kHz}$ (also see Fig. 5.6a). This frequency range is therefore chosen as the interrogation range for the beamforming. The result demonstrates that the radiated noise at the frequency range where reduction occurs is originated from the trailing edge of the flat plate. Both the hardware setup and the ambient conditions are exactly the same between the experiments for the flat plate with straight trailing edge and the flat plate with serrated

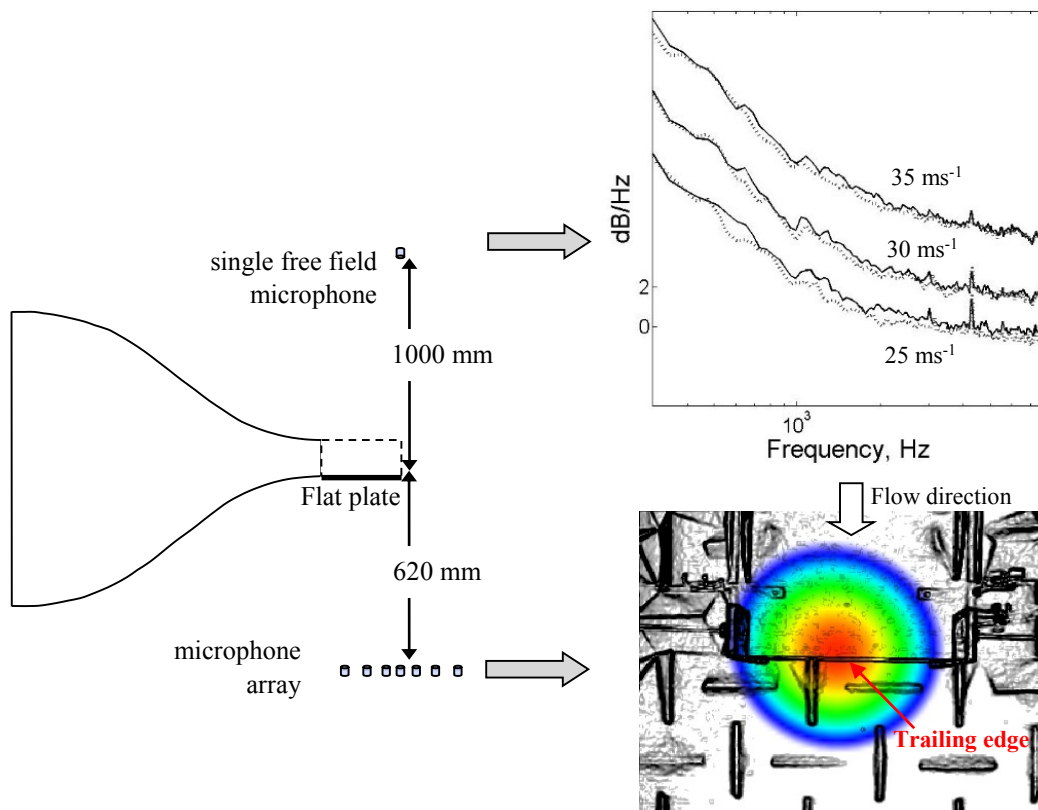


Figure 5.2 Experimental setup for the measurements of self-noise produced by flat plate fitted in turn with a straight trailing edge and a serrated trailing edges. Noise spectra produced by straight trailing edge (—) and serrated sawtooth trailing edge (···) at freestream velocities of 25, 30 and 35 ms⁻¹ are measured by the single free field microphone. The microphone array is used to locate the noise source.

sawtooth trailing edge. Geometrical modification of the trailing edge from straight to serration is therefore the main reason where noise reduction is observed in the results.

Some theories [Amiet (1976), Howe (1999)] assume a full Kutta condition at the trailing edge when formulating the expression for the far field noise. The current flat plate configuration means that flow is only present on one side of the surface. The radiated self-noise level will therefore be lower than when considering a flow on both sides of the surface, though the spectral shape is not expected to be significantly different. This explains the smaller amount of broadband noise reduction achieved by serrated sawtooth trailing edge in the current flat plate configuration compared to an airfoil, where a broadband noise reduction between 3 dB and 7 dB is observed, as also shown in Chapter 4 [Oerlemans (2009), Gruber (2011)].

5.3 Wall heat transfer on a serrated trailing edge

A good contrast in colour display by the liquid crystal is predominantly found in inhomogeneous fluid flows such as the transitional boundary layer or laminar separation. In the present study, the boundary layers for both, the straight trailing edge and serrated sawtooth trailing edge are already in a turbulent state. As a result, the variation of the turbulent heat transfer, which could potentially restrict the colour range over which the liquid crystals can effectively display temperature differences, is not expected to be significant. However, as it turns out, some interesting features are clearly displayed by the liquid crystals on the serrated sawtooth trailing edge.

The wall surface was only heated slightly and the characteristics of the turbulent boundary layer would not be modified by a considerable amount. Once heated, a long setting time is allowed to ensure that the wall temperature always reaches a saturated state across the whole plate surface. The sequence of experiments normally begins with the straight trailing edge first, where the add-on inserts were attached. After photos were taken, the add-on inserts are removed *in situ* in order to change the trailing edge into a serrated sawtooth type. It is important to note that during this short interval the room temperature and flow conditions do not change considerably. Therefore, a simple comparison with the surface temperature between the straight trailing edge and the serrated sawtooth trailing edge will be sufficient.

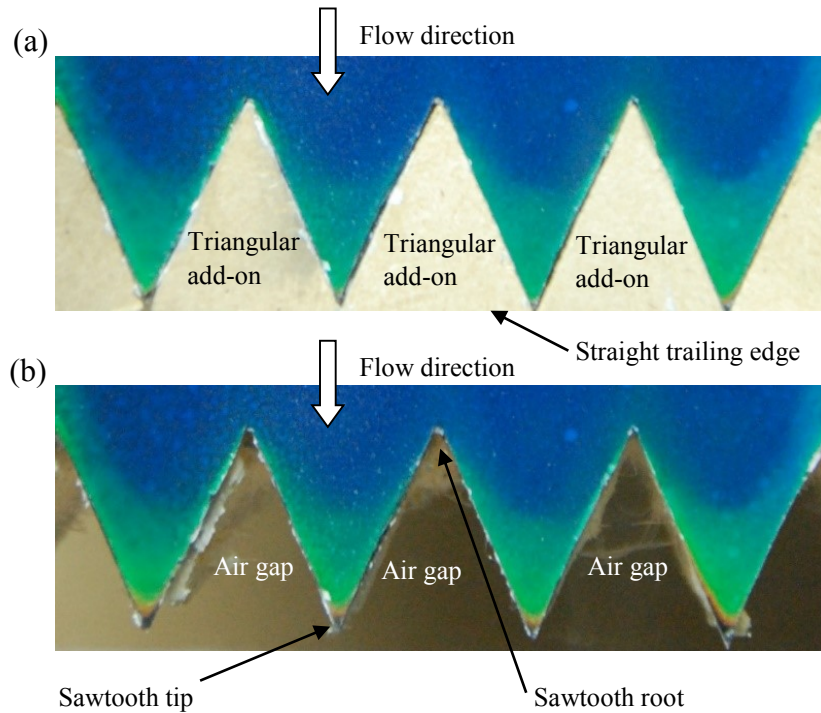


Figure 5.3 Raw thermochromic liquid crystal images for the (a). Straight trailing edge; and (b). Serrated sawtooth trailing edge, with $2h = 20$ mm and $\phi = 25^\circ$.

Fig.5.3 shows the raw liquid crystal images of the straight and serrated sawtooth trailing edges, which were taken under exactly the same flow conditions and room temperature as well as with the same printed circuit board body and amount of heating applied on it. After the whole surface temperature maps are processed in the cases of the straight and serrated sawtooth trailing edges, the temperature difference contour map $\Delta\theta(x, z) = \theta_{\text{serration}}(x, z) - \theta_{\text{straight}}(x, z)$, where θ is the wall temperature, can then be obtained. The result is shown in Fig. 5.4. Note that a negative $\Delta\theta$ value means that the serrated sawtooth has a lower temperature than the non-serrated, straight case at the same location. The opposite is true for the positive $\Delta\theta$. Since the non-isothermal condition in the current study is achieved by heating the test object in cold air, a lower surface temperature implies that the convective heat transfer rate is higher. Therefore, the lower temperatures on the sawtooth side edges and the sawtooth tips clearly indicate the presence of higher convective heat transfer rates.

It can be noted from the raw liquid crystal images in Fig.5.3 that the distribution of heat is not very uniform. The colour variation in the spanwise direction is not caused by the flow variables. It is mainly caused by some imperfections regarding the PCB design where relatively large gaps between successive V-shaped copper tracks exist at the sawtooth.

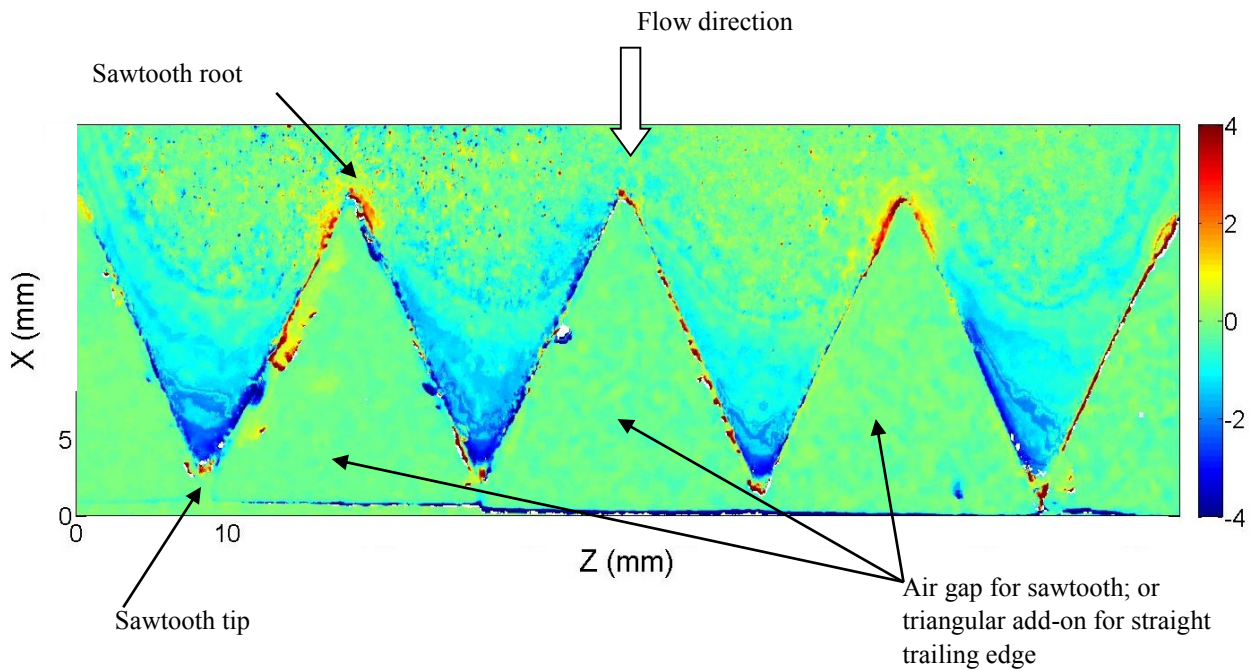


Figure 5.4 Surface contour map of $\Delta\theta$ ($^{\circ}\text{C}$) obtained by the liquid crystal technique. The geometrical parameters for the serrated sawtooth trailing edge is $2h = 20$ mm and $\phi = 25^{\circ}$.

This has no impact on the accuracy of the $\Delta\theta$ contour map in Fig. 5.4 because it is a relative quantity. To confirm that spanwise flow variable has no role in the liquid crystal colour play, a repeatability test is performed on another heater plate of the same overall dimension. The trailing edge of this heater plate, however, has a smaller serration angle of $\phi = 12.5^{\circ}$ while the root-to-tip distance is maintained at $2h = 20$ mm. The gap between each successive V-shaped copper track in this sharper sawtooth is much smaller. As a result, the heat can be distributed more evenly. The raw images of the liquid crystal for the straight and serrated sawtooth trailing edges, which both were subjected to the same flow conditions, room temperature and amount of heating to the PCB, are presented in Fig. 5.5. The liquid crystal images are more vivid and clearly support the findings that lower surface temperature (higher heat transfer) exists near the sawtooth side edges and sawtooth tips.

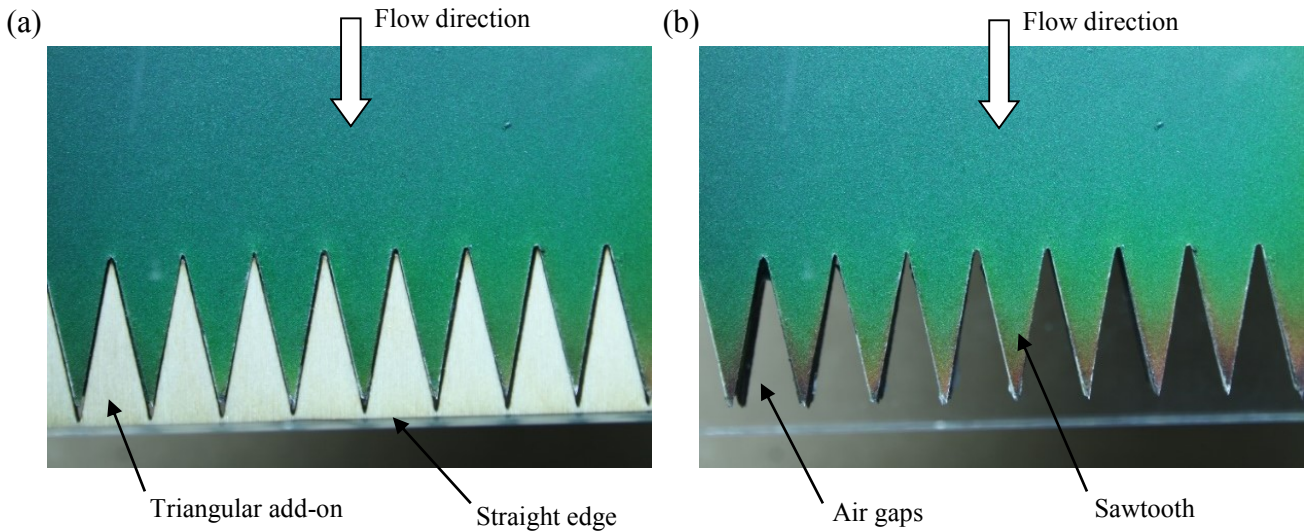


Figure 5.5 Raw thermochromic liquid crystal images for the (a). Straight trailing edge; and (b). Serrated sawtooth trailing edge, with $2h = 20$ mm and $\phi = 12.5^\circ$.

A uniform turbulent boundary layer should exist across the span of the straight trailing edge. Based on the liquid crystal results, higher heat transfer rates near the side edges and tips of the serrated sawtooth trailing edge are clearly demonstrated. This suggests that a convective regime, which is much stronger than a two-dimensional turbulent boundary layer, should exist for a serrated sawtooth trailing edge. Supported by further experimental evidence which will be discussed later, it is believed that the low temperature region near the sawtooth oblique side edge is caused by a convective, pressure-driven vortical structure. The much lower temperature near the sawtooth tip is probably caused by the amalgamation of the vortical structures on both sides.

5.4 Unsteady wall pressure on a serrated trailing edge

5.4.1 Power spectral density

A comparative study is also performed in this section, using the methodology described previously in Section 5.1, for the wall pressure *PSD* produced by the straight and serrated sawtooth trailing edges. As shown in Fig.5.1, the measurement points comprise 34 locations of 01–09, A1–A9, B1–B7, C1–C5, D1–D3 and E1 for both trailing edges. Note that the locations 01–09 are situated upstream of the sawtooth roots.

After all the wall pressure *PSD* are calculated, the following quantity can be obtained:

$$\Delta\eta(x, z, f) = 10 \log_{10} \left[\frac{\overline{P}'^2_{straight}(x, z, f)}{\overline{P}'^2_{sawtooth}(x, z, f)} \right], \quad (\text{eq. 5.1a})$$

where $\bar{P}'^2(x, z, f)$ is the mean square pressure at each measurement point of either the straight or the sawtooth serrated trailing edges. $\Delta\eta(x, z, f)$ thus represents the difference in wall pressure *PSD* level between the two trailing edges in the $x - z$ plane at a particular frequency. A negative $\Delta\eta$ value denotes that the wall pressure *PSD* for the serrated sawtooth is higher than the non-serrated, straight case at the same location. The opposite is true for the positive $\Delta\eta$ value. When the wall pressure *PSD* is integrated across the frequency range, an overall spectral energy level roughly equal to the root-mean-square value is obtained. Accordingly, another comparative quantity $\Delta\varepsilon(x, z)$ can be defined:

$$\Delta\varepsilon(x, z) = 10 \log_{10} \left[\frac{\int_{f \in J} \bar{P}'^2_{straight}(x, z, f) df}{\int_{f \in J} \bar{P}'^2_{sawtooth}(x, z, f) df} \right]. \quad (\text{eq. 5.1b})$$

Previously in Section 5.2, it has been shown that small level of noise reduction can be achieved by the serrated sawtooth trailing edge in a flat plate configuration. Figure 5.6a represents the difference in sound pressure level (ΔSPL) between a straight and a serrated sawtooth trailing edge at 30 ms^{-1} free jet velocity. The positive ΔSPL denotes noise reduction, and the opposite is true for the negative ΔSPL .

The frequency in Fig.5.6a is represented by the non-dimensional Strouhal number ($f\delta^*/U_\infty$), where δ^* is the boundary layer displacement thickness at a reference location C3 measured directly inside the aeroacoustic wind tunnel facility, and U_∞ is the local freestream velocity. The non-dimensionalisation of the frequency is to enable comparison with the wall pressure *PSD* in Fig. 5.6b, which was obtained in a separate wind tunnel. Similarly, the Strouhal number $f\delta^*/U_\infty$ is used to represent the frequency in Fig. 5.6b, where δ^* was also measured *in situ* at location C3. Note that the streamwise dimensions of the flat plates used for the aeroacoustic and flow tests, including their sawtooth geometries, are the same. The discrepancies of the measured U_∞ and δ^* between both tests are 1.3% and 9.6%, respectively. The use of Strouhal number could therefore minimize the margin of error when comparing the flow and acoustic results.

In Fig. 5.6a, the ΔSPL fluctuates around the zero level at $f\delta^*/U_\infty > 0.126$. However, at $0.027 < f\delta^*/U_\infty < 0.126$ (indicated by the shaded region), a clearer pattern of noise reduction can be identified. Contour maps of $\Delta\eta$ at $f\delta^*/U_\infty = 0.023, 0.041, 0.049, 0.061, 0.082$ and 0.183 are shown in Fig. 5.6b. At $f\delta^*/U_\infty = 0.023$, where noise reduction by the serrated sawtooth

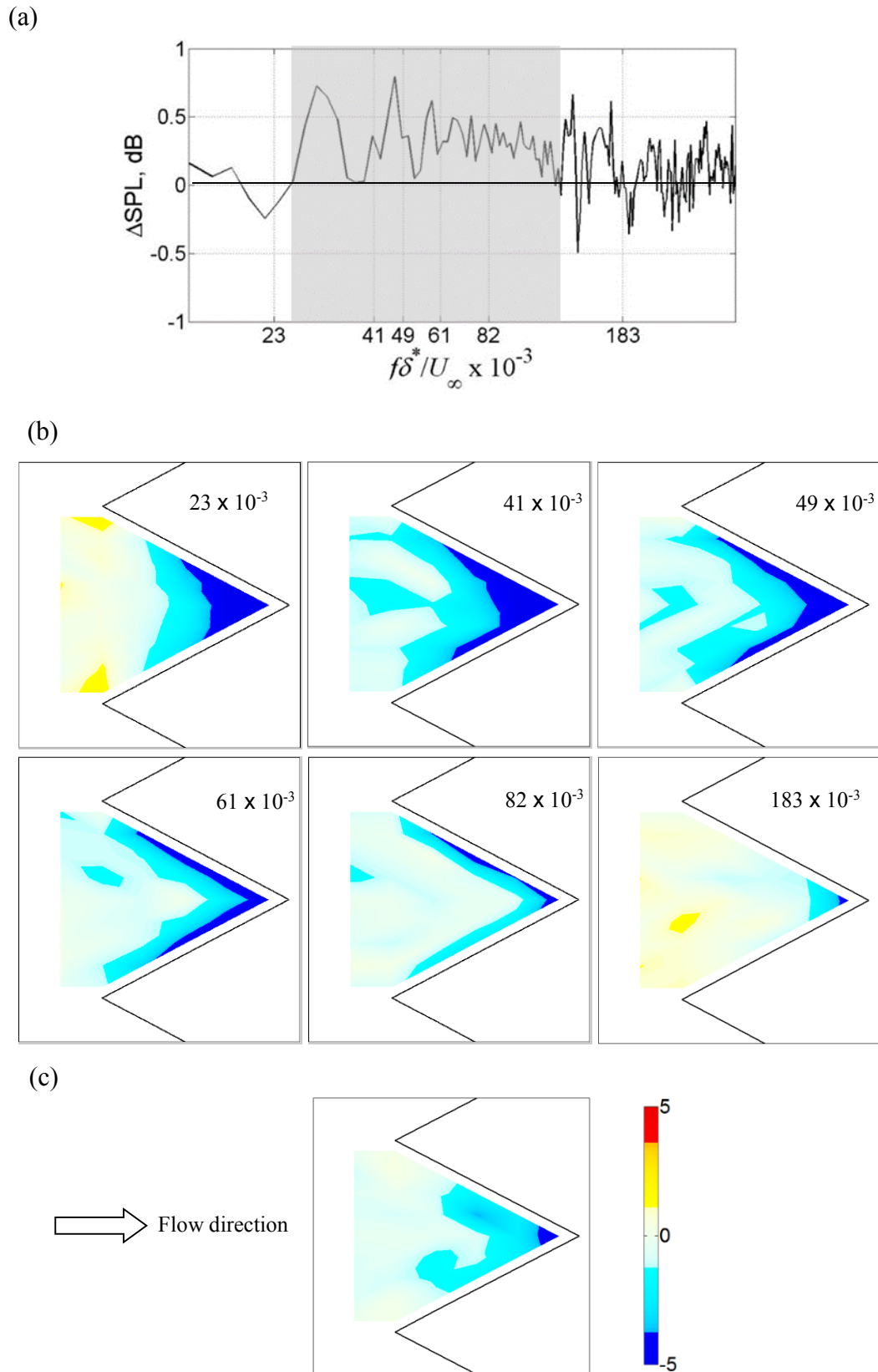


Figure 5.6 a). ΔSPL (dB); b). Contour maps of $\Delta \eta$ (dB) at different Strouhal numbers, and c). Contour map of $\Delta \varepsilon$ (dB) integrated over $J = (97, 21950)$ Hz. Note that all the figures in a), b) and c) correspond to the same free jet velocity of 30 ms^{-1} . Same colour-scale applies to the contour maps in b) and c).

trailing edge is yet to establish, the dominant *PSD* level for the wall pressure is concentrated around the sawtooth tip only. At $0.041 < f\delta^*/U_\infty < 0.082$, where noise reduction is observed, the dominant *PSD* level for the wall pressure seems to diffuse from the sawtooth tip towards the upstream direction along the sawtooth side edges. At $f\delta^*/U_\infty = 0.183$, where noise reduction ceases to exist, the wall pressure *PSD* level for the serrated sawtooth becomes almost similar to the non-serrated, straight trailing edge. The above comparison between the acoustic spectra and flow spectra suggests that the reduction in noise radiation should be accompanied by the co-existence of a high *PSD* level in wall pressure at the sawtooth side edges and the sawtooth tip. When the wall fluctuating pressure is integrated across $J = (97, 21950)$ Hz in equation 5.1b), the resulting $\Delta\varepsilon$ contour in Fig. 5.6c also produces high spectral energy levels at location close to the sawtooth side edges and the sawtooth tip. The wall pressure spectral energy distribution thus correlates very well with the liquid crystal results ($\Delta\theta$) presented in Section 5.3.

The possible effect of acoustical back-scattering is noted. In this case the total wall pressure measured by microphones near the sawtooth side edge and the sawtooth tip could include both the incidence pressure and the scattered pressure. Moreover, the total wall pressure measured near the sawtooth tip could be amplified further by the multiple back-scattering of acoustic waves from the two side edges. Because the effect of acoustic back-scattering is frequency-dependent with the largest decay rate occurring at high frequencies, the integration of the measured wall pressure across a whole range of frequencies in equation 5.1 should help to reduce this effect. In addition, the boundary layer incidence pressure is understood to be considerably larger in magnitude than the scattered pressure [Brooks and Hodgson (1981)]. Most importantly, the variations of $\Delta\varepsilon$ in Fig. 5.6c are found to be highly correlated with the $\Delta\theta$ contour map in Fig. 5.4. It is important to note that the $\Delta\theta$ contour would not be affected by the acoustical back-scattering at all. Therefore, the hypothesis of strong turbulence/vortical fluctuations near the sawtooth side edge and the sawtooth tip is still valid. This issue will be further addressed in Section 5.5 when the cross spectral distribution between the boundary layer velocity fluctuations and the unsteady wall pressure, as well as the characteristics of momentum/turbulence transports in time domains, are analysed.

5.4.2 Streamwise and spanwise coherence and phase functions

The results in the previous section were obtained by a single microphone. In order to investigate the coherence γ^2 and phase ϕ of the turbulent eddies, a pair of microphones in various combinations of Δx (streamwise spacing) and Δz (spanwise spacing) was used to measure the unsteady wall pressures simultaneously for both the straight and serrated sawtooth trailing edges. Due to the large amount of data obtained, only selective results are presented here. Fig 5.7 shows the phase spectra for the streamwise arrangement of microphones (i.e. $\Delta x > 0$, $\Delta z = 0$). Note that the pairing of the microphones is identified using the notations from Fig 5.1. For example, if one microphone is located at the tip and another one at 4 mm behind it, then this pairing will be represented by D2–E1. The same principle applies throughout this chapter.

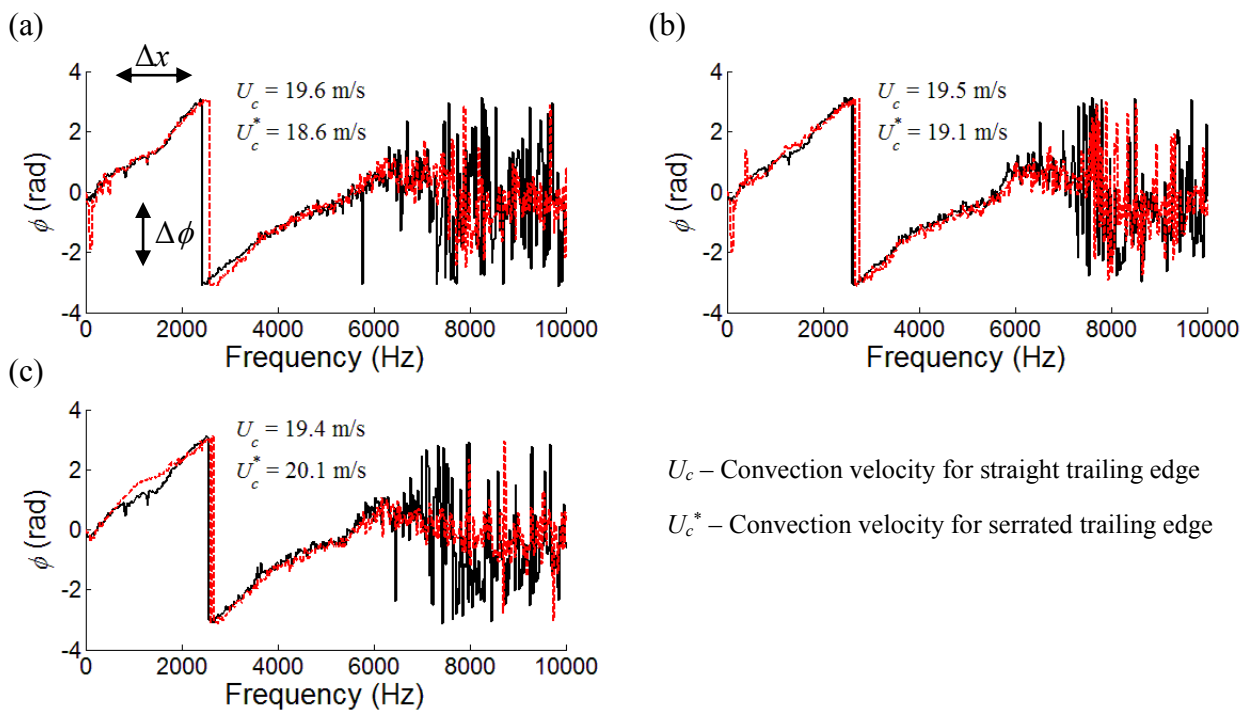


Figure 5.7 Streamwise phase spectra ϕ (rad) for the straight (black) and serrated sawtooth (red) trailing edges of the following microphone pairs: a). B4–C3; b). B2–C1; and c). D2–E1.

The phase spectra can be further implemented for the calculation of the convection velocity U_c by:

$$U_c = \frac{2\pi f \Delta x}{d\phi} . \quad (\text{eq. 5.2})$$

The calculated convection velocities are included in Fig. 5.7. It is generally observed that the turbulent eddies propagate at a similar speed in the streamwise direction regardless of the type of trailing edges used. This observation also applies to the case when the microphone pair is close to the sawtooth side edge (e.g. B2–C1) and

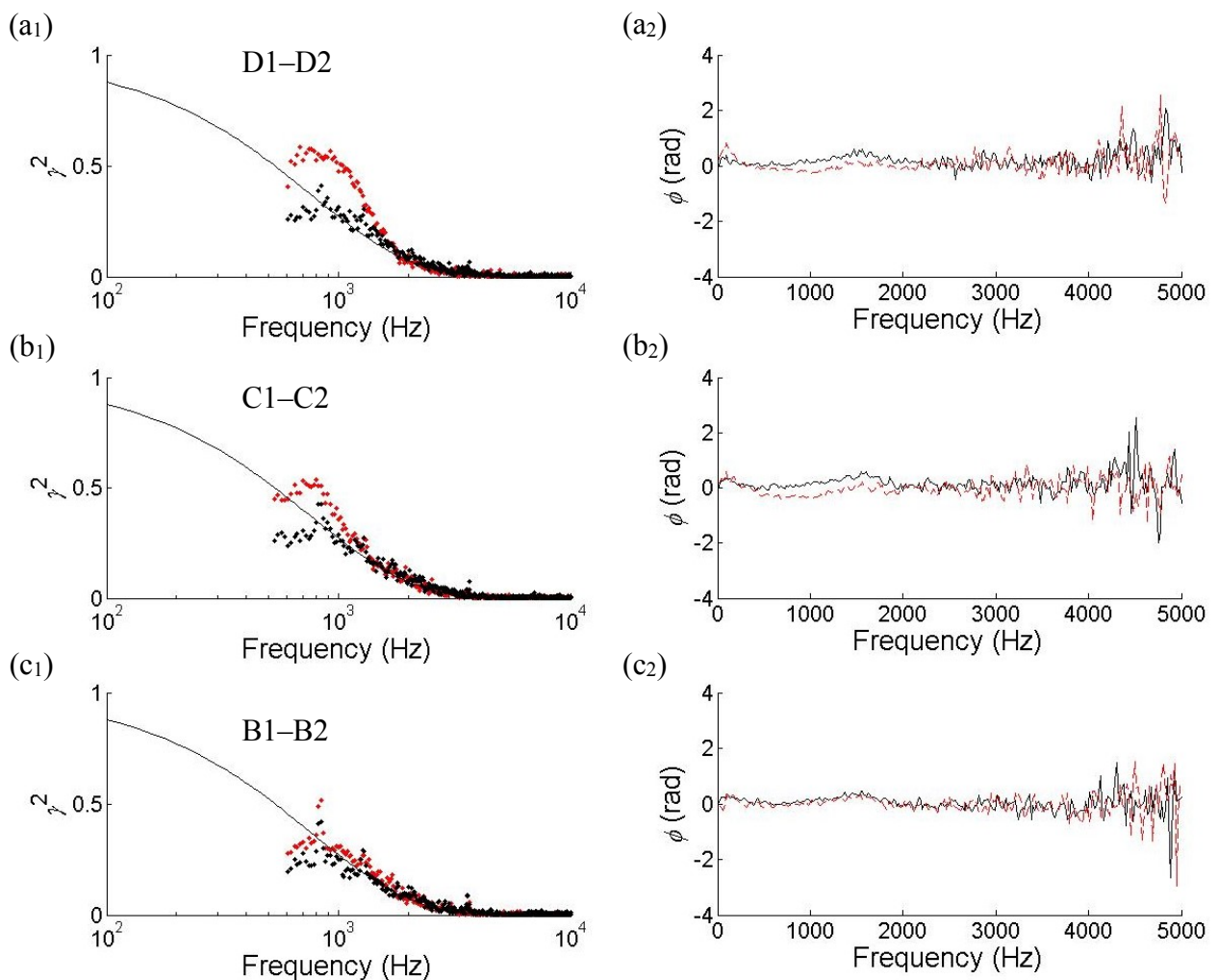


Figure 5.8 Spanwise coherence γ^2 (\bullet straight trailing edge, \bullet serrated trailing edge) and the phase spectra ϕ (— straight trailing edge, - - - serrated trailing edge). The solid lines in the coherence γ^2 plots are calculated from the empirical model by Brooks and Hodgson (1981).

the sawtooth tip (e.g. D2–E1) where stronger turbulence activities have been identified previously for a serrated sawtooth trailing edge (i.e. note that the abrupt line occurs due to the phase presented in rad).

Some spanwise coherence spectra (i.e. $\Delta x = 0$, $\Delta z > 0$) are presented in Fig. 5.8 for the following cases: D1–D2, C1–C2 and B1–B2. The corresponding phase spectra are also shown. The measured coherences in the spanwise direction are compared with an empirical model [Brooks and Hodgson (1981)]:

$$\gamma^2(f) = \exp\left(-\frac{2\pi f}{bU_c} \Delta z\right), \quad (\text{eq. 5.3})$$

where b is the Corcos constant and the value is adjusted to best-fit the measured spanwise coherence spectra. In the current study, the adjustment is made against the measured coherence function for the straight trailing edge and it was found that a value of 0.5 fits well for all the straight trailing edge cases. Some interesting features can be observed for the serrated sawtooth trailing edge. The measured spanwise coherences at the region near the sawtooth tip (i.e. D1–D2) are higher and do not fit well with the empirical curve until about 2 kHz. This trend is also repeated at the upstream location C1–C2, although the difference in coherence spectra level between the straight and serrated sawtooth trailing edges becomes smaller. At the even further upstream location B1–B2, there is no longer any discernible difference between the straight and serrated sawtooth trailing edges. The above phenomena are also reflected in the corresponding phase spectra. The microphone pairs D1–D2, C1–C2 and B1–B2 are always in phase for the straight trailing edge, which indicates that there is no turbulence convection velocity in the spanwise direction. However, a difference is observed in the cases of B1–B2, the microphone pairs of D1–D2 and C1–C2 for the serrated sawtooth trailing edge as they are not in phase at frequencies below 2 kHz. Based on the earlier observation of stronger turbulence activities near the sawtooth side edges, and the spanwise coherences and phase functions presented in this section, there is a strong suggestion that the significant turbulence activities are associated with a vortical flow, which probably originates at a location close to C1 at the sawtooth surface.

Measurements are also performed for microphone pairs with both streamwise and spanwise separations (i.e. $\Delta x > 0$, $\Delta z > 0$). The associated phase spectra are also used to determine the turbulence convection speeds. The results will be discussed in Section 5.6.

5.5 Turbulent boundary layer developed on a serrated sawtooth trailing edge

The previous sections concern the steady and unsteady *near wall* properties of the straight and serrated sawtooth trailing edges. To provide a better understanding of the mechanisms involved, some statistical turbulence quantities in the boundary layer are also studied. Boundary layer measurements took place at locations C1, C3 and E1. Note that the wall pressure data is also acquired simultaneously with the cross wire during each measurement. The wall pressure data will be used for the velocity–pressure cross spectral analysis in Section 5.5.1, and will also act as a reference signal for the boundary layer velocity conditional-averaging in Section 5.5.2.

5.5.1 Time-averaged turbulence quantities

Boundary layer profiles of Reynolds shear stress $-\overline{u'v'}/U_\infty^2$ are shown in Fig. 5.9. As shown in Fig. 5.1, C3 is located at $x = h$ from the trailing edge (the total length of the sawtooth is $2h$) and in the plane of symmetry of the sawtooth. At this location there is no noticeable difference in the Reynolds shear stress between the straight and serrated sawtooth trailing edges (Fig. 5.9a). This result corresponds well with the liquid crystal techniques and unsteady wall pressure spectral contour maps. These measurements demonstrate that the area in the vicinity of C3 is isolated from the side edge vortical structures. C1 is also located at $x = h$ from the trailing edge, but near the side edge of the

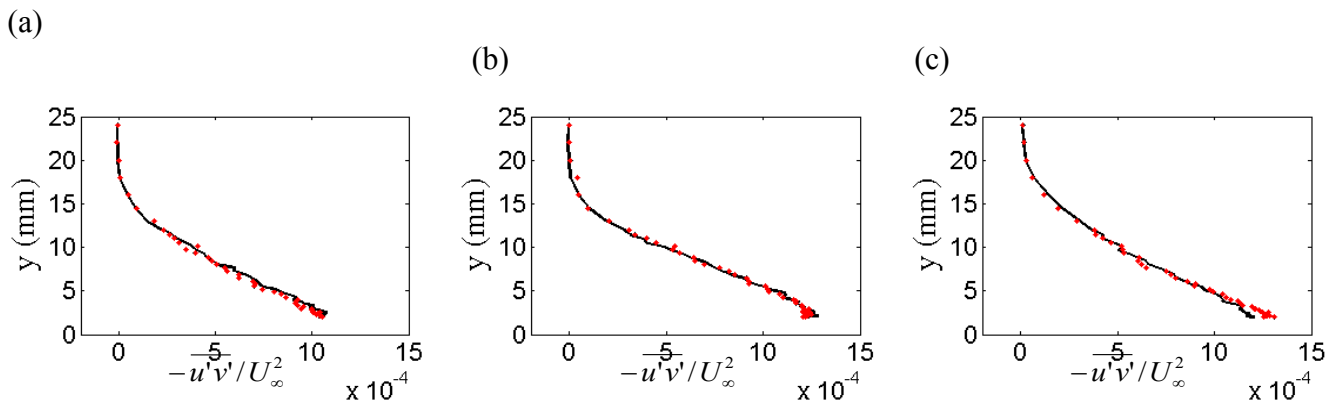


Figure 5.9 Time-averaged Reynolds shear stresses $-\overline{u'v'}/U_\infty^2$ boundary layer profiles measured at locations (a) C3; (b) C1; and (c) E1 for both of the straight (—) trailing edge and serrated sawtooth (•) trailing edge.

sawtooth. Based on a qualitative assessment of the surface temperature and the unsteady wall pressure spectral contour maps, location C1 is just about to submerge into the side edge vortical structures. Although the time-averaged Reynolds shear stress profiles between the straight trailing edge and serrated sawtooth trailing edge are similar (Fig. 5.9b), the dynamic momentum/turbulence transports at C1 in the case of the serration sawtooth trailing edge is somehow different from the straight trailing edge. This will be discussed further in the next section.

E1 is situated near the sawtooth tip. The local turbulent boundary layer at this location is expected to interact strongly with the oblique vortical structures. This is manifested in Fig. 5.9c where a slightly higher (up to 8% difference) turbulence shear stress level is observed at the near wall region of the serrated sawtooth trailing edge. The spectral level of the velocity fluctuating components $\Phi_{u'}$ and $\Phi_{v'}$ are also examined and the results are shown in Fig. 5.10. For the serrated trailing edge at location E1, both of the $\Phi_{u'}$ and $\Phi_{v'}$ in Fig. 5.10c exhibit spectral humps with a central frequency occurring at a Strouhal number ($f\delta^*/U_\infty$) of about 0.045 at $y/\delta^* \approx 1.7$ (Coincidentally, the same Strouhal number also corresponds to the maximum level of noise reduction in Fig. 5.6a). The existence of velocity spectral humps in the boundary layer provides further evidence that vortical structures can be produced by a serrated sawtooth trailing edge, but not by a straight trailing edge. At locations C3 and C1, as shown in Fig. 5.10a and Fig. 5.10b respectively, the $\Phi_{u'}$ and $\Phi_{v'}$ remain similar between the straight and serrated sawtooth trailing edges, where no velocity spectral hump is found.

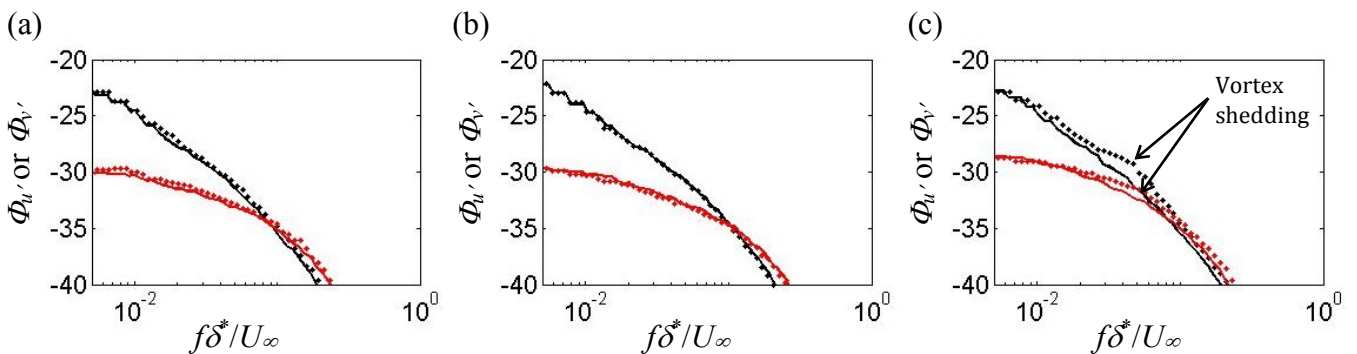


Figure 5.10 Comparison of the fluctuating velocity spectral densities of $\Phi_{u'}$ and $\Phi_{v'}$ at $y/\delta^* \approx 1.7$ for locations (a). C3; (b). C1; and (c). E1, between the straight trailing edge and sawtooth trailing edge. Explanation of symbols: $\Phi_{u'}$ (—straight trailing edge, • sawtooth trailing edge); $\Phi_{v'}$ (—straight trailing edge, • sawtooth trailing edge).

Further analysis on the cross spectra is attempted to establish a relationship between the product of the two-component velocity fluctuations ($u'v'$) and the surface pressure fluctuation p' . The cross spectra provide information about the flow features responsible for the wall pressure generation. Fig 5.11 shows the cross spectra $\Phi_{(u'v'),p'}$ near the tip of the sawtooth (E1). Note that the level is in decibel. For the serrated sawtooth trailing edge in Fig. 5.11b, the level of $\Phi_{(u'v'),p'}$ is higher than the straight edge counterpart (Fig. 5.11a) especially at low frequencies. A new quantity $\Delta\Phi = [\Phi_{(u'v'),p'}(\text{straight}) - \Phi_{(u'v'),p'}(\text{sawtooth})]$ is also introduced. A negative $\Delta\Phi$ therefore implies that the level of contribution ($u'v'$) in the boundary layer to the wall pressure generation by a serrated sawtooth trailing edge is greater than for the straight trailing edge, and vice versa. The contour map of $\Delta\Phi$ in Fig. 5.11c relates to the velocity–wall pressure cross spectra. In the figure, a distinct division line at a Strouhal number of about 0.05 can be observed. This value is similar to the Strouhal number pertaining to the spectral hump peaks in Fig. 5.10c which are determined by the fluctuating velocity spectral in the boundary layer. Therefore it is clear that below a Strouhal number of 0.05, the ($u'v'$) fluctuating term across the boundary layer contributes significantly to the wall pressure generation.

In order to further study the net cross spectral level, another quantity $\Delta\zeta$, which is related to $\Delta\Phi$, is introduced:

$$\Delta\zeta(x, y, z) = 10 \log_{10} \left[\frac{\int (u'v' \cdot \bar{P}'^2)_{\text{straight}}(x, y, z, f) df}{\int (u'v' \cdot \bar{P}'^2)_{\text{sawtooth}}(x, y, z, f) df} \right]. \quad (\text{eq. 5.4})$$

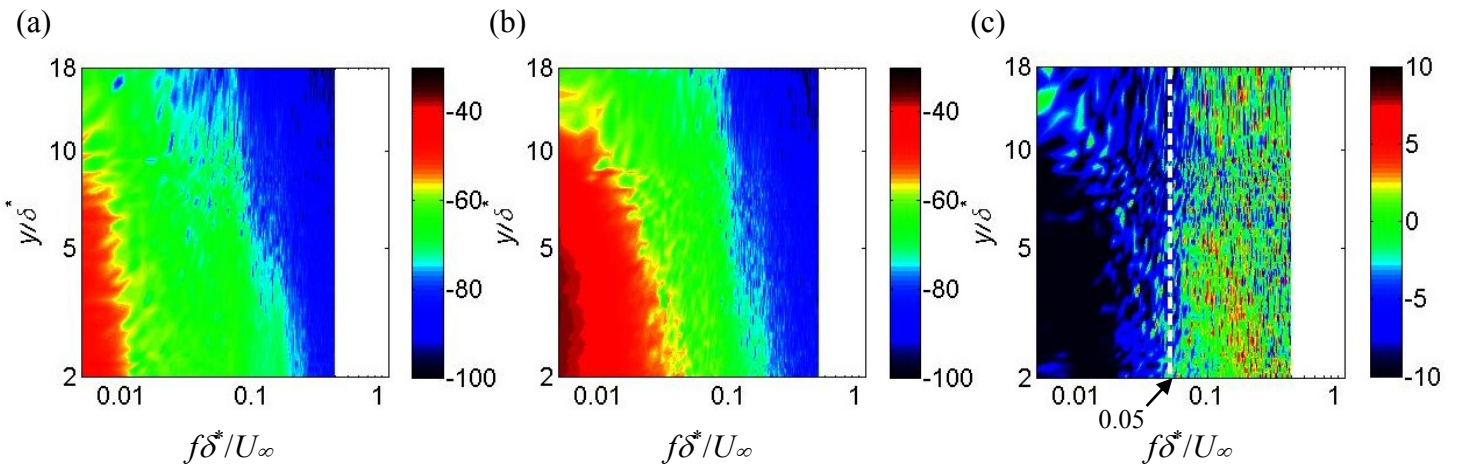


Figure 5.11 Comparison of velocity–wall pressure cross spectral densities at location E1 for (a). straight trailing edge ($\Phi_{o(u'v'),p'}$); (b). serrated sawtooth trailing edge ($\Phi^*(u'v'),p'$); and (c). $\Delta\Phi = [\Phi_{o(u'v'),p'} - \Phi^*(u'v'),p']$.

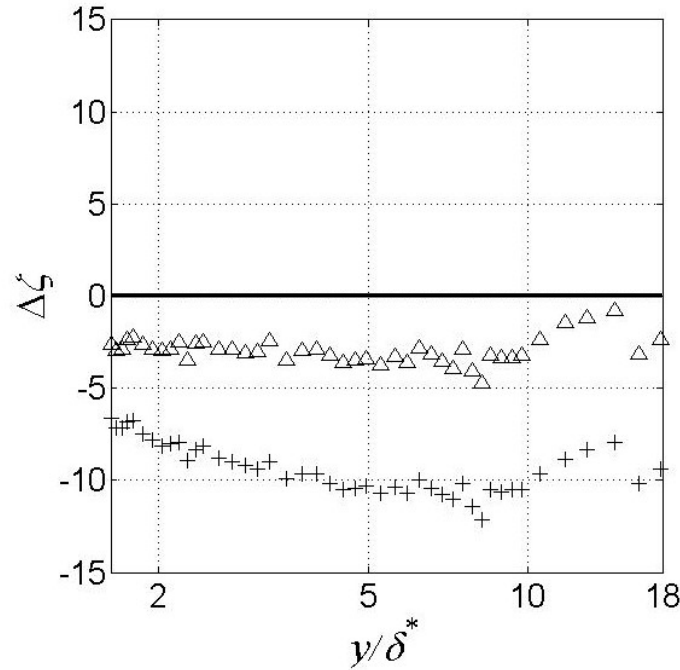


Figure 5.12 Distribution of $\Delta\zeta$ across the boundary layer at location E1, which represents cross spectra between the $(u'v')$ and the absolute pressure fluctuations p' (+), or the normalized pressure fluctuations p'/p_{rms} (Δ).

As shown in Fig. 5.12, the considerable deficit of about -10 dB in $\Delta\zeta$ indicates that a close causal relationship exists between the boundary layer turbulence and the wall pressure fluctuation near the sawtooth tip.

It should be noted that the wall pressure spectrum level $\Phi_{p'}$ near the sawtooth tip for a serrated sawtooth trailing edge is substantially larger than for the straight trailing edge. Hence, there is a possibility that the results presented in Fig. 5.11b might have been biased towards producing a larger level of $\Phi_{(u'v'),p'}$ for the serrated sawtooth trailing edge. To investigate this issue further, the wall pressure raw data is normalized with the root-mean-square pressure, P_{rms} , and then a “normalized” power spectral density (or cross power spectral density) can be calculated. Because a clear dividing line for the Strouhal number has been demonstrated earlier in the $\Delta\Phi$ contour, this analysis will only focus on Strouhal numbers < 0.05 . The power spectral densities of the normalized wall pressure $\Phi_{(p'/P_{rms})}$ for both the straight and serrated sawtooth trailing edges are plotted in Fig. 5.13a. The figure shows that the two cases collapse well. The cross spectral density function between the product of the two-component velocity fluctuations $(u'v')$ within a boundary layer and the now normalized wall pressure is denoted by $\Phi_{(u'v').(p'/P_{rms})}$. Subsequently, $\Phi_{(u'v').(p'/P_{rms})}$ can be calculated for both the straight and serrated sawtooth trailing edges, before a new $\Delta\Phi$ is obtained. As shown in Fig. 5.13b, the new $\Delta\Phi$ contour

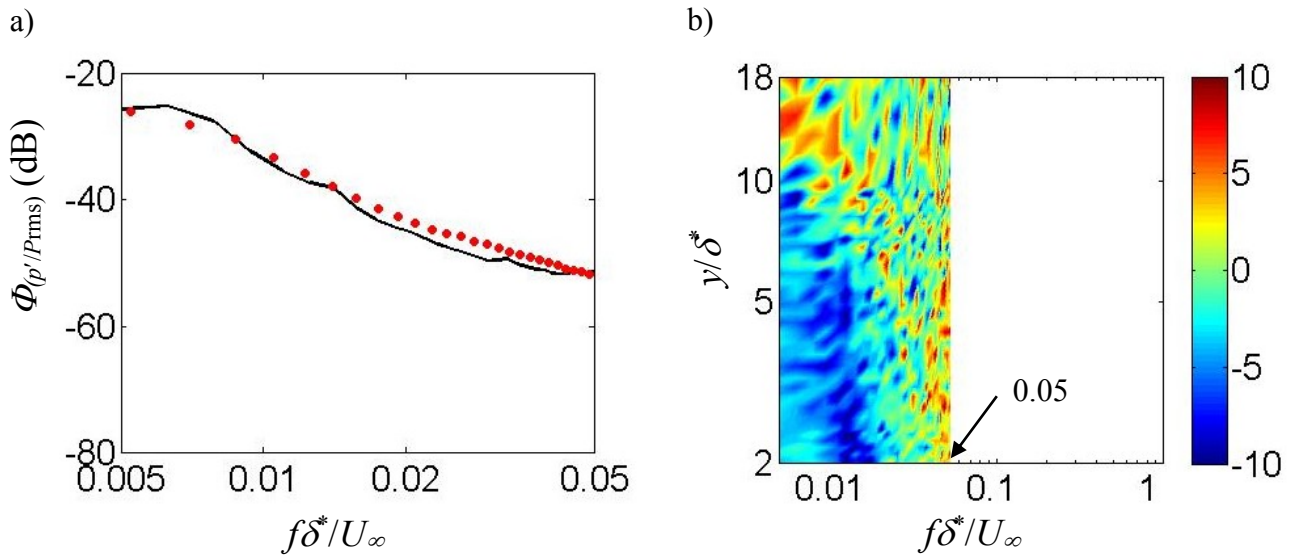


Figure 5.13 a). Power spectral densities at location E1 for the straight trailing edge $\Phi_{o(p'/Prms)}$ (—) and serrated sawtooth trailing edge $\Phi^*(p'/Prms)$ (\bullet); (b). $\Delta\Phi = [\Phi_{o(u'v')}(p'/Prms) - \Phi^*(u'v')(p'/Prms)]$.

still demonstrates a higher level of $\Phi_{(u'v')}(p'/Prms)$ for a serrated sawtooth trailing edge. The corresponding $\Delta\zeta$ has an average level of -3.5 dB, which is shown in Fig. 5.12. These results therefore support the earlier notion that the high level of wall pressure fluctuation is mainly contributed by the dynamics of the boundary layer instead of the acoustic back scattering.

5.5.2 Conditional-averaged velocity perturbations, rms velocity fluctuations and Reynolds shear stresses

The basis of the conditional-averaging technique is similar to Sagrado (2007) and Daoud (2004). In this method the positive wall pressure peaks and negative wall pressure troughs in the time domain can be used as references for the ensemble averaging of the mean and fluctuating velocity signals. To illustrate the technique, the wall pressure signal in the time domain is plotted in Fig. 5.14. First, arbitrarily thresholds of $\pm 1.5P_{rms}$ were selected to identify the blocks of time relative to the dominant positive and negative wall pressure oscillations, where P'_{rms} is the rms value of a wall pressure data set. The pressure peak (or trough) at each identified time block is assigned to $\tau = 0$. Therefore $\tau < 0$ and $\tau > 0$ represent times in advance and time delay, respectively, from the occurrence of the pressure peak/trough. Once the times at which the pressure peaks/troughs have been

identified for the entire pressure signals, the velocity signals can be ensemble-averaged accordingly. Approximately 1400 ensembles were available to calculate the conditional-averaged velocities at each measurement point. Using this simple method, some coherent structures can be identified from the turbulent boundary layer. It is noted that, as far as the turbulent boundary layer is concerned, the origin of the unsteady wall pressure signals could mainly be inside the buffer layer [Schewe (1983)]. Therefore, the interpretations of the conditional averaged-velocity at large y locations should be treated with some cautions. Another point to consider is that the slight phase shift between the wall pressure and the X-wire signals will not affect the current ensemble analysis.

The identification of the coherent structures is taken on the basis of triple decomposition of the velocity field [Reynolds and Hussain (1972), Cantwell and Coles (1983)]:

$$U_i(x, y, z, t) = U_{m,i}(x, y, z) + u_{c,i}(x, y, z, t) + u_{r,i}(x, y, z, t). \quad (\text{eq. 5.5})$$

The index i represents the velocity components in the x and y directions. U is the instantaneous velocity, U_m is the mean velocity, u_c is the coherent velocity (i.e. the velocity which can be correlated across the structure) and U_r the incoherent (random) velocity fluctuations. The coherent velocity u_c can be calculated by taking the difference between the ensemble-averaged total velocity and time-averaged mean velocity, $u_c = \langle U \rangle - U_m$. Note that the angular brackets represent ensemble-averaging, which are based on the

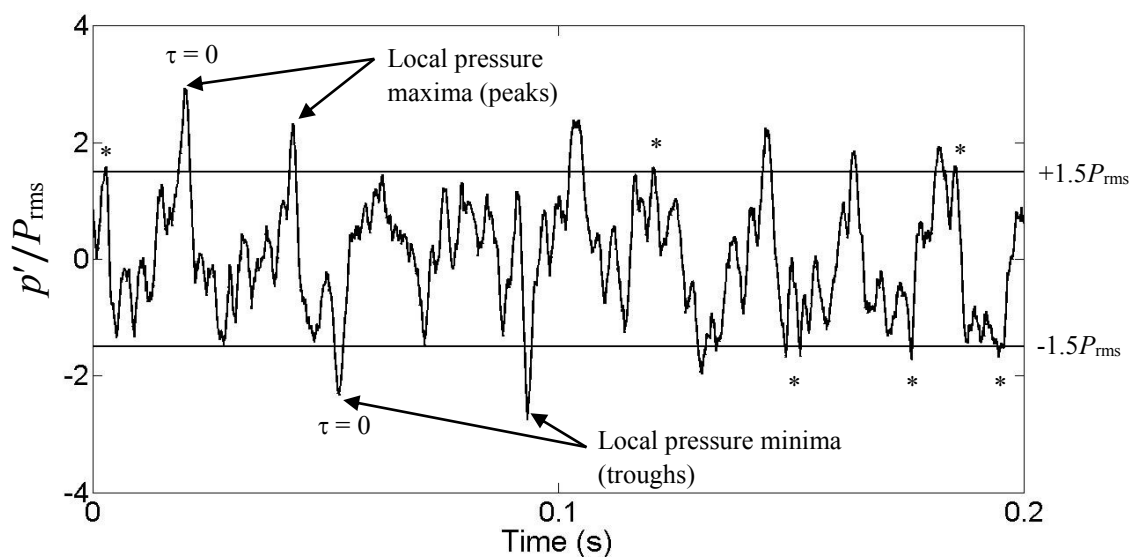


Figure 5.14 Surface pressure signals and the two threshold lines ($\pm 1.5P_{rms}$) selected to calculate the conditionally-averaged velocity associated with the pressure peaks and troughs. The minor pressure peaks and troughs, which are marked as * in the figure, are not included for the ensemble.

positive wall pressure $\langle +P \rangle$ and negative wall pressure $\langle -P \rangle$ that exceed the threshold values of $\pm 1.5P_{\text{rms}}$. The velocity perturbation, which measures the momentum excess or deficit caused by a coherent structure, is obtained by scaling the coherent velocity with the local freestream velocity U_∞ . The temporal variations of the velocity perturbations, \tilde{u} and \tilde{v} , are therefore:

$$\tilde{u}(x, y, z, t) = \frac{\langle U(x, y, z, t) \rangle - U_m(x, y, z)}{U_\infty(x, z)}, \quad (\text{eq. 5.6a})$$

$$\tilde{v}(x, y, z, t) = \frac{\langle V(x, y, z, t) \rangle - V_m(x, y, z)}{U_\infty(x, z)}. \quad (\text{eq. 5.6b})$$

Similarly, if the temporal variations of the rms fluctuations of U and V at each measurement point are represented by u_{rms} and v_{rms} respectively, they can be calculated as:

$$u_{\text{rms}}(x, y, z, t) = \sqrt{\frac{\sum_{i=1}^N [U(x, y, z, t) - \langle U(x, y, z, t) \rangle]^2}{N}}, \quad (\text{eq. 5.7a})$$

$$v_{\text{rms}}(x, y, z, t) = \sqrt{\frac{\sum_{i=1}^N [V(x, y, z, t) - \langle V(x, y, z, t) \rangle]^2}{N}}, \quad (\text{eq. 5.7b})$$

where N is the number of realizations. Finally, the temporal variations of the Reynolds shear stress $\langle u'v' \rangle$ can be calculated from the following equation:

$$\langle u'v' \rangle(x, y, z, t) = \sum_{i=1}^N \frac{[U(x, y, z, t) - \langle U(x, y, z, t) \rangle][V(x, y, z, t) - \langle V(x, y, z, t) \rangle]}{N}. \quad (\text{eq. 5.8})$$

5.5.3 Coherent-like structure analysis

5.5.3.1 General characteristics of the coherent-like structures on a two-dimensional turbulent boundary layer

It would be useful to discuss the general characteristics of a canonical turbulent boundary layer first. For this reason, the results presented in this sub-section are only related to the unserrated, straight trailing edge. Contour maps of \tilde{U} and \tilde{V} for $\langle +P \rangle$ and $\langle -P \rangle$ pertaining to location C3 are shown in Fig. 5.15. Note that the axes in the figures are scaled with the local boundary layer displacement thickness (δ^*) and freestream velocity (U_∞).

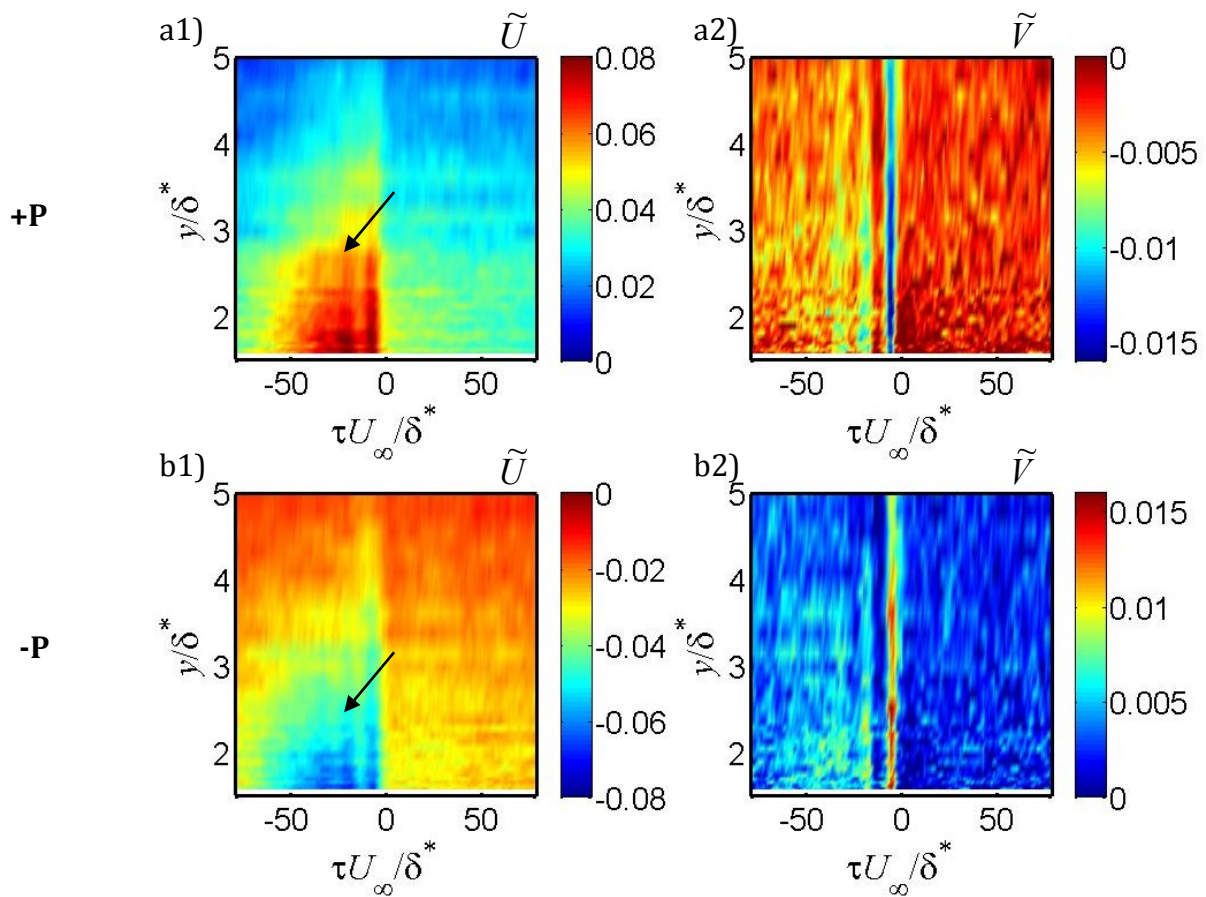


Figure 5.15 Contours of \tilde{U} and \tilde{V} for: (a1, a2), $\langle +P \rangle$ surface pressure; (b1, b2), $\langle -P \rangle$ surface pressure. The measurement location is at C3 for the straight trailing edge.

By examining the \tilde{U} contours for $\langle +P \rangle$ in Fig. 5.15(a1), \tilde{U} is mainly positive at $\tau U_\infty / \delta^* \leq 0$ (prior the occurrence of the pressure peak) and a coherent structure is discernible. However, the \tilde{V} velocity perturbations near the pressure peak in Fig. 5.15(a2) are found to be mostly negative in sign, which contradict their \tilde{U} perturbation counterparts.

The high momentum excess at $\tau U_\infty / \delta^* < 0$ for the \tilde{U} perturbation contours, i.e. ($\tilde{U} > 0$), could be analogous to an instantaneous fluctuating velocity for which $u' > 0$ (this correlation will be examined later). The corresponding \tilde{V} perturbations of $\tilde{V} < 0$ should then denote negative instantaneous fluctuating velocity $v' < 0$. This combination therefore suggests that a Q4-quadrant event is dominant for the case of $\langle +P \rangle$. Physically, a high-speed flow is sweeping towards the near wall region (or to the back of hairpin vortices) following a bursting event which is associated with the organized structures in a turbulent boundary layer [Kim et al (1971), Head and Badyopadhyay (1981), Panton (2001)].

As shown in Fig. 5.15(b₁), a coherent structure is also discernible for the $\langle -P \rangle$ case although it is now characterized by negative values of \tilde{u} at $\tau U_\infty / \delta^* \leq 0$ (prior the occurrence of the pressure trough). The \tilde{V} velocity perturbations in Fig. 5.15(b₂) are mostly positive in sign against their \tilde{U} perturbation counterparts. Similarly, the combination of ($\tilde{U} < 0, u' < 0$) and ($\tilde{V} > 0, v' > 0$) suggests the presence of a Q2-quadrant event. Physically, low-momentum fluid is ejected between the counter rotating legs of the hairpin vortices. The lifted low-momentum fluids, which are long and persistent in the higher velocity buffer layer, will eventually oscillate and break up. This cyclic event is commonly recognized as the main mechanisms for the generation of turbulent energy [Kim et al (1971), Head and Badyopadhyay (1981), Panton (2001)].

In Reynolds decomposition the instantaneous velocity fluctuation u' is the difference between the instantaneous velocity U and time-mean velocity U_m . The ensemble-average of the velocity fluctuation, which will produce non-zero values, is therefore related to the coherent velocity, i.e. $\langle u' \rangle = \langle U - U_m \rangle = u_c$. This relationship allows the ensemble-averaged velocity perturbations to be used to describe the quadrant events of a turbulent boundary layer as in the previous paragraphs. To illustrate this, plots of instantaneous u' and v' distribution at $y/\delta^* = 1.4, 3.2$ and 5.7 for the $\langle +P \rangle$ and $\langle -P \rangle$ cases are shown in Fig. 5.16. The figure shows the contribution to the Reynolds shear stress from each quadrant as a function of y/δ^* . There are approximately 1400 data points (representing all ensembles) in each plot, which displays a collection of u' and v' data points that correspond to $\tau U_\infty / \delta^*$ occurring at either the pressure peaks (for the $\langle +P \rangle$ case) or pressure troughs (for the $\langle -P \rangle$ case). Essentially, the unsteady wall pressure signals have

been used to identify the quadrant events in the total turbulence production. In the relatively near wall region at $y/\delta^* = 1.4$ and 3.2 , as shown in Fig. 5.16(a₁) and Fig. 5.16(a₂) respectively, most of the u' and v' data points for the pressure peaks can be found in the Q4–quadrant. However, for the pressure troughs the u' and v' data points concentrate in the Q2–quadrant (Fig. 5.16(b₁) and Fig. 5.16(b₂)). At the slightly higher location, $y/\delta^* = 5.7$, the u' and v' data points associated with both the pressure peaks and troughs seem to be slightly concentrated within the Q2–quadrant, as shown in Fig. 5.16(a₃) and Fig. 5.16(b₃) respectively. In general, however, they are more evenly distributed among the other quadrants at this height.

Each of the plots in Fig. 5.16 also contains hyperbolas corresponding to $|u'v'| = 6 \times \overline{-u'v'}$, which serve to identify the instantaneous Reynolds shear stresses $u'v'$ that are larger than

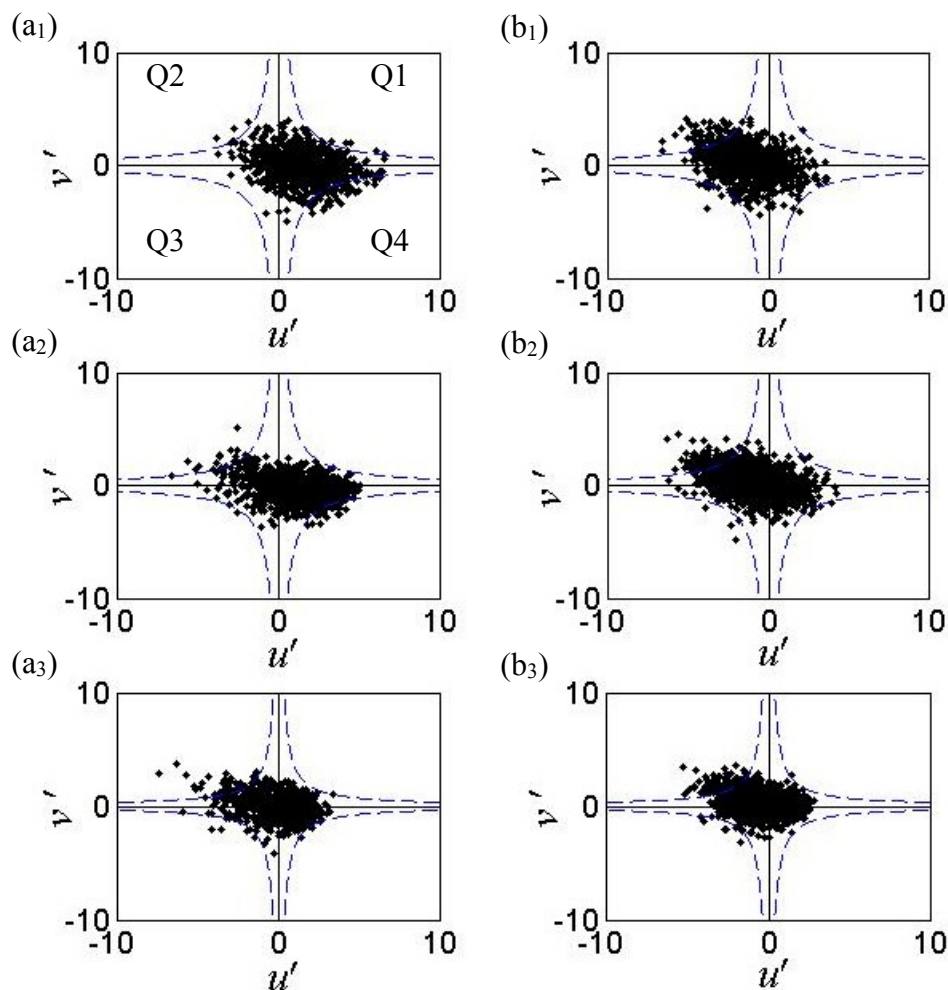


Figure 5.16 Distributions of instantaneous u' and v' that correspond to: (a₁, a₂, a₃). Pressure peaks at $y/\delta^* = 1.4, 3.2$ and 5.7 , respectively; (b₁, b₂, b₃). Pressure troughs at $y/\delta^* = 1.4, 3.2$ and 5.7 , respectively. The measurement location is at C3 for the straight trailing edge. The broken lines (---) represent the hyperbola $|u'v'| = 6 \times \overline{-u'v'}$.

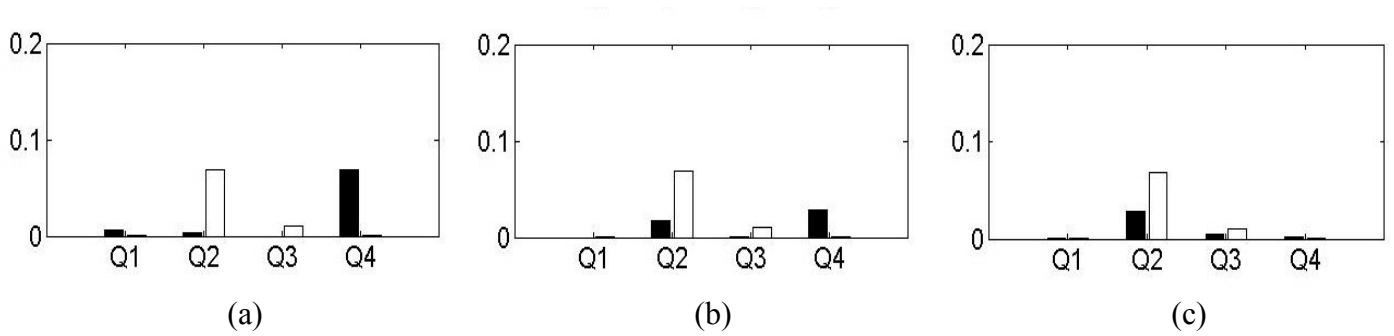


Figure 5.17 Fractions of the “intense” $u'v'$ events that correspond to the pressure peaks (black bars) and the pressure troughs (white bars) at different quadrants (Q1, Q2, Q3 and Q4). The subfigures are: (a). $y/\delta^* = 1.4$; (b). $y/\delta^* = 3.2$; and (c). $y/\delta^* = 5.7$. The measurement location is at C3 for the straight trailing edge.

six times the mean Reynolds shear stress (symbols outside the hyperbolas). Note that the constant value of six for the above equation is chosen arbitrarily to distinguish the intense $u'v'$ events from others.

The bar chart in Fig. 5.17 represents the fraction of the intense $u'v'$ events of each quadrant to the total number of ensembles for the positive peaks and negative troughs. The figure contains results for the straight trailing edge at location C3, which clearly illustrates the dominance of the sweep event at the near wall region with the ejection event dominating away from the wall. Note that a similar analysis of the intense $u'v'$ events at the same location C3 for a sawtooth serrated trailing edge also produces the same trends.

The coherent motion of the substructures in a turbulent boundary layer with respect to the $\langle +P \rangle$ and $\langle -P \rangle$ cases can also be described by the velocity fluctuations u_{rms}/U_∞ , v_{rms}/U_∞ and Reynolds shear stresses $-\langle u'v' \rangle / (U_\infty)^2$ in Fig. 5.18. For the $\langle +P \rangle$ case of the straight trailing edge, in Fig. 5.18(a₁), the wall inward sweeping motion is accompanied by particularly low values of u_{rms}/U_∞ between $-40 < \tau U_\infty / \delta^* < 20$, as well as predominantly low values of v_{rms}/U_∞ throughout the time of flight in Fig. 20(a₂). The velocity fluctuations in Fig. 5.18(a₁) and Fig. 5.18(a₂) and the high-momentum fluids in Fig. 5.15(a₁) demonstrate that the $\langle +P \rangle$ case is associated with a low turbulence production, which is further manifested in the Reynolds shear stress $-\langle u'v' \rangle / (U_\infty)^2$ contour in Fig. 5.18 (a₃). On the other hand, the ejection event produces much higher Reynolds shear stress levels in the $\langle -P \rangle$ case (see Fig. 5.18(b₃)). A similar observation can also be found in the v_{rms}/U_∞ levels in Fig. 5.18(b₂).

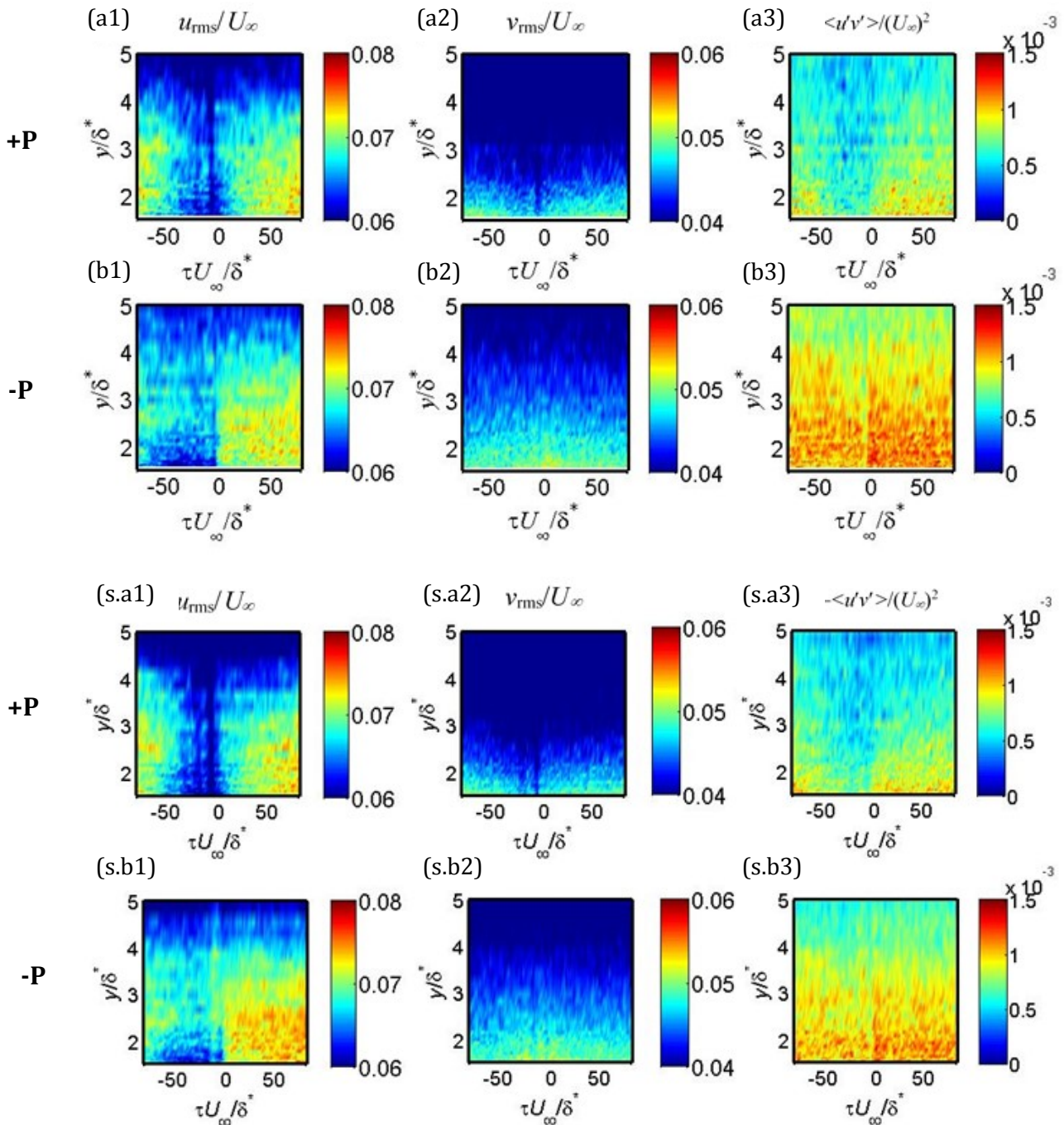


Figure 5.18 Contours of u_{rms}/U_∞ , v_{rms}/U_∞ and $\langle u'v' \rangle / (U_\infty)^2$ for: (a1, a2, a3). $\langle +P \rangle$ surface pressure; (b1, b2, b3). $\langle -P \rangle$ surface pressure. The measurement location is at C3 for the straight trailing edge.

(Bottom) The equivalent contours at point C3 on the serrated trailing edge are denoted as: (s.a1, s.a2, s.a3). $\langle +P \rangle$ surface pressure; (s.b1, s.b2, s.b3). $\langle -P \rangle$ surface pressure.

For the comparison of the velocity perturbations, *rms* velocity fluctuations and Reynolds shear stresses between the straight and serrated trailing edge at location C3, the equivalent contours of the serrated sawtooth trailing edge are depicted in (s.a1, s.a2, s.a3) for the $\langle +P \rangle$ case and (s.b1, s.b2, s.b3) for the $\langle -P \rangle$ case. It can be seen that there is a great similarity between the two trailing edges as they appear almost identical. In other words, the sawtooth does not affect the momentum transfers and turbulence transports at a location outside of the sawtooth side edge and sawtooth tip. This is consistent with the surface temperature and unsteady wall pressure spectral contour maps presented earlier.

5.5.3.2 Development of the coherent-like structures near the sawtooth side edges

This section focuses on the momentum transfers and turbulence transports at a location close to the side edge of a serrated sawtooth trailing edge (i.e. location C1). Comparisons will be made against the straight trailing edge at the same location. For brevity, only the velocity perturbations \tilde{U} and Reynolds shear stresses $-\langle u'v' \rangle / (U_\infty)^2$ are discussed in this section. For ease of comparison, the results are presented using the notations:

$$\Delta\tilde{U} = \tilde{U}_{\text{straight}} - \tilde{U}_{\text{sawtooth}} \quad (\text{eq. 5.9})$$

$$\Delta\psi = -\langle u'v' \rangle / (U_\infty)_{\text{straight}}^2 + \langle u'v' \rangle / (U_\infty)_{\text{sawtooth}}^2. \quad (\text{eq. 5.10})$$

As shown in Fig. 5.19(a₁), the predominantly positive $\Delta\tilde{U}$ demonstrates that the high-momentum wall sweeping event at $\tau U_\infty / \delta^* < 0$, which is associated with $\langle +P \rangle$, becomes less significant near the sawtooth side edge for the serrated trailing edge. Interestingly, in

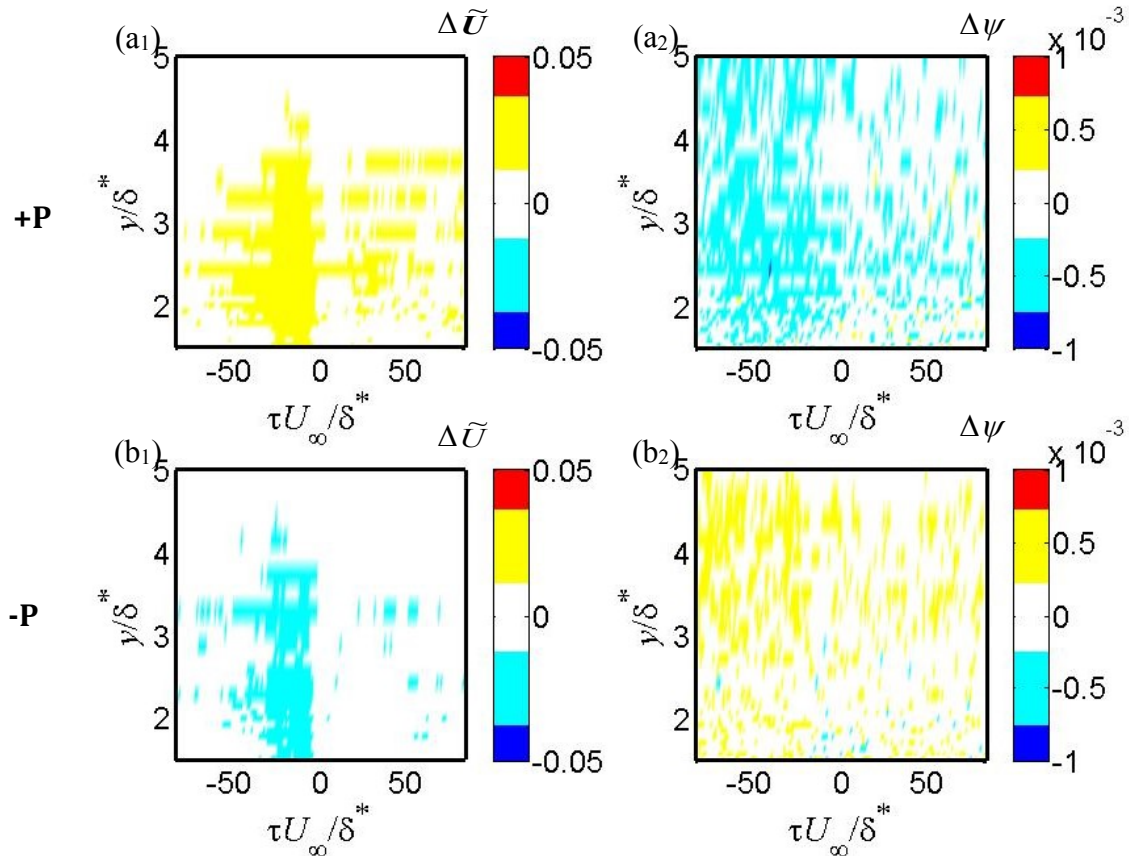


Figure 5.19 Contours of \tilde{U} and $\Delta\psi$ for: (a1, a2), $\langle +P \rangle$ surface pressure; (b1, b2), $\langle -P \rangle$ surface pressure. The measurement location is at C1 for both of the straight and serrated sawtooth trailing edge.

Fig. 5.19(b₁), the predominantly negative $\Delta\tilde{U}$ during the $\langle -P \rangle$ cycle demonstrates that the low-momentum ejection event near the sawtooth side edge for the serrated trailing edge is also less significant. The above momentum transfers ($\Delta\tilde{U}$) of the substructures near a sawtooth side edge are also manifested in the turbulence production observed in the $\Delta\psi$ contours. As shown in Fig. 5.19 (a₂), a higher Reynolds shear stress level is generally produced during the $\langle +P \rangle$ cycle near the sawtooth side edge of the serrated trailing edge because of the predominantly negative values of $\Delta\psi$. This implies that the becalmed effect of the wall sweeping of high-momentum fluids is less significant near the sawtooth side edge. On the other hand, because of the weakened ejection and bursting of low-momentum fluids near the sawtooth side edge of the serrated trailing edge during the $\langle -P \rangle$ cycle, Fig. 5.19 (b₂) shows a predominantly positive value of $\Delta\psi$. This means that the serrated trailing edge produces a Reynolds shear stress level which is lower than the straight edge counterpart. As a result, the mechanism of turbulence production based on the sweep-and-eject model near the side edge of the serrated

sawtooth trailing edge is quite different from the turbulence production mechanism on the straight trailing edge.

Despite the change in flow dynamics near the sawtooth side edge of the serrated trailing edge, the time-averaged Reynolds shear stresses $-\overline{u'v'}/U_\infty^2$ profiles for the straight and serrated sawtooth trailing edges are actually quite similar (see Fig. 5.9c for location C1). The anti-correlation of the sweeps and ejections gives rise to Reynolds shear stress. The results presented in Fig. 5.19 are therefore mainly due to the simultaneously weakened sweep and ejection motions near the sawtooth side edge of the serrated trailing edge. In this scenario, the sweeps will contain higher than usual Reynolds shear stress levels while the ejections will produce the opposite, resulting in an overall balanced level as manifested in the time-averaged Reynolds shear stress.

However, as will be discussed in the next section, considerably different flow dynamics can be found near the sawtooth tip.

5.5.3.3 Development of the coherent-like structures near the sawtooth tip

Fig. 5.20 presents the contour maps of $-\langle u'v' \rangle / (U_\infty)^2$ at E1, which is the location close to the sawtooth tip. The most striking feature in the figure is that the Reynolds shear stresses are anti-correlated between the straight and serrated sawtooth trailing edges with respect to the $\langle +P \rangle$ and $\langle -P \rangle$ cycles. The becalmed effect of the wall sweeping motion during the $\langle +P \rangle$ cycle, as demonstrated in the straight trailing edge in Fig. 5.20(a₁), is totally absent in the case of the serrated sawtooth trailing edge as in Fig. 5.20 (a₂). However, a seemingly high-momentum wall sweeping motion is present for the serrated sawtooth trailing edge during the $\langle -P \rangle$ cycle in Fig. 5.20 (b₂). This contradicts the straight trailing edge in which the boundary layer is mostly characterized by high turbulence production during this particular cycle (see Fig. 5.20 (b₁)).

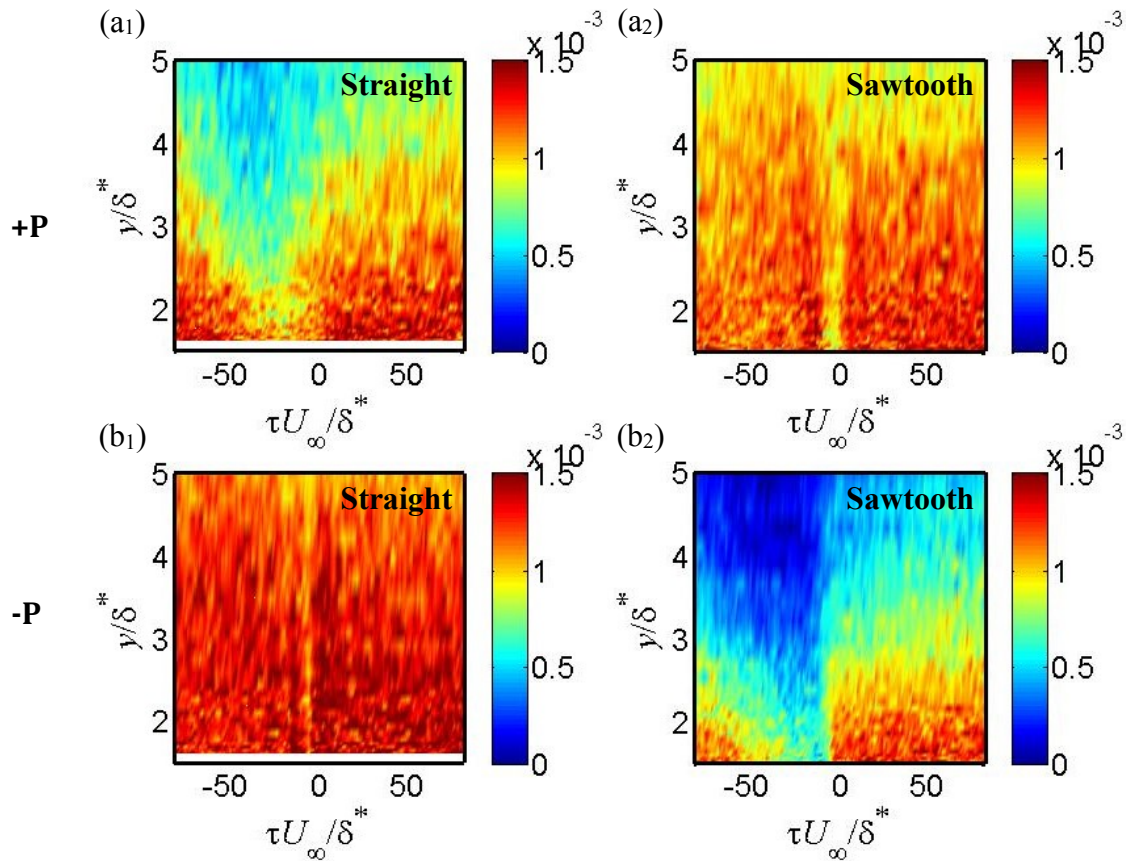


Figure 5.20 Contours of $-\langle u'v' \rangle / (U_\infty)^2$ for: (a₁, a₂), $\langle +P \rangle$ surface pressure; (b₁, b₂), $\langle -P \rangle$ surface pressure. The measurement location is at E1 for both of the straight trailing edge and serrated sawtooth trailing edge.

Previously, it was demonstrated that the unsteady wall pressure PSD level and the wall heat transfer will increase significantly near the sawtooth tip. This can be further illustrated in Fig. 5.21 by the comparison of wall pressure time-signals between the straight and serrated sawtooth trailing edges at location E1. Therefore, the use of wall pressure peaks and troughs as the reference signals at location E1 for the serrated sawtooth trailing edge is likely to contain certain elements of vortical flow in the ensemble-averaged momentum/turbulent quantities. The Reynolds shear stress contours in Fig. 5.20(a₂) and Fig. 5.20(b₂) should then reflect the turbulent boundary layer flow subjected to interaction with the side edge vortical flow. As a result, a direct comparison of the ensemble-averaged Reynolds shear stress contours between the straight and serrated sawtooth trailing edges is not straightforward.

The mechanism which is responsible for producing the opposite temporal pattern of the Reynolds shear stress in Fig. 5.20 could be explained by the idealized schematics in Fig. 5.22, which depict the propagation of the pressure-driven disturbances in a convective vortical pattern along the oblique side edge of a serrated sawtooth trailing edge.

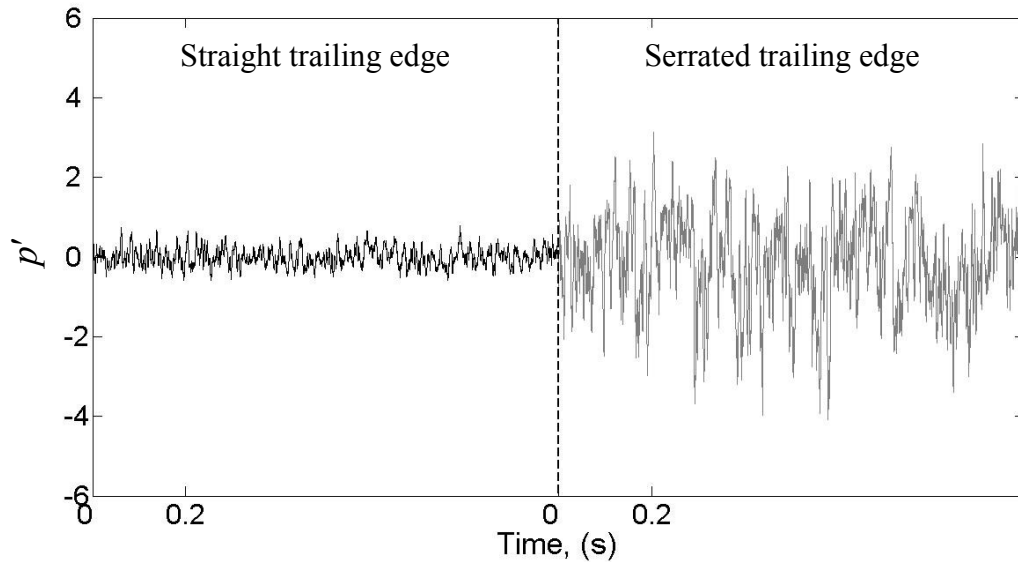


Figure 5.21 Comparison of the surface pressure signal amplitudes measured at location E1 between the straight trailing edge and serrated sawtooth trailing edge. Note that both of the pressure signals were measured by the same microphone and signal amplifier.

This type of flow interaction has two main characteristics which should be noted:

1. As demonstrated in Fig. 5.21, the level of pressure fluctuations produced by the vortical flow is significantly larger than the level of pressure fluctuations produced by the viscous effect in the turbulent boundary layer.
2. The sweep and ejection of the turbulent boundary layer will be affected in accordance with the phase of the convecting vortical structure.

The following discussion is only related to the serrated sawtooth trailing edge. Considering first the $\langle +P \rangle$ case on the left-hand-side of Fig. 5.22, the wall-inward motion of the arriving vortices will induce large positive pressure fluctuations across the boundary layer. Based on the characteristic described above, the positive pressure fluctuations could already be captured by the surface microphone sensor at some distances downstream. During the same phase when the microphone is measuring the positive pressure fluctuation, the finite area above it (indicated by the shaded box) will be subjected to an upward motion of the vortices where the low-momentum fluid is entrained from the wall. To demonstrate this, ensemble-averaged velocity $\langle U \rangle / U_\infty$ for the

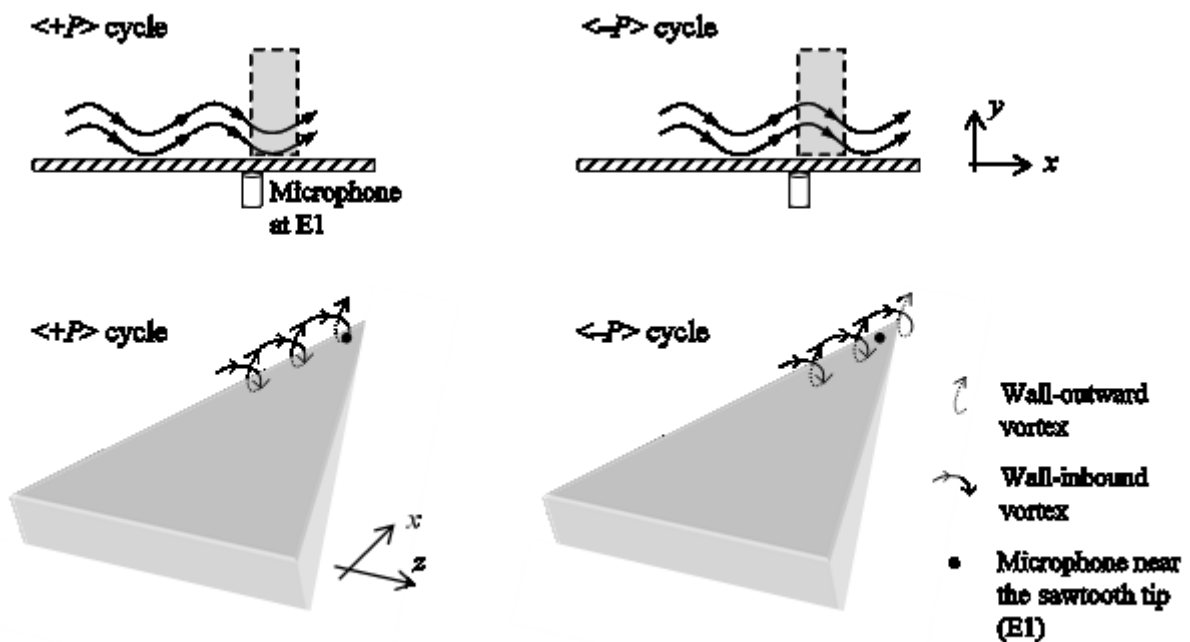


Figure 5.22 Schematics to illustrate the propagations of the pressure-driven vortical structures near the sawtooth side edge towards the tip for the $\langle +P \rangle$ and $\langle -P \rangle$ cycles. Top figures: side view; bottom figures: isometric view. Drawings are not to scale.

straight and serrated sawtooth trailing edges during the $\langle +P \rangle$ cycle are compared in Fig. 5.23 (a₁) and Fig. 5.23 (a₂), respectively. It can be seen that lower level of $\langle U \rangle / U_\infty$ is produced in the boundary layer for the serrated sawtooth trailing edge prior to the arrival of the pressure peak. Because the shaded box in Fig. 5.22 coincides with the cross-wire probe, a predominantly upward low-momentum fluid, with a high value of Reynolds shear stress in the boundary layer as manifested in Fig. 5.20 (a₂), will be measured.

After one half of a period, as demonstrated at the right-hand-side of Fig. 5.22, the vortices upstream of the surface microphone sensor will be predominantly subjected to wall-outward motion because of the convective nature of the vortices. The microphone will

therefore measure negative wall pressure fluctuations $\langle -P \rangle$ during this phase. Using the same principle described in the previous paragraph, the vortices will induce high momentum fluids sweeping towards the wall in the shaded box. This is also manifested in the $\langle U \rangle / U_\infty$ contours for the straight and serrated sawtooth trailing edges in Fig. 5.23(b₁) and Fig. 5.23(b₂), respectively. The explanation for the significantly reduced Reynolds shear stress level in the boundary layer during this half-cycle, as shown in Fig. 5.20(b₂), is thus provided.

As a summary, the vortical structure near the tip of a serrated sawtooth trailing edge, the ensemble-averaged velocities measured by the cross-wire within the boundary layer are out of phase with the wall pressure signals.

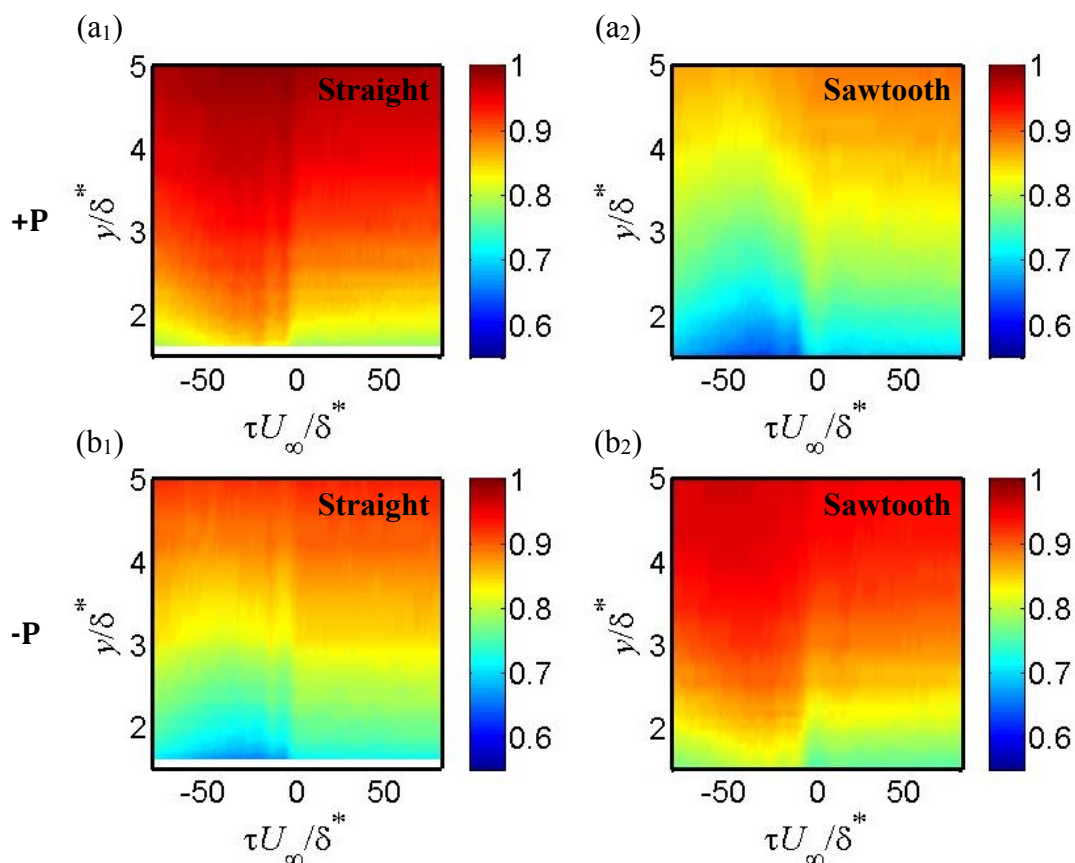


Figure 5.23 Contours of $\langle U \rangle / U_\infty$ for: (a₁, a₂), $\langle +P \rangle$ surface pressure; (b₁, b₂), $\langle -P \rangle$ surface pressure. The measurement location is at E1 for both of the straight trailing edge and serrated sawtooth trailing edge.

5.6 Identification of vortical structures along the serration edge

In the liquid crystal experiment, the sawtooth's oblique side edges and tips are shown to exhibit a lower temperature than the straight trailing edge, whilst the temperature difference at other places remains unchanged. A lower surface temperature is caused by higher heat transfer rate, which is associated with a higher level of turbulence. A repeatability test on another sawtooth configuration by the liquid crystal technique also produces the same result.

Wall pressure PSD at 34 locations is mapped on a complete sawtooth surface. An equivalent distribution of the wall pressure spectral energy is also obtained for the straight trailing edge. The frequency range over which the noise reduction occurs is found to feature the co-existence of strong wall pressure fluctuations near the sawtooth side edges and the sawtooth tips. The wall spectral energy, which is obtained from the integration of the wall pressure PSD with frequency, also resembles strong fluctuations at locations near the sawtooth oblique side edge and sawtooth tip. The contribution of the acoustic back-scattered pressure to the wall pressure spectral energy, if any, has been proven to be negligible in the current case.

Extensive streamwise and spanwise coherence measurements were performed. Generally, it was found that the convective velocities of the turbulent eddies in the streamwise direction (but without the spanwise spacing) are very similar for both the straight and sawtooth serrated trailing edges. On the other hand, when the microphone pairs are separated in the spanwise direction (but without the streamwise spacing), some noticeable differences are found:

1. The measured spanwise wall pressure coherence functions for the *straight trailing edge* follow the predicted curves. The measured phase differences in the spanwise direction are almost zero, which suggest that there is no convection velocity in this direction.
2. However, for the *serrated sawtooth trailing edge*, the measured spanwise coherence functions at regions close to the sawtooth oblique side edge and tip are slightly higher than the straight edge counterparts.

As previously introduced in Section 2.2.3, Amiet (1976) specifies that $S_{pp}(\omega) \propto I_y(\omega) S_{qq}(\omega)$. The variations of the spanwise coherence (which relates to the spanwise correlation length l_y) are generally not too significant between a straight and a serrated sawtooth trailing edge. However, the overall wall pressure spectrum S_{qq} (and heat transfer) in a serrated sawtooth trailing edge is found to be higher than the straight edge counterpart. This result contradicts the Amiet's model and the observation of noise reduction by a serrated sawtooth trailing edge. In order to explain the cause of this contradiction, the investigation then focuses on the flow structures developed on a serrated sawtooth surface.

Boundary layer measurements were performed at several locations on the sawtooth/straight surfaces using a cross-wire. The time-averaged Reynolds shear stress profiles are generally similar when comparing the straight and serrated sawtooth trailing edges, except at the sawtooth tip where an increase of up to 8% in the near wall region has been observed. The *PSD* of u' and v' also reveal a prominent spectral hump, which suggests the presence of a strong vortex shedding near the sawtooth tip.

Cross spectral analysis was performed near the sawtooth tip for the product of the boundary layer velocity fluctuations ($u'v'$) and the wall pressure fluctuation p' directly below the cross-wire. A large cross spectral level near the sawtooth tip is noticed, which implies that the wall pressure fluctuation is mainly caused by the local boundary layer hydrodynamics. The cross spectral results thus further exclude the effect of acoustic back scattering. Boundary layer velocity and wall pressure signals were also analyzed using the conditional-averaging technique to investigate the temporal variations of the coherent structures in the straight and serrated sawtooth trailing edges. Both the momentum and turbulence properties at the main body of the serrated sawtooth trailing edge are similar in characters to the straight trailing edge. Near the sawtooth oblique side edge, the turbulence substructures exhibit simultaneously weakened sweeping and ejection motions. Despite the shifting dynamics of the local turbulence transport, the mean turbulence level remains about the same across the boundary layer. However, near the sawtooth tip, an extensive flow mixing between the turbulent boundary layer and the pressure-driven vortical structure is clearly demonstrated.

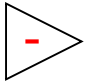
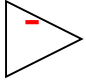
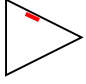
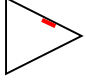
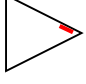
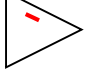
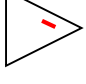
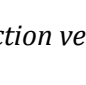
Microphone pair		Δx (mm)	Δz (mm)	U_c for straight trailing edge (ms ⁻¹)	U_c for serrated trailing edge (ms ⁻¹)	Difference in U_c (%)
B4-C3		4	0	19.6	18.6	5.1
B2-C1		4	0	19.5	19.1	2.1
B1-C1		4	2	24.5	12.9	47.3
C1-D1		4	2	24.2	10.2	57.9
D1-E1		4	2	23.5	13.2	43.8
B2-C2		4	2	24.3	24.7	-1.6
C2-D2		4	2	22.7	24.4	-7.5

Table 5.1. Convection velocities determined by the phase spectral

The identification of the pressure-driven, oblique vortical structures and their interaction with the nominally turbulent boundary layer needs further investigation. The analysis now focuses on the convection velocity of the turbulent eddies on the straight and serrated sawtooth trailing edges. Assuming that Taylor's hypothesis is true for the propagating turbulent eddies, the phase spectrum between a pair of microphone sensors can be used to calculate the convection velocities U_c (Eq. 2). The results of seven configurations are summarized in Table 5.1. Note that, as far as the straight trailing edge is concerned, a larger convection velocity is generally observed for the cases when the microphone sensors are spaced obliquely (i.e. Δx & $\Delta z > 0$) compared with the case when only streamwise separation is present. This is because for an oblique separation the gradient $d\phi(f)/df$ from the phase spectrum becomes smaller, and the effective distance $(\Delta x^2 + \Delta z^2)^{0.5}$ also slightly increases.

The differences in convection velocity between the straight and serrated sawtooth trailing edges remain small when the microphone sensors are separated by $\Delta x = 4$ mm and $\Delta z = 0$ (i.e. the B4-C3 and B2-C1 cases in Table 5.1). Conversely, as shown in Table 5.1, large differences in convection velocity have been observed between the straight and serrated

trailing edges for the cases B1–C1 (47% difference), C1–D1 (58% difference) and D1–E1 (44% difference). These microphone pairs share the same characteristics of $\Delta x = 4$ mm and $\Delta z = 2$ mm. Most importantly, they are all located very near the sawtooth oblique side edge. However, the difference in convection velocities along the serration angle becomes small again further away from the sawtooth oblique side edge, e.g. B2–C2 and C2–D2 in Table 5.1.

According to Amiet (1976) and Howe (1999), the wetted spanwise extent of the trailing edge is proportional to the radiated noise level. Despite the minor variation of l_y , as well as the increase of S_{qq} for a serrated sawtooth trailing edge discussed earlier, it is interesting that noise reduction can still be achieved despite the fact that the ratio of the wetted lengths between a straight trailing edge and a serrated sawtooth trailing edge is equal to $\sin(\varphi)$. The reasons might be related to Howe's theory, which is also summarised in Gruber et al (2011). They stated that not all the eddies over various length scales and energies in flow velocity fluctuations (i.e. boundary layer turbulence wavenumber components) could scatter efficiently into noise by a serrated sawtooth trailing edge, except those that arrive near perpendicularly to the serration angle φ . However, wavenumber components that deviate from the mean flow direction can also affect the radiation integral term and subsequently the noise scattering. Therefore, the serration is acting as a filter for the turbulence wavenumber components.

Howe's theory could be further supplemented by the presence of vortical structures along the sawtooth side edges. Table 5.2 represents several schematics showing the propagations of boundary layer pressure waves at different trailing edges. Because the wall pressure S_{qq} is generally dominated by the streamwise wavenumber components in the convective region, consideration is only given to the boundary layer pressure wave that propagates at a small angle, φ' , with respect to the mean flow direction. Case A and case C represent $+\varphi'$ and $-\varphi'$ respectively, while Case B represents $\varphi' = 0^\circ$. For all cases, noise should be scattered at both the tip and the oblique side edges of the sawtooth. The mechanisms proposed by Howe (1990,1991) and Gruber et al. (2011) on the noise reduction by a serrated sawtooth trailing edge are likely to be suited for Case B and Case C. In Case A, the boundary layer pressure waves will propagate in an angle close to the oblique vortical structures. The interaction between them has been shown to cause a

significant reduction of momentum and kinetic energy of the boundary layer pressure waves. Ultimately, noise scattering will be less effective for this particular case.

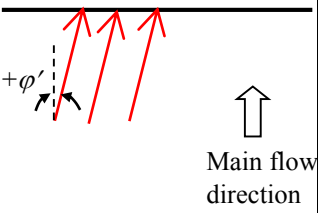
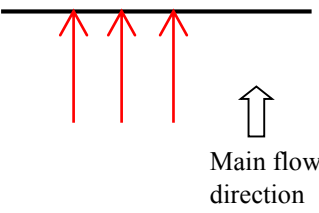
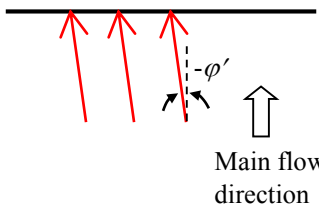
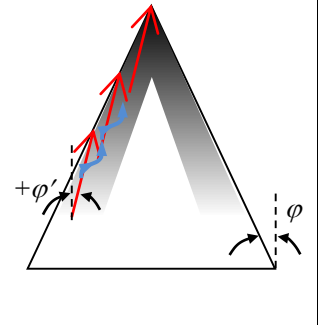
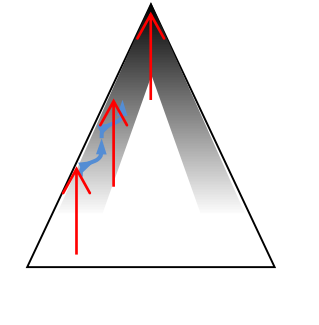
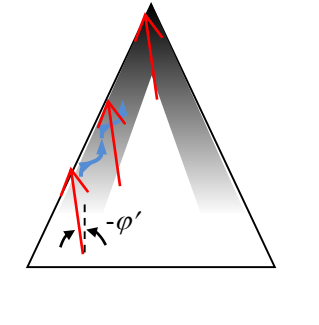
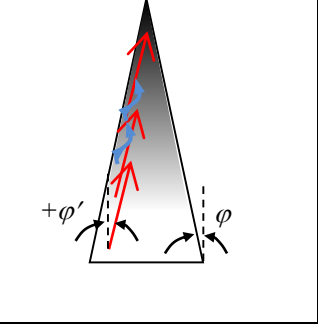
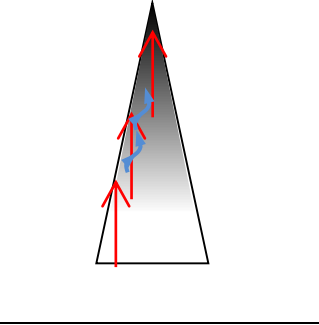
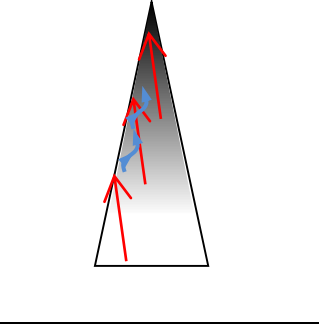



	Case A	Case B	Case C
Straight trailing edge			
Sawtooth trailing edge (wide serration angle)			
Sawtooth trailing edge (narrow serration angle)			
	 Side edge vortical structures	 Regions of high surface heat transfer and wall pressure fluctuations	 Pressure waves of various incidence angles

Table 5.2 Schematics to illustrate the propagations of the boundary layer pressure waves of various incidence angles to the different trailing edges. Note that both the wide and narrow serration angles have the same $2h$. Drawings are not to scale.

According to Howe (1991), a sawtooth trailing edge can potentially achieve self-noise reduction up to $10 \times \log_{10} \left(1 + (1/\tan \phi)^2 \right)$ dB. Although it remains debatable if such an asymptotic level can be realistically achieved, it has been universally agreed that a maximum noise reduction would require the serration angle ϕ to be small (also demonstrated in Chapter 4). This specification is associated with the angle between the sawtooth side edge and the boundary layer pressure waves, $(\phi - \phi')$. If $(\phi - \phi') \rightarrow 0$, or ϕ

$\approx \varphi'$, the level of momentum and kinetic energy reductions of the boundary layer pressure waves in Case A are expected to be the greatest because they are propagating almost parallel with the sawtooth side edges/vortical structures. Based on the results in Table 5.1, the losses in momentum and kinetic energy can be as high as 50% and 75%, respectively. On the other hand, the most effective noise scattering should occur at a small value of φ' . The above two conditions stipulate that a narrow serration will be more effective in noise reduction. Another explanation is that the vortical structure will also occupy more surface area per sawtooth for a narrow-angle than for a wide-angle serrated sawtooth. This is supported by comparison of the liquid crystal results between a wide-angle sawtooth and a narrow-angle sawtooth (Fig. 5.4 vs. Fig. 5.5), where both cases have the same $2h$. Therefore, noise scattering at the tips and side edges of the narrow-angle sawtooth will be weaker, despite the fact that the total length of the wetted serrated edge per unit span, and the total number of tips, are actually increased.

5.7 Investigation of the vortex shedding mechanism past a non-flat plate serrated trailing edge

After the investigation of the boundary layer flow over a sawtooth serration, this section focuses on the vortex shedding mechanism in the near wake of an airfoil with non-flat plate type serrations. The vortex shedding tonal noise due to the partial bluntness of the non-flat plate type serrations was previously demonstrated in Chapter 4. As shown in Table 5.3 the non-flat plate trailing edge geometries are denoted as 'S1' and 'S3', according to the terminology also used in Chapter 4. Additionally a straight blunt trailing edge is investigated here, denoted as 'SB'.

Description	Notation	Serr. Length $2h, mm$	Wavelength $\lambda/h [\varphi, deg]$	Bluntness (ϵ), mm
Fully blunt	SB	n/a	0[0°]	5.7
Serrated	S1	20	0.49[7°]	5.7
Serrated	S2	20	0.85[12°]	5,7
Serrated	S3	20	1.87[25°]	5.7

Table 5.3 Trailing edge geometries for the investigation of vortex shedding mechanism

5.7.1 Water tunnel dye flow visualisation

In order to investigate the mechanism responsible for the narrowband vortex shedding noise generation a flow visualisation test was carried out in a water tunnel (described in Section 3.4.1). A separate NACA 0012 airfoil of a 200 mm chord was manufactured with an identical S3 trailing-edge serration geometry, which is scaled to yield the same $2h/C$ value. The flow visualization tests were performed in the water at a low speed of 0.04 ms^{-1} , corresponding to a Reynolds number of approximately 0.9×10^4 based on the chord length. The low speed was chosen in order to visualise a reasonably clear vortex shedding pattern at around this speed region. Although the Reynolds number for this hydrodynamic test is generally lower than the aeroacoustic noise measurements in this thesis, the airfoil was tripped to produce a turbulent boundary layer at the trailing edge, roughly equivalent to the turbulent noise source generated in the noise test presented in chapter 4. This airfoil was positioned at $\theta = 5^\circ$ with respect to the mean flow direction of the water tunnel with a $300 \times 450 \text{ mm}$ cross-sectional area. Blue colour dye was injected at a constant flow rate near the root of one of the sawtooth as shown in Fig. 5.24. In the figure, snapshots of six time frames ($\Delta t = 0.375 \text{ s}$) are shown. The filled arrows represent upwash flow (pressure surface to suction surface) within a sawtooth gap; the nonfilled arrows represent downwash flow (suction surface to pressure surface) within a sawtooth gap. Flow in the vicinity of the sawtooth is characterised by a periodic oscillatory motion of the upwash and downwash of the blue dye at a frequency of about 1.3 Hz. If this frequency is scaled with the bluntness of the serration root ϵ , the resulting hydrodynamic Strouhal number is about 0.19. This value compares reasonably well with the Strouhal numbers for the narrowband vortex shedding noise produced by the S3 case, which are in the range from 0.14 to 0.17, depending slightly upon the flow speed and angle of attack (to be discussed in Section 5.7.2). Therefore, there is strong evidence that the vortex shedding noise is produced by the periodic oscillation of flow within the sawtooth gap.

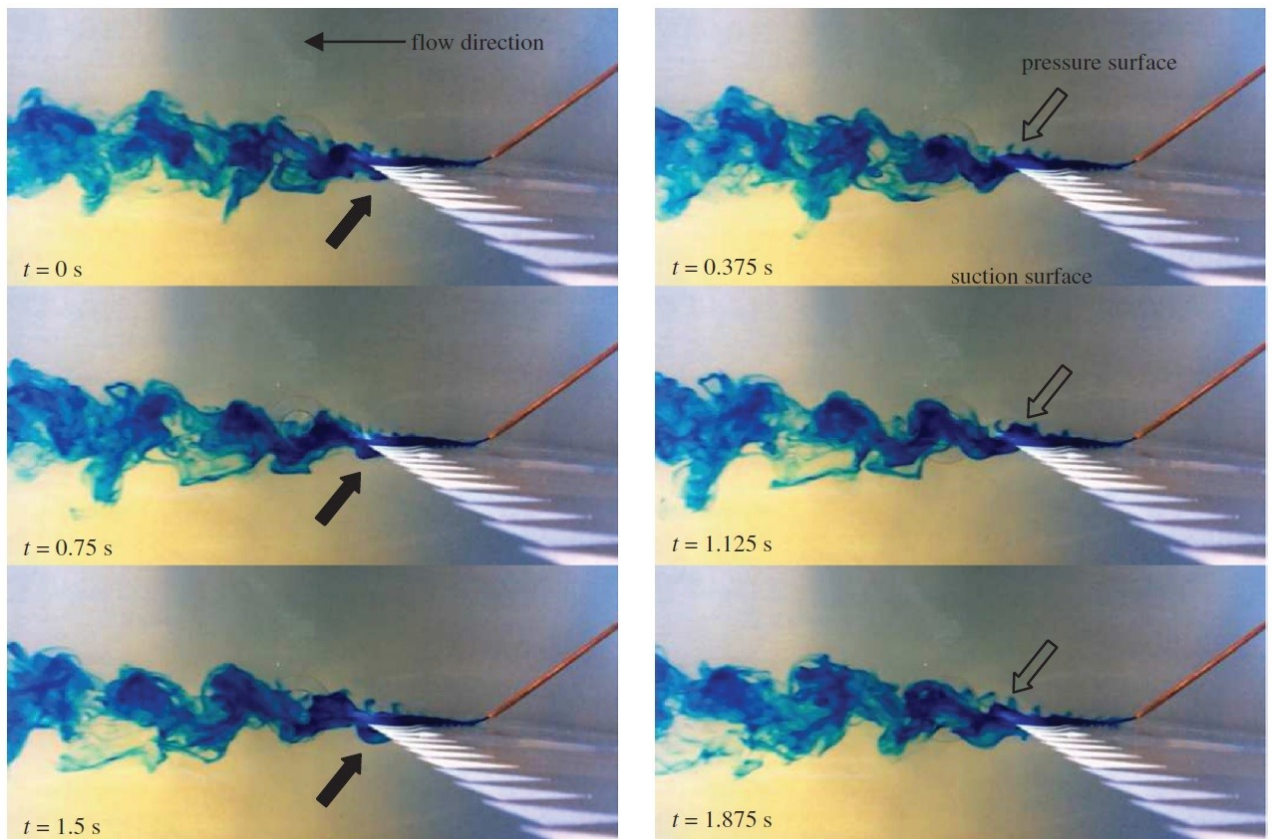


Figure 5.24 Sequence of wake flows produced by a S3-type serrated trailing edge at $\theta = 5^\circ$ tested in a water tunnel

5.7.2 Strouhal number dependency and spanwise coherence in the near wake of non-flat plate serrations

Fig. 5.25 shows a plot of the Strouhal number for the vortex shedding noise ($f_d \varepsilon / U$), defined with respect to the bluntness ε and flow velocity U , suggesting that there is no universal Strouhal number dependency for the S1, S2, and S3 cases. If an airfoil has a two-dimensional blunt trailing edge, with a constant ε across the airfoil span and the same value as the S1, S2, and S3 cases, the corresponding Strouhal numbers ($f_d \varepsilon / U$) are predicted to be constant with the flow velocity [Brooks (1989)]. The measured Strouhal numbers for the S1, S2, and S3 cases are found to vary between $U^{0.1}$ and $U^{0.15}$.

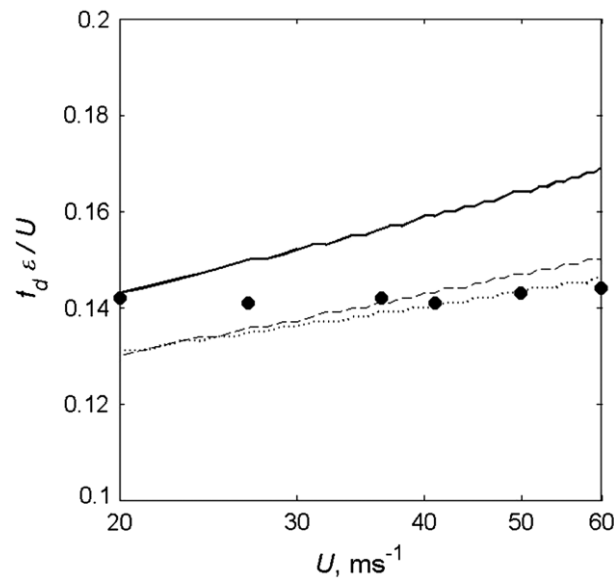


Figure 5.25 Distributions of the Strouhal number of the vortex shedding noise produced by a tripped airfoil versus U , with S1 (\cdots), S2 ($---$), S3 ($—$) and 2D-blunt (same ε , but with φ and $\lambda/h=0$, represented by \bullet) trailing edges at $\theta=4.2^\circ$.

Flow passing through a sawtooth region could be highly three dimensional in nature. When the airfoil is set at an angle of attack, the static pressure difference across the suction and pressure surfaces will force the flow to wrap around each of the sawtooth side edges in a manner similar to the wingtip vortices of a three-dimensional airfoil. Note that this type of spanwise secondary flow is different with the longitudinal vortices that are shed from the blunt serration roots. The possible interaction between the secondary flow with the longitudinal vortices has been shown to significantly affect the coherence of the vortex shedding street in the wake flow. To quantify this effect, the spanwise coherences γ^2 of the airfoil wake turbulence velocity for three types of trailing edges, S2, S3, and SB, were measured at $\theta = 5^\circ$ in a closed-section wind tunnel. Here, SB is a two dimensionally blunt, non-serrated trailing edge with the same bluntness ε as the S2 and S3 serrated trailing edges. The spanwise coherence function γ^2 is defined as

$$\gamma^2 = \frac{|\Phi_{vi} \Phi_{vj}(f)|^2}{\Phi_{vivi}(f) \Phi_{vjvj}(f)} \quad (\text{eq. 5.11})$$

where $0 \leq \gamma^2 \leq 1$. $\Phi_{v_i v_j}(f)$ is the cross spectrum between the two streamwise fluctuating velocity signals v_i and v_j . The velocity measurement v_i was measured by a single hot wire situated at a fixed, stationary position of $x = 15$ mm downstream of the sawtooth tip or $(15 + 2h)$ mm behind the SB blunt trailing edge.

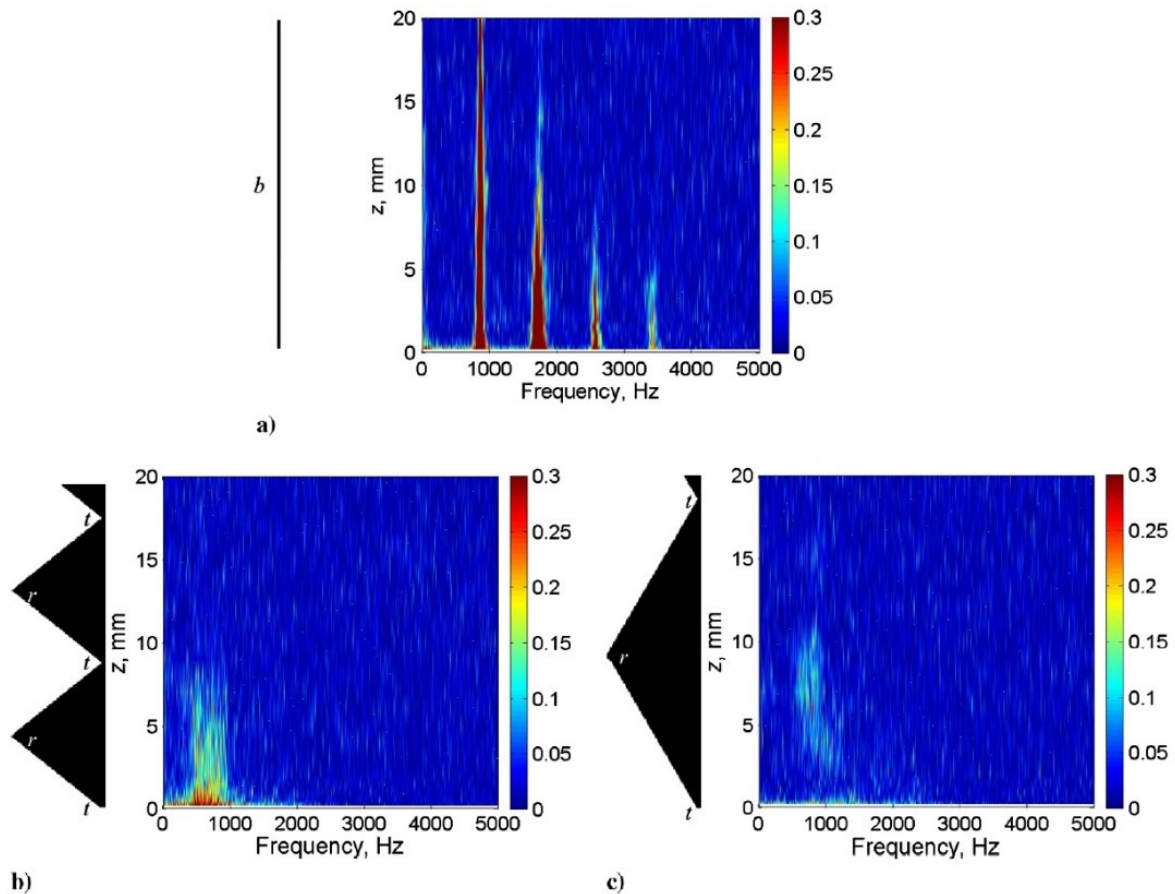


Figure 5.26 Colour maps of γ^2 for the cases of (a) SB, (b) S2, and (c) S3 trailing edges measured at $\theta = 5^\circ$ and $U = 20 \text{ ms}^{-1}$. 'b', 'r' and 't' denote 'blunt', 'root' and 'tip' respectively.

The velocity measurement v_j was measured by another single hot wire situated at the same downstream x position but was traversed along the spanwise z direction. $\Phi_{v_i v_i}(f)$ and $\Phi_{v_j v_j}(f)$ are the autospectra of each individual fluctuating velocity signal. The overhear ratios of the DANTEC 55P11 probe was selected as 1.6, which should also minimize thermal interference between the wires when they are close to each other. The results of γ^2 for the SB, S2, and S3 cases of a tripped airfoil are shown in Fig. 5.26. Each figure is accompanied by a sketch on the left hand side to illustrate the serration/blunt geometries. The symbols 'b', 'r' and 't' denote 'blunt', 'root' and 'tip' respectively. The stationary, reference point for the γ^2 function is situated at $z = 0$. Note that the γ^2 function here is a measure of the spanwise coherence of the spanwise vortex shedding. Strong spanwise coherence can be observed for the SB case, which clearly indicates that the wake

flow is mainly characterized by longitudinal vortex shedding. For the S2 serrated case, the spectral frequency is broader than the SB case with a reduced spanwise coherence level. The wake flow emanated from the root region, although still predominantly characterized by longitudinal vortex shedding, is already affected considerably by the secondary flow. As expected, there is also no coherence between each successive sawtooth. For the S3 serrated trailing edge, an overall very low-spanwise coherence level is observed. This indicates that the wake flow is highly three-dimensional in this case, in which the serration angle φ is the largest.

For the case of a small value of φ (or λ/h), the total number of serration “blunt roots” per unit span is increased. This tends to reduce the strength of the spanwise secondary flow, whereas the longitudinal vortex shedding (caused by the bluntness at the root region) is expected to be considerably coherent. This is manifested in the sound power spectra which was presented in Chapter 4 (Fig. 4.3) in which it can be seen that the sound power of the narrowband vortex shedding noise increases as φ decreases. It also explains that the Strouhal number, which corresponds to the narrowband frequencies produced by a trailing edge with a “full” two-dimensional bluntness ($\varphi = 0$), tends to agree better with those produced by a serrated trailing edge of low φ as demonstrated in Figure 5.25. Conversely, for a trailing edge with a larger serration angle (e.g., the S3 case), the more prominent secondary flow is expected to interact more strongly with the longitudinal vortex shedding. This process leads to a modification to the narrowband frequency and also reduces its sound power level. Based on this behaviour, it can be concluded that, as far as a tripped boundary layer is concerned, a serrated trailing edge with large serration angle φ would produce a lower level of the vortex shedding noise.

5.8 Discussion

Noise measurements in an anechoic chamber confirm that turbulent broadband noise reduction can be achieved by a serrated sawtooth trailing edge in a flat plate configuration similarly to an airfoil configuration. The investigation then focuses on the velocity and thermal properties of turbulent boundary layer on a serrated sawtooth surface in order to establish the causal relationship between the noise and the near field observations. Noise reductions are found to occur at a fairly large frequency range. The same frequency range is also associated with high levels of wall pressure power spectral density near the sawtooth tip and the sawtooth side edges. Initially, the dominant fluctuating components

occupy mainly at a region close to the sawtooth tip. At higher frequencies, these structures will shift to the sawtooth side edges and slowly disappearing altogether outside the frequency range where noise reduction ceases to exist.

Both the turbulent boundary layers on a straight trailing edge, and on a serrated sawtooth trailing edge, contain coherent structures in the form of hairpin-type vortices to regenerate themselves through the sweep-and-eject mechanism. However, by conditional-averaging the turbulent boundary layer, the results suggest that the dynamics and behaviours of the hairpin-type vortices on a serrated sawtooth trailing edge cannot be the only driving force for the noise reduction. Instead, the interaction between the hairpin vortices and the non-viscous, pressure-driven oblique vortices is the main reason to produce the significant levels of heat transfer/wall pressure fluctuation (S_{qq}) as well as the reduction in convection rate of the turbulence structures near the sawtooth tip and the side edges.

Based on the Amiet's model, the increase of S_{qq} near the sawtooth side edges and sawtooth tip should have increased the radiated noise level S_{pp} . It is conjectured that this effect, however, is small in comparison with the $\sim 50\%$ loss in momentum and $\sim 75\%$ loss in kinetic energy near the sawtooth side edges through the viscous-inviscid interaction between the turbulent eddies and the oblique vortical structures, respectively. This interaction provides an effective mechanism for the redistribution of the momentum and turbulent energy near the sawtooth tip and side edges, and reduces the scattering-efficiency of the hydrodynamic pressure waves into trailing edge noise.

Regarding the vortex shedding mechanism involved over an airfoil with a non-flat plate serrated trailing edge, it was demonstrated that the vortex shedding in the near wake comprises a highly three dimensional flow. Hence, the vortex shedding by the partial bluntness of the serrations is altered through the flow over the serrations, when compared to a fully blunt trailing edge. This could be shown through a dye flow visualisation experiment, carried out at an angle of attack $\alpha=5^\circ$ where the highly three-dimensional wake-flow could be observed past the serrated airfoil. By scaling the frequency of the upwash and downwash of the blue dye, the resulting hydrodynamic Strouhal number matches well with the Strouhal number of the narrowband vortex shedding noise. This provides strong evidence that the vortex shedding noise is indeed produced by the periodic oscillation of flow within the sawtooth gap.

The spanwise coherence was measured in the near wake in an aerodynamic test, where the serrated trailing edges could be compared with a blunt trailing edge of the same bluntness. It is shown that by the lower spanwise coherence of a sawtooth caused by the existence of spanwise secondary flow (which differs with the longitudinal vortices that are shed from the blunt serration roots). The strouhal numbers of the tonal frequencies produced by the serrated trailing edge are found to vary between 0.1 and $U^{0.15}$ whilst the fully blunt trailing edge provides a constant Strouhal number throughout the flow velocity.

5.9 Outlook

The results presented on the turbulent flow *over* a serrated trailing, are related to the turbulent flow over a flat plate where there is no flow on the other side. Although it is outside the scope of the present PhD work, in order to thoroughly investigate this issue, an experiment to investigate the flow physics over an airfoil with a serrated trailing edge, where flow exists on both the suction and pressure surfaces, was carried out. The test was performed in the wake field produced by a NACA0012 airfoil with a straight trailing edge and a non-flat plate serrated trailing edge (S3). A triple-sensor hot wire probe (TSI-1299) was used to measure the three-velocity components in the wake flow. Again, boundary layer tripping elements were applied close to the leading edges of both the suction and pressure sides. The serrated trailing edge of the airfoil (S3), which has exactly the same sawtooth parameters as the current flat plate case, can achieve up to ~ 5 dB broadband noise sound power reduction as it was shown in chapter 4. The rationale behind the airfoil wake experiment is to examine whether the footprints of the oblique vortical structure, as well as the longitudinal vortex shedding emanating from the partial-blunt roots, can be found in the airfoil's near wake.

Figure 5.27a shows the streamwise vorticity contour in y - z plane at $x/C = 1.03$ for the airfoil with a straight trailing edge. C is the airfoil chord. The freestream velocity is 20 ms^{-1} and the airfoil is set at 3° angle of attack. The streamwise vorticity produced by the serrated trailing edge is plotted in Fig. 5.27b. Note that a 5.7mm bluntness exists at each of the sawtooth roots.

For the straight trailing edge, the wake flow is characterized by alternately positive and negative regions of streamwise vorticity across the span of the airfoil. This is common in a wake flow where spanwise rib-like structures are present. However, for the serrated trailing edge, the wake field is more complex. At the region close to the sawtooth roots,

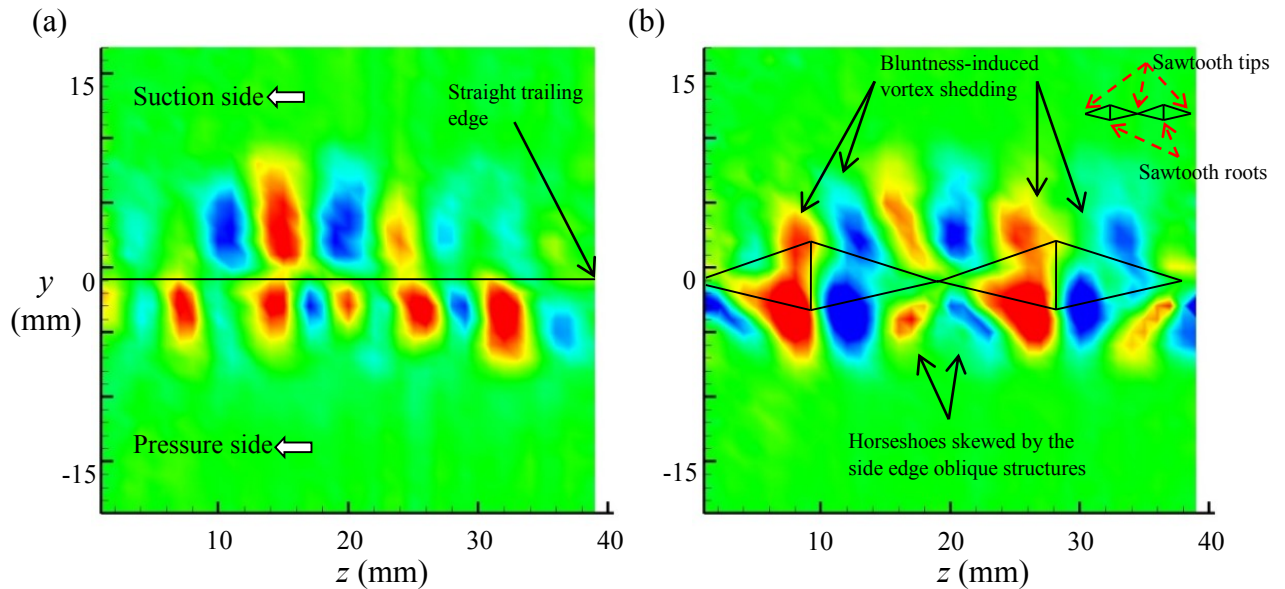


Figure 5.27 Contours of streamwise vorticity produced by a NACA0012 airfoil at $x/C = 1.03$, and 3 degree angle of attack, with a (a). Straight trailing edge; and (b). Serrated sawtooth trailing edge of $2h = 20$ mm and $\phi = 25^\circ$.

large streamwise vortical structures are developed across the suction and pressure sides, which is caused by the bluntness-induced vortex shedding emanated from the sawtooth roots. At the region of the sawtooth tips, the otherwise rib-like structures become more skewed and oblique in shape (especially at the pressure side) and they also tend to mirror around the sawtooth tip. This could be due to the interaction between the rib-like vortices and the side edge oblique vortical structure identified earlier in the chapter. The results in Fig. 5.27 thus provide a hint that the side edge oblique vortical structure observed in the flat plate configuration might also be present in the airfoil case.

Chapter 6

Porosity-Serrated trailing edge devices for airfoil self-noise reduction

This chapter presents a new concept which further improves the non-flat plate serration type trailing edge to achieve a complete reduction of airfoil self-noise across a wide frequency range. The concept maintains exactly the same serration geometries as presented in the previous chapters with the additional use of porous metal foams to fill the gaps between adjacent members of the sawtooth, therefore termed as '*porosity-serrated trailing edges*'. With the addition of the porous materials, the trailing edge will appear straight with no change in its three-dimensional shape. The noise performance of porosity-serrated trailing edges will be presented in the following sections, with analysis focusing on the blunt noise suppression and the broadband noise reductions. The mechanism of broadband noise reduction will also be studied. There are two possible broadband noise reduction mechanisms. One is associated with the oblique edges due to the serrations, and the other potentially arises from porosity, allowing the pressure and suction sides of the airfoil to 'communicate', thereby reducing the acoustic dipole strength at the trailing edge. It will be shown amongst others that the reduction of the broadband noise is primarily caused by the serration effect. Additionally, the lift and drag characteristics will be presented and compared to a straight baseline case. Finally, thin brush bundles were also tested which further extend the porosity-serrated concept, as comparable noise reduction capabilities are found.

6.1 Preliminary concepts which returned only partial success

Prior to the development of the poro-serrated trailing edges, a variety of trailing edge concepts was investigated to eliminate the vortex shedding while maintaining the broadband noise reduction capability. However, they proved partially successful or in some cases ineffective. Table 6.1 shows a summary of the prototypes comprising variations of the original non-flat plate serration design “S3” of $\varphi=25^\circ$, $2h=20\text{mm}$, $\varepsilon=5.7$, discussed in Chapter 4, where it became clear that improvements were required to make the concept effective and viable. The contour maps in table 6.1 depict the difference in sound pressure level, ΔSPL , between a straight and a serrated trailing edge at $\alpha=0^\circ$. Positive values represent noise reductions and negative values represent noise increase.

A first modification was attempted through wrapping a mesh screen around the serrated trailing edge. Although it is not shown here, the vortex shedding could be reduced more effectively at $\alpha=4.2^\circ$ and at the same time larger broadband noise reductions can be demonstrated than at $\alpha=0^\circ$. The rationale behind this is to introduce some flow resistance at the sawtooth gaps to inhibit the formation of the vortex shedding. However, as shown in table 6.1b, this approach is not effective at all in suppressing the vortex shedding noise at $\alpha=0^\circ$ and it seems that the level of broadband noise reduction is also reduced when compared to the non-flat plate type serrated trailing edges seen in Table 6.1a. In addition, some noise increase is observed at very high frequency ($>10\text{kHz}$), which presumably is caused by the surface roughness induced by the mesh screen on the surface.

The design shown in Table 6.1c consists of a 0.5mm thick flat plate placed within the serration root in order to inhibit the generation of vortex in its vicinity. Although this proves to be effective in suppressing the vortex shedding noise, the serration effect on the broadband noise reduction is also virtually eliminated, as the noise behavior became more similar to the baseline straight trailing edge. The concept in Table 6.1d shows an induced porosity to the same 0.5mm flat plate where multiple holes of 1mm diameter were drilled through to give a $\sim 70\%$ porosity. Through the holes it is hoped that the porosity can again provide the appropriate flow resistance to inhibit the formation of vortex shedding, whilst

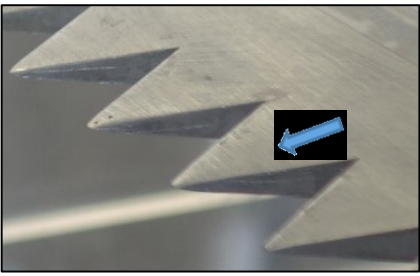
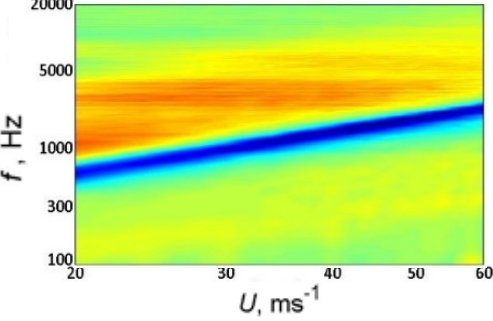
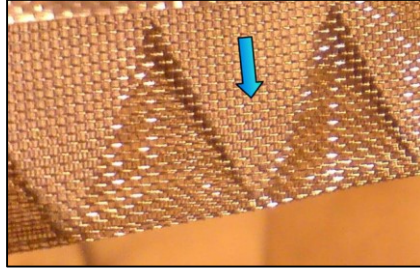
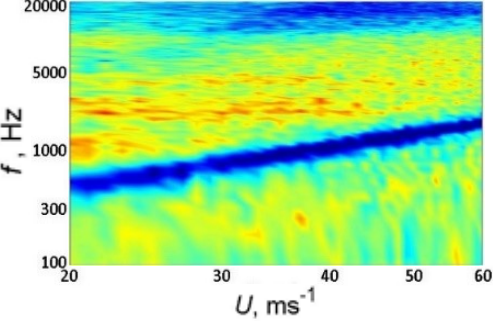
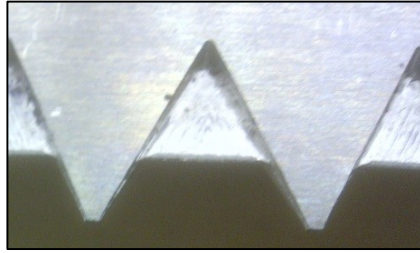
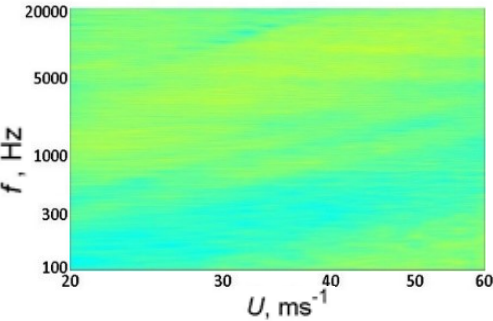
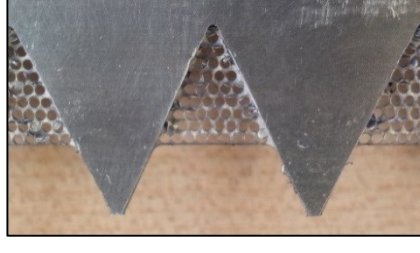
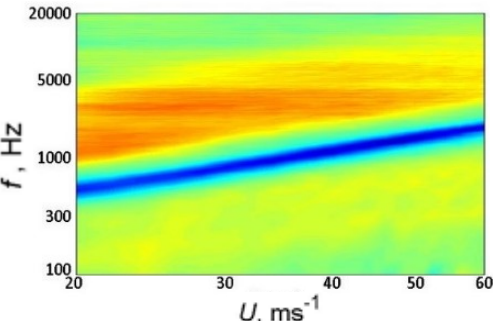
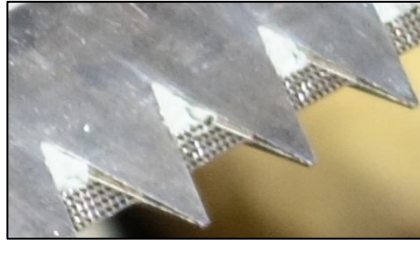
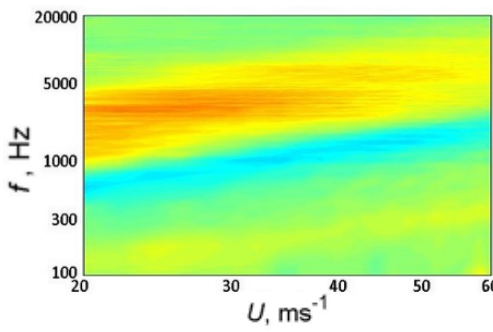
<p>a) Non-flat plate serrations</p>		
<p>b) Non-flat plate serrations with wrapped mesh</p>		
<p>c) Non-flat plate serrations with 0.5mm thin plate inserts</p>		
<p>d) Non-flat plate serrations with 'porous' 0.5mm thin plate inserts</p>		
<p>e) Non-flat plate serrations with 'semi -porous' 0.5mm thin plate insert</p>		

Table 6.1 Development of the preliminary design concepts for the elimination of vortex shedding of non-flat plate serrations. The blue arrows indicate the direction of the airflow.

retaining the effect of serration in the broadband noise reduction. However, the resulting contour map is almost identical to the original non-flat plate serration in Table 6.1a. A slightly better performance, when compared to the above cases, was achieved through blocking the upper half of the holes close to the root on the design of Table 6.1d, as seen in Table 6.1e. A moderation of the vortex shedding noise is achieved retaining most of the broadband noise reductions by the serration effect. This result encourages further investigation of using porous materials within the serration roots.

The results presented in Table 6.1d and 6.1e provide an avenue for further improving the serration technology. It seems that by introducing an adequate flow resistance in the sawtooth gap, the tendency of vortex shedding can be minimized. In the following, a porous material which would fill the gap was introduced to eliminate bluntness and at the same time balance the interaction of the pressure and suction surfaces which should be appropriate to attain the serration effect and eliminate the vortex shedding. The poro-serrations show to successfully achieve this goal. The proto type porous insert is shown in Figure 6.1a) and its modified variation of brush-type inserts as the porous medium is shown in Figure 6.1b).

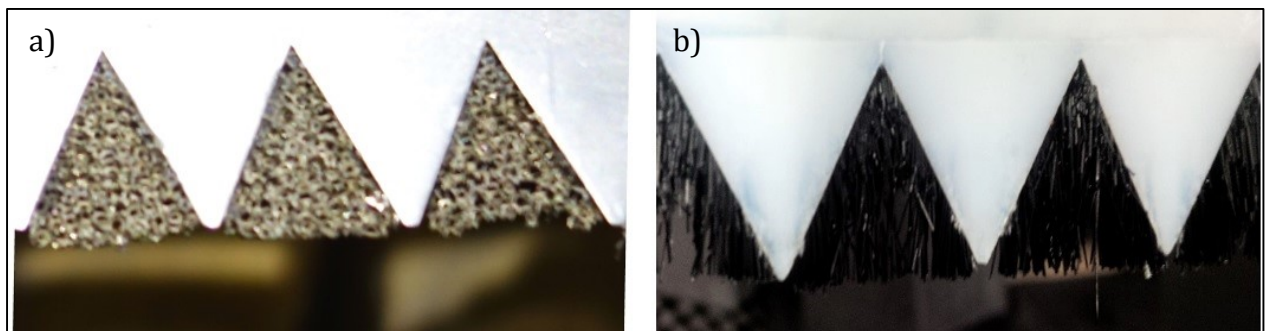


Figure 6.1 poro-serrated trailing edges with (a) porous metal foam and (b) brush inserts

6.2 Poro-serration concepts and models

A total of nine trailing edge sections, including a sharp, straight trailing edge to serve as the baseline case, were investigated for this chapter. Table 6.2 summarises the geometrical parameters and drawings of these trailing edge sections. In particular, the poro-serrated trailing edges S1⁺ and S3⁺ represent the core of investigation in this study. Note that (S1, S1⁺) and (S3, S3⁺, S3⁻, S3^Δ and S3^o), share the same $2h$ and ε values but have

different values of φ and λ/h . The S1-group of serrations therefore has a narrower sawtooth angle compared to the S3-group of serrations as in Chapter 4. As already mentioned, the porous metal foams were cut exact to match the shape of the interstices, so that the airfoil with either the S1+ or S3+ poro-serrated trailing edge would have a continuous NACA0012 profile throughout the chord length. Similarly, solid blocks were also cut precisely to match the shape of the interstices in the S3- trailing edge. Another point to note is that only one type of porous metal foam, of flow resistivity $r = \sim 8 \text{ kPa s/m}^2$, was investigated here. Tripping tapes were placed at about $0.15C$ from the leading edge of the NACA0012 airfoil on both sides to artificially trigger the boundary layers into turbulent.

The free field measurements of the airfoil self-noise were conducted in the open jet wind tunnel at Brunel University. Moreover, some repeatability tests on the noise performance are made in the case of the S3 and S3+ serrations in DARP Rig at the University of Southampton. The range of jet speeds under investigation was between 20 ms^{-1} and 60 ms^{-1} , with a step size of 2 ms^{-1} , corresponding to Reynolds numbers based on C of 2×10^5 and 6×10^5 respectively. In this study, the airfoil noise will focus on the angle of attack of $\alpha = 0^\circ$, however, some complimentary results for the noise performance at angles of attack $\alpha = 2.81^\circ$ are provided too. As described in Section 3.1.2, the far field noise measurements at the Brunel Aeroacoustic Wind Tunnel were made by a condenser microphone at polar angles of $\Theta = 90^\circ$ at a distance of 1.0 m from the airfoil trailing edge at mid span. The noise data were acquired at a sampling frequency of 44 kHz for 10s. An acoustic camera with a 0.35 m diameter carbon-body ring array consisting of 32 microphones (as described in Section 3.1.2) was used to beamform the noise source radiated from the airfoil.

To investigate the footprints of the vortex shedding in the wake subjected to the poro-serrated trailing edge, single hot-wire probe was used to measure the mean and fluctuating velocities of the airfoil wake. The hot-wire probe was attached to a computer-controlled two-dimensional traverse system (described in section 3.5.1).


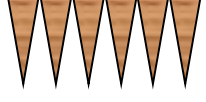


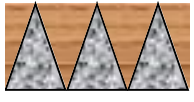
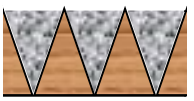
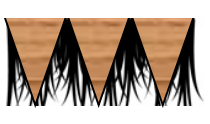






Symbols	Descriptions	Illustrations
S0	Baseline, straight, solid trailing edge	
S1	Nonflat plate serrated trailing edge; $2h = 20$ mm, $\varphi = 7^\circ$, $\lambda/h = 0.49$ and $\varepsilon = 5.7$ mm	
S1 ⁺	(Poro-Serrated trailing edge) Same parameters as S1; sawtooth gaps filled with porous metal foams	
S3	Nonflat plate serrated trailing edge; $2h = 20$ mm, $\varphi = 25^\circ$, $\lambda/h = 1.87$ and $\varepsilon = 5.7$ mm	
S3 ⁺	(Poro-Serrated trailing edge) Same parameters as S3; sawtooth gaps filled with porous metal foams	
S3 ⁻	Same parameters as S3; opposite to S3 ⁺ ; porous sawtooth, gaps filled with solid surface	
S3 ^Δ	(Poro-Serrated trailing edge) Same parameters as S3; sawtooth gaps <u>partially</u> filled with thin layer of brushes	
S3 ^o	Same parameters as S3; Sawtooth gaps remain open; Sawtooth made from porous metal foams	
SP	Porous, straight trailing edge; same porous material as those in S1 ⁺ and S3 ⁺ ; same $2h$ as S1, S1 ⁺ , S3, S3 ⁺ , S3 ⁻ , S3 ^Δ and S3 ^o	
 Solid  Porous insert  Porous serration  Brushes		

Table 6.2 Summary of all the trailing edge devices tested in this study. Note the trailing edge drawings are all subjected to the main stream flow from top to bottom. Drawings are not to scale.

6.3 Poro-serration experimental results

6.3.1 Noise results

The spectra of the noise produced by the group of serrations (S0, S1, S1⁺) and (S0, S3, S3⁺) were measured at a velocity of $U = 40 \text{ ms}^{-1}$, which are shown in Figs. 6.3a–b respectively. The figures demonstrate that airfoil trailing edge serrations cut into the main body of the airfoil (S1, S3), or with the metal porous foam filling the gaps between adjacent members of the sawtooth (S1⁺, S3⁺), has a substantial effect on the radiated noise spectra compared

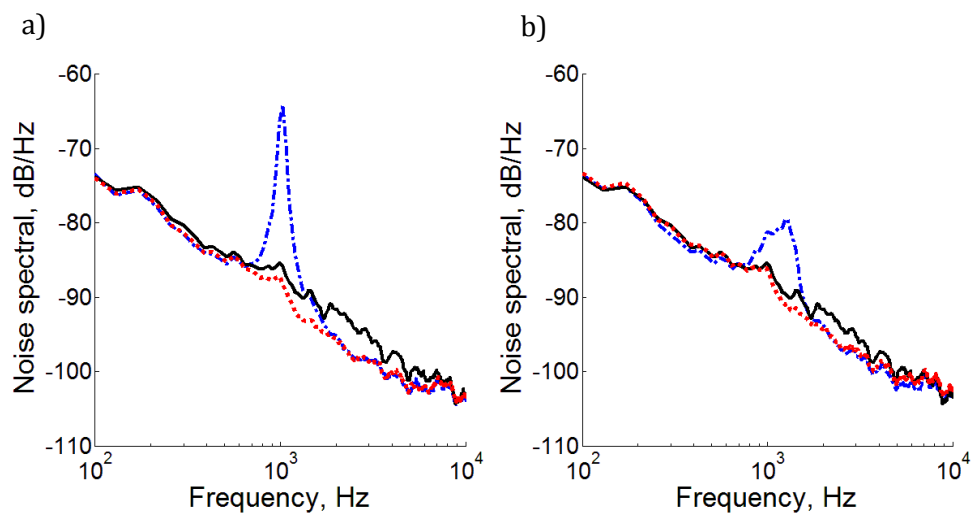


Figure 6. 3 Comparisons of the noise spectral measured at $U = 40 \text{ ms}^{-1}$ for a) S0 (—), S1 (— · —), S1⁺ (· · ·) trailing edges; and b) S0 (—), S3 (— · —), S3⁺ (· · ·) trailing edges.

to the untreated baseline trailing edge S0. First, as expected, a tonal increase is produced for both the S1 and S3 serrations due to the bluntness-induced vortex shedding in the wake. The peak in the noise spectrum produced by the S1 serrated trailing edge has a narrower frequency bandwidth and larger noise magnitude than that produced by the S3 serrated trailing edge. As previously explained in Chapter 4, the S1 serration has a greater number of “blunt roots” per unit span leading to greater spanwise coherence of the longitudinal vortex shedding for the narrower serration angle. Therefore a serrated trailing edge with a narrower serration angle, such as the S1 case, should produce a higher tone noise level.

At frequencies well above the vortex shedding frequencies both the S1 and S3 serrated trailing edges provide broadband noise reductions across a large range of frequency. In

some cases, noise reduction in excess of 5dB is observed. The narrower serration is found to provide greater noise reductions than the wider serration, consistent with the theoretical predictions of Howe (1991). In conclusion, therefore, a serration cut into the main body of an airfoil with a narrower serration angle provides better broadband noise reduction, but more intense vortex shedding noise. With metal foam now introduced between adjacent teeth, both S1⁺ and S3⁺ porous-serrations not only *completely* suppress the bluntness-induced vortex shedding noise, but also provide a consistently lower noise level compared to the baseline straight trailing edge.

Comparing the proposed poro-serrated trailing edge S1⁺ with its S1 counterpart reveals similar levels of broadband noise reduction at frequencies, f , greater than about 1.7 kHz. In addition, the spectral shapes follow a similar frequency oscillation pattern at $f > 1.7$ kHz. The same observation applies to the S3⁺ and S3 trailing edges, where similar levels of broadband noise reduction are observed at $f > 1.85$ kHz and both follow the same spectral shape.

Another significant advantage of introducing metal foam in the gaps between adjacent teeth is that increases in noise at very high frequencies (>10 kHz), produced with the use of conventional flat plate type serrated trailing edges, as reported by Gruber et al. (2011) are avoided. They attributed this noise increase to the presence of cross-jet through the gaps between adjacent teeth. However, with the introduction of metal foam now filling this gap, this mechanism is now avoided and no increase in noise is observed over the frequency range of interest up to 20 kHz. The following section will discuss more thoroughly the impact of introducing the (S1⁺, S3⁺) poro-serrated trailing edges to the airfoil self-noise reduction.

Although not presented here for clarity reasons, a few noise measurements were carried out at $\alpha = 2.82^\circ$ (i.e. at a geometrical angle of 10° tested in the DARP Rig) where poro-serrated trailing edges yield a very similar outcome for the noise performance. It is subject of further research to investigate higher angles of attack in detail.

6.3.2 Suppression of the bluntness-induced vortex shedding tonal noise

As the source of the vortex shedding tonal noise is located at the airfoil's near wake region a hot-wire probe was used to measure the wake flow in a two-dimensional y - z plane at $x/C = 1.03$ for the S0, S1 and S1+ trailing edges. The flow measurement was carried out *in situ* at the Brunel aeroacoustic wind tunnel, i.e., the identical experimental condition to

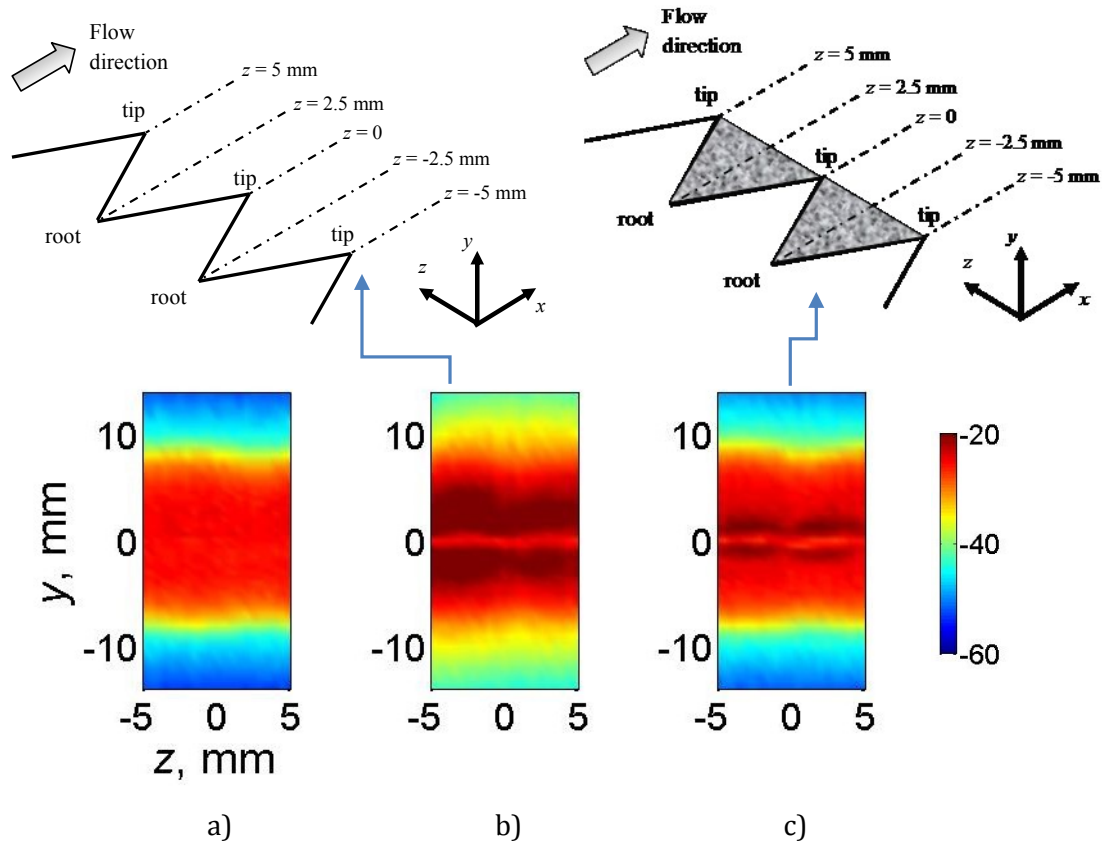


Figure 6.4 Comparisons of the near wake fluctuating velocity spectral density ($10\log_{10}$) measured at $x/C = 1.03$ and at $U = 40 \text{ ms}^{-1}$ for a) S0; b) S1 and c) S1+ trailing edges. All the spectral maps correspond to $f = 1 \text{ kHz}$.

the noise measurements presented in Fig. 6.3a where $U = 40 \text{ ms}^{-1}$. The hot-wire measurements were made over the plane of $(y, z) = (\pm 14 \text{ mm}, \pm 5 \text{ mm})$, at a resolution of 0.5 mm in both directions. As shown in Fig. 6.4, $z = -5, 0$ and 5 mm correspond to the tip of the sawtooth; whilst $z = -2.5$ and 2.5 mm correspond to the root of the sawtooth, where $y = 0$ corresponds to the trailing edge.

Figures 6.4a–c show contour maps of the fluctuating velocity spectral density at a frequency of 1 kHz for the S0, S1 and S1+ trailing edges, respectively. This frequency corresponds to the spectral peaks produced by the S1 serrated trailing edge as demonstrated in Fig. 6.3a. For the S0 baseline case, where no tone noise is observed, the fluctuating velocity spectrum is uniform across the spanwise (z) direction. However, for the non-flat plate serrated trailing edge S1 in Figure 6.4b, the level of fluctuating velocity spectrum is much higher. Large velocity fluctuation can also extend to the otherwise freestream region ($y > 12 \text{ mm} \in y < -12 \text{ mm}$). The large velocity fluctuation is seen to be fairly uniform across the z direction, thus lending further support to the observation that stronger coherent vortex shedding can be produced by a narrow angle serrated trailing edge.

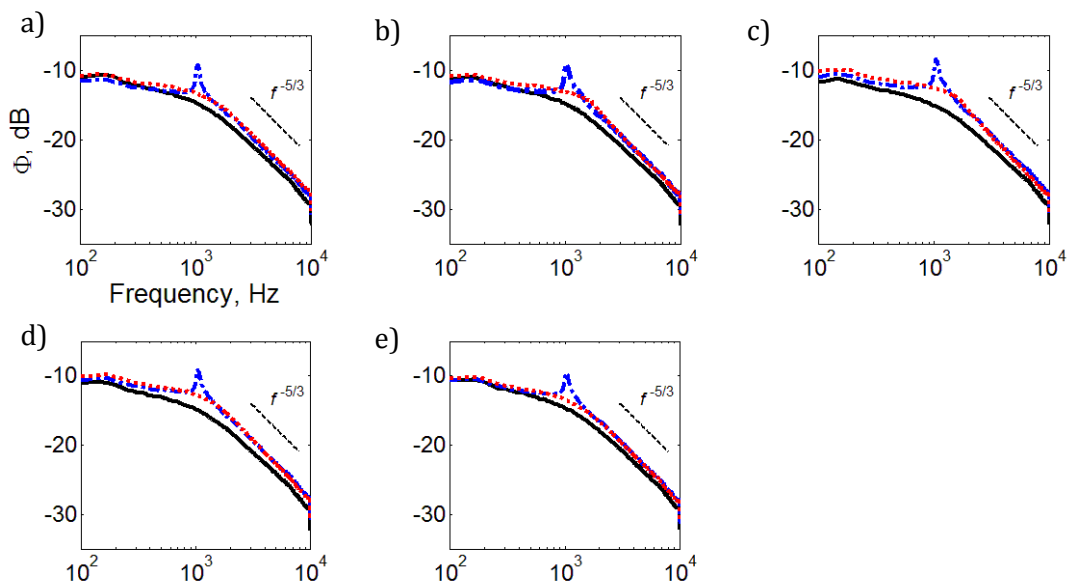


Figure 6.5 Comparisons of the near wake Φ , dB measured at $x/C = 1.03$ and at $U = 40 \text{ ms}^{-1}$ for S0 (—), S1 (---), S1+ (···) trailing edges at: a) $z = 0$ mm (sawtooth tip); b) $z = 1$ mm; c) $z = 2.5$ mm (sawtooth root); d) $z = 4$ mm; and e) $z = 5$ mm (sawtooth tip)

As soon as the gaps between adjacent members of the sawtooth are filled with the porous metal foams (S1+), Figure 6.4c indicates that the fluctuating velocity spectral contour map becomes almost identical with that produced by the baseline S0 trailing edge. The only exception is that the S1+ poro-serrated trailing edge produces extra feature comprising two narrow, slightly wavy lines of large velocity fluctuations mirrored at around the $y = 0$ line. These are likely to be caused by the rough surface of the porous metal foams where the turbulence level of the near wall boundary layer is enhanced. The waviness of the two lines is caused by the different extent of roughness length of the porous metal foams

across the spanwise direction, i.e. maximum near the sawtooth roots ($z = \pm 2.5$ mm) but minimum at the sawtooth tip ($z = 0, \pm 5$ mm).

The overall wake spectral energy at a particular z location, $\Phi(z, f)$, can be estimated from:

$$\Phi(z, f) = 10 \log_{10} \int \phi'(z, f) dy \quad (\text{eq. 6.1})$$

where $\phi(f)$ is the fluctuating velocity spectrum in the wake flow. Figures 6.5a–e compare the $\Phi(z, f)$ for the S0, S1 and S1+ serrations at $z = 0$ (tip), $z = 1$ mm, $z = 2.5$ mm (root), $z = 4$ mm and $z = 5$ mm (tip), respectively. The dominant narrowband peaks in the wake for the S1 serrated trailing edge, which occur at approximately 1 kHz, match exactly the acoustic tones measured by the free field microphone in Figure 6.3a. When the serrated trailing edge is replaced with the S1+ serration the narrowband peaks in the wake are completely suppressed across the whole range of z . The overall wake spectral energy levels produced by the S1 serrated and S1+ poro-serrated trailing edges are quite similar beyond the tone frequency (i.e. $f > 1$ kHz). All the S0, S1 and S1+ spectra feature the same high frequency roll-off of $f^{-5/3}$, but the serrated spectral (S1 and S1+) exhibit a 2 dB offset with the baseline, S0 spectrum near the root region.

6.3.3 Broadband noise reduction

In the previous section, only noise results at $U = 40$ ms⁻¹ were presented. Here the performance of the poro-serrated trailing edges is examined at other velocities. The difference in Sound Pressure Level (ΔSPL) between a baseline, straight trailing edge (S0) and the serrated trailing edges (S1, S1+, S3 and S3+) is calculated by

$$\Delta\text{SPL} = \text{SPL}_{\text{baseline}} - \text{SPL}_{\text{serration}}$$

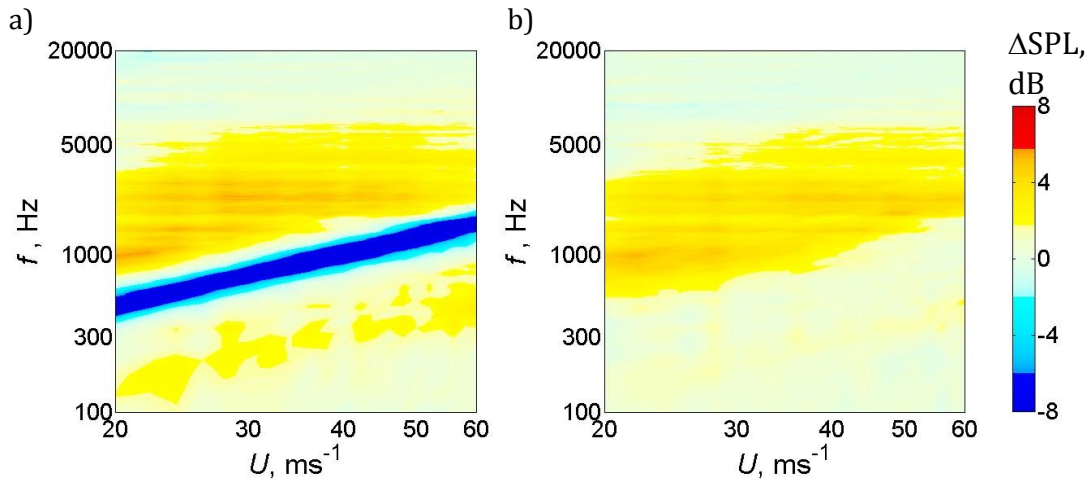


Figure 6.6 Colormaps of the ΔSPL , dB, for the vortex shedding tonal noise reduction and turbulent broadband noise reduction by using a) S1 serrated trailing edge; and b) S1+ poro-serrated trailing edge.

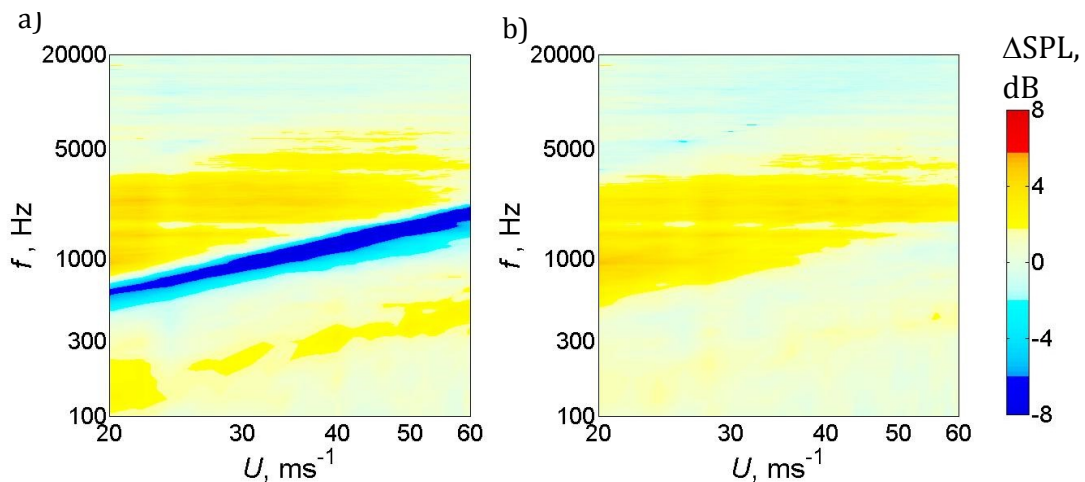


Figure 6.7 Colormaps of the ΔSPL , dB, for the vortex shedding tonal noise reduction and turbulent broadband noise reduction by using a) S3 serrated trailing edge; and b) S3+ poro-serrated trailing edge.

Figures 6.6a and 6.6b, and 6.7a and 6.7b show contour maps of ΔSPL as a function of frequency and mean velocity ($U = 20\text{--}60\text{ ms}^{-1}$) for the S1 and S1+ serrations, and for the S3 and S3+ serrations, respectively. For the serrated trailing edges S1 and S3 in Figures 6.6a and 6.7a, significant Strouhal-dependent tonal ‘rungs’ over a narrowband frequency range (light to dark blue colors) are accompanied by substantial broadband noise reduction over a larger frequency range (yellow to red colors). The tonal rung is related to the bluntness-induced vortex shedding noise where it becomes less significant as the serration angle increases. The level of broadband noise reduction also reduces as the

serration angle increases. This phenomenon has been observed similarly for the non-flat plate serrations.

As shown in Figure 6.6b and 6.7b, the current work represents a substantial improvement in noise control performance in that the tonal rungs can now be completely suppressed by the addition of porous metal foams in the gaps between the teeth, whilst the efficiency of broadband noise reduction is completely preserved. Within the velocity range under investigation here, up to 7 dB broadband noise reduction can be achieved.

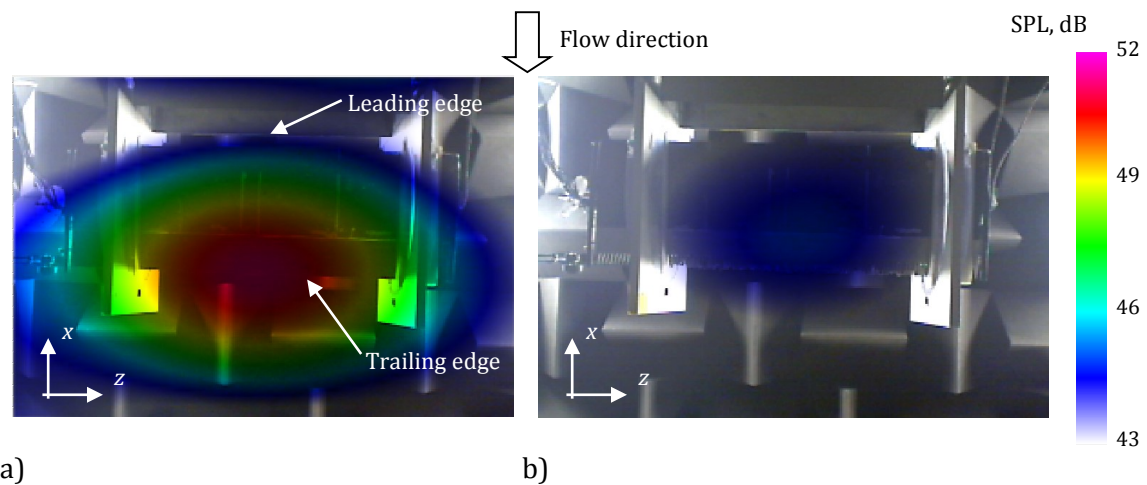


Figure 6.8 Comparisons of the acoustic maps at 2.3 kHz at $U = 40 \text{ ms}^{-1}$ for a) baseline S0 trailing edge and b) S1+ poro-serrated trailing edge.

Beamforming was applied to estimate the location of the noise source through the use of the acoustic camera. Figure 6.8a shows the noise map corresponding to the baseline, S0 case at $U = 40 \text{ ms}^{-1}$. The frequency in the figure is 2.3 kHz, which corresponds to where the broadband noise reduction occurs (see Figure 6.3a). The noise map in Figure 6.8a demonstrates that the broadband noise, as seen from the previous noise spectral measured by a single microphone, is mainly radiated from the straight trailing edge of the airfoil. In Figure 6.8b, where the trailing edge is now replaced with the S1+ porous-serration type, the noise map demonstrates a significantly reduced level of broadband noise radiation from the trailing edge by more than 5 dB.

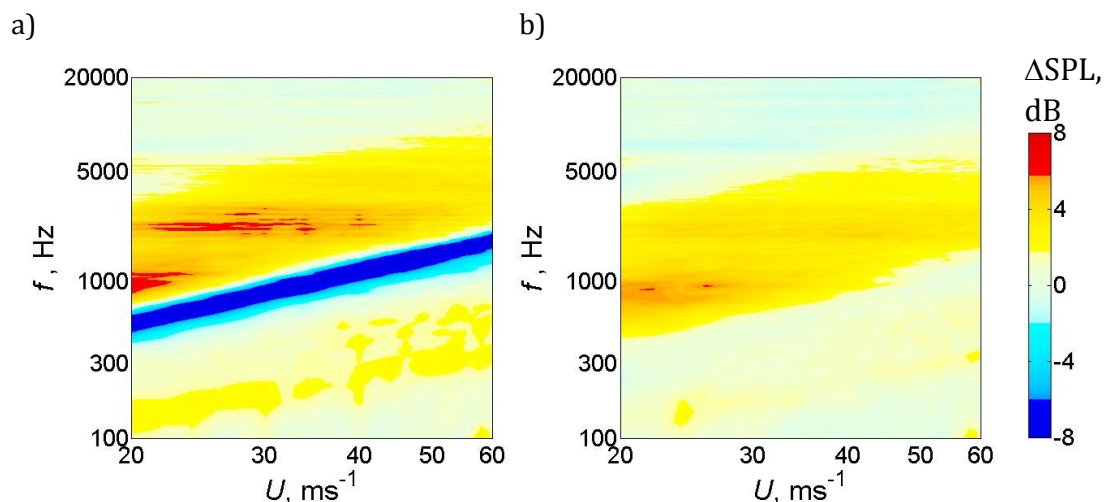


Figure 6.9 Colormaps of the ΔSPL , dB, for the vortex shedding tonal noise reduction and turbulent broadband noise reduction by using a) S3 serrated trailing edge; and b) S3⁺ poro-serrated trailing edge. This repeatability test was performed at the ISVR anechoic chamber.

As mentioned in Section 6.2 an identical experiment has been performed in the open jet wind tunnel rig at the ISVR, University of Southampton which confirm repeatability. Figures. 6.9a and 6.9b show the corresponding contour maps of ΔSPL , as a function of frequency and mean velocity ($U = 20\text{--}60 \text{ ms}^{-1}$), for the S3 serrated and S3⁺ poro-serrated trailing edges, respectively. Comparing Figs. 6.7a–b and Figs. 6.9a–b shows good repeatability of the noise performance by the S3 and S3⁺ trailing edges. The poro-serrated trailing edge concept and its abilities to completely suppress bluntness-induced vortex shedding noise and significantly reduce broadband noise have been re-confirmed.

6.3.4 Mechanism of Broadband Noise Reduction – by Serration, or by Porosity?

The fully porous airfoil has shown to achieve significant broadband noise reductions [Geyer et al. (2010)]. However, by making the airfoil fully porous, the overall lift is reduced and drag is increased significantly. In order to recover some of the aerodynamic performance for a fully porous airfoil, Geyer and Sarradj (2014) used a thin PVC film to cover the main part of the airfoil body, thereby exposing only a partially porous trailing edge. If s denotes the chordwise extent of the porous trailing edge, it took the value of $0.05 < s/C < 0.5$ in Geyer and Sarradj's experiment. They observed that broadband noise was still reduced by the partially porous trailing edge, which they attributed to the damping of the hydrodynamic pressure fluctuations by the porosity at the trailing edge.

The S1⁺ and S3⁺ poro-serrated trailing edges investigated in this study utilize porous metal foams to fill the gaps between adjacent members of the sawtooth. As illustrated in the drawings in Table 6.2, the region near the trailing edges of S1⁺ and S3⁺ exhibits a zigzag-like solid-porous surface, i.e. the solid sawtooth and the “inverted” porous sawtooth both have approximately the same surface areas. Whether the broadband noise reduction by the S1⁺ and S3⁺ poro-serrated trailing edges is due to the serration or increased porosity, or both, will be determined next.

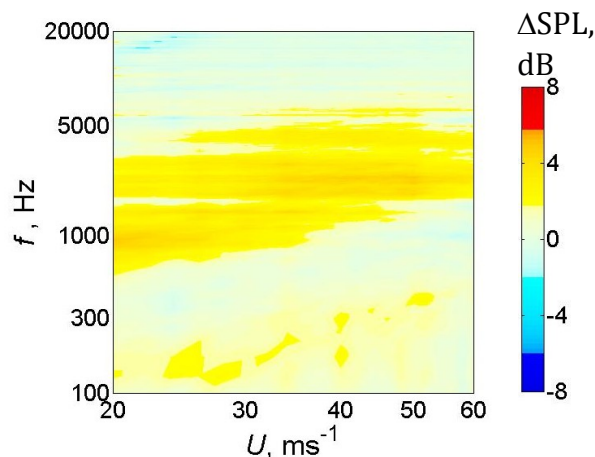


Figure 6.10 Colormap of the ΔSPL , dB, for the turbulent broadband noise reduction by using the S3^A trailing edge (serrated trailing edge filled with brushes).

To determine the noise reduction mechanism, several unconventional serrated trailing edge devices were manufactured and tested. The first is denoted here as the S3^A serration, as illustrated in Table 6.2. This configuration comprises a thin layer of brushes in place of the porous metal foam to lightly fill the gaps between adjacent members of the S3 sawtooth. The rationale behind the introduction of brushes is to inhibit vortex shedding

at the blunt root region, as an alternative to the porous structures. The corresponding noise map of ΔSPL versus frequency and mean flow speed is shown in Fig 6.10. By comparing Fig. 6.7b and Fig 6.10, the $S3^A$ serrated trailing edge is seen to be as effective as the $S3^+$ poro-serrated trailing edge in suppressing vortex shedding tonal noise. Moreover, the frequency range over which broadband noise reduction achieved by the $S3^A$ serrated trailing edge is even slightly wider than the $S3^+$ poro-serrated trailing edge, especially in the mid to higher velocity regions. This results strongly suggest that the broadband noise reduction by the $S3^+$ (and also $S1^+$) poro-serrated trailing edge is due to the serration and not porosity. Further work is needed to understand the behavior and performance of this new configuration ($S3^A$), which certainly offers a foundation for future investigation.

The brushes in the $S3^A$ serrated trailing edge must be relatively thin. If the brush density

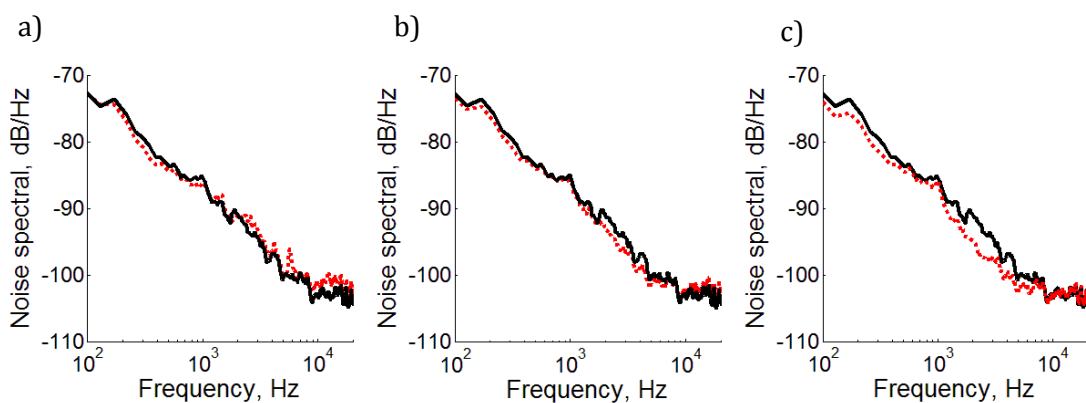


Figure 6.11 Comparisons of the noise spectral measured at $U = 40 \text{ ms}^{-1}$ between the baseline $S0$ trailing edge (—) and the $S3^A$ serrated trailing edge ($\cdot\cdot\cdot$) with a) thick; b) medium and c) thin brush bundles that fill the gaps between adjacent members of the sawtooth.

at each sawtooth gap is too high, the effectiveness of the broadband noise reduction will be negated. At the same time, some high frequency noise increases will also result. This behavior is reflected in Figures. 6.11a–c for the noise spectral measured at $U = 40 \text{ ms}^{-1}$ by the $S3^A$ serrated trailing edge with “thick”, “medium” and “thin” brush densities at the sawtooth gaps. Note that the “medium” and “thin” brush densities are approximately 60% and 30%, respectively, of the “thick” brush density. The results demonstrate that the overall noise performance improves as the brush density reduces.

The second trailing edge device is referred to as $S3^-$ ‘serrated-porous’ trailing edge, which can be regarded as an inverted version of the $S3^+$ poro-serrated trailing edge. As illustrated in Table 6.2, whilst the sawtooth is replaced with porous metal foam, the former gaps are now filled with solid, nonporous object. The corresponding noise map of

Δ SPL versus frequency and flow speed is shown in Figure 6.12. Because of the absence of the blunt surface exposure for the S3⁻ serrated-porous trailing edge, bluntness-induced vortex shedding tonal noise is not produced. However, it is observed that the S3⁻ serrated-porous trailing edge is less effective than its S3⁺ counterpart in terms of the broadband noise reduction. Comparing Fig. 6.7b and Fig. 6.12 reveals that noise reductions only occur at a much lower frequency than the S3⁺ poro-serrated trailing edge, and the frequency

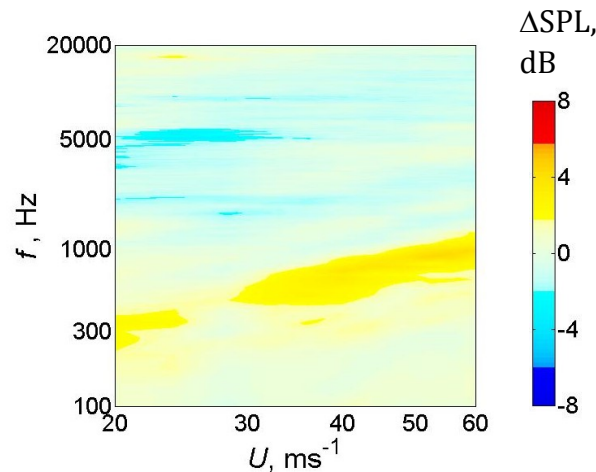


Figure 6.12 Colormap of the Δ SPL, dB, by using the S3⁻ (inverted, opposite to S3⁺); serrated trailing edge

bandwidths are also smaller. In addition, the S3⁻ serrated-porous trailing edge produces higher noise level than the baseline S0 trailing edge at $f > 1$ kHz across the whole velocity range. Therefore, the overall noise performance of the S3⁻ serrated-porous trailing edge is not satisfactory.

The third trailing edge device investigated in this section is denoted as SP. This trailing edge device is formed by machine cutting porous metal foam to produce a continuous trailing edge profile, which is then attached to the solid airfoil body, thus resembling the partially porous, straight trailing edge concept of Geyer and Sarradj (2014). Note that the SP partially porous trailing edge does not contain any serration pattern. The porous metal foam section of SP has $s = 20$ mm, which is the chordwise extent of porous material from the trailing edge. Hence, it is kept to exactly the same value as $2h$ of the S1⁺ and S3⁺ poro-serrated trailing edges. The corresponding noise map of Δ SPL versus frequency and flow speed for the SP partially porous trailing edge is shown in Figure 6.13. Noise reductions are seen to be limited to the higher flow speeds of $U > 30$ ms⁻¹. At $f > 8$ kHz, at all velocities, noise is observed to increase which is likely to be caused by the surface roughness of the

porous metal foams. Also present in the noise map is a weak, Strouhal-dependent narrowband ‘rung’. This is likely to be caused by a vortex shedding event, although the exact cause and origin of this feature are not presently known.

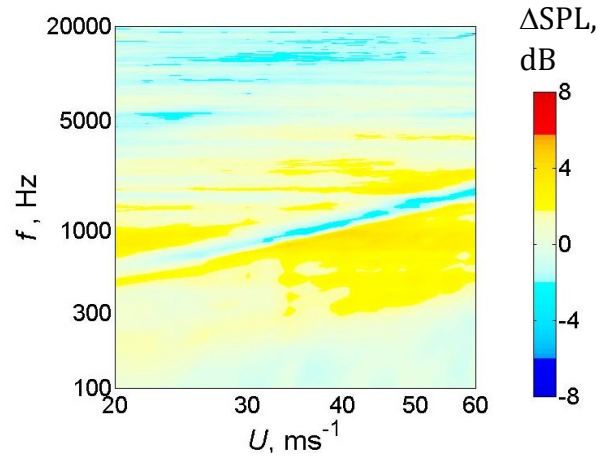


Figure 6. 13 Colormap of the ΔSPL , dB, by using the SP partially porous trailing edge.

Both the SP partially porous trailing edge and S3⁻ serrated-porous trailing edge are only effective in noise reduction at low frequencies with a narrow bandwidth. This is markedly different if compared with the S1, S1⁺, S3, S3⁺ and S3^Δ serrated trailing edges, which all have demonstrated superior noise reduction capabilities. The S3⁻ serrated-porous trailing edge contains the same amount of porous metal foam as the S3⁺ counterpart per unit span, and yet it only achieves noise reduction in similar frequency bandwidth as the partially porous SP trailing edge that does not feature sawtooth serration at all. Therefore, there is strong evidence that the broadband noise reduction achieved by the S1⁺ and S3⁺ poro-serrated trailing edges is mainly caused by the effect of the serration, not the porous metal foam.

6.4 Aerodynamic forces produced by poro-serrated trailing edges

Aerodynamic measurements were made in a conventional closed working section wind tunnel at Brunel University as described in Section 3.2.2.1. It is used for measurements of the lift and drag produced by the NACA0012 airfoil with different trailing edge devices as per the Table 6.2. The airfoil model was mounted horizontally across the entire width of the 0.5 m x 0.5 m test section with a free-stream turbulence intensity of about 0.2–0.3%. In order to quantify the effect of the serration on aerodynamic performance a 3-component strain gauge force balance was used to measure the lift and drag forces produced by the airfoil (see Section 3.2.2.2) for the angles of attack from 0° to 20°.

As earlier discussed, most serrated trailing edges from previous investigations have been in the form of flat plate inserts. However, these alter the airfoil geometry and affect the global circulation around it, thus possibly leading to a deterioration in the aerodynamic performance.

The proposed trailing edge type preserves the original airfoil shape with the advantage that aerodynamic performance is not compromised. This section will investigate the effect of these various serrations on the lift coefficient (C_L) and drag coefficient (C_D) of the NACA0012 airfoil with the S1⁺ and S3⁺ poro-serrated trailing edges at an angles of attack (α) from 0° to 20°. The aerodynamic conditions may be different from the open jet wind tunnel used for the noise test but could still be useful for assessing changes in the aerodynamic performance. The velocity of the wind tunnel was set at 24 ms⁻¹ during the force measurements. For consistency the tripping elements near the airfoil's leading edge on both sides were retained.

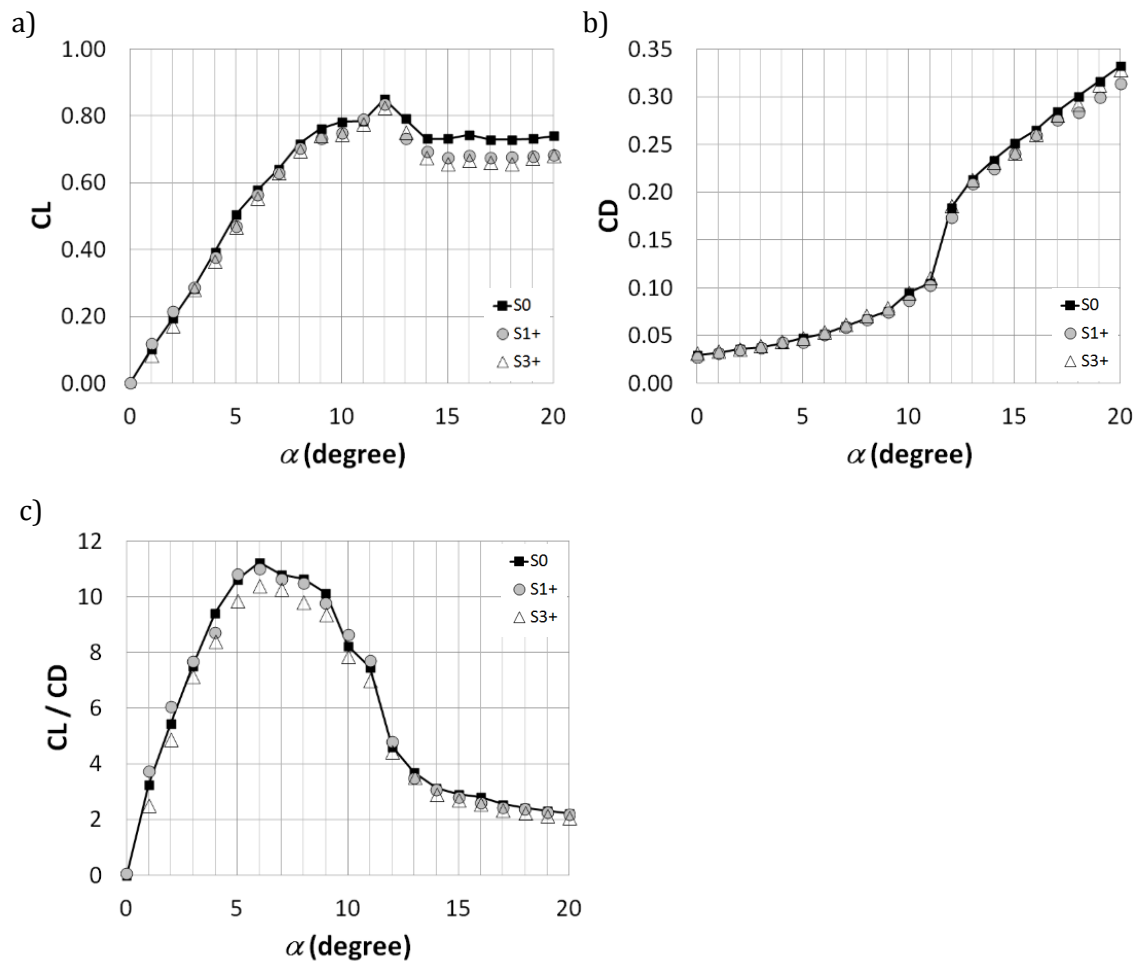


Figure 6.14 Comparisons of the aerodynamic forces produced by the S0 trailing edge (baseline), as well as the S1+ and S3+ poro-serrated trailing edges at $U = 30 \text{ ms}^{-1}$ for a) C_L ; b) C_D and c) C_L/C_D against the angles of attack, α .

Figure 6.14a presents the lift coefficients C_L versus angle of attack α for the S0, S1+ and S3+ trailing edges. For the baseline S0 trailing edge, C_L increases linearly with α at a rate of approximately 0.1 per degree up to $\alpha = 5^\circ$. Above this angle, the C_L increases at a slower rate and deviates from the thin airfoil theory. This may be due to the thickening of the boundary layer at the airfoil's suction side and the dominance of viscous effects. The stall angle is seen to occur at $\alpha \approx 12^\circ$, beyond which the C_L drops significantly, reaching a plateau at $14^\circ < \alpha < 20^\circ$. When the airfoil is replaced with the S1+ and S3+ poro-serrated trailing edges, the variations in C_L are similar to the S0 baseline case up to $\alpha \approx 8^\circ$. At angles, $8^\circ < \alpha < 12^\circ$ (stall angle), the S1+ and S3+ poro-serrated trailing edges perform slightly worse than the baseline S0 trailing edge, but deviate by no more than 4%. The S1+ and S3+ poro-serrated trailing edges also perform slightly worse at the post-stall regime, with a C_L now reduced by up to 10% compared to the baseline S0 case.

Figure 6.14b presents the drag coefficient C_D versus α for the S0, S1⁺ and S3⁺ trailing edges. For the S0 baseline trailing edge, the linearity of C_D with α is also observed up to $\alpha = 5^\circ$. Above this angle C_D increases at a higher rate. The stall angle at $\alpha = 12^\circ$ in the C_D curve is accompanied by a significant increase in C_D . As expected, C_D then further increases at a much higher rate with α at the post-stall regime. First the effect on C_D of the S3⁺ porous-serration is examined. Despite the increased surface roughness due to the porous metal foams, C_D associated with the S3⁺ poro-serrated trailing edge follows almost exactly the same behavior as the baseline S0 trailing edge throughout the pre-stall, and post-stall regimes up to $\alpha = 16^\circ$. At $\alpha > 16^\circ$, the S3⁺ poro-serrated trailing edge provides lower C_D than the baseline S0 case. Not only does the S1⁺ poro-serrated trailing edge never exceed the C_D values of the S0 trailing edge, but it also performs better than the S0 trailing edge at the post-stall regime, affording a maximum of 6% lower drag.

Another useful parameter used to examine the aerodynamic performance of the serrated airfoil is the lift-to-drag ratio (C_L/C_D). A large value of C_L/C_D is desired as it entails the maximum lift force generation with minimal drag penalty. Figure 6.14c shows the C_L/C_D versus α for the S0, S1⁺ and S3⁺ trailing edges. For the baseline S0 trailing edge, the ratio C_L/C_D steadily increases with α , reaching a maximum value at $\alpha = 6^\circ$. Between $6^\circ < \alpha < 9^\circ$, C_L/C_D falls steadily. After that the C_L/C_D undergoes a significant drop at $\alpha = 10^\circ$. A second significant drop happens again at $\alpha = 12^\circ$, corresponding to the stall angle. At $\alpha > 12^\circ$, at the post-stall regime, the C_L/C_D steadily declines with α . Examination of the S3⁺ poro-serrated trailing edge reveals that its C_L/C_D is consistently lower than the baseline S0 case. The largest discrepancy occurs at $4^\circ < \alpha < 9^\circ$, where up to a 17% difference is obtained. However, the S1⁺ poro-serrated trailing edge, which has a narrower serration angle, recovers its C_L/C_D to almost the same level as the baseline S0 trailing edge throughout the range of α in both the pre-stall and post-stall regimes. The remarkable recovery of C_L/C_D by the S1⁺ poro-serrated trailing edge is thus very encouraging.

Although the aerodynamic results provided in this section are far from exhaustive, they suggest that the best recovery of the aerodynamic performances for a poro-serrated trailing edge is related to the one with the smallest serration angle. This finding could have anticipated because the smallest serration angle entails a more periodic discontinuity of the porous metal foams in the spanwise direction, and that a constant porous medium as part of an airfoil is likely to be more detrimental for its aerodynamic

forces. Remarkably, this criterion for maintaining the aerodynamic performances is the same for achieving the optimal broadband noise reduction.

6.5 Near wall velocity Power Spectral Density and its implication to the Δ SPL noise contour maps

Sections 6.3.1 and 6.3.2 of this chapter have demonstrated the capability of the S1⁺ and S3⁺ poro-serrated trailing edges to completely suppress vortex shedding noise that would otherwise be produced by the S1 and S3 serrated trailing edges, whilst at the same time maintaining the same level of broadband noise reduction. It could be confirmed that broadband noise reductions by the S1⁺ and S3⁺ poro-serrated trailing edges can be attributed solely to the serration effect (in Section 6.3.3), even though by filling the gaps

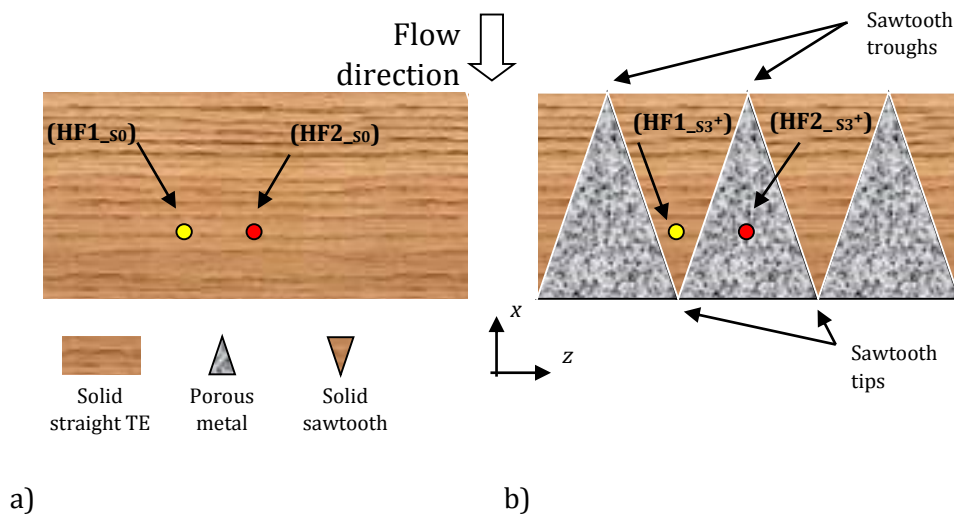


Figure 6.15 Schematics illustrating the locations of the hot-film sensors HF1 and HF2 with relative to the a) S0 trailing edge and b) S3⁺ poro-serrated trailing edge. Drawings are not to scale.

between adjacent members of the sawtooth in S1⁺ and S3⁺ a seemingly “straight” trailing edge is formed (see Figure 6.15a–b). However, further question remains for the increased surface roughness introduced by the porous metal foams and its implication to the noise radiation.

To address these issues two surface-mounted hot-film sensors (HF1 and HF2) were located onto the baseline S0, and the S3+ poro-serrated trailing edges at $x/C \approx 0.95$ but spaced 6 mm apart in the spanwise direction. This spanwise spacing for the S3+ poro-serrated trailing edge is designed such that one hot-film (HF1) is situated within the solid, nonporous sawtooth surface, while another hot-film (HF2) is situated within the porous metal foam, as illustrated in Figure 6.15b. The exact locations of HF1 and HF2 in the S3+ poro-serrated trailing edge are replicated for the S0 straight trailing edge (Figure 6.15a), though both hot-film sensors are now situated on the solid surface. The hot-film sensors were operated in a constant-temperature mode with a relatively mild overheat ratio of

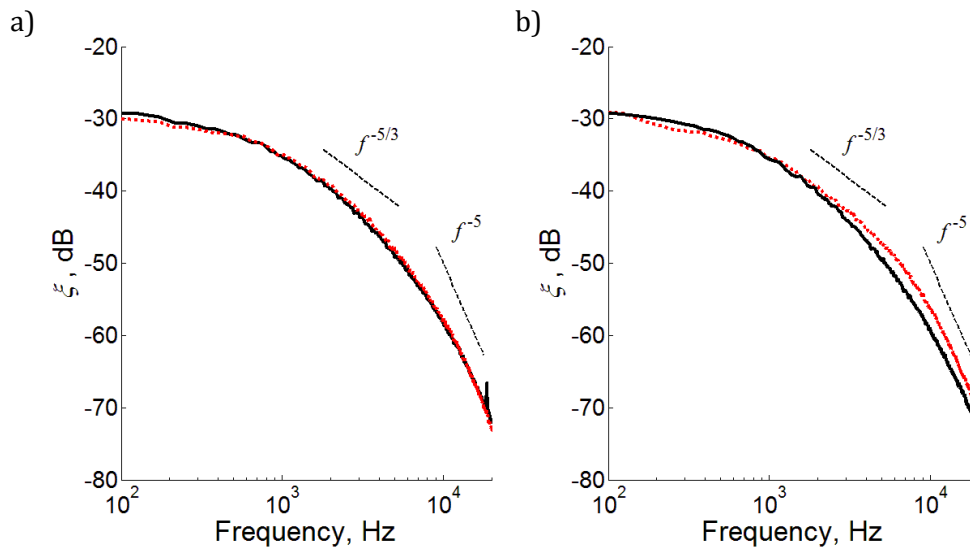


Figure 6. 16 Comparisons of the near wall fluctuating spectral (ξ , dB) measured by the hot-film sensors at $U = 40 \text{ ms}^{-1}$ for the a) HF1_{S0} (—) & HF1_{S3+} (· · ·) and b) HF2_{S0} (—) & HF2_{S3+} (· · ·).

1.4 to avoid adding excessive heating to the near wall boundary layer. Both are sampled simultaneously at 20 kHz.

The fluctuating signals measured by the hot-film sensor are non-dimensionalised by their standard deviation values, respectively. Figure 6.16a shows the corresponding spectra measured by the HF1_{S0} and HF1_{S3+} sensors at $U = 40 \text{ ms}^{-1}$. Note that the subscript denotes a particular type of trailing edge used. The mid-frequency and high-frequency roll-off of approximately $f^{-5/3}$ and f^{-5} , respectively, for both HF1_{S0} and HF1_{S3+} suggest that the turbulent boundary layer is fully developed². On the other hand, as shown in Figure. 6.16b, HF2_{S3+} (situated on the porous surface) produces slightly lower spectral level at low frequency, but considerably higher level at $f > 2.2 \text{ kHz}$, than the HF2_{S0} counterpart.

² This might only be true at $x/C = 0.95$. As shown in Chapter 5, the existence of some oblique vortical structures along the side edges of the solid-surfaced sawtooth is likely to yield different fluctuating spectral characteristics if x/C is closer to unity, i.e. towards the sawtooth tip.

Measurements of the surface mounted hot-film signals are performed at $20 < U < 60 \text{ ms}^{-1}$. The following parameter is introduced:

$$\Delta \xi_i (U, f) = \xi_{i_s0} (U, f) - \xi_{i_s3^+} (U, f), \quad (3)$$

where ξ is the power spectral density level measured by a particular type of hot-film sensor, $i = 1$ or 2 , for either the S0 and S3⁺ trailing edges. $\Delta \xi_1$ is designed to show the difference in power spectral density levels between HF1_{S0} and HF1_{S3⁺}, where both hot-film sensors are situated on solid surfaces. Likewise, $\Delta \xi_2$ will show the difference in power spectral density levels between HF2_{S0} and HF2_{S3⁺}, but the HF2_{S0} is situated on a solid surface and the HF2_{S3⁺} is on a porous surface. The largely zero value of $\Delta \xi_1$ in Figure 6.17a confirms that both the power spectral densities at locations HF1_{S0} and HF1_{S3⁺} are similar throughout the frequency-velocity domain. However, the $\Delta \xi_2$ contour in Figure 6.17b contains some significant variations. Three distinct zones can be identified from the figure:

1. Zone I (low frequency range) has a slight positive level of $\Delta \xi_2$ up to 2 dB.
2. Zone II (mid frequency range) contains the $\Delta \xi_2$ which is largely close to zero value.
3. Zone III (high frequency range) is characterized by a considerable negative level of $\Delta \xi_2$ up to -6 dB.

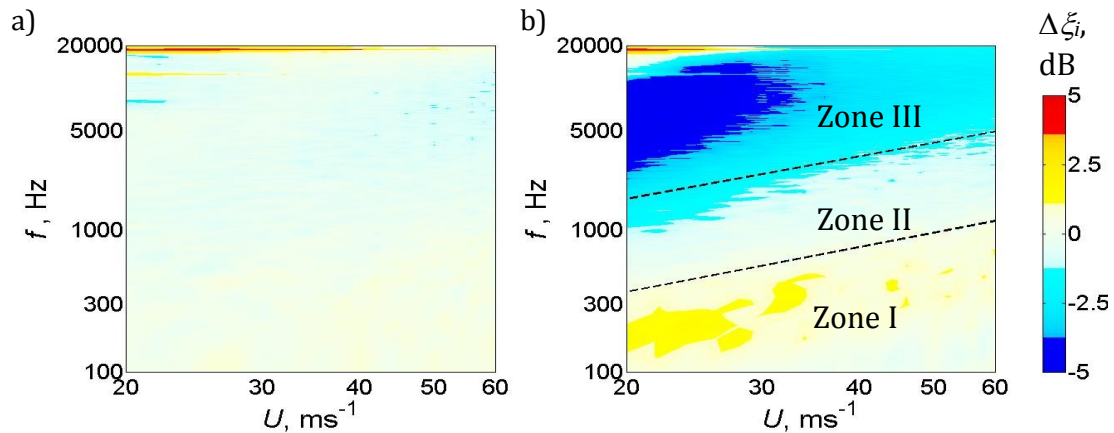


Figure 6.17 Colourmaps of a) $\Delta \xi_1$ and b) $\Delta \xi_2$.

It is assumed that the power spectral density measured by the hot-film sensors near the trailing edge shares a close causality with the radiated noise spectrum. Therefore, a predominantly negative level of $\Delta \xi_2$ in Zone III implies that the porous surface produces higher power spectral density level than the solid, non-porous surface. Because Zone III

is largely in a high frequency range, the negative level of $\Delta\xi_2$ could translate to a noise increase by the S3⁺ poro-trailing edge at high frequency. A positive level of $\Delta\xi_2$ in Zone I (low frequency range) would suggest that noise reduction is possible. Likewise, a zero level of $\Delta\xi_2$ in Zone II (mid frequency range) could stipulate an unchanged noise level. To verify the above conjectures, Zones I, II and III are embedded into a Δ SPL contour map in Fig. 6.17b. The following summarizes the outcomes of the comparison:

1. The negative level of $\Delta\xi_2$ in Zone III does not result in noise increase.
2. Noise reduction at Zone I is not realized despite the slight positive level of $\Delta\xi_2$.
3. Most crucially, most of the broadband noise reduction observed in the Δ SPL actually occurs at Zone II, where the level of $\Delta\xi_2$ is largely zero.

In summary, none of the initial conjectures are true regarding the effect of porous metal foams to the radiated noise. Despite that the porous metal foam will increase the overall ‘roughness’ of the trailing edge surface, it does not seem to increase the high frequency noise, nor to reduce the low frequency noise significantly. The only effect the porous metal foams could exert on the overall noise radiation for the S3⁺ poro-serrated trailing edge is to undermine the bluntness exposed by the serration roots, thus avoiding the vortex shedding tonal noise. Despite that the addition of the porous metal foam will cause the trailing edge to appear ‘straight’, it does not enhance the scattering efficiency that one would expect from a straight, unserrated trailing edge. Therefore the broadband noise reduction observed in the Δ SPL contours for the S1⁺ and S3⁺ poro-serrated trailing edges is primarily caused by the serration effect, and not by the porous metal foams.

Finally, the results provide thus far could provide a hint about the mechanism underpinning the broadband noise reduction by the S1⁺ and S3⁺ poro-serrated trailing edges. Table 6.3 summarizes the Δ SPL (f, U) for the S3-type trailing edges (S3, S3⁺, S3⁻, S3^Δ and S3^o), as well as the SP. In the table, Zones I, II and III identified from the $\xi_2(f, U)$ contour are also superimposed in each of the Δ SPL (f, U) contour maps. It is clear that the Δ SPL (f, U) associated with the above trailing edge devices could be categorized into two distinct groups (Group A and Group B). The S3, S3⁺ and S3^Δ trailing edges belong to Group A, from which significant broadband noise reduction is achieved at Zone II. On the other hand, the

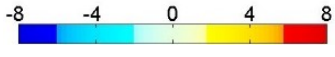

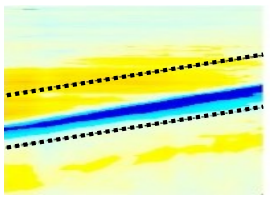

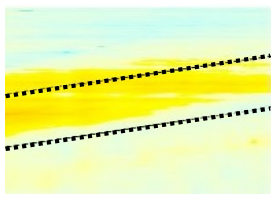

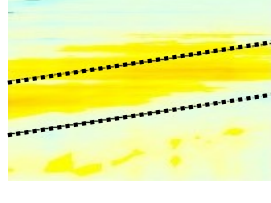
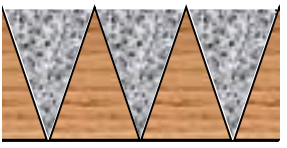
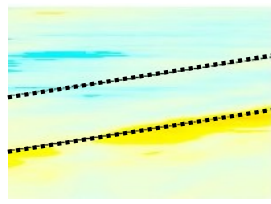
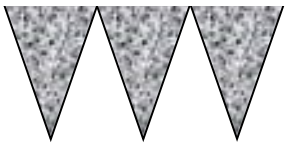
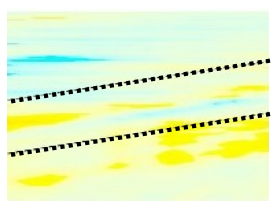

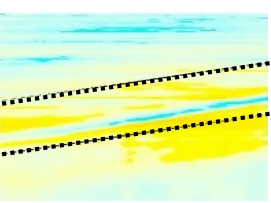
Notation	Illustrations		$\Delta\text{SPL}(f, U)$, dB 
S3		Group A	 <div style="display: flex; justify-content: space-between; width: 100%;"> Zone III Zone II Zone I </div>
S3 ⁺			 <div style="display: flex; justify-content: space-between; width: 100%;"> Zone III Zone II Zone I </div>
S3 ^Δ			 <div style="display: flex; justify-content: space-between; width: 100%;"> Zone III Zone II Zone I </div>
S3 ⁻		Group B	 <div style="display: flex; justify-content: space-between; width: 100%;"> Zone III Zone II Zone I </div>
S3 ^o			 <div style="display: flex; justify-content: space-between; width: 100%;"> Zone III Zone II Zone I </div>
SP			 <div style="display: flex; justify-content: space-between; width: 100%;"> Zone III Zone II Zone I </div>

Table 6.3 Summary of all the noise performances in ΔSPL , dB, for the S3, S3⁺, S3⁻, S3^Δ, S3^o and SP trailing edge devices tested in this study. Positive level of ΔSPL denotes noise reduction, and vice versa. The three zones (I, II and III) in the ΔSPL maps were identified from the $\Delta\xi^2$ contours in Fig. 6.17b.

Group B trailing edges ($S3^-$, $S3^0$ and SP) could only produce noise reductions in the lower frequency region of Zone I. The frequency bandwidth is also narrower, and these trailing edges seem to be only effective at $U > 30 \text{ ms}^{-1}$. In addition, noticeable level of noise increase occurs at Zone III, and some in Zone II.

A common feature of the Group A trailing edges ($S3$, $S3^+$ and $S3^\Delta$) is that their sawtooth serrations are made from solid surfaces. Likewise, all the trailing edges in Group B ($S3^-$ and $S3^0$) have their sawtooth serrations, including a partially porous, unserrated trailing edge in the SP case, made from porous metal foam. Such distinction stipulates that an effective broadband noise reduction would require the sawtooth serrations to be made from solid surface. It remains an interesting question that a sawtooth serration made from porous metal foams, even if it shares the same geometrical parameters as the sawtooth surface made from solid surface, could not demonstrate a similar capability in broadband noise reduction. The answer may be related to the acoustic scattering efficiency of the turbulent wavenumber components on a porous sawtooth serration.

6.6 Discussion

This chapter reports the study on the aeroacoustic properties of a NACA0012 airfoil with a number of poro-serrated trailing edge devices ($S1$, $S1^+$, $S3$, $S3^+$, $S3^-$, $S3^\Delta$, $S3^0$ and SP). In particular, the trailing edges $S1^+$ and $S3^+$ with metal foam inserts represent the core of investigation, and the suggestion of brush inserts between the serration gaps comprises a further subject for further investigation. All these trailing edge devices, when integrated to an airfoil body, will retain the original airfoil's shape and offer better structural stability than the conventional, flat plate type serrated trailing edge. The free field noise measurements, as well as the wake flow measurement, were carried out inside an aeroacoustic wind tunnel facility at Brunel University. The range of jet speeds under investigation was between 20 ms^{-1} and 60 ms^{-1} , corresponding to Reynolds numbers based on airfoil chord of 2×10^5 and 6×10^5 respectively. The lift and drag forces produced by the airfoil when fitted with the poro-serrated trailing edges were quantified in a separate aerodynamic wind tunnel.

The use of S1 and S3 serrated trailing edges will result in sound pressure level reduction of the broadband noise up to 7 dB. However, noise increase caused by the vortex shedding from the exposed blunt roots is also very significant, especially for the S1 case. The use of porous metal foams to fill the gaps between adjacent members of the sawtooth, as demonstrated by the S1⁺ and S3⁺ poro-serrated trailing edges, can completely suppress the vortex shedding tonal noise, whilst the level of broadband noise reduction remains unaffected. These poro-serrated trailing edges also demonstrated an excellent repeatability in noise performance when tested in another aeroacoustic facility. There is little aerodynamic penalty if these poro-serrated trailing edges are integrated to the airfoil body. Another benefit these poro-serrated trailing edges exhibit over the flat plate type serrated trailing edge, is the absence of noise increase at high frequency. A trend discernible from the current results is that the S1⁺ poro-serrated trailing edge (with a narrower serration angle) performs better acoustically and aerodynamically than the S3⁺ counterpart.

Two possible broadband noise reduction mechanisms could be associated with the poro-serrated trailing edges. One associated with the oblique edges due to the serrations, as discussed in Chapter 5, and the other arising from porosity which allows the pressure and suction sides to 'communicate' therefore reducing the acoustic dipole strength at the trailing edge. No correlation has been found between the broadband noise reduction and the porous metal foams. The only effect the porous metal foams could exert on the noise radiation for the poro-serrated trailing edge is to undermine the bluntness exposed by the serration roots, thus avoiding the vortex shedding tonal noise. There are clear evidences that the main mechanism underpinning the broadband noise reduction by a poro-serrated trailing edge should come from the serration effect.

Another promising concept developed in this study is the S3^Δ serrated trailing edge where the gaps between adjacent members of sawtooth were partially filled with thin brushes instead of the porous metal foams. The levels of noise reduction for both the vortex shedding tonal noise and the turbulent broadband noise are similar with the S3⁺ poro-serrated trailing edge. More interestingly, the S3^Δ serrated trailing edge achieves broadband noise reduction over a wider bandwidth in frequency range than the S3⁺ poro-serrated trailing edge, especially at higher velocity.

For all the trailing edge devices tested, two main groups can be formed based on the noise performances. The first group (S1, S3, S1⁺, S3⁺ and S3^Δ) is characterized by a solid sawtooth serration and every member within this group consistently demonstrated a

significant trailing edge broadband noise reduction. The second group ($S3^-$ and $S3^0$), where every member within this group utilizes sawtooth made from porous metal foams, offers no advantage on the broadband noise reduction even though it shares the same geometrical parameters of serration as the first group. The reason for this may be related to the acoustic scattering efficiency of the turbulence on a porous sawtooth serration.

Chapter 7

Conclusions and further work

7.1 Conclusions overview

This thesis presents results of an experimental investigation focusing the “*non-flat plate*” type sawtooth serrated trailing edge for the reduction of trailing edge broadband noise. This configuration is superior when compared to add on type flat plate serrations, from the aspect of structural integrity by directly cutting the serrations into the airfoil main body.

With regard to the objectives initially set, Chapters 4, 5 and 6 describe the effort towards a successful achievement of these targets. Initially, the non-flat plate configuration was assessed successfully for its noise characteristics in relation to various serration geometries. It was generally shown that good levels of broadband noise reduction can be achieved, with the overall noise reduction however being compromised by the bluntness-induced narrowband vortex shedding noise (**Chapter 4**).

Much effort was also devoted to effectively study the fundamental mechanism of broadband noise reduction by a serrated trailing edge, which comprises an extensive experimental investigation on the turbulent boundary layer characteristics when passing over a sawtooth surface (**Chapter 5**). The various experiments focus on the near wall properties (heat transfer, wall pressure power spectral density and coherence function) and the time-averaged velocity power spectral density and Reynolds shear stresses. The turbulent boundary layer velocity signals are also conditionally averaged to obtain the temporal variation of the momentum and turbulence properties across the sawtooth surface. Acoustic measurements were performed, where the results not only confirm that broadband noise reduction can be achieved by a serrated sawtooth trailing edge, but also prove a causal relationship between the radiated noise and the near field hydrodynamic observations. The results presented in this chapter can help to improve the understanding of the mechanism underpinning the noise reduction by a serrated sawtooth trailing edge, and also to provide an avenue for further development of other control techniques based on similar physical principles.

Finally, a new approach to promote the non-flat plate type serrated trailing edge was developed successfully in this PhD work (**Chapter 6**). Key to the noise reduction method is the use of porous materials located between adjacent members of sawtooth to fill the gap simultaneously preserving the airfoil profile throughout the chord length. Considerable broadband noise reductions were achieved whilst completely suppressing the narrowband vortex shedding noise at the blunt part of the serration root. Regarding the levels of noise reduction, there are only a very few alternative technologies to date which are capable of delivering a comparable noise performance.

The flow resistance of the metal foam is shown to inhibit vortex shedding, provided that the flow resistance is within a certain range. In this PhD work, the porous metal foam of moderate flow resistivity ($r = \sim 8 \text{ kPa s/m}^2$) has been found to suppress vortex shedding noise while maintaining the benefits of the serrated trailing edge, i.e. the broadband noise reductions which are simultaneously achieved without any loss of efficiency. The combination of porosity and serrations at the trailing edge is thereby termed as “*Poro-Serrated trailing edge*” throughout this thesis.

A more detailed summary of main findings of this thesis is presented below.

7.1.1 Non-Flat plate serrations (Chapter 4)

Extensive acoustic measurements were performed for four non-flat plate type serrated trailing edges at three angles of attack ($\alpha=0^\circ$, 1.4° and 4.2°), across flow speeds between 20ms^{-1} and 60ms^{-1} , which correspond to the Reynolds number of 2×10^5 and 6×10^5 , respectively, based on the airfoil chord.

- Significant narrowband vortex shedding noise is observed. This extraneous noise source thus compromises the benefit of turbulent broadband noise reduction provided by the serration.
- With regard to the turbulent broadband noise, the trend observed in the current experimental study agrees with the theoretical model by Howe, who states that a smaller serration angle φ is required to maximise the level of broadband noise reduction. The largest level of noise reduction observed in the current study, using the non-flat plate serrated trailing edge, is about 6.5-7dB. However, this value is significantly smaller than Howe’s theoretically predicted values of $\sim 20\text{-}30\text{dB}$. It should be stated that the average level of broadband noise reduction obtained in

the current study is consistent with experimental findings by others. The discrepancy between Howe's model and most of the experimental findings is likely to be caused by the assumption of frozen turbulence in the model, which implies perfect destructive coherent interferences along the sawtooth oblique edges. In depth investigation of the mechanism of broadband noise reduction by sawtooth serration was carried out and the results are discussed in Chapter 5.

- By taking into account the narrowband vortex shedding noise, small to moderate Overall Sound Power Level (OAPWL) reductions can still be achieved by the non-flat plate serration provided that the serration angle is sufficiently large to limit the spanwise coherence of the vortex shedding, and that the angle of attack is sufficiently large. It is found that the reduction in OAPWL can reach a maximum of 3dB at an effective angle of attack of $\alpha=4.2^\circ$.
- Aerodynamic force measurements show that the lift and drag coefficients of the airfoil subjected to the non-flat plate serrated trailing edges are similar to the baseline, sharp trailing edge case throughout the pre-stall regime. For the post-stall regime, the lift coefficient is slightly reduced, but the drag coefficient is also reduced. The combination of these results in a very similar lift-to-drag ratio among the cases for both the pre- and post-stall regimes.

7.1.2 Mechanism of broadband noise reduction by serrated trailing edge (Chapter 5)

Results of an experimental study on turbulent flow over a flat plate with a serrated sawtooth trailing edge are presented in this chapter. After tripping the boundary layer to become turbulent, the turbulence-induced broadband noise sources at the sawtooth serrated trailing edge is studied by several experimental techniques.

- Broadband noise reduction by the serrated sawtooth trailing edge can be realistically achieved in the flat plate configuration.
- A conditional-averaging technique was applied for the boundary layer data where a pair of pressure-driven oblique vortical structures near the sawtooth side edges is identified. These structures are shown to amalgamate at the sawtooth tip. The interaction between the vortical structures and the local turbulent boundary layer results in a redistribution of the momentum transport and turbulence energy near

the sawtooth side edges and tips. This interaction can affect the scattering efficiency and reduce the radiated broadband noise level.

- The variations of wall pressure power spectral density and the spanwise coherence (which relates to the spanwise correlation length) in a sawtooth trailing edge play a minor role in the mechanisms involved for the reduction of self-noise radiation. According to Amiet's model, an increased wall pressure (S_{qq}) near the sawtooth side edges and sawtooth tip would result to increased radiated noise level (S_{pp}). This effect, however, is considered to be insignificant as its contribution will be small when compared to the ~50% loss in momentum and ~75% loss in kinetic energy near the sawtooth side edges through the viscous-inviscid interaction between the turbulent eddies and the oblique vortical structures respectively.
- To relate the present result of the flat plate configuration with a realistic airfoil, the near wake of an NACA0012 airfoil with non-flat plate serrations was measured by a triple hot-wire probe to determine the streamwise vorticity of the velocity. At $\alpha=5^\circ$, at the region of the sawtooth tips, the vortical structures identified by the streamwise vorticity are more skewed and oblique in shape, and also tend to mirror around the sawtooth tips, for the non-flat plate serrated trailing edge than those produced by a baseline, sharp trailing edge. This suggests that the wake structure is strongly influenced by the side edge oblique structures originated from the sawtooth surface as identified earlier. This observation provides a hint that the side edge oblique vortical structure observed in the flat plate configuration is also very likely to be present in the airfoil case. Therefore, the mechanism of broadband noise reduction studied in the flat plate configuration will share a large degree of similarity with the airfoil case.

7.1.3 "Poro-serrated" trailing edge (Chapter 6)

A new trailing edge concept was developed, which originated from the non-flat plate serrations by introducing a porous material, or brush bundle, to fill the serration gaps of the partially blunt roots. The investigation of the new concept reaches to the following conclusions.

- This concept substantially improves the overall noise performance of the non-flat plate trailing edge serration type as it can completely suppress the bluntness-induced vortex shedding noise from non-flat plate serrations. Most importantly,

turbulent broadband noise reductions of up to 7dB can be achieved by incorporating a porous material or thin brush bundle to fill the serration gaps. It is worth noting, however, that only a single porous material is tested in the current work. Therefore, the concept offers a possibility to achieve an even larger level of broadband noise reduction by testing different types of porous materials on their variations in flow resistance, permeability and porosity.

- After testing more configurations (e.g. SP, S3⁻ and S3^o), it can be concluded that the main mechanism responsible for the broadband noise reduction observed in the experiment is primarily due to the sawtooth serration. For example, when a straight porous trailing edge without the serration (SP) is used, only a limited level (and frequency range) of noise reduction is observed. As far as the particular porous metal foam used in the present study is concerned, its effect on the radiated noise is limited to the suppression of the narrowband vortex shedding noise. The possibility of additional noise reductions by another porous material is however not to be excluded.
- The aerodynamic performances of the “poro-serrated” trailing edge in lift and drag are very close in comparison with the baseline, sharp trailing edge throughout the pre-stall regime. In the post-stall regime, both, the poro-serrated trailing edges S1⁺ and S3⁺ yield a smaller lift coefficient, but also a smaller drag coefficient, if compared to the baseline sharp trailing edge. Generally speaking, the poro-serrated trailing edge with a narrower serration angle, S1⁺, appears to perform slightly better and almost identical to the baseline case, including the lift-to-drag ratio.
- The poro-serrated trailing edges do not cause any noise increase throughout the frequency range investigated here, which covers the audible frequency range. It is worth noting that this is a substantial improvement over the conventional flat plate type serrated trailing edge where noise increase at high frequency is always observed (Oerlemans et al. 2009 and Gruber 2012).
- The most significant contribution of this thesis is therefore the successful development of the poro-serrated trailing edge that offers (1) significant broadband noise reduction, (2) no noise increase throughout the audible range, (3) no change of the overall airfoil shape, (4) no compromise of the aerodynamic performance, and (5) good structural integrity. The poro-serrated trailing edge might revive the researchers interest of the non-flat plate serration concept and

most importantly could improve the industrial worthiness of the serration technology in achieving low noise radiation in the relevant applications.

7.2 Suggestions for future work

The concept of poro-serrated trailing edges could be further developed to improve the technological readiness level. A viable path for the continuation of the work is a parametric study of varying the sawtooth geometries and different porous materials (in terms of flow resistance, permeability, pore size, rigidity and pore structure) at the gaps of the teeth, over a wider range of Reynolds numbers and angles of attack. If an optimal porous material selection could be identified, then further reductions in the broadband noise levels may be possible. In terms of the serration geometries, some unconventional shapes such as the slitted sawtooth geometries [Gruber (2012)], or combination of sawtooth and wavy trailing edges could be investigated.

A pair of pressure-driven, oblique vortical structures near the sawtooth side edges was identified in the current work. The interaction between the oblique vortical structures and the local turbulent boundary layer will then cause deficiencies in the momentum and kinetic energy that ultimately affect the noise scattering efficiency. Based on similar physical principles, reduction of broadband noise might be achieved by placing an array of miniature vortex generators, or vertical blade devices, near the sharp trailing edge to artificially generate oblique vortex shedding.

Finally, the effectiveness of the trailing edge serrations on noise radiation depends on whether the turbulent boundary layer remains attached at the trailing edge region. For a high pressure loading configuration, i.e. when the airfoil is subjected to a large angle of attack, the boundary layer could already be separated near the trailing edge on the suction side, subsequently rendering any form of trailing edge serration as ineffective. The humpback whale is known to be able to maneuver its flipper at a large angle of attack due to the leading edge serration/undulation/tubercles. Inspired by this feature, many researches have successfully demonstrated boundary layer separation control on airfoil with leading edge serrations. Therefore, to be more widely industrially compatible, the poro-serrated trailing edge developed in this study could also incorporate leading edge serrations to allow the airfoil operating at a wide range of pressure loadings.

References

- ACARE - Advisory Council for Aeronautics Research in Europe, (2001). *European Aeronautics : A vision for 2020: Meeting society's needs and winning global leadership, report of the European Commission*. European Commission.
- ACARE - Advisory Council for Aeronautics Research in Europe, (2011). *Flightpath 2050 Europe's Vision for Aviation*. Report of the High Level Group on Aviation Research, report of the European Commission.
- Adrian, R. (2007). Hairpin vortex organization in wall turbulence. *Physics of Fluids*, 19(4), pp.041301-041301.
- Adrian, R., Meinhart, C. and Tomkins, C. (2000). Vortex organization in the outer region of the turbulent boundary layer. *Journal of Fluid Mechanics*, 422, pp.1-54.
- Airbus, (2013). Global Market Forecast, *Future Journeys 2013-2032*.
- Amiet, R. (1976). Noise due to turbulent flow past a trailing edge. *Journal of Sound and Vibration*, 47(3), pp.387-393.
- Amiet, R. (1978). Effect of the incident surface pressure field on noise due to turbulent flow past a trailing edge. *Journal of Sound and Vibration*, 57(2), pp.305-306.
- Arbey, H. and Bataille, J. (1983). Noise generated by airfoil profiles placed in a uniform laminar flow. *Journal of Fluid Mechanics*, 134(-1), pp.33-47.
- ATAG - Air Transport Action Group, (2015). *Aviation Benefits Beyond Borders Report*.
- Bachmann, T. (2010). *Anatomical, morphometrical and biomechanical studies of barn owls' and pigeons' wings*.
- Bachmann, T., Klän, S., Baumgartner, W., Klaas, M., Schröder, W. and Wagner, H. (2007). Morphometric characterisation of wing feathers of the barn owl *Tyto alba pratincola* and the pigeon *Columba livia*. *Front Zool*, 4(1), pp.23-23.
- Baughn, J. (1995). Liquid crystal methods for studying turbulent heat transfer. *International Journal of Heat and Fluid Flow*, 16(5), pp.365-375.

- Blake, W. (1988). *Mechanics of Flow-Induced Sound and Vibration. Vol. I: General Concepts and Elementary Sources and Vol. II Complex Flow-Structure Interaction* by William K. Blake. *Journal of the Acoustical Society of America*.
- Braun K.A. van der Borg, A. G. M. Dassen, F. Doorenspleet, A. Gordner, J. Ocker, and R. Parchen, (1999). *Serrated trailing edge noise. European wind energy conference, Nice*.
- Braun, K., Gordner, v.d. Borg N.J.C.M., Dassen A.G.M., Doorenspleet F., Parchen R., (1998). *Serrated trailing edge noise (STENO), Publishable Final Report*.
- Brooks, T. and Hodgson, T. (1981). *Trailing edge noise prediction from measured surface pressures. Journal of Sound and Vibration, 78(1), pp.69-117*.
- Brooks, T. and Marcolini, M. (1986). *Airfoil tip vortex formation noise. AIAA Journal, 24(2), pp.246-252*.
- Brooks, T., Pope, D. and Marcolini, M. (1989). *Airfoil self-noise and prediction. [Washington, D.C.]: National Aeronautics and Space Administration, Office of Management, Scientific and Technical Information Division*.
- Browne, L., Antonia, R. and Chua, L. (1989). *Calibration of X-probes for turbulent flow measurements. Experiments in Fluids, 7(3), pp.201-208*.
- CAA, (2011). *Civil Aviation Authority (UK) Insight Note: Aviation Policy For The Environment*.
- Cantwell, B. and Coles, D. (1983). *An experimental study of entrainment and transport in the turbulent near wake of a circular cylinder. Journal of Fluid Mechanics, 136(-1), pp.321-374*.
- Castellano, R. (2012). *Alternative Energy Technologies. Old City Publishing*.
- Chase, D. (1975). *Noise Radiated from an Edge in Turbulent Flow. AIAA Journal, 13(8), pp.1041-1047*.
- Chase, D. (1987). *The character of the turbulent wall pressure spectrum at subconvective wavenumbers and a suggested comprehensive model. Journal of Sound and Vibration, 112(1), pp.125-147*.

- Chong, T., Joseph, P. and Davies, P. (2009). Design and performance of an open jet wind tunnel for aero-acoustic measurement. *Applied Acoustics*, 70(4), pp.605-614.
- Chong, T., Joseph, P. and Gruber, M. (2010) An Experimental Study of Airfoil Instability Noise with Trailing Edge Serrations. *16th AIAA/CEAS Aeroacoustics Conference*.
- Chong, T. and Joseph, P. (2013). An experimental study of airfoil instability tonal noise with trailing edge serrations. *Journal of Sound and Vibration*, 332(24), pp.6335-6358.
- Chong, T., Joseph, P. and Gruber, M. (2013). Airfoil self-noise reduction by non-flat plate type trailing edge serrations. *Applied Acoustics*, 74(4), pp.607-613.
- Crighton, D. (1975). Basic principles of aerodynamic noise generation. *Progress in Aerospace Sciences*, 16(1), pp.31-96.
- Curle, N. (1955). The Influence of Solid Boundaries upon Aerodynamic Sound. *Proceedings of the Royal Society A: Mathematical, Physical and Engineering Sciences*, 231(1187), pp.505-514.
- Daoud, M. (2004). Stochastic estimation of the flow structure downstream of a separating/reattaching flow region using wall-pressure array measurements. *ASME 2004 Heat Transfer/Fluids Engineering Summer Conference*, pp. 793-798.
- Dassen T., Parchen R., Bruggeman J. , Hagg F., (1996). Results of a wind tunnel study on the reduction of airfoil self-noise by the application of serrated blade trailing edges. *In Proc. of the European Union Wind Energy Conference and Exhibition, Göteborg, pp.800-803*.
- Delingpole, J. (2014). Wind farm noise: a government cover-up, *Telegraph Blogs*. [online] News - Telegraph Blogs. Available at: <http://blogs.telegraph.co.uk/news/jamesdelingpole/100248760/wind-farm-noise-a-government-cover-up> [Accessed 10 Dec. 2014].
- Desquesnes, G., Terracol, M. and Sagaut, P. (2007). Numerical investigation of the tone noise mechanism over laminar airfoils. *Journal of Fluid Mechanics*, 591, pp.155-182.
- DLR, (2015). *DLR - QICE*. [online] Qice.dlr.de. Available at: http://www.qice.dlr.de/pages/dlr_as.htm [Accessed 5 Nov. 2014].

- Doolan, C. (2013). A Review of Wind Turbine Noise Perception, Annoyance and Low Frequency Emission. *Wind Engineering*, 37(1), pp.97-104.
- EWEA - European Wind Energy Association, (2014). Wind Energy Scenarios for 2020, *A report by the European Wind Energy Association*.
- FAA - Federal Aviation Administration, (2007). Managing the Challenge of Growth. [online] Available at: http://www.faa.gov/air_traffic/environmental_issues/media/managing_challenge.pdf [Accessed 5 Jan. 2015].
- Finez A, Jondeau E., Roger M., and Jacob M.C., (2010). Broadband noise reduction with trailing edge brushes. *16th AIAA/CEAS Aeroacoustics Conference*.
- Fink M., Bailey D., (1980). Airframe noise reduction studies and clean-airframe noise. *NASA Contractor Report 159311*.
- Franzoni, L. (1998). An innovative design of a probe-tube attachment for a 1 2 -in. microphone. *J. Acoust. Soc. Am.*, 104(5), p.2903-2910.
- Garcia Sagrado, A. (2007). Boundary layer and trailing edge noise sources. PhD Thesis.
- General Electric, (2014). [online] Gereports.com. Available at: <http://www.gereports.com/post/92442325225/how-loud-is-a-wind-turbine> [Accessed 14 Dec. 2014].
- Geyer, T. and Sarradj, E. (2014). Trailing Edge Noise of Partially Porous Airfoils. *20th AIAA/CEAS Aeroacoustics Conference*.
- Geyer, T., Sarradj, E. and Fritzsche, C. (2010a). Measurement of the noise generation at the trailing edge of porous airfoils. *Exp Fluids*, 48(2), pp.291-308.
- Geyer, T., Sarradj, E. and Fritzsche, C. (2010b). Porous airfoils: noise reduction and boundary layer effects. *International Journal of Aeroacoustics*, 9(6), pp.787-820.
- Geyer, T., Sarradj, E. and Fritzsche, C. (2014). Measuring owl flight noise. *Internoise 2014*.
- Geyer T., Sarradj E. and Fritzsche C. (2011). *Silent Flight of the Owl: Results of Acoustic Bird Flyover Measurements*.
- Graham, J. (1976). Turbulent flow past a porous plate. *Journal of Fluid Mechanics*, 73(03),

pp.565-591.

Graham, R. (1934). The silent flight of owls. *Journal of the Royal Aeronautical Society* 286, pp. 837-843.

Greiser, E. (2006). Risikofaktor nächtlicher Fluglärm - macht Fluglärm krank?
Epi.Consult GmbH, Musweiler & Institut für Public Health und Pflegeforschung, Universität Bremen.

Grimwood C.J., Skinner C.J., Raw G.J., (2002). The UK National Noise Attitude Survey 1999/2000. *Noise Forum Conference.*

Gruber M., Joseph P., and Chong T., (2010). Experimental investigation of airfoil self - noise and turbulent wake reduction by the use of trailing edge serrations. *16th AIAA/CEAS Aeroacoustics Conference, Stockholm, June 2010.*

Gruber, M. (2012). Airfoil noise reduction by edge treatments. PhD Thesis. University of Southampton.

Gupta, A., Laufer, J. and Kaplan, R. (1971). Spatial structure in the viscous sublayer. *Journal of Fluid Mechanics*, 50(03), pp.493-512.

Head, M. and Bandyopadhyay, P. (1981). New aspects of turbulent boundary-layer structure. *Journal of Fluid Mechanics*, 107(-1), pp.297-338.

Herr M., Rossignol K., J. Delfs, Lippitz N., Mössner M., (2014). Specification of Porous Materials for Low-Noise Trailing-Edge Applications. *20th AIAA/CEAS Aeroacoustics Conference.*

Herr, M. (2006). Experimental study on noise reduction through trailing edge brushes. *New Results in Numerical and Experimental Fluid Mechanics.*

Hillingdon.gov.uk, (2013). *London Borough of Hillingdon - Heathrow referendum: Hillingdon votes against expansion.* [online] Hillingdon.gov.uk. Available at: <http://www.hillingdon.gov.uk/article/26825/Heathrow-referendum-Hillingdon-votes-against-expansion> [Accessed 23 Oct. 2014].

Howe, M. (1978). A review of the theory of trailing edge noise. *Journal of Sound and Vibration*, 61(3), pp.437-465.

- Howe, M. (1978). A review of the theory of trailing edge noise. *Journal of Sound and Vibration*, 61(3), pp.437-465.
- Howe, M. (1979). On the Added Mass of a Perforated Shell, with Application to the Generation of Aerodynamic Sound by a Perforated Trailing Edge. *Proceedings of the Royal Society A: Mathematical, Physical and Engineering Sciences*, 365(1721), pp.209-233.
- Howe, M. (1991a). Aerodynamic noise of a serrated trailing edge. *Journal of Fluids and Structures*, 5(1), pp.33-45.
- Howe, M. (1991b). Noise produced by a sawtooth trailing edge. *Journal of the Acoustical Society of America*, 90(1), pp.482-482.
- ICAO - International Civil Aviation Organization, (2013). *Night Flight Restrictions*. Worldwide Air Transport Conference (ATCONF).
- Ikeda, M. and Takaishi, T. (2004). Perforated Pantograph Horn Aeolian Tone Suppression Mechanism. *QR of RTRI*, 45(3), pp.169-174.
- Johnson, R. (1998). *The handbook of fluid dynamics*. Boca Raton, Fla.: CRC Press.
- Jones, K. and Rhodes, D. (2013). *Aircraft noise, sleep disturbance and health effects*. London: Stationery Office.
- Jones L. Sandberg R., (2010). Numerical investigation of airfoil self-noise reduction by addition of trailing-edge serrations. *16th AIAA/CEAS Aeroacoustics Conference, Stockholm, 2010*.
- Jones, L. and Sandberg, R. (2012). Acoustic and hydrodynamic analysis of the flow around an aerofoil with trailing-edge serrations. *Journal of Fluid Mechanics*, 706, pp.295-322.
- Jørgensen, F. (2005). How to measure turbulence with hot-wire anemometers. *Skovlunde: Dantec Dynamics*.
- Kim, H., Kline, S. and Reynolds, W. (1971). The production of turbulence near a smooth wall in a turbulent boundary layer. *Journal of Fluid Mechanics*, 50(01), pp.133-160.
- Kingan, M. and Pearse, J. (2009). Laminar boundary layer instability noise produced by

- an aerofoil. *Journal of Sound and Vibration*, 322(4-5), pp.808-828.
- Kline S. J., Reynolds W. C., Schraub R. A., and Runstadler P.W., (1967). The structure of turbulent boundary layers. *Journal of Fluid Mechanics*, 30(4), pp. 741-773.
- Kline, S., Afgan, N. and Zanic, Z. (1990). *Near-wall turbulence*. New York: Hemisphere Pub. Corp.
- Knepper, A. (2005). *Examination of three candidate technologies for high-lift devices on an aircraft wing*. Cranfield: Cranfield University.
- Kroeger, R., Grushka, H. and Helvey, T. (1971). *Low Speed Aerodynamics for Ultra-Quiet Flight*. Ft. Belvoir: Defense Technical Information Center.
- Lekakis, I., Adrian, R. and Jones, B. (1989). Measurement of velocity vectors with orthogonal and non-orthogonal triple-sensor probes. *Experiments in Fluids*, 7(4), pp. 228-240.
- Lekakis, I. (1996). Calibration and signal interpretation for single and multiple hot-wire/hot-film probes. *Meas. Sci. Technol.*, 7(10), pp.1313-1333.
- Lighthill, M. (1951). On Sound Generated Aerodynamically. I. General Theory. *Proceedings of the Royal Society A: Mathematical, Physical and Engineering Sciences*, 211(1107), pp.564-587.
- Lighthill, M. (1954). On Sound Generated Aerodynamically. II. Turbulence as a Source of Sound. *Proceedings of the Royal Society A: Mathematical, Physical and Engineering Sciences*, 222(1148), pp.1-32.
- Lilley GM, (1998). A study of the silent flight of the owl. *4th AIAA/CEAS aeroacoustics conference AIAA Paper*.
- Little, B. (1989). Propfan Test Assessment (PTA). [Cleveland, Ohio]: *National Aeronautics and Space Administration, Lewis Research Center*.
- Lowson, MV, Fiddes SP, Nash, (1994). Laminar boundary layer aeroacoustic instabilities. *AIAA paper*, 94-0358.
- Mcdonough, JM. (2007). Introductory lectures on turbulence physics, mathematics and modelling.

- Moreau, D. J., Brooks, L. A., and Doolan, C. J., (2012). On the Noise Reduction Mechanism of a Flat Plate Serrated Trailing Edge at Low-to-moderate Reynolds Number. *AIAA Paper 2012-2186*.
- Moreau, S. and Roger, M. (2009). Back-scattering correction and further extensions of Amiet's trailing-edge noise model. Part II: Application. *Journal of Sound and Vibration*, 323(1-2), pp.397-425.
- Morris, M. (2012). *Waterloo Wind Farm Survey April 2012*.
- MTU Aero Engines, (2012). *On the horizon: Whispering jets*. MTU Aero Engines Report.
- Oerlemans, S. (2014). *Low-noise wind turbine design*. PhD Thesis.
- Oerlemans, S., Fisher, M., Maeder, T. and Kögler, K. (2009). Reduction of Wind Turbine Noise Using Optimized Airfoils and Trailing-Edge Serrations. *AIAA Journal*, 47(6), pp.1470-1481.
- Ozcan HK., Nemlioglu S., (2006). In-cabin noise levels during commercial aircraft flights. *Canadian Acoustics*, Vol 34(4), pp. 31-35.
- Pagano, M. (2009). *Are wind farms a health risk? US scientist identifies 'wind turbine syndrome'*. [online] The Independent. Available at: <http://www.independent.co.uk/environment/green-living/are-wind-farms-a-health-risk-us-scientist-identifies-wind-turbine-syndrome-1766254.html> [Accessed 5 Jan. 2015].
- Panton, R. (2001). Overview of the self-sustaining mechanisms of wall turbulence. *Progress in Aerospace Sciences*, 37(4), pp.341-383.
- Paterson, R. and Amiet, R. (1977). Noise and Surface Pressure Response of an Airfoil to Incident Turbulence. *Journal of Aircraft*, 14(8), pp.729-736.
- Paterson, R., Amiet, R. and Munch, C. (1975). Isolated Airfoil-Tip Vortex Interaction Noise. *Journal of Aircraft*, 12(1), pp.34-40.
- Paterson, R., Vogt, P., Fink, M. and Munch, C. (1973). Vortex Noise of Isolated Airfoils. *Journal of Aircraft*, 10(5), pp.296-302.
- Pope, S. (2000). *Turbulent flows*. Cambridge: Cambridge University Press.

- Powell, A. (1959). On the Aerodynamic Noise of a Rigid Flat Plate Moving at Zero Incidence. *The Journal of the Acoustical Society of America*, 31(12), p.1649.
- Prandtl, L. (1905). Verhandlungen des dritten internationalen Mathematiker-Kongresses in Heidelberg vom 8 bis 13 August, 1904. *Bulletin of the American Mathematical Society*, pp.484-484.
- Pröbsting, S. (2011). Coherent structures at the serrated trailing-edge. Master Thesis. TU Delft.
- Pröbsting, S., Serpieri, J. and Scarano, F. (2014). Experimental investigation of aerofoil tonal noise generation. *Journal of Fluid Mechanics*, 747, pp.656-687.
- Revell J, Kuntz H, Balena F, Horne W, Storms B, Dougherty R, (1997). Trailing edge flap noise reduction by porous acoustic treatment. 3rd AIAA/CEAS aeroacoustics conference.
- Reynolds, W. and Hussain, A. (1972). The mechanics of an organized wave in turbulent shear flow. Part 3. Theoretical models and comparisons with experiments. *Journal of Fluid Mechanics*, 54(02), pp.263-288.
- Robinson, S. (1991). Coherent Motions In The Turbulent Boundary Layer. *Annual Review of Fluid Mechanics*, 23(1), pp.601-639.
- Robinson, S. (1993). The kinematics of turbulent boundary layer structure. *Moffett Field, Calif.: National Aeronautics and Space Administration, Ames Research Center*.
- Rodriguez, O. (1991). Base drag reduction by control of the three-dimensional unsteady vortical structures. *Experiments in Fluids*, 11(4), pp.218-226.
- Roger M. and Moreau S., (2002). Trailing Edge Noise Measurements and Prediction for Subsonic Loaded Fan Blades. *AIAA Paper*, No. 2002-2460.
- Rolls-Royce Plc., (2005). The Jet Engine. 6th ed. Rolls-Royce Plc.
- Sabatino, D. (2015). Turbulence Research | Daniel Sabatino. [online] Sites.lafayette.edu. Available at: <http://sites.lafayette.edu/sabatind/turbulence-research/> [Accessed 5 Nov. 2014].
- Saddoughi, S., and Veeravalli, S., (1994). Local isotropy in turbulent boundary layers at

- high Reynolds number. *Journal of Fluid Mechanics* 268, pp. 333-372.
- Sarradj E, Geyer T., (2007). Noise generation by porous airfoils. *13th AIAA/CEAS aeroacoustics conference, AIAA paper*.
- Sarradj, E., Fritzsche, C. and Geyer, T. (2011). Silent Owl Flight: Bird Flyover Noise Measurements. *AIAA Journal*, 49(4), pp.769-779.
- SBC, (2011). *Wind Power, SBC*. [online] Sbc.slb.com. Available at: <http://www.sbc.slb.com/SBCInstitute/Publications/Wind.aspx> [Accessed 7 Nov. 2014].
- Scheidegger, A., (1974) *The physics of flow through porous media*, 3rd ed. University of Toronto Press, Toronto
- Schewe, G. (1983). On the structure and resolution of wall-pressure fluctuations associated with turbulent boundary-layer flow. *Journal of Fluid Mechanics*, 134(-1), pp.311-328.
- Smith, C. and Metzler, S. (1983). The characteristics of low-speed streaks in the near-wall region of a turbulent boundary layer. *Journal of Fluid Mechanics*, 129(-1), pp.27-54.
- Süddeutsche Zeitung GmbH, G. (2013). *Flughafen München - "Münchner stoppen dritte Startbahn*. [online] Süddeutsche.de. Available at: http://www.sueddeutsche.de/thema/Dritte_Startbahn [Accessed 5 Nov. 2014].
- Tam, C. (1974). Discrete tones of isolated airfoils. *The Journal of the Acoustical Society of America*., 55(6), pp.1173-1177.
- The Future of Air Transport, White paper (2003). Department for Transport (UK).
- Theodorsen T., (1952). Mechanism of turbulence. *Proceedings of the Second Midwestern Conference on Fluid Mechanics, Ohio State University*., pp.1-18.
- Traub P , Engel K, (2012). *Noise Aspects of Future Jet Engines*. MTU Aero Engines Report, LTH Anlage A ,.
- Tsui, C. and Flandro, G. (1977). Self-induced sound generation by flow over perforated duct liners. *Journal of Sound and Vibration*, 50(3), pp.315-331.

- Ver, (1982). Perforated Baffles Prevent Flow-Induced Acoustic Resonances in Heat Exchangers. Proceedings DAGA/FASE 82, pp. 531-534.
- Ver, I. (1987). Noise of jet engine test cells. *Jet Engine Test Cell Meeting, Noise of jet engine test cells.*
- Wagner, S., Bareiss, R. and Guidati, G. (1996). *Wind turbine noise.* Berlin: Springer.
- Wallace, J., Brodkey, R. and Eckelmann, H. (1977). Pattern-recognized structures in bounded turbulent shear flows. *Journal of Fluid Mechanics*, 83(04), pp.673-693.
- Whatever happened to propfans. (2007). *Flight International*, (07-12).
- Williams, J. and Hall, L. (1970). Aerodynamic sound generation by turbulent flow in the vicinity of a scattering half plane. *Journal of Fluid Mechanics*, 40(04), pp.657-670.
- Yu J. C and Joshi M. C., (1979). On Sound Radiation from the Trailing Edge of an Isolated Airfoil in a Uniform Flow. *AIAA Conference Paper.*
- Zhong, S., Chong, T. and Hodson, H. (2003). A Comparison of Spreading Angles of Turbulent Wedges in Velocity and Thermal Boundary Layers. *Journal of Fluids Engineering.*, 125(2), pp.267-274.